

Advances in Civil Engineering

Risk and Reliability Assessment for Hazard Control

Lead Guest Editor: S. Mahdi Seyed-Kolbadi

Guest Editors: Angelo Marcelo Tuset and Wahyu Caesarendra





Risk and Reliability Assessment for Hazard Control

Advances in Civil Engineering

Risk and Reliability Assessment for Hazard Control

Lead Guest Editor: S. Mahdi Seyed-Kolbadi

Guest Editors: Angelo Marcelo Tuset and Wahyu
Caesarendra



Copyright © 2023 Hindawi Limited. All rights reserved.

This is a special issue published in "Advances in Civil Engineering." All articles are open access articles distributed under the Creative Commons Attribution License, which permits unrestricted use, distribution, and reproduction in any medium, provided the original work is properly cited.






Chief Editor

Cumaraswamy Vipulanandan, USA













Associate Editors

Chiara Bedon , Italy
Constantin Chalioris , Greece
Ghassan Chehab , Lebanon
Ottavia Corbi, Italy
Mohamed ElGawady , USA
Husnain Haider , Saudi Arabia
Jian Ji , China
Jiang Jin , China
Shazim A. Memon , Kazakhstan
Hossein Moayedi , Vietnam
Sanjay Nimbalkar, Australia
Giuseppe Oliveto , Italy
Alessandro Palmeri , United Kingdom
Arnaud Perrot , France
Hugo Rodrigues , Portugal
Victor Yepes , Spain
Xianbo Zhao , Australia

Academic Editors

José A.F.O. Correia, Portugal
Glenda Abate, Italy
Khalid Abdel-Rahman , Germany
Ali Mardani Aghabaglou, Turkey
José Aguiar , Portugal
Afaq Ahmad , Pakistan
Muhammad Riaz Ahmad , Hong Kong
Hashim M.N. Al-Madani , Bahrain
Luigi Aldieri , Italy
Angelo Aloisio , Italy
Maria Cruz Alonso, Spain
Filipe Amarante dos Santos , Portugal
Serji N. Amirkhania, USA
Eleftherios K. Anastasiou , Greece
Panagiotis Ch. Anastasopoulos , USA
Mohamed Moafak Arbili , Iraq
Farhad Aslani , Australia
Siva Avudaiappan , Chile
Ozgur BASKAN , Turkey
Adewumi Babafemi, Nigeria
Morteza Bagherpour, Turkey
Qingsheng Bai , Germany
Nicola Baldo , Italy
Daniele Baraldi , Italy

Eva Barreira , Portugal
Emilio Bastidas-Arteaga , France
Rita Bento, Portugal
Rafael Bergillos , Spain
Han-bing Bian , China
Xia Bian , China
Huseyin Bilgin , Albania
Giovanni Biondi , Italy
Hugo C. Biscaia , Portugal
Rahul Biswas , India
Edén Bojórquez , Mexico
Giosuè Boscato , Italy
Melina Bosco , Italy
Jorge Branco , Portugal
Bruno Briseghella , China
Brian M. Broderick, Ireland
Emanuele Brunesi , Italy
Quoc-Bao Bui , Vietnam
Tan-Trung Bui , France
Nicola Buratti, Italy
Gaochuang Cai, France
Gladis Camarini , Brazil
Alberto Campisano , Italy
Qi Cao, China
Qixin Cao, China
Iacopo Carnacina , Italy
Alessio Cascardi, Italy
Paolo Castaldo , Italy
Nicola Cavalagli , Italy
Liborio Cavaleri , Italy
Anush Chandrappa , United Kingdom
Wen-Shao Chang , United Kingdom
Muhammad Tariq Amin Chaudhary, Kuwait
Po-Han Chen , Taiwan
Qian Chen , China
Wei Tong Chen , Taiwan
Qixiu Cheng, Hong Kong
Zhanbo Cheng, United Kingdom
Nicholas Chileshe, Australia
Prinya Chindaprasirt , Thailand
Corrado Chisari , United Kingdom
Se Jin Choi , Republic of Korea
Heap-Yih Chong , Australia
S.H. Chu , USA
Ting-Xiang Chu , China


Zhaofei Chu , China
Wonseok Chung , Republic of Korea
Donato Ciampa , Italy
Gian Paolo Cimellaro, Italy
Francesco Colangelo, Italy
Romulus Costache , Romania
Liviu-Adrian Cotfas , Romania
Antonio Maria D'Altri, Italy
Bruno Dal Lago , Italy
Amos Darko , Hong Kong
Arka Jyoti Das , India
Dario De Domenico , Italy
Gianmarco De Felice , Italy
Stefano De Miranda , Italy
Maria T. De Risi , Italy
Tayfun Dede, Turkey
Sadik O. Degertekin , Turkey
Camelia Delcea , Romania
Cristoforo Demartino, China
Giuseppe Di Filippo , Italy
Luigi Di Sarno, Italy
Fabio Di Trapani , Italy
Aboelkasim Diab , Egypt
Thi My Dung Do, Vietnam
Giulio Dondi , Italy
Jiangfeng Dong , China
Chao Dou , China
Mario D'Aniello , Italy
Jingtao Du , China
Ahmed Elghazouli, United Kingdom
Francesco Fabbrocino , Italy
Flora Faleschini , Italy
Dingqiang Fan, Hong Kong
Xueping Fan, China
Qian Fang , China
Salar Farahmand-Tabar , Iran
Ilenia Farina, Italy
Roberto Fedele, Italy
Guang-Liang Feng , China
Luigi Fenu , Italy
Tiago Ferreira , Portugal
Marco Filippo Ferrotto, Italy
Antonio Formisano , Italy
Guoyang Fu, Australia
Stefano Galassi , Italy

Junfeng Gao , China
Meng Gao , China
Giovanni Garcea , Italy
Enrique García-Macías, Spain
Emilio García-Taengua , United Kingdom
DongDong Ge , USA
Khaled Ghaedi, Malaysia
Khaled Ghaedi , Malaysia
Gian Felice Giaccu, Italy
Agathoklis Giaralis , United Kingdom
Ravindran Gobinath, India
Rodrigo Gonçalves, Portugal
Peilin Gong , China
Belén González-Fonteboa , Spain
Salvatore Grasso , Italy
Fan Gu, USA
Erhan Güneyisi , Turkey
Esra Mete Güneyisi, Turkey
Pingye Guo , China
Ankit Gupta , India
Federico Gusella , Italy
Kemal Hacıfendioglu, Turkey
Jianyong Han , China
Song Han , China
Asad Hanif , Macau
Hadi Hasanzadehshooiili , Canada
Mostafa Fahmi Hassanein, Egypt
Amir Ahmad Hedayat , Iran
Khandaker Hossain , Canada
Zahid Hossain , USA
Chao Hou, China
Biao Hu, China
Jiang Hu , China
Xiaodong Hu, China
Lei Huang , China
Cun Hui , China
Bon-Gang Hwang, Singapore
Jijo James , India
Abbas Fadhil Jasim , Iraq
Ahad Javanmardi , China
Krishnan Prabhakan Jaya, India
Dong-Sheng Jeng , Australia
Han-Yong Jeon, Republic of Korea
Pengjiao Jia, China
Shaohua Jiang , China

MOUSTAFA KASSEM , Malaysia
Mosbeh Kaloop , Egypt
Shankar Karuppanan , Ethiopia
John Kechagias , Greece
Mohammad Khajehzadeh , Iran
Afzal Husain Khan , Saudi Arabia
Mehran Khan , Hong Kong
Manoj Khandelwal, Australia
Jin Kook Kim , Republic of Korea
Woosuk Kim , Republic of Korea
Vaclav Koci , Czech Republic
Loke Kok Foong, Vietnam
Hailing Kong , China
Leonidas Alexandros Kouris , Greece
Kyriakos Kourousis , Ireland
Moacir Kripka , Brazil
Anupam Kumar, The Netherlands
Emma La Malfa Ribolla, Czech Republic
Ali Lakirouhani , Iran
Angus C. C. Lam, China
Thanh Quang Khai Lam , Vietnam
Luciano Lamberti, Italy
Andreas Lampropoulos , United Kingdom
Raffaele Landolfo, Italy
Massimo Latour , Italy
Bang Yeon Lee , Republic of Korea
Eul-Bum Lee , Republic of Korea
Zhen Lei , Canada
Leonardo Leonetti , Italy
Chun-Qing Li , Australia
Dongsheng Li , China
Gen Li, China
Jiale Li , China
Minghui Li, China
Qingchao Li , China
Shuang Yang Li , China
Sunwei Li , Hong Kong
Yajun Li , China
Shun Liang , China
Francesco Liguori , Italy
Jae-Han Lim , Republic of Korea
Jia-Rui Lin , China
Kun Lin , China
Shibin Lin, China

Tzu-Kang Lin , Taiwan
Yu-Cheng Lin , Taiwan
Hexu Liu, USA
Jian Lin Liu , China
Xiaoli Liu , China
Xuemei Liu , Australia
Zaobao Liu , China
Zhuang-Zhuang Liu, China
Diego Lopez-Garcia , Chile
Cristiano Loss , Canada
Lyan-Ywan Lu , Taiwan
Jin Luo , USA
Yanbin Luo , China
Jianjun Ma , China
Junwei Ma , China
Tian-Shou Ma, China
Zhongguo John Ma , USA
Maria Macchiaroli, Italy
Domenico Magisano, Italy
Reza Mahinroosta, Australia
Yann Malecot , France
Prabhat Kumar Mandal , India
John Mander, USA
Iman Mansouri, Iran
André Dias Martins, Portugal
Domagoj Matesan , Croatia
Jose Matos, Portugal
Vasant Matsagar , India
Claudio Mazzotti , Italy
Ahmed Mebarki , France
Gang Mei , China
Kasim Mermerdas, Turkey
Giovanni Minafò , Italy
Masoomah Mirrashid , Iran
Abbas Mohajerani , Australia
Fadzli Mohamed Nazri , Malaysia
Fabrizio Mollaioli , Italy
Rosario Montuori , Italy
H. Naderpour , Iran
Hassan Nasir , Pakistan
Hossein Nassiraei , Iran
Satheeskumar Navaratnam , Australia
Ignacio J. Navarro , Spain
Ashish Kumar Nayak , India
Behzad Nematollahi , Australia

Chayut Ngamkhanong , Thailand
Trung Ngo, Australia
Tengfei Nian, China
Mehdi Nikoo , Canada
Youjun Ning , China
Olugbenga Timo Oladinrin , United Kingdom
Oladimeji Benedict Olalusi, South Africa
Timothy O. Olawumi , Hong Kong
Alejandro Orfila , Spain
Maurizio Orlando , Italy
Siti Aminah Osman, Malaysia
Walid Oueslati , Tunisia
SUVASH PAUL , Bangladesh
John-Paris Pantouvakis , Greece
Fabrizio Paolacci , Italy
Giuseppina Pappalardo , Italy
Fulvio Parisi , Italy
Dimitrios G. Pavlou , Norway
Daniele Pellegrini , Italy
Gatheeshgar Perampalam , United Kingdom
Daniele Perrone , Italy
Giuseppe Piccardo , Italy
Vagelis Plevris , Qatar
Andrea Pranno , Italy
Adolfo Preciado , Mexico
Chongchong Qi , China
Yu Qian, USA
Ying Qin , China
Giuseppe Quaranta , Italy
Krishanu ROY , New Zealand
Vlastimir Radonjanin, Serbia
Carlo Rainieri , Italy
Rahul V. Ralegaonkar, India
Raizal Saifulnaz Muhammad Rashid, Malaysia
Alessandro Rasulo , Italy
Chonghong Ren , China
Qing-Xin Ren, China
Dimitris Rizos , USA
Geoffrey W. Rodgers , New Zealand
Pier Paolo Rossi, Italy
Nicola Ruggieri , Italy
JUNLONG SHANG, Singapore




Nikhil Saboo, India
Anna Saetta, Italy
Juan Sagaseta , United Kingdom
Timo Saksala, Finland
Mostafa Salari, Canada
Ginevra Salerno , Italy
Evangelos J. Sapountzakis , Greece
Vassilis Sarhosis , United Kingdom
Navaratnarajah Sathiparan , Sri Lanka
Fabrizio Scozzese , Italy
Halil Sezen , USA
Payam Shafigh , Malaysia
M. Shahria Alam, Canada
Yi Shan, China
Hussein Sharaf, Iraq
Mostafa Sharifzadeh, Australia
Sanjay Kumar Shukla, Australia
Amir Si Larbi , France
Okan Sirin , Qatar
Piotr Smarzewski , Poland
Francesca Sollecito , Italy
Rui Song , China
Tian-Yi Song, Australia
Flavio Stochino , Italy
Mayank Sukhija , USA
Piti Sukontasukkul , Thailand
Jianping Sun, Singapore
Xiao Sun , China
T. Tafsirojjan , Australia
Fujiao Tang , China
Patrick W.C. Tang , Australia
Zhi Cheng Tang , China
Weerachart Tangchirapat , Thailand
Xiabin Tao, China
Piergiorgio Tataranni , Italy
Elisabete Teixeira , Portugal
Jorge Iván Tobón , Colombia
Jing-Zhong Tong, China
Francesco Trentadue , Italy
Antonello Troncone, Italy
Majbah Uddin , USA
Tariq Umar , United Kingdom
Muahmmad Usman, United Kingdom
Muhammad Usman , Pakistan
Mucteba Uysal , Turkey

Ilaria Venanzi , Italy
Castorina S. Vieira , Portugal
Valeria Vignali , Italy
Claudia Vitone , Italy
Liwei WEN , China
Chunfeng Wan , China
Hua-Ping Wan, China
Roman Wan-Wendner , Austria
Chaohui Wang , China
Hao Wang , USA
Shiming Wang , China
Wayne Yu Wang , United Kingdom
Wen-Da Wang, China
Xing Wang , China
Xiuling Wang , China
Zhenjun Wang , China
Xin-Jiang Wei , China
Tao Wen , China
Weiping Wen , China
Lei Weng , China
Chao Wu , United Kingdom
Jiangyu Wu, China
Wangjie Wu , China
Wenbing Wu , China
Zhixing Xiao, China
Gang Xu, China
Jian Xu , China
Panpan , China
Rongchao Xu , China
HE YONGLIANG, China
Michael Yam, Hong Kong
Hailu Yang , China
Xu-Xu Yang , China
Hui Yao , China
Xinyu Ye , China
Zhoujing Ye, China
Gürol Yildirim , Turkey
Dawei Yin , China
Doo-Yeol Yoo , Republic of Korea
Zhanping You , USA
Afshar A. Yousefi , Iran
Xinbao Yu , USA
Dongdong Yuan , China
Geun Y. Yun , Republic of Korea

Hyun-Do Yun , Republic of Korea
Cemal YİĞİT , Turkey
Paolo Zampieri, Italy
Giulio Zani , Italy
Mariano Angelo Zanini , Italy
Zhixiong Zeng , Hong Kong
Mustafa Zeybek, Turkey
Henglong Zhang , China
Jiupeng Zhang, China
Tingting Zhang , China
Zengping Zhang, China
Zetian Zhang , China
Zhigang Zhang , China
Zhipeng Zhao , Japan
Jun Zhao , China
Annan Zhou , Australia
Jia-wen Zhou , China
Hai-Tao Zhu , China
Peng Zhu , China
QuanJie Zhu , China
Wenjun Zhu , China
Marco Zucca, Italy
Haoran Zuo, Australia
Junqing Zuo , China
Robert Černý , Czech Republic
Süleyman İpek , Turkey

Contents

Attenuation Relationships for the Horizontal Component of Peak Ground Acceleration (PGAH) Using Gene Expression Programming (GEP) and Group Method of Data Handling (GMDH)

Mehrassa Ajam , Mohammad Shamekhi Amiri , and Hossein Pahlavan 
Research Article (14 pages), Article ID 8394046, Volume 2023 (2023)


Mechanical Analysis of Junction Pier of Fuzhou-Xiamen High-Speed Railway Rigid-Frame Bridge

Fangwen Weng  and Fuxing Liu 
Research Article (16 pages), Article ID 7563415, Volume 2023 (2023)


Closure Scheme Analysis of 3 × 70 m Bearingless Integral Rigid Frame Bridge of Fuzhou Xiamen High-Speed Railway

Fangwen Weng  and Xiangui Li 
Research Article (11 pages), Article ID 6357539, Volume 2023 (2023)



The Behavior of RC Beams Strengthened with Steel Fiber Concrete Layer by ANSYS Simulation

Thanh Quang Khai Lam  and Thi My Dung Do 
Research Article (17 pages), Article ID 4711699, Volume 2023 (2023)

Shield Cutting Pile-Group Implementation Effects on the Superstructure

Chi Zhang, Shiju Ma , Yuancheng Guo, Mingyu Li, and Kui Fu
Research Article (12 pages), Article ID 4958566, Volume 2022 (2022)


Convergence Study of Variational Space-Time Coupled Least-Squares Frameworks in Simulation of Wave Propagation in Viscoelastic Medium

M. A. Saffarian , A. R. Ahmadi, and M. H. Bagheripour 
Research Article (14 pages), Article ID 1764236, Volume 2022 (2022)

Numerical and Large-Scale Laboratory Study of Rock Column Groups in Sandy Soil Behavior Improvement

Ali Yousefi Samangani  and Reza Naderi
Research Article (11 pages), Article ID 9259093, Volume 2022 (2022)

Evaluation of the Seismic Behavior Based on the Performance of Special Steel Moment Frames by Modified Energy Method and Force Design Method

Ramin Bagherzadeh, Abolfazl Riahi Nouri , Mohammad Sajjad Massoudi, Mohammad Ghazi, and Farzan Haddad Shargh
Research Article (22 pages), Article ID 6718796, Volume 2022 (2022)

Estimating the Geological Strength Index (GSI) in Regional Seismic-Landslide Zonation Using the Empirical Regression Model

M. E. Mirabedini , E. Haghshenas , and N. Ganjian
Research Article (14 pages), Article ID 4798523, Volume 2022 (2022)

Fire Risk Assessment and Experimental Study of Transformer Insulating Oil





Ji Jun, Chen Xin, Li Lin, Zhu Hui , Nie Jing kai, and Han Yu
Research Article (12 pages), Article ID 7185045, Volume 2022 (2022)

Stress Performance Evaluation of Shield Machine Cutter Head during Cutting Piles under Masonry Structures

Fei Peng, Shiju Ma , Mingyu Li, and Kui Fu

Research Article (11 pages), Article ID 4111637, Volume 2022 (2022)

Prediction of Long-Term Prestress Loss and Crack Resistance Analysis of Corroded Prestressed Concrete Box-Girder Bridges

Yiming Yang , Huang Tang , Yu Mao , and Xinzhong Wang 

Research Article (16 pages), Article ID 1309936, Volume 2022 (2022)

Research Article

Attenuation Relationships for the Horizontal Component of Peak Ground Acceleration (PGA_H) Using Gene Expression Programming (GEP) and Group Method of Data Handling (GMDH)

Mehrasa Ajam , Mohammad Shamekhi Amiri , and Hossein Pahlavan 

Faculty of Civil Engineering, Shahrood University of Technology, Shahrood, Iran

Correspondence should be addressed to Mohammad Shamekhi Amiri; shamekhi@shahroodut.ac.ir

Received 27 June 2022; Revised 6 December 2022; Accepted 13 April 2023; Published 4 December 2023

Academic Editor: Angelo Marcelo Tusset

Copyright © 2023 Mehrasa Ajam et al. This is an open access article distributed under the Creative Commons Attribution License, which permits unrestricted use, distribution, and reproduction in any medium, provided the original work is properly cited.

Earthquake is one of the natural disasters that has always influenced human life. It is not currently possible to predict exactly when and where an earthquake will occur, nor how large it will be. It is also impossible to prevent an earthquake. However, by designing seismic-resistant structures, the amount of financial losses and casualties can be reduced. This resistant design requires the use of earthquake risk analysis. By using the earthquake risk analysis, it will be possible to estimate the parameters of the strong ground motion, including acceleration, velocity, and displacement in each area. Estimating the parameters of strong ground motion will be possible just by obtaining the appropriate attenuation relationship. The aim of this paper is to present an appropriate attenuation relationship to estimate the horizontal component of the possible occurrence of peak ground acceleration in each region. Two methods were used to calculate attenuation relationship: gene expression programming (GEP) and group method of data handling (GMDH). In the first step, an up-to-date and comprehensive catalog consisting of 1,185 earthquake records that occurred around the world has been prepared. In the next step, the parameters of magnitude, hypocentral distance, and shear wave velocity of these records have been used as variables of the attenuation relationship. Then, the fitness function (f) was determined, and attenuation relationships were calculated using GEP and GMDH. The amount of fitness function (f) was obtained 766.12 from 1,000 in the GEP method and 767.77 from 1,000 in the GMDH method. The values of the fitness function, residuals and comparison plots showed a high-agreement between “the values predicted by the attenuation relationships” and “the actual values observed in the earthquakes.” Finally, according to the results of this research, it can be said that the use of GEP and GMDH methods has provided better results than the other similar researches. Also, the use of up-to-date records makes the results of this research more reliable than the previous researches.

1. Introduction

Human life has always been influenced by the natural disasters such as floods, storms, and earthquakes. These disasters have always threatened human life and property. The occurrence of these natural disasters will never stop and posterity will always be threatened. One of the most important and unpredictable events is an earthquake. Many earthquakes usually occur annually in the world. Some of them occur in vacant and barren areas, which are certainly not considered a threat to humans. Some earthquakes are so mild that they are not even felt by humans and are only recorded by the accelerometers. However, high-intensity

earthquakes may occur in residential environments and pose a constant threat to humans.

Japan, the United States, China, India, New Zealand, and Iran are considered as the seismic countries in the world. In Japan, from 1945 to 1995, 14 earthquakes with a magnitude greater than 6.5-Richter happened in 50 years that, left more than 8,000 victims. The Fukushima earthquake (2011) with a moment magnitude about 9, is one of the strongest earthquakes in Japan since 1900. The record for the largest earthquake in history with a moment magnitude 9.5 also belongs to Chile, which occurred in 1960 [1].

Earthquakes had been considered an unknown phenomenon several centuries ago. However, today scientific advances

made in the field of seismic geotechnical engineering and more knowledge of the internal structure of the earth have led to the understanding of the various phases of the earthquake and its effects on the earth's movement. Despite the achieved progress, it is impossible to predict its occurrence anywhere in the world, but it is possible to prepare for it by building seismic-resistant structures. The purpose of designing earthquake resistant structures is to construct structures that withstand seismic loads, do not undergo a lot of damage and rescue the inhabitants. To achieve this goal, it is necessary to predict and estimate the severity of possible earthquakes in each area following its various features. This goal is possible just through risk analysis. The prerequisite of risk analysis studies is to identify the parameters of strong ground motion for different areas [2].

The amount of strong ground motion is attributed to the magnitude, source to site distance, the source mechanism (type of faulting), geology of the region, surface topography, and dynamic properties of the material propagation [3]. Also, other parameters including soil nonlinear behavior, directivity, rupture propagation, and basin effects on ground motion can be even more effective than some of the above mentioned independent parameters [4].

In order to determine the impact of various earthquake parameters on a structure or a site located at a distance from the earthquake center, attenuation relationships are used.

Attenuation relationships are usually presented for important earthquake characteristics such as peak horizontal and vertical acceleration, peak ground velocity (PGV), elastic response spectra, and inelastic response spectra. The largest number of attenuation relationships is presented for peak ground acceleration (PGA) estimation.

The purpose of the present study is to present a new global attenuation relationship to estimate the horizontal component of peak ground acceleration (PGAH) using the two methods of gene expression programming (GEP) and group method of data handling (GMDH) and compare the results.

2. Overview of the Attenuation Relationships

Attenuation relations were first introduced in the 1960s by Neumann. Neumann [5] provided the attenuation model of PGA in 1954 for earthquakes in America. The only parameter involved was the distance of the accelerograph from the earthquake's center. In Newman's attenuation relationship, even the role of earthquake magnitude was ignored. Subsequently, models were developed from the 1970s to mid-1980s by Milne and Davenport [6], Esteva [7], Denham and Small [8], Donovan [9], Esteva and Villaverde [10], Orphal and Lahoud [11]. In these models, in addition to the distance of the accelerometer from the earthquake center, the magnitude of the earthquake was also included in the calculations. However, the strong role of soils in providing these relationships and the amount of damage was still ignored. Following the damage caused by the 1964 earthquakes in Niigata, Japan, and Alaska, progress was made in expanding the effective parameters in the attenuation relationships. Since 1976, a

new parameter indicating soil type was added to the attenuation relationship [12]. After that, many attenuation models were presented by various researchers for the different regions, some of them are explained below.

In 1981, Joyner and Boore [13] proposed a new attenuation relationship based on the North American earthquakes. The catalog consisted of earthquakes with surface wave magnitude (M_S) from 5 to 7.7 and records were taken from stations less than 370 km from the epicenter. Also, soil type has been effective in estimating acceleration as a coefficient for both soil and rock [13].

The Atkinson and Boore [14] attenuation model was also presented in 1990 based on North American earthquakes with a moment magnitude (M_W) between 5 and 7, which occurred at a distance of 10–100 km of earthquake accelerometers.

Sarma and Free [15] presented Equation 1 in 1995

$$\log(\text{PGA}) = -3.436 + 0.8532M - 0.0192M^2 - (0.9011 \times \log(R)) - 0.002R - 0.0316S, \quad (1)$$

where M , R , and PGA are the magnitude, the hypocentral distance (km) and PGA (cm/s^2), respectively. Also, the variable S in this relation is "zero" for the rock and "one" for the soil.

Following advances in technology and computer science in the early 21st century, intelligent methods have emerged and gradually replaced traditional methods. These changes led to the creation of more complex models in attenuation relationships. In 2007, Sobhaninejad et al. [16] used the intelligent genetic algorithm (GA) method to provide an attenuation relationship. Subsequently, Cabalar and Cevik [17] introduced a new attenuation relationship for Turkey in 2009 using the same method. In 2010, Ornthammarath et al. [18] also introduced a new relationship in which the shear wave velocity was also involved in this relationship and is shown in Equation (2).

$$\log(\text{PGA}) = -2.622 + 0.643M_W - 1.249 \log\left(\sqrt{r_{jb}^2 + 3.19^2}\right) + 0.344S_s, \quad (2)$$

where M_w is the moment magnitude, r_{jb} is Joyner–Boore distance (km), and PGA is the peak ground acceleration (cm/s^2). S_s that specifies the type of soil is selected according to the value of shear wave velocity as Equation 3.

$$\begin{aligned} 360(\text{m/s}) \leq V_{S_{30}} \leq 750(\text{m/s}) &\longrightarrow S_s = 1 \\ 750(\text{m/s}) < V_{S_{30}} &\longrightarrow S_s = 0. \end{aligned} \quad (3)$$

Other researchers who have used this method to present attenuation relationships including Kermani et al. [19], Jafarian et al. [20], Alavi and Gandomi [21], Ghodrati et al. [22, 23], and Gandomi et al. [24]. The relationship presented by Alavi and Gandomi [21] in 2011 is as Equation (4).

$$\begin{aligned} \ln(\text{PGA}) = & 6 - \ln(R_{\text{ClstD}}) + \frac{-1}{6} (\ln(R_{\text{ClstD}}))^2 \\ & + \frac{M_w}{6} \ln(R_{\text{ClstD}}) + \frac{6}{V_{s,30}} + (\ln(R_{\text{ClstD}}))^3 (V_{s,30})^{-1} \\ & + 64 \times \left[-8 - V_{s,30} + (5 \times V_{s,30} \sin(\lambda)) + \frac{V_{s,30}}{M_w - 7} \right]^{-1} \end{aligned} \quad (4)$$

In this relation, M_w is the moment magnitude, R_{ClstD} is the closest distance to the rupture surface (km), $V_{s,30}$ is the average shear-wave velocity over the top 30 m of the site (m/s), and PGA is the peak ground acceleration (cm/s^2).

One of the most recent attenuation relations was offered by Kumar et al. [25]. The relationship that was determined for the northeastern Himalaya region is presented as Equation (5):

$$\log(\text{PGA}) = -1.497 + 0.3882M - 1.19\log(R + e^{0.2876M}), \quad (5)$$

where M is the magnitude, R is the hypocentral distance (km), and PGA is the peak ground acceleration (cm/s^2). This relationship is based on the earthquakes that occurred in the northeastern part of the Himalayas with a magnitude range of 4–6.8.

In 2018, Javan-Emrooz et al. [26] presented Equation (6):

$$\begin{aligned} \log(\text{PGA}) = & \log \left[\frac{M}{\sqrt{\log(e^{s^{a3}} + e^M - R - (1/F))}} \right] \\ & + \ln \left[\frac{M+1}{RM} \right] + \ln(\log(\sqrt{M})) + 3. \end{aligned} \quad (6)$$

In this relation, M and R are the moment magnitude and the hypocentral distance (km), respectively. Also, PGA is the peak ground acceleration in centimeters per square second (cm/s^2). This attenuation model is based on earthquakes in northern Iran with a range of moment magnitude (M_w) of 4.5–7.4 and a hypocentral distance of 2–100 km.

Also, Erken et al. [27] provided attenuation relation equations by using nonlinear regression analysis in Northwest Anatolia region for two different site conditions.

Karimi-Ghalehjouh and Mahinroosta [28] presented attenuation relationship of horizontal and vertical PGA using regression analysis fuzzy logic model in Iranian plateau. In this study, three different site conditions were considered: rock, stiff soil, and soft soil [28].

Shiuly et al. [29] in 2020 presented a new model for prediction of PGA by using artificial neural network (ANN) and GA in Himalayan region for earthquake data recorded in rock sites.

One of the most recent suggested relationships is the Abdelfattah et al. [30] model, which was presented in 2021 as Equation (7).

$$\log(\text{PGA}) = -1.36 + 0.85M_L - 0.85\log(r) - 0.005r, \quad (7)$$

where M_L is the local magnitude, R is the hypocentral distance (km), and PGA is the peak ground acceleration (cm/s^2).

Also, in 2021 Kumar et al. [31] offered an attenuation relationship using regression based on the earthquakes that occurred in the central Himalayas with a magnitude range of 5–6.8.

Pourzeynali and Khadivyan [32] have provided attenuation relationship of horizontal and vertical PGA using regression analysis for Alborz zone of Iran.

3. Data Collection

The first step to present the attenuation relationship is to prepare a catalog of occurred earthquakes in a sufficient number and with high accuracy. In the present study, considering that the final relationship is global, records from all over the world were used and were chosen completely randomly and with appropriate dispersion. These records are obtained from the PEER (Public Employees for Environmental Responsibility (<https://ngawest2.berkeley.edu/>)) website by using the possibility of filtering the information of records such as earthquake record number, earthquake name, earthquake recording station name, earthquake occurrence date, earthquake magnitude, fault distance, rupture radius, shear wave velocity, etc. which can be used from one or more of them. In this study, only the filters of magnitude and distance were used, then 1,218 records were found, which include earthquakes that occurred continuously from 1938 onwards.

As mentioned before, in this research, the horizontal component of the PGA is considered the target. Also, magnitude, distance, and the shear wave velocity were considered as variables of the seismic attenuation model. In the following, each of these parameters is described.

3.1. Magnitude (M_w). The magnitude of the earthquake indicates the amount of energy released by the earthquake and is directly related to it. Therefore, it will have the greatest impact on the amount of strong ground motion and it can be considered as the most important and effective parameter in determining the attenuation relationships. Magnitude has a direct effect on the horizontal component of PGA. The higher magnitude of earthquake occurrence will cause higher parameters of strong ground motion at a certain distance from the source of the earthquake.

Magnitude is expressed in different scales due to the variety of recorded seismic waves and the institutions and devices recording these earthquakes. The magnitude types are local magnitude (M_L), surface-wave magnitude (M_S), body-wave magnitude (m_b), and moment magnitude (M_w). Local magnitude (M_L) based on amplitude recorded by Wood Anderson seismograph, surface-wave magnitude (M_S) based on Riley wave amplitude, and body-wave magnitude (m_b) based on P-wave amplitude are measured. According to the saturation effects, although the energy released during an earthquake increases, the seismic properties do

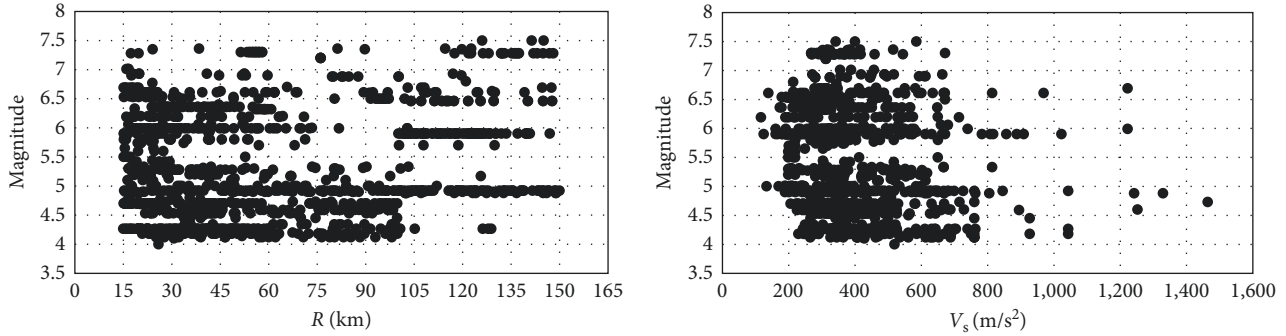


FIGURE 1: Magnitude distribution diagrams in terms of distance and shear wave velocity.

not necessarily increase at the same rate. Therefore, these three scales do not have high accuracy in large earthquakes [14]. The moment magnitude is independent of the characteristics of the earth's motion and can accurately define the magnitude of earthquakes. Therefore, in this research, moment magnitude has been used. To prepare the earthquake catalog in this research, earthquakes with a moment magnitude of 4–7.5 have been used because earthquakes with a magnitude of less than 4 are not considered dangerous for construction engineering structures.

3.2. Distance (R). The distance indicates the path that seismic waves pass from the source of the earthquake to the site. It is the second effective parameter in the attenuation relationships. The distance has an inverse effect on the parameters of the strong ground motion, so if the distance from the site to the epicenter is longer, the PGA will be smaller. The distance in seismology is expressed with different types, which types are: the shortest horizontal distance to the vertical rupture image (r_{jb}), the shortest distance to the rupture surface (r_{rup}), the shortest distance to the seismic rupture surface (r_{seis}), and distance from the epicenter (r_{hypo}) [23].

In this study, the path taken by the waves from the source of the earthquake to the desired site is the most effective parameter on the ground motion. The used catalog data have a hypocentral distance (r_{hypo}) from 15 to 150 km.

3.3. Shear Wave Velocity (V_s). Although most of the path, passed by the waves, is in the bedrock, these waves often pass through a layer of soil at the end of the path. This layer of soil can play a major and significant role in changing the frequency of waves reached to the surface of the ground. It can also cause the damping of some frequencies or intensify other frequencies and change the magnitude of the earthquake. Therefore, this is necessary to consider the ground type and tectonic conditions in providing attenuation relationships [3]. Substrate properties can be entered into computations in both qualitative and quantitative forms. If the effect of this parameter is considered qualitatively, based on the shear wave values, the ground type is divided into several categories and the effect of the ground type is entered as constant coefficients in the calculation of attenuation relationships. If the soil effect is considered quantitatively, the value of shear wave velocity will be used in the relations. According to the ability of the methods used in this research,

the effect of the soil type parameter has been applied quantitatively and using the value of shear wave velocity on the attenuation relationships. Obviously, this approach has increased the accuracy of calculations.

3.4. Preparing the Final Catalog. In the first step, data have been collected and a preliminary catalog has been prepared to consist of magnitude, distance, and shear wave velocity of the 1,218 earthquake records. In the next step, all the records were processed using Seismosignal software and considering the appropriate correction frequency range of 0.2–30 [33]. Then the peak acceleration of each recorded earthquake at each station was taken. The important point in this section is that there are three components of acceleration in three orthogonal directions per record, but in the present study, whereas the study was done on the horizontal component of acceleration, the vertical component was set aside. Then for the horizontal components were considered to be the most critical case and for this purpose, square root of the sum of the squares (SRSS) of two orthogonal components was used.

After this stage, due to error possibility in recording and extracting the records, the records were corrected through sorting in an incremental magnitude. In the next step, the graph was drawn in terms of the horizontal component of PGA. Then the points of the graph that have relatively large dispersion were removed from the earthquake catalog. After this step, 1,185 records remain as the final records that are involved in the attenuation relationship. Magnitude distribution diagrams in terms of distance and shear wave velocity in Figure 1 and the number of records in terms of magnitude and distance in Figure 2 are shown.

4. Methods for Estimation of the Attenuation Relationships in This Research

4.1. Gene Expression Programming (GEP). GEP is a developed GA and genetic programming (GP) that was proposed by Ferreira [34] in 1999. It can be said that this algorithm, like GA and GP, is a GA that uses people as a population, choosing is based on the suitability and introduction of the genetic diversity using one or more genetic operators.

The main elements in GEP are just two elements, chromosomes and expression trees. The structure of chromosomes is organized in such a way that it allows the creation of multiple genes, and each of them is identified as a

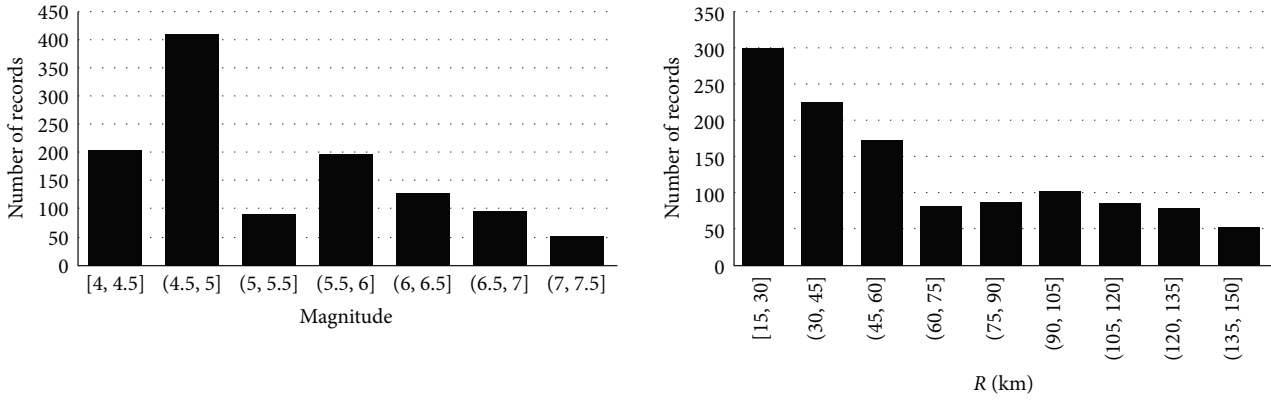


FIGURE 2: Number of records in terms of magnitude and distance.

subexpression tree. The structure of genes is also designed so that each gene has a head and a tail, and this structural and functional organization of the gene in the GEP always ensures the production of valid programs, and it is not important how much they change the depth of the chromosome. Expression trees are also genetic information encoded in chromosomes. As in nature, the process of decoding information is called translation, and this translation clearly indicates the type of code and set of rules. The genetic code is also very simple and shows the one-to-one relationship between chromosome symbols and functions or terminals. The rules are also very simple, they determine the organization consisting of functions and terminals in the development trees and the type of interaction between subexpression trees [35, 36].

Figure 3 shows the steps of the GEP and the operators defined in this algorithm are also shown in Table 1.

4.2. Group Method of Data Handling (GMDH). The GMDH is used to identify the behavior of nonlinear systems. Among all intelligent computational methods, the GMDH method is known as a self-organized system with a very complex nonlinear problem solving capacity [37, 38].

The GMDH was proposed by Ivakhnenko [39] in 1971. In this algorithm, by keeping the input variables in a flexible network, a connection is made between the input variables and the output, and the possibility of initial estimation of the output by regression equations including small subsets of input variables is provided. Each of these small subsets contains 2–3 independent variables [40, 41]. The main purpose of this method is to build a network based on a quadratic transfer function. The number of hidden layers and neurons, effective input variables, and the optimal structural model is automatically determined in this algorithm [42].

The communication between the input and output variables is done by the data management neural network in a group method which is a nonlinear function called Volterra series, which is as Equation (8).

$$\hat{y} = a_0 + \sum_{i=1}^m a_i x_i + \sum_{i=1}^m \sum_{j=1}^m a_{ij} x_i x_j + \sum_{i=1}^m \sum_{j=1}^m \sum_{k=1}^m x_j a_{ijk} x_i x_j x_k + \dots \quad (8)$$

The Volterra series is processed as a quadratic polynomial by utilizing the following relation (Equation 9).

$$G(x_i, x_j) = a_0 + a_1 x_i + a_2 x_j + a_3 x_i^2 + a_4 x_j^2 + a_5 x_i x_j. \quad (9)$$

The purpose of the data management algorithm is to find fixed and unknown coefficients a_i in a group method, which will be obtained by regression methods, based on obtaining the least squares of error for each pair of input variables x_i and x_j [43, 44].

5. Results

In this research, 80% of the records were considered as training records and the remaining 20% as testing records. The method of selecting these records is that the testing records are in the range of training records and allow comparison. As mentioned, in this study, the parameters of magnitude, hypocentral distance, and shear wave velocity are defined as variables and the PGA as a target function.

5.1. Results of Gene Expression Programming (GEP). Finally, after several trials, the best answer with the highest accuracy and least error was considered as the final answer. The final relationship chromosomes are shown in Figure 4. In this relation, $d_0 = M$, $d_1 = R$, $d_2 = V$, and the values of the coefficients c_0 and c_1 for each chromosome are given after that. Also, the links of chromosomes are sum operator (+). By replacing the variables, mathematical operators and the link operator (+) in the calculated equation, the global attenuation relationship for the PGA was obtained as Equation (10).

$$\log(\text{PGA}) = \frac{(-1.553V - R^2 - 9.095R)}{R \times \text{Exp}(M)} + \sqrt[6]{\text{Exp}\left(\frac{5.61 - R}{M - 1.37}\right)} + \sqrt[3]{9.999 - \sqrt[3]{V/M + M + 8.967}}. \quad (10)$$

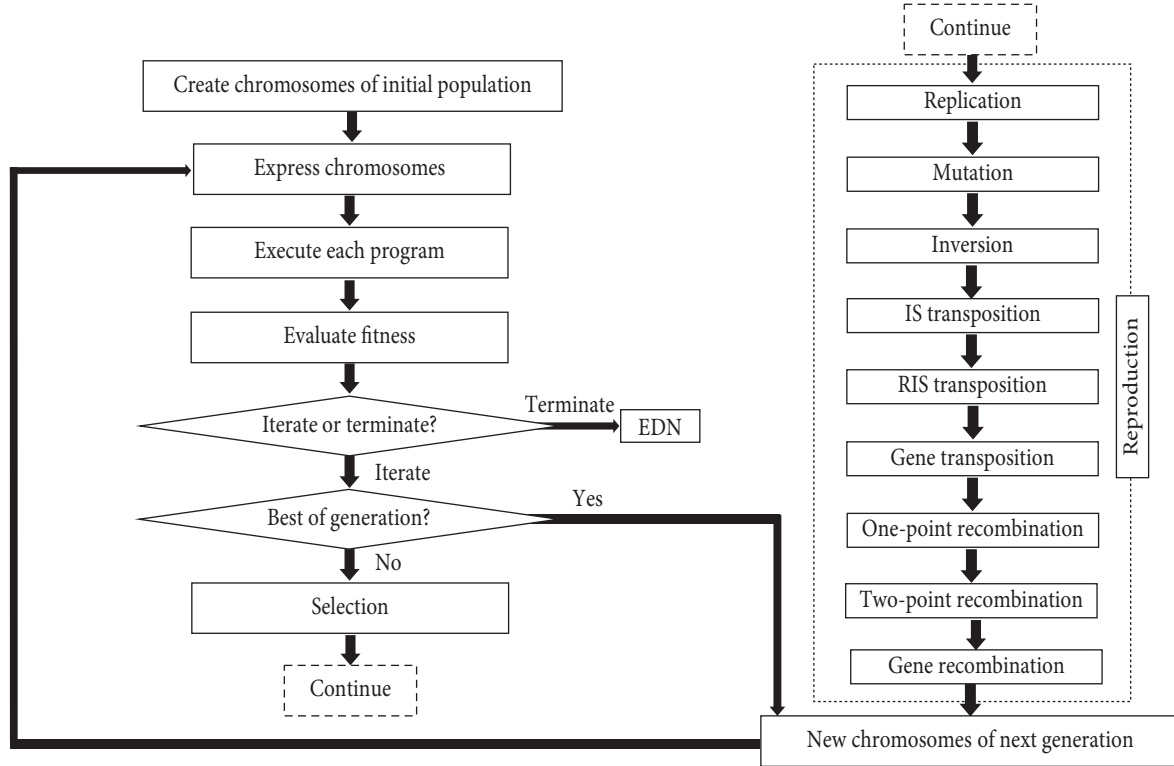


FIGURE 3: The flowchart of gene expression programming [36].

TABLE 1: Operators defined in gene expression programming.

Name	Representation	Weight
Addition	+	4
Subtraction	-	4
Multiplication	*	4
Division	/	1
Square root	Sqrt	1
Exponential	Exp	1
Natural logarithm	Ln	1
x to the power of 2	X2	1
x to the power of 3	X3	1
Cube root	3Rt	1

In this relationship, M is the magnitude, R is the hypocentral distance (km), V is the shear wave velocity (m/s), and PGA is peak ground acceleration (cm/s^2). For better visualization of the results, PGA diagrams were drawn in terms of magnitude and hypocentral distance.

$$\begin{aligned}
 / - E / - d0 * d1 d1 c1 d2 c0 & \quad c0 = -1.553, c1 = 9.095 \\
 S 3 E / - + c0 d1 c1 d0 & \quad c0 = 5.61, c1 = -1.37 \\
 3 - c0 3 + / - d2 d0 d0 c1 & \quad c0 = 9.999, c1 = -8.967
 \end{aligned}$$

FIGURE 4: Expression trees of attenuation relationship of the peak ground acceleration.

Figure 5 shows the PGA variation curve in terms of hypocentral distance (15–150 km) for three magnitudes of 4.5, 5.5, and 6.5. In this diagram, the shear wave velocity is considered 400 m/s. As can be seen, the PGA decreases nonlinearly as it moves away from the epicenter. Figure 6 also shows the PGA variation curve in terms of magnitude (4–7.5) for five hypocentral distances of 20, 30, 60, 100, and 150 km. In this diagram, the shear wave velocity is considered 400 m/s. As can be seen, with increasing magnitude, the PGA increases nonlinearly.

5.2. Results of Group Method of Data Handling (GMDH). The final attenuation relationship obtained from the GMDH method is shown in Equation (11).

$$\begin{aligned}
 \log(\text{PGA}) = & -1788.07 + (3192.56\sqrt[3]{M}) + (-7.7484\sqrt[3]{R}) + (-1664.47\sqrt[3]{M^2}) \\
 & + (-6.97 \times 10^{-5} \times V\sqrt[3]{V}) + (5.715\sqrt[3]{M}\sqrt[3]{R}) + (170.807M\sqrt[3]{M}) \\
 & + (-10.447M^2) + (3.096 \times 10^{-6} \times RV) + (-0.505M\sqrt[3]{R}).
 \end{aligned} \tag{11}$$

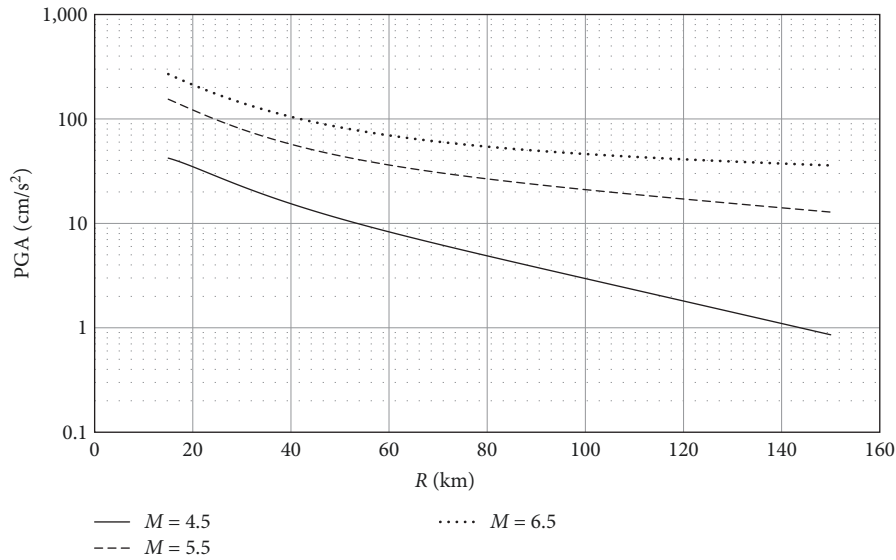


FIGURE 5: The peak ground acceleration variation curve in terms of hypocentral distance.

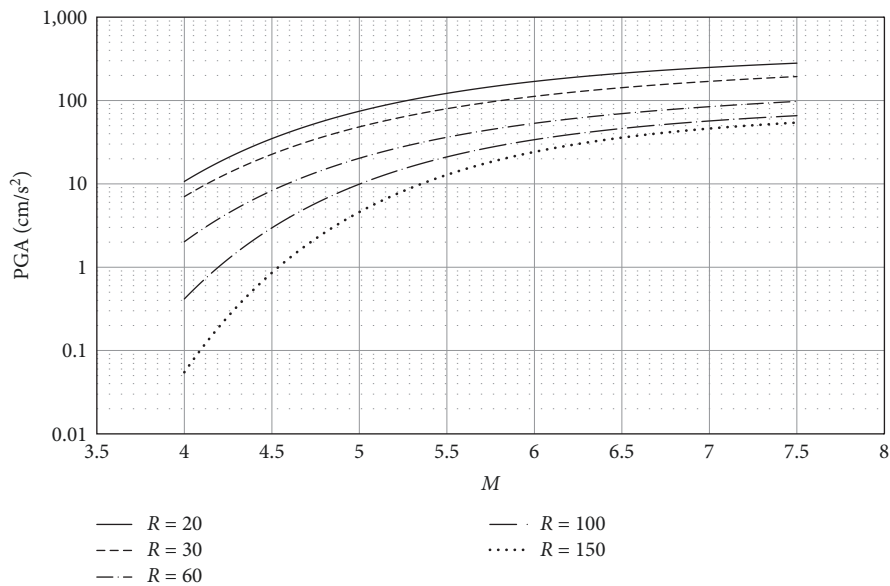


FIGURE 6: The peak ground acceleration variation curve in terms of magnitude.

In this relationship, M is the magnitude, R is the hypocentral distance (km), V is the shear wave velocity (m/s), and PGA is peak ground acceleration (cm/s^2).

Figures 7 and 8 show the changes in PGA with the attenuation relationship calculated by the GMDH method in terms of magnitude and hypocentral distance.

Figure 7 shows the PGA variation curve in terms of hypocentral distance (15–150 km) for 3 magnitudes of 4.5, 5.5, and 6.5. In this diagram, the shear wave velocity is considered 400 m/s. As can be seen, the PGA decreases nonlinearly as it moves away from the epicenter. Figure 8 also shows the PGA variation curve in terms of magnitude (4–7.5) for five hypocentral distances of 20, 30, 60, 100,

and 150 km. In this diagram, the shear wave velocity is considered 400 m/s. As can be seen, while magnitude increases, the PGA increases nonlinearly.

In Figures 5–8, it can be seen that in addition to the nonlinearity of the diagrams, the lines of each diagram do not follow a pattern. While in the past researches, usually the lines in each diagram had a single pattern. The reason, is due to the methods used in this research. In the past, a fixed formula was used to calculate attenuation relations, which only considered fixed coefficients as variables for different regions. But in the GEP and GMDH methods, due to the nonlinear changes of the chromosomes and the terms of the equation, the patterns are not assumed to be constant.

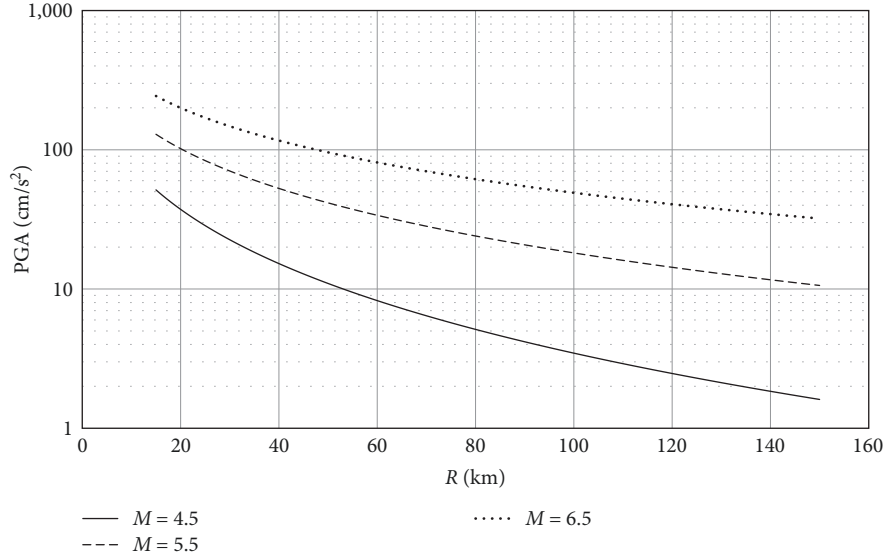


FIGURE 7: The peak ground acceleration variation curve in terms of hypocentral distance for three magnitudes of 4.5, 5.5, and 6.5.

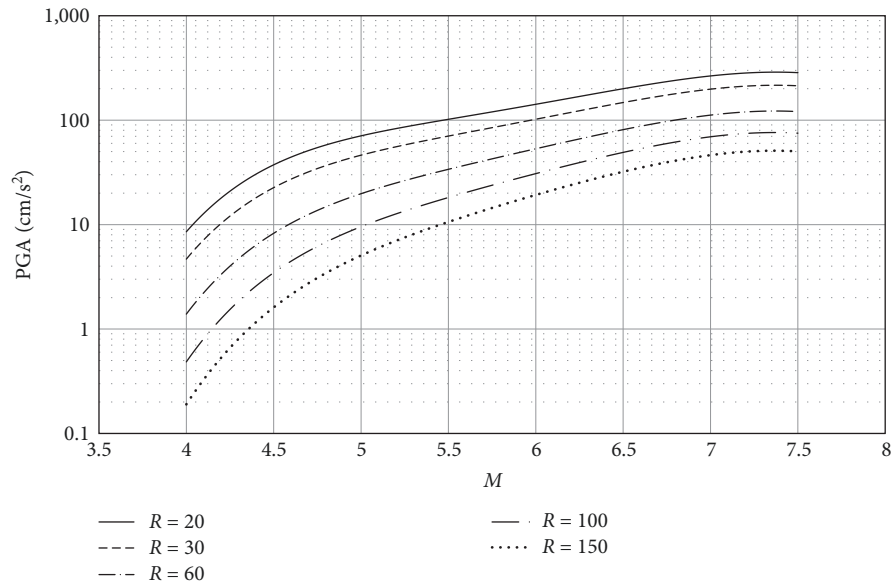


FIGURE 8: The peak ground acceleration variation curve in terms of magnitude for five hypocentral distances of 20, 30, 60, 100, and 150 km.

5.3. Verification and Comparison of Results. As mentioned before, the attenuation relationships obtained from GEP and GMDH methods have high accuracy. The accuracy of each of the relationships presented in this research can be measured with the parameters defined below.

One of these parameters is the root-mean-square error (RMSE), which can be evaluated and calculated by Equation (12).

$$\text{RMSE} = \sqrt{\frac{1}{n} \sum_{i=1}^n (\text{PGA}_{\text{actual}_i} - \text{PGA}_{\text{model}_i})^2}. \quad (12)$$

In the above relation, $\text{PGA}_{\text{actual}}$ is the PGAH values of the target and the $\text{PGA}_{\text{model}}$ is the PGAH values obtained from

the final attenuation relationship presented in this article. It is clear when the predicted values and the target values are equal, the RMSE will be zero, and as this number increases, it indicates more error and less compliance between the target value and the predicted value.

Now by using the RMSE value, the value of the fitness function (f) is calculated from Equation (13).

$$f = \frac{1,000}{1 + \text{RMSE}}. \quad (13)$$

As a result, from the above equation, the amplitude of the changes in the fit function is 0–1,000. The maximum value is 1,000 for zero error and shows the high proportion of the

TABLE 2: Values of RMSE, f , R^2 , and SD for the recent studies and present study.

Standard deviation of residuals	Coefficient of determination (R^2)	Fitness function (f)	Root mean square error (RMSE)		Method
0.307	0.77	765.103	0.307	Training results	Present Study (GEP)
0.298	0.79	770.209	0.298	Testing results	
0.3024	0.777	767.425	0.303	Training results	Present Study (GMDH)
0.2988	0.788	769.15	0.3	Testing results	
0.385	0.689	610.037	0.639	Training results	Sarma and Free [15]
0.388	0.697	607.147	0.647	Testing results	
0.396	0.685	645.29	0.549	Training results	Ornthammarath et al. [18]
0.399	0.694	642.508	0.556	Testing results	
0.391	0.63	712.277	0.404	Training results	Alavi and Gandomi [21]
0.385	0.668	714.677	0.399	Testing results	
0.361	0.697	732.24	0.366	Training results	Kumar et al. [25]
0.359	0.716	733.956	0.362	Testing results	
0.308	0.657	760.668	0.315	Training results	Javan-Emrooz et al. [26]
0.306	0.658	760.52	0.314	Testing results	
0.27	0.496	685.5	0.4	Training results	Abdelfattah et al. [30]
0.267	0.502	683.7	0.46	Testing results	

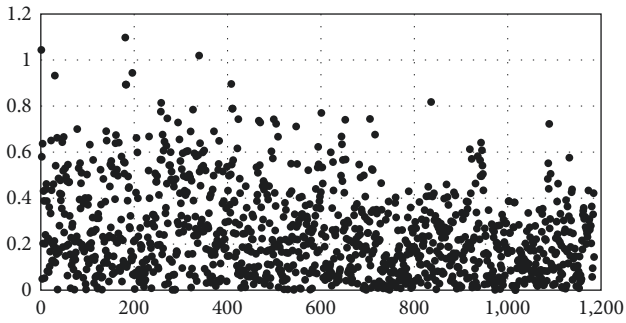


FIGURE 9: Residual trends of inter and intraevent error in the GEP method.

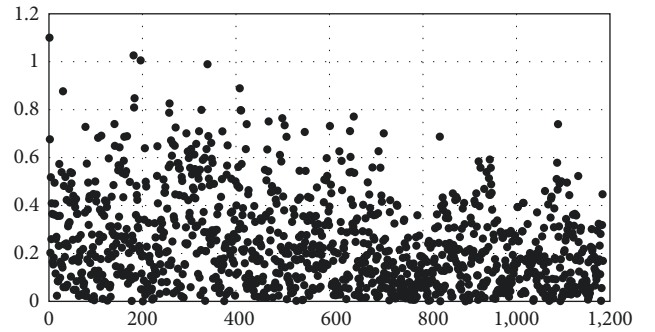


FIGURE 10: Residual trends of inter and intraevent error in the GMDH method.

predicted values with measured values from the previous earthquakes that are the most possible ideal state. The lower value of the fitness function shows a more inadequate matching.

Another parameter that was used to calculate the accuracy is the coefficient of determination (R^2), which can be determined by Equation (14).

$$R^2 = \left(\frac{\sum_{i=1}^n (\text{PGA}_{\text{actual}_i} - \overline{\text{PGA}_{\text{actual}}}) (\text{PGA}_{\text{model}_i} - \overline{\text{PGA}_{\text{model}}})}{\sqrt{\sum_{i=1}^n (\text{PGA}_{\text{actual}_i} - \overline{\text{PGA}_{\text{actual}}})^2 \sum_{i=1}^n (\text{PGA}_{\text{model}_i} - \overline{\text{PGA}_{\text{model}}})^2}} \right)^2. \quad (14)$$

The range of changes of this parameter is 0–1. The closer this number is to one, the greater the match between the predicted values and the target, and overall, there is a higher accuracy in the results.

Another parameter used in this research to measure accuracy is the standard deviation (SD) of residuals. Using Equation (15) the SD of residuals can be calculated.

$$\text{SD} = \sqrt{\frac{\sum_{i=1}^n \left(\left| \text{PGA}_{\text{actual}_i} - \text{PGA}_{\text{model}_i} \right| - \overline{\left| \text{PGA}_{\text{actual}_i} - \text{PGA}_{\text{model}_i} \right|} \right)^2}{n-1}}. \quad (15)$$

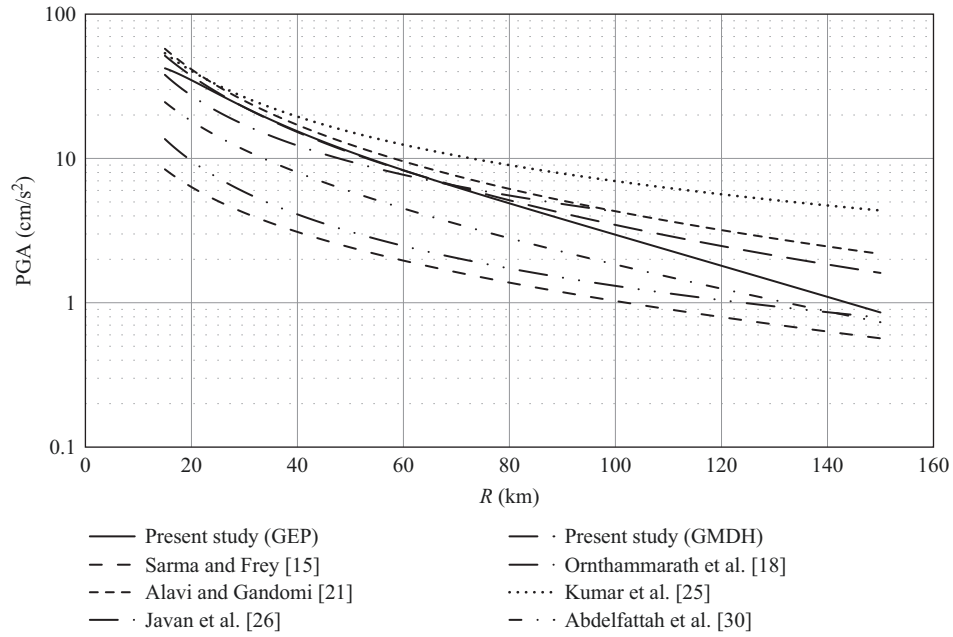


FIGURE 11: The PGAH change curve in terms of hypocentral distance for earthquakes with magnitudes of 4.5 and shear wave velocities of 400 m/s.

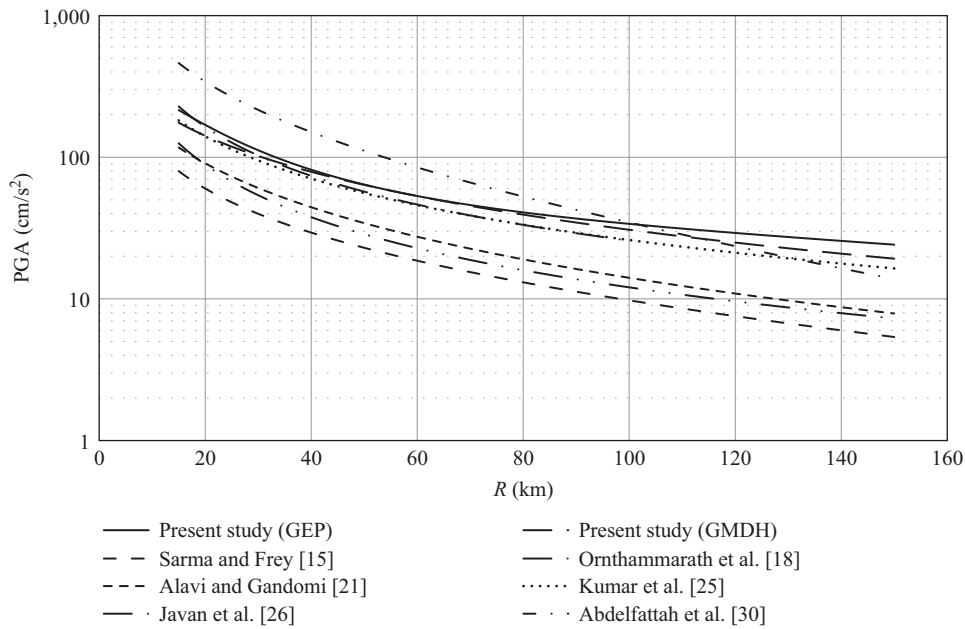


FIGURE 12: The PGAH change curve in terms of hypocentral distance for earthquakes with magnitudes of 6 and shear wave velocities of 400 m/s.

For each attenuation relationship obtained from GEP and GMDH methods, the parameters of RMSE, Fitness function, Coefficient of determination, and SD of residuals were calculated and presented in Table 2.

On the other hand, to show the agreement between target and predicted values, it is possible to present a diagram for the difference values between these parameters. These scatter

diagrams for GEP and GMDH methods are drawn in Figures 9 and 10, respectively.

Finally, in this section, the relationships presented in this study are compared with some relationships presented in the past. For comparison, it was tried to use attenuation relationships calculated by the other methods. The relationships selected for comparison are: Sarma and Frey [15], Ornthammarath et al.

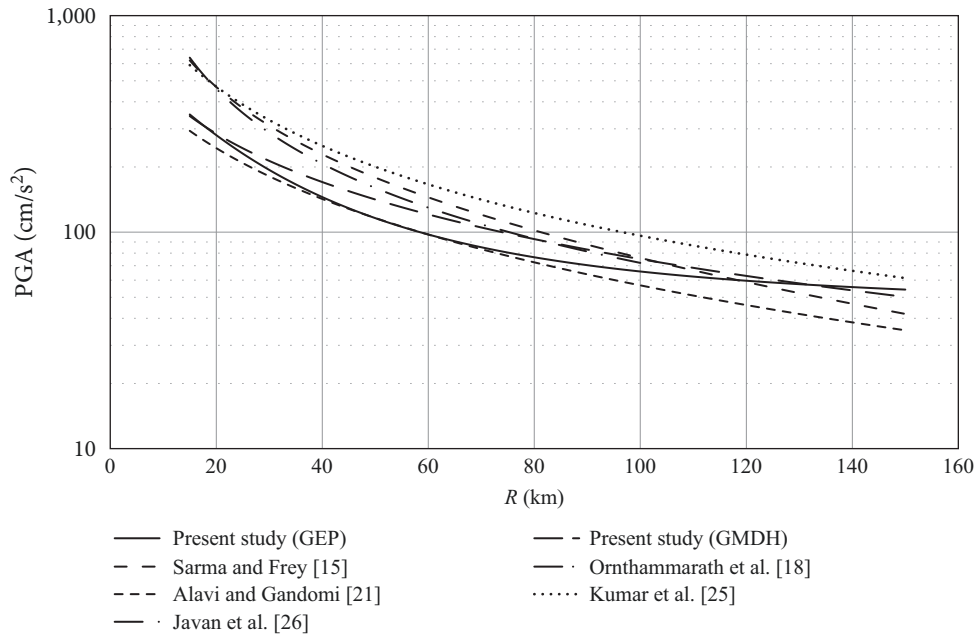


FIGURE 13: The PGAH change curve in terms of hypocentral distance for earthquakes with magnitudes of 7.5 and shear wave velocities of 400 m/s.

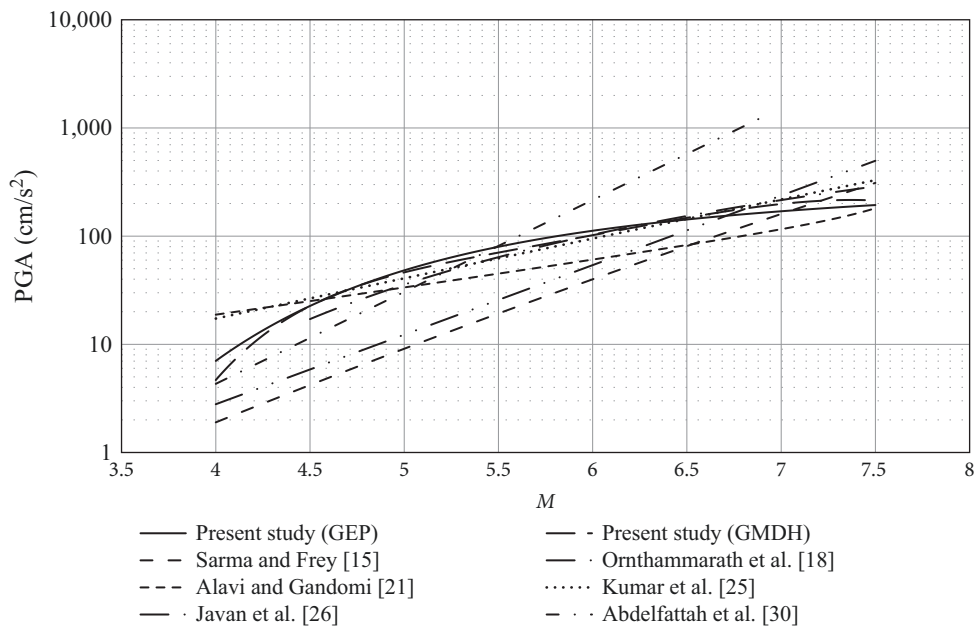


FIGURE 14: The PGAH change curve in terms of magnitude for a hypocentral distance of 30 km and shear wave velocities of 400 m/s.

[18], Kumar et al. [25], and Abdelfattah et al. [30], were presented in 1995, 2010, 2017 and 2021, respectively. Also, the relationships of Alavi and Gandomi [21] and Javan et al. [26], which were obtained using intelligent algorithms. For comparison, the values of parameters RMSE, Fitness function, Coefficient of determination, and SD of residuals were calculated for each of these relationships and presented in Table 2. As seen from Table 2, the values of Fitness function and Coefficient of determination in the present study have the highest values and

the values of RMSE and SD of residuals have the lowest values compared to the other methods. From this comparison, it can be concluded the methods used in this research are appropriate and highly accurate.

In the continuation of the comparison with other attenuation relationships, comparative diagrams were drawn. The PGAH change curve in terms of hypocentral distance of 15–150 km for earthquakes with magnitudes of 4.5, 6, and 7.5 and shear wave velocities of 400 m/s, for the results of the

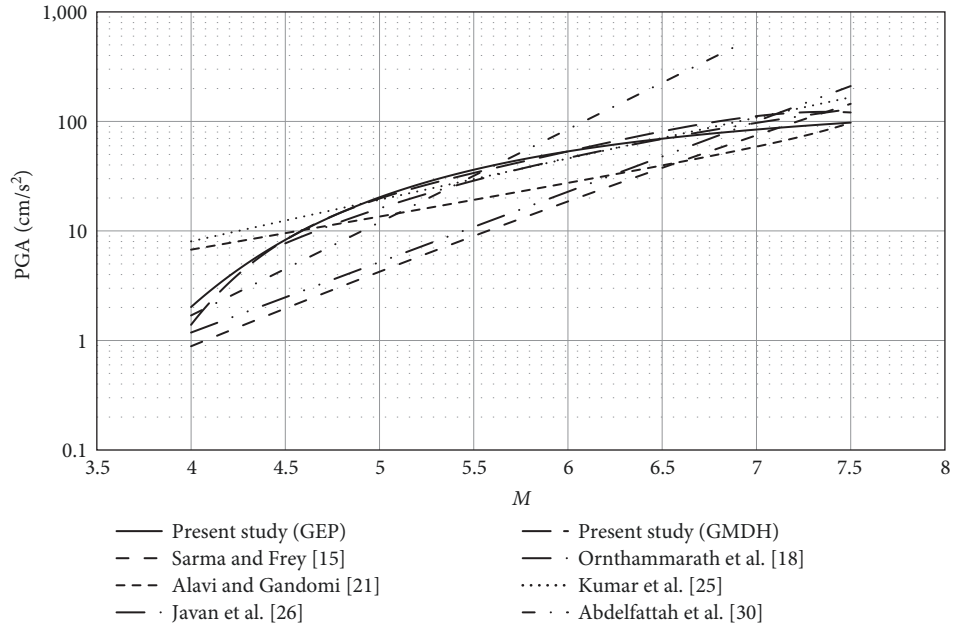


FIGURE 15: The PGAH change curve in terms of magnitude for a hypocentral distance of 60 km and shear wave velocities of 400 m/s.

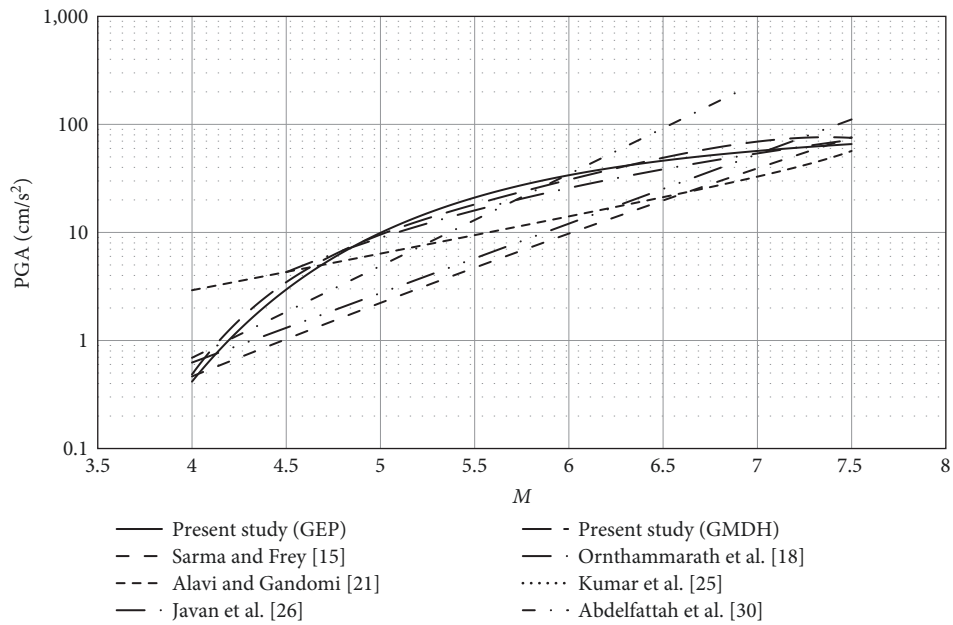


FIGURE 16: The PGAH change curve in terms of magnitude for a hypocentral distance of 100 km and shear wave velocities of 400 m/s.

present study and the mentioned researches, are shown in Figures 11–13. As a result, there is an acceptable correlation between the results of the present study and the previous studies.

Also, the horizontal component of the PGA change curve in terms of magnitude is 4–7.5, for a hypocentral distance of 30, 60, and 100 km and shear wave velocities of 400 m/s, belong to the results of the present study and the mentioned researches are shown in Figures 14–16. As it is clear from the graphs, the values obtained from the relationships presented

in this research are in the range of other researches and have a good match.

6. Conclusion

Every year, new earthquakes occur, accelerometers are installed in new areas and the accelerometer network expands, and in general, the earthquake catalog becomes more complete and accurate. On the other hand, providing new methods for

regression has caused that new attenuation relationships are always needed in earthquake risk analysis.

In this study, correcting the existing records and deleting some of them, 1,185 earthquake records were used to provide the attenuation relationship of the horizontal component of PGA. The records used have a moment magnitude of 4–7.5 and a hypocentral distance of 15–150 km. The parameters of moment magnitude, hypocentral distance, and shear wave velocity were considered as variables and the square root of the sum of the squares of peak ground horizontal acceleration in two horizontal orthogonal directions was treated as an objective function. Then new attenuation relationships were extracted by the GEP and the GMDH.

One of the innovations of this research is the addition of the shear wave velocity parameter as a variable in the attenuation relationship, which was rarely seen in the past researches.

The most important advantage of using GEP and GMDH methods in this research is that a predetermined pattern was not used to calculate relationships. As seen, in past researches, PGA changes in terms of magnitude were assumed to be linear, but in this research, it was shown that these changes are nonlinear. Also, changes in terms of hypocentral distance are not assumed to have a fixed pattern and it is observed that the pattern also changes in different intervals. For this reason, as it is clear from the comparisons, the accuracy of these methods is higher and shows a lower amount of error than the previous researches.

Data Availability

The data used in this research have been uploaded in the supplemental files section.

Conflicts of Interest

The authors declare that they have no conflicts of interest.

References

- [1] K. Satake and B. F. Atwater, "Long-term perspectives on giant earthquakes and tsunamis at subduction zones," *Annual Review of Earth and Planetary Sciences*, vol. 35, no. 1, pp. 349–374, 2007.
- [2] M. Ajam, M. S. Amiri, and H. Pahlavan, "Attenuation relationship for the horizontal component of peak ground acceleration (PGAH) using gene expression programming (GEP)," in *Presented at the Eighth International Conference on Seismology and Earthquake Engineering (SEE8)*, Tehran, Iran, 11–13 November 2019.
- [3] S. L. Kramer, *Geotechnical Earthquake Engineering*, Pearson Education India, 1996.
- [4] P. G. Somerville and R. W. Graves, "Characterization of earthquake strong ground motion," in *Landslide Tsunamis: Recent Findings and Research Directions*, J. P. Bardet, F. Imamura, C. E. Synolakis, E. A. Okal, and H. L. Davies, Eds., Pageoph Topical, pp. 1811–1828, Springer, Birkhäuser, Basel, 2003.
- [5] F. Neumann, *Earthquake Intensity and Related Ground Motion*, University of Washington Press Seattle, Washington, 1954.
- [6] W. G. Milne and A. G. Davenport, "Distribution of earthquake risk in Canada," *Bulletin of the Seismological Society of America*, vol. 59, no. 2, pp. 729–754, 1969.
- [7] L. Estevea, *Seismic Risk and Seismic Design Decisions*. 1970, Massachusetts Inst, Tech., Cambridge. Univ. of Mexico, Mexico City.
- [8] D. Denham and G. R. Small, "Strong motion data centre: bureau of mineral resources, Canada," *Bulletin of the New Zealand Society for Earthquake Engineering*, vol. 4, no. 1, pp. 15–30, 1971.
- [9] N. C. Donovan, *A Statistical Evaluation of Strong Motion Data: Including the February 9, 1971*, San Fernando Earthquake, Dames & Moore San Francisco, CA, USA, 1973.
- [10] L. Estevea and R. Villaverde, "Seismic risk, design spectra and structural reliability," *The 5th World Conference on Earthquake Engineering*, vol. 2, pp. 2586–2596, 1973.
- [11] D. L. Orphal and J. A. Lahoud, "Prediction of peak ground motion from earthquakes," *Bulletin of the Seismological Society of America*, vol. 64, no. 5, pp. 1563–1574, 1974.
- [12] M. Trifunac, "Preliminary analysis of the peaks of strong earthquake ground motion—dependence of peaks on earthquake magnitude, epicentral distance, and recording site conditions," *Bulletin of the Seismological Society of America*, vol. 66, no. 1, pp. 189–219, 1976.
- [13] W. B. Joyner and D. M. Boore, "Peak horizontal acceleration and velocity from strong-motion records including records from the 1979 Imperial Valley, California, earthquake," *Bulletin of the Seismological Society of America*, vol. 71, no. 6, pp. 2011–2038, 1981.
- [14] G. M. Atkinson and D. M. Boore, "Recent trends in ground motion and spectral response relations for North America," *Earthquake Spectra*, vol. 6, no. 1, pp. 15–35, 1990.
- [15] S. Sarma and M. Free, "The comparison of attenuation relationships for peak horizontal acceleration in intraplate regions," in *Proceedings of the Fifth Pacific Conference on Earthquake Engineering*, 1995.
- [16] G. Sobhaninejad, A. Noorzad, and A. Ansari, "Genetic algorithm (GA): A new approach in estimating strong ground motion attenuation relations," in *Proceedings of the Fourth International Conference on Earthquake Geotechnical Engineering*, 2007.
- [17] A. F. Cabalar and A. Cevik, "Genetic programming-based attenuation relationship: an application of recent earthquakes in Turkey," *Computers & Geosciences*, vol. 35, no. 9, pp. 1884–1896, 2009.
- [18] T. Ornthammarath, J. Douglas, R. Sigbjörnsson, and C. G. Lai, "Assessment of strong ground motion variability in Iceland," in *Proceedings of Fourteenth European Conference on Earthquake Engineering*, Citeseer, 2010.
- [19] E. Kermani, Y. Jafarian, and M. H. Baziar, "A new attenuation model for peak ground acceleration in soil sites using genetic programming," in *2nd International Conference on New Developments in Soil Mechanics and Geotechnical Engineering*, Near East University, Nicosia, North Cyprus, 2009.
- [20] Y. Jafarian, E. Kermani, and M. H. Baziar, "Empirical predictive model for the v_{max}/a_{max} ratio of strong ground motions using genetic programming," *Computers & Geosciences*, vol. 36, no. 12, pp. 1523–1531, 2010.
- [21] A. H. Alavi and A. H. Gandomi, "Prediction of principal ground-motion parameters using a hybrid method coupling artificial neural networks and simulated annealing," *Computers & Structures*, vol. 89, no. 23–24, pp. 2176–2194, 2011.
- [22] G. Ghodrati Amiri, M. S. Amiri, and Z. Tabrizian, "Ground motion prediction equations (GMPEs) for elastic response spectra

- in the Iranian plateau using gene expression programming (GEP)," *Journal of Intelligent & Fuzzy Systems*, vol. 26, no. 6, pp. 2825–2839, 2014.
- [23] G. G. Amiri, M. S. Amiri, P. Namiarnian, and A. Emadzadeh, "Attenuation relationship for inelastic earthquake spectra in Iran," *Proceedings of the Institution of Civil Engineers - Structures and Buildings*, vol. 168, no. 5, pp. 313–325, 2015.
- [24] A. H. Gandomi, A. H. Alavi, M. Mousavi, and S. M. Tabatabaei, "A hybrid computational approach to derive new ground-motion prediction equations," *Engineering Applications of Artificial Intelligence*, vol. 24, no. 4, pp. 717–732, 2011.
- [25] A. Kumar, H. Mittal, R. Kumar, and R. S. Ahluwalia, "Empirical attenuation relationship for peak ground horizontal acceleration for North–East Himalaya," *Vietnam Journal of Earth Sciences*, vol. 39, no. 1, pp. 47–57, 2017.
- [26] H. Javan-Emrooz, M. Eskandari-Ghadi, and N. Mirzaei, "Prediction equations for horizontal and vertical PGA, PGV, and PGD in northern Iran using prefix gene expression programming," *Bulletin of the Seismological Society of America*, vol. 108, no. 4, pp. 2305–2332, 2018.
- [27] A. Erken, G. Şengül Nomaler, and Z. Gündüz, "The development of attenuation relationship for Northwest Anatolia region," *Arabian Journal of Geosciences*, vol. 11, no. 2, pp. 1–15, 2018.
- [28] B. Karimi Ghalehjough and R. Mahinroosta, "Peak ground acceleration prediction by fuzzy logic modeling for Iranian plateau," *Acta Geophysica*, vol. 68, no. 1, pp. 75–89, 2020.
- [29] A. Shiuly, N. Roy, and R. B. Sahu, "Prediction of peak ground acceleration for Himalayan region using artificial neural network and genetic algorithm," *Arabian Journal of Geosciences*, vol. 13, no. 5, pp. 1–10, 2020.
- [30] A. K. Abdelfattah, A. Al-Amri, K. Abdelrahman, M. Fnais, and S. Qaysi, "Attenuation relationships of peak ground motions in the Jazan Region," *Arabian Journal of Geosciences*, vol. 14, no. 3, pp. 1–9, 2021.
- [31] P. Kumar, B. P. Chamoli, A. Kumar, and A. Gairola, "Attenuation relationship for peak horizontal acceleration of strong ground motion of Uttarakhand region of central Himalayas," *Journal of Earthquake Engineering*, vol. 25, no. 12, pp. 2537–2554, 2021.
- [32] S. Pourzeynali and A. Khadivyan, "Attenuation relationships for horizontal and vertical peak and spectral accelerations for Alborz zone of Iran," *Journal of Earthquake Engineering*, vol. 26, no. 14, pp. 7469–7485, 2022.
- [33] A. G. Ghodrati, M. Zahedi, S. Gholami, and A. Mahdavian, "Appropriate frequency band for correcting Iranian accelerograms in different site conditions," 2004.
- [34] C. Ferreira, "Gene expression programming: a new adaptive algorithm for solving problems," 2001.
- [35] C. Ferreira, "Gene expression programming in problem solving," in *Soft Computing and Industry*, pp. 635–653, Springer, 2002.
- [36] C. Ferreira, *Gene Expression Programming: Mathematical Modeling by an Artificial Intelligence*, Vol. 21, Springer, 2006.
- [37] H. S. Hwang, "Fuzzy GMDH-type neural network model and its application to forecasting of mobile communication," *Computers & Industrial Engineering*, vol. 50, no. 4, pp. 450–457, 2006.
- [38] N. Amanifard, N. Nariman-Zadeh, M. H. Farahani, and A. Khalkhali, "Modelling of multiple short-length-scale stall cells in an axial compressor using evolved GMDH neural networks," *Energy Conversion and Management*, vol. 49, no. 10, pp. 2588–2594, 2008.
- [39] A. G. Ivakhnenko, "Polynomial theory of complex systems," *IEEE Transactions on Systems, Man, and Cybernetics*, vol. SMC-1, no. 4, pp. 364–378, 1971.
- [40] S. J. Farlow, "The GMDH algorithm," in *Self-Organizing Methods in Modeling: GMDH Type Algorithms*, vol. 54, p. 350, CRC Press, 1984.
- [41] Y. Pachepsky, W. Rawls, D. Giménez, and J. P. C. Watt, "Use of soil penetration resistance and group method of data handling to improve soil water retention estimates," *Soil and Tillage Research*, vol. 49, no. 1-2, pp. 117–126, 1998.
- [42] I. Ebtehaj, H. Bonakdari, A. H. Zaji, H. Azimi, and F. Khoshbin, "GMDH-type neural network approach for modeling the discharge coefficient of rectangular sharp-crested side weirs," *Engineering Science and Technology, an International Journal*, vol. 18, no. 4, pp. 746–757, 2015.
- [43] H. Iba, H. deGaris, and T. Sato, "A numerical approach to genetic programming for system identification," *Evolutionary Computation*, vol. 3, no. 4, pp. 417–452, 1995.
- [44] N. Nariman-Zadeh, A. Darvizeh, A. Jamali, and A. Moeini, "Evolutionary design of generalized polynomial neural networks for modelling and prediction of explosive forming process," *Journal of Materials Processing Technology*, vol. 164-165, pp. 1561–1571, 2005.

Research Article

Mechanical Analysis of Junction Pier of Fuzhou-Xiamen High-Speed Railway Rigid-Frame Bridge

Fangwen Weng  and Fuxing Liu 

CCCC Second Harbor Engineering Company Ltd., Wuhan 430040, China

Correspondence should be addressed to Fangwen Weng; sponerock@hbut.edu.cn

Received 2 October 2022; Revised 15 November 2022; Accepted 22 March 2023; Published 24 April 2023

Academic Editor: S. Mahdi S. Kolbadi

Copyright © 2023 Fangwen Weng and Fuxing Liu. This is an open access article distributed under the Creative Commons Attribution License, which permits unrestricted use, distribution, and reproduction in any medium, provided the original work is properly cited.

The continuous rigid structure bridge on both sides of the Quanzhou Bay Crossing Bridge uses double-limbed thin-walled flexible piers for the junction piers between the links, and the whole bridge has no bearings. In China, the monolithic bearing-free prestressed concrete continuous rigid-frame bridge is used in railway bridges. The junction pier between the two adjacent couplets is a double-leg thin-walled flexible pier. The single leg thin-walled pier is connected with half of the pier-top segment. During the construction process, the block with numbered zero on the top of the pier is temporarily anchored and connected. Symmetrical cantilevered baskets are used on both sides for construction, and after the mid-pier cantilevered construction is completed, the temporary anchoring device for the block with numbered zero is removed. Because the structural system conversion is required in the construction, the mechanical properties of the junction pier will change greatly before and after the conversion, so it is very necessary to calculate and analyze it to master. In this paper, the finite element model of the connecting pier is established accurately, the stress and deformation of each part of the connecting pier under unfavorable working conditions is analyzed in detail, the seismic spectrum analysis under the action of common earthquake and rare earthquake is carried out, and the stress and deformation law of the structure is expounded, which can provide some reference for the construction of similar projects in the future.

1. General Situation of the Project

1.1. Introduction to Rigid Bridge Intersection Piers. The approach bridge on both sides of the main bridge of Fuzhou-Xiamen high-speed railway is an integral bearing-free prestressed concrete continuous rigid-frame bridge. The continuous rigid structure bridge on both sides of the Quanzhou Bay Crossing Bridge uses double-limbed thin-walled flexible piers for the junction piers between the links, and the whole bridge has no bearings. In China, the monolithic bearing-free prestressed concrete continuous rigid-frame bridge is used in railway bridges. The structure of the grouted mortise-tenon joints used in the prefabricated structure is complicated, and the force applied to them is special, but there was very little research on these joints before [1].

The thickness of the box girder roof of the zero block of the connecting pier is gradually changed from 90 cm to 40 cm, and the pier-top segment and the pier body are consolidated with the thick bottom plate. The structure is basically the same as the zero block of the middle pier, except that there is a beam joint in the center of the box girder and the design theoretical width is 15 cm.

The total length of block zero is 12 m, the height of the beam tapers from 660 cm to 607.5 cm, the thickness of the web of block zero tapers from 90 cm to 70 cm, and the thickness of the outer web is increased to 100 cm where it meets the pier. 1.9 m thick cross partitions are provided at the end of the box girder and two 160 cm × 140 cm manholes are provided at each end, the thickness of the bottom plate tapers from 1.5 m to 1.051 m, and water drainage holes are

provided (the flood effect is considered in this element [2]). The thickness of the base plate is gradually changed from 1.5 m to 1.051 m, and drainage holes are provided. The structure of the zero block of the junction pier is shown in Figure 1.

1.2. Anchorage Prestressing of the Zero Block of the Transfer Pier. Common manipulators include rigid manipulators and flexible manipulators. Flexible joint manipulators have significant advantages over traditional rigid manipulators in terms of response speed, control accuracy, and load-to-weight ratio, but they are highly nonlinear and strongly coupled, which brings great challenges to the controller design [3]. The anchorage prestressing in the zero block of the junction pier includes permanent prestressing and temporary prestressing.

The permanent prestressed tendons ST1, ST1, and ST2 use 15 ϕ 15.24 steel strands, while SB1', SB2', SB3', SB5, SB6, and SB7 use 19 ϕ 15.24 steel strands. The layout of permanent prestressed tendons is shown in Figure 2.

The overhanging sections of the junction pier are set up with 2 bundles of SB1', SB2', and SB3' in the corresponding webs from M1 to M8, 4 bundles of SBS and a spare east bundle of SBY in the M1 section of the bottom plate, 4 bundles of SB4 in the M2 section, 2 bundles of SB3 in the M3 section, 4 bundles of SB2 in the M4 section, and 4 bundles of SB1 in the M5 section. The arrangement of prestressing steel bundles in the overhanging sections of the junction pier is shown in Figure 3.

The setting of temporary anchoring prestress can reduce the amount of cast-in-place support and improve the construction efficiency in the construction of rigid-frame bridge. Except for the cast-in-place support for block zero of the transfer pier, the hanging basket cantilever casting technology is adopted for other beam sections. In order to ensure the smooth implementation of the suspension casting construction, the temporary prestress is designed to be set on the transfer pier.

Under the influence of the beam joint at the top of the pier, in order to ensure the construction safety of the cantilever segment, the zero block is temporarily anchored so that the segments on both sides of the beam joint of the zero block form an integral joint. The temporary anchoring of Block Z includes anchoring of the partition plate, as well as anchoring of the top and bottom plates. PSB830 ϕ 25 precision-rolled threaded steel is used for the temporary anchoring of the partition plate, which is horizontally and longitudinally anchored on both sides of the beam joint. The stress during anchoring and tension control is 740MPa. The finished rolled rebar is located on and below the manhole, with a total of 4 rows. There are 24 vertical spacing 80 cm and horizontal spacing 40 cm in the upper 2 rows of the manhole and 24 vertical spacing 57 cm and 40 cm horizontal spacing in the lower 2 rows of the manhole, as shown in Figure 4.

The transverse distance between the permanent prestressed steel beam and the temporary prestressed steel beam at the roof is 25 cm. The distance between them is 69 cm at the floor. The web spacing is 80 cm and 55 cm, respectively.

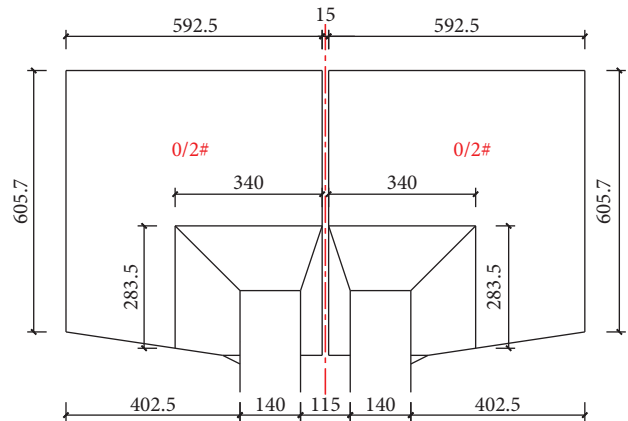


FIGURE 1: Schematic diagram of the structure of the No. 0 block of the junction pier.

The relative relationship between temporary prestress and permanent prestress is shown in Figure 4.

1.3. Transverse Limiting Device. In order to ensure that the final bridge line type meets the requirements of design and construction technical specifications, transverse limiters are installed at the end of the beam between two pairs of 3×70 m rigid frame and between 3×70 m rigid frame and 2×70 m rigid frame, and each transfer pier has two sets. The transverse limiter is installed in the reserved slot at the end of the beam. The height of the groove is 67 cm and the length is 82 cm. The structure and installation position of the lateral limiter are shown in Figure 5.

2. Key Construction Technology of No. 0 Block of Junction Pier

After the bracket is precompressed, the side formwork, end formwork, and beam seam formwork of the box girder are installed, and then, the bottom web reinforcement and prestressed metal bellows are installed. Then, the inner cavity scaffold is set up, and the inner roof formwork, roof reinforcement, and precast box girder concrete are installed. The relevant construction process of “No. 0 block” of junction pier is shown in Figure 6.

2.1. Installation and Fixing of Beam Seam Formwork. Through the experimental study of six kinds of beam joint support methods (Figure 5), it is found that using 10 mm steel plate as plane formwork and 2.21 mm visa plates as beam joint support has the best mechanical properties and the smallest deformation. The support mode of this kind of beam joint is adopted in the actual construction.

The beam joint support method is to install the prestressed groove template at the bottom plate first, then install the plane template, and finally, install the remaining groove and manhole template in place in turn. The two Vesar plates are fixed with $M5 \times 60$ cross-groove self-tapping screws, and processed in blocks. During processing, holes are opened at the corresponding prestressed pipeline position. After the

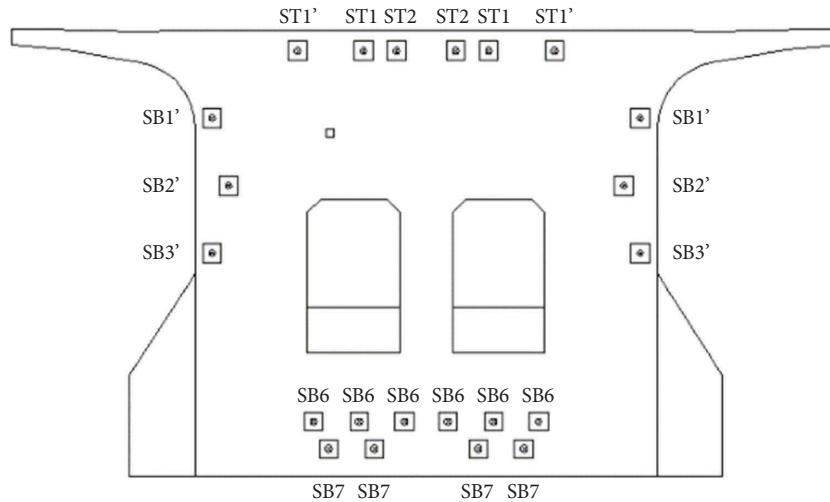


FIGURE 2: Permanent prestressing layout.

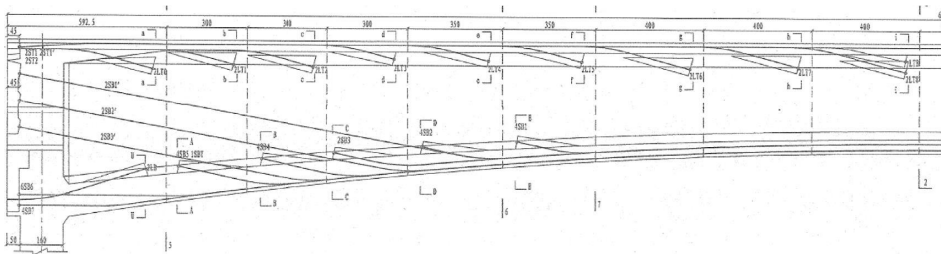


FIGURE 3: Layout diagram of prestressed steel tendons for cantilever casting segments of junction piers.

assembly of the bottom dies and side die of the zero block is completed, the whole lifting is carried out. The beam seam template is overall located on the bottom die as shown in Figure 7.

In nonlinear finite element analysis, it is necessary to have the right assumption of the nonlinear behavior of prestressed reinforced concrete (PC), such as cracking and plasticity of concrete, yielding of reinforcing steel, tension stiffening, and shear retention [4]. After the installation of the beam joint formwork is completed, one end of the equal angled steel with 50 degree is welded on both sides of the steel skeleton, and the other end is used to hold the formwork. The top of the formwork is welded on the side formwork to fix the formwork to prevent the beam joint formwork from floating during the concrete pouring process. The concrete pouring process should be controlled at all times.

The construction of the zero block of the transfer pier is completed, only the reserved slot and the hole template are removed, and the construction of the closure section corresponding to the transfer pier and the adjacent middle piers on both sides is completed in accordance with the construction closure sequence. After all the prestress is tensioned according to the design drawings, the temporary anchorage prestress of the zero block of the transfer pier is lifted, the prestressed pipeline is cut off, and the plane template of the beam joint and the beam support are removed by the Visa plate.

2.2. Prestress Construction. After the construction of the transfer pier-top section and each cantilever section is completed, the concrete strength reaches 95% of the design strength, and the elastic modulus reaches 100% of the design value, and the tension is carried out after the age is not less than 5 days. Tension 2LT0, 2LB, tension control stress of steel strand tension is 1,280 MPa, tension control stress of finishing rolled rebar is 740 MPa, temporary prestressed rebar and temporary prestressed steel strand hole are not grouted. In the construction process, with the prestress tension of each section, the section stress at the beam joint increases gradually, and the increase of the compression of the beam joint support may lead to the relaxation of the temporary prestress. Therefore, the temporary prestress should be checked after the completion of the construction of each section, and the relaxation of the prestressed steel strand or the finishing rolled screw steel should be supplemented.

The permanent prestress tension adopts 450T hydraulic jack, the size is A472 × 374 mm, and the stroke is 200 mm. The prestressed cable at the roof is tensioned by putting the bridge deck into the jack, and the prestressed cable at the floor is tensioned by putting the jack into the manhole. When the prestressed cable at the web is tensioned, 5 cm holes are reserved at the prestressed cable corresponding to the beam joint template, and the jack is fixed and tensioned by the wire rope, as shown in Figure 8.

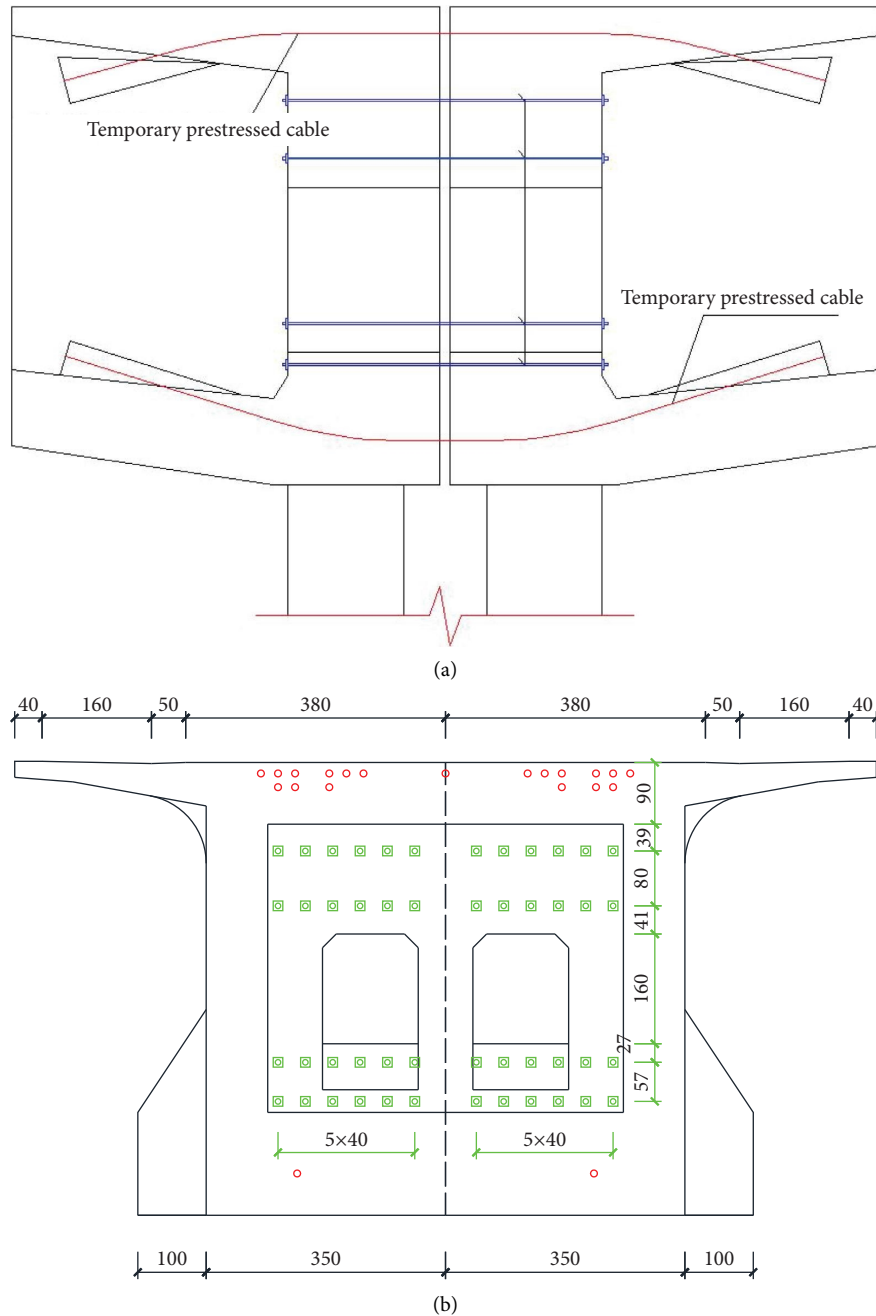


FIGURE 4: Schematic diagram of the temporary Anchorage structure of the junction pier.

3. Finite Element Analysis

The structure of the transfer pier is more complex and the modeling is more difficult. If the model is established according to the real structure, it will cause abnormal grid division, resulting in nonconvergence of calculation or inaccurate settlement results, so it is necessary to simplify the model. However, this will greatly reduce the reality of the model and reduce the credibility of the analysis results. In this paper, due to the use of the advanced BIM modeling technology (as shown in Figure 9), the parameterized method is used to optimize the model, and the best meshing result is obtained on the basis of

not significantly simplifying the model, which not only satisfies the reality of the model but also makes the finite element calculation proceed smoothly. For the mechanical analysis work in the structural design phase, data conversion and information transfer between the BIM model and finite element model have become the main factors limiting its efficiency and quality, with the development of the BIM technology application in the whole life cycle [5].

The high mesh quality of the finite element model and the lack of excessive simplifications improve the confidence of the computational analysis and speed up the finite element solution.



FIGURE 5: Visa plate compression test.

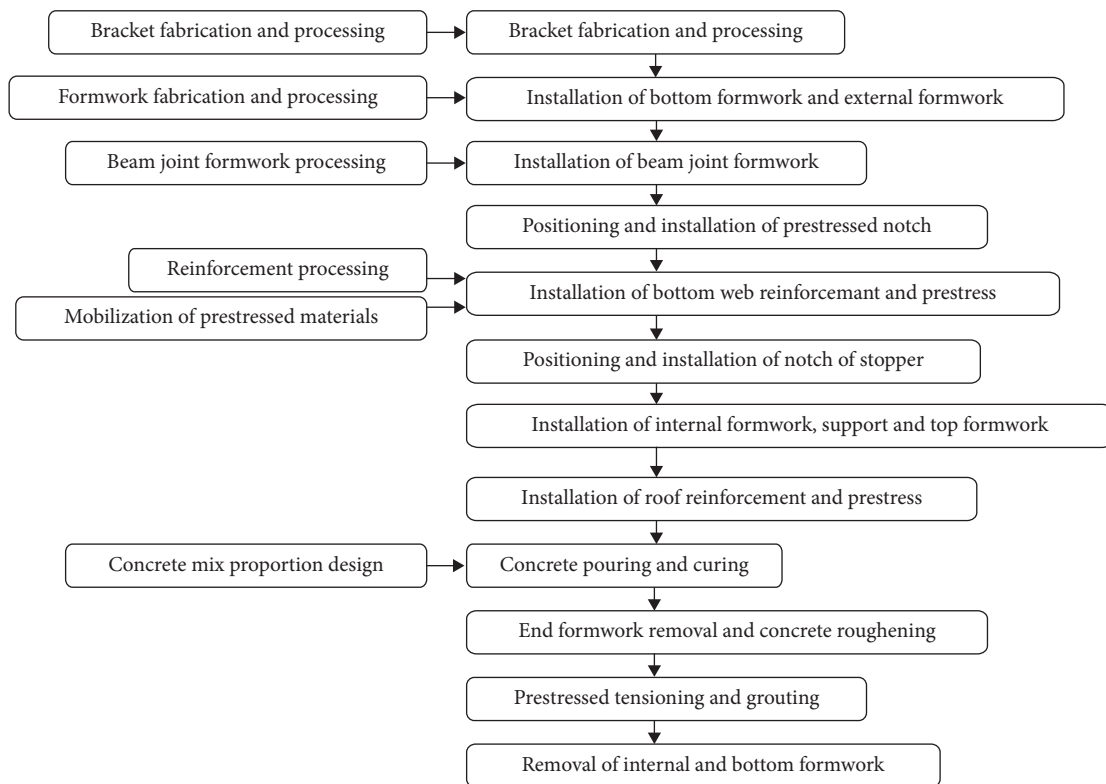


FIGURE 6: Construction flowchart of No. 0 block of junction pier.

3.1. *Finite Element Modelling.* In this paper, ABAQUS general finite element analysis software is used for numerical calculation, and the three-dimensional model optimized by the BIM technology is directly imported into the finite element software for meshing. The three structures will interact in the calculation and analysis, namely, the concrete

structure of the transfer pier, the beam-slit support structure composed of Visa plate and steel plate, and the permanent and temporary prestressed anchorage system. In order to make the calculation and analysis more accurate, the finite element model truly restores the size and position of the three components, as shown in Figure 10.

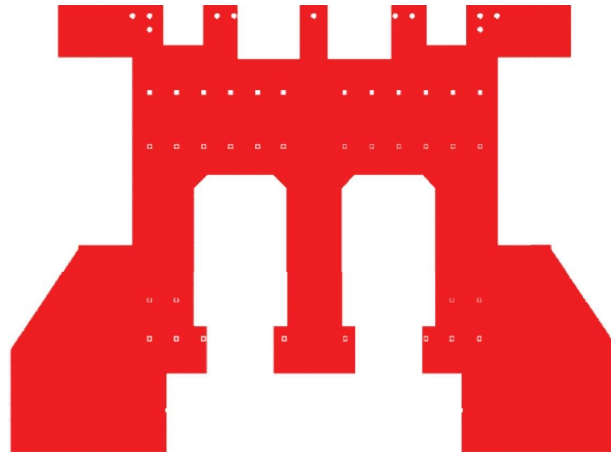


FIGURE 7: Processing schematic of beam seam template.

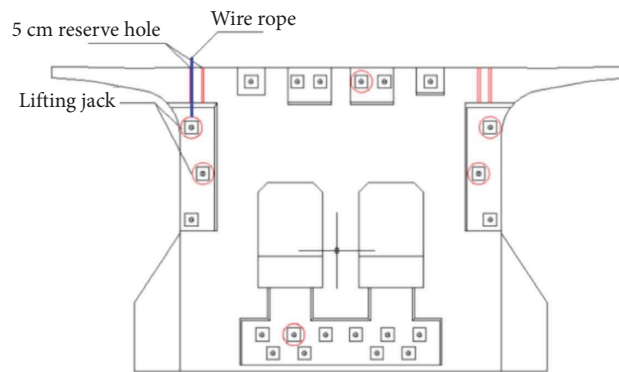


FIGURE 8: Layout of temporary prestressed tensioned jacks.



FIGURE 9: The BIM model and finite element model.

The object of calculation and analysis in this paper is No. 85 connecting pier. The height of the pier is 49.264 m and the height of both legs is 30 m, which is one of the highest three connecting piers. The connecting pier and Visa plate adopt solid element, and the steel bundle adopts cable element, with a total of 128,337 elements and 146,959 nodes. The cable element is embedded in the solid element, and the fixed boundary conditions are set on the bottom of the cap, and the material properties are shown in Table 1.

Before the analysis of the transfer pier, the beam element model is used to calculate and analyze the cantilever construction stage of the transfer pier, and the deformation on both sides of the transfer pier in each construction stage is obtained, which is applied as a boundary condition to the two ends of the solid element model of the transfer pier. Each deformation represents a construction stage. After the construction of block zero of the transfer pier is completed, the cantilever construction shall be continued on both sides

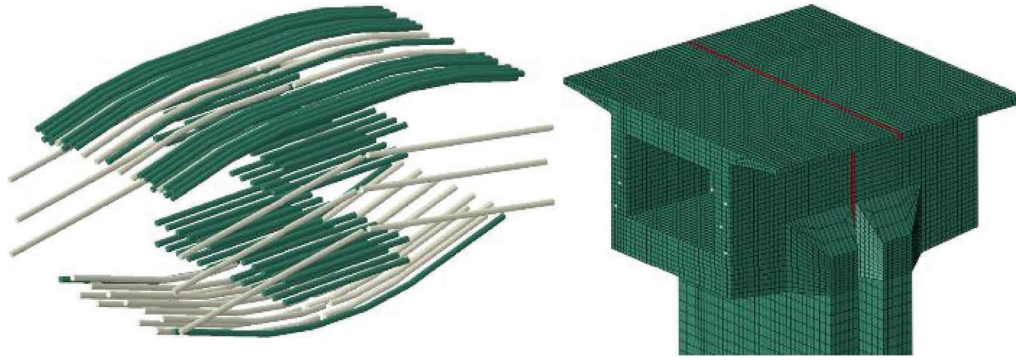


FIGURE 10: Prestressed steel beam and the Visa plate.

TABLE 1: Material properties.

Materials	Density (kg/m ³)	Elastic modulus (GPa)	Poisson's ratio
C50 concrete	2,500	35	0.2
Visa board	780	7.6	0.15
Steel products	7850	210	0.25

until the nine construction stages of the closure are shown in Figure 11 and Table 2.

3.2. Static Result Analysis. Due to the temporary anchorage of the zero blocks, it is equivalent to the rigid frame pier in the construction process before closure. The construction load mainly depends on the temporary prestressed steel beam and the finish rolling rebar. The tension control stress of the steel strand is 1,280 MPa, and the tension control stress of the finish rolling rebar is 740 MPa. In the calculation, the controlled prestress construction is applied by changing the temperature load of the material. The stress state before concrete closure is consistent with the middle pier of the rigid-frame bridge, and the deformation is shown in Figure 12.

It can be seen from the figure that due to the application of temporary anchorage prestress, the part of the structure is in a compression state, and the local concrete near the application of prestress has complex stress and large stress. As can be seen from the figure, due to the application of temporary anchorage prestress, the part of the structure is in a state of compression, and the local concrete near the prestress is complex, and there is a large stress. The time-frequency characteristics of the longitudinal displacements of bearings and expansion joints are analyzed using the empirical wavelet transform. The long-term characteristics of the longitudinal displacements of bearings and expansion joints in the operation period are explored [6].

Figure 13 shows the deformation diagram of the prestressed steel bundle and fine threaded steel bar in the second stage of construction. It can be seen that due to the application of prestress, the deformation of steel bundle and rebar is only about 1 mm.

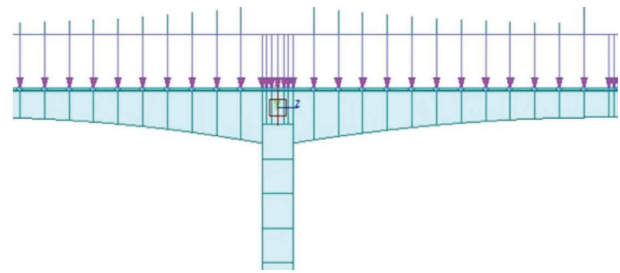


FIGURE 11: Calculation of the integral construction stage of the beam element model.

TABLE 2: Deflection of zero blocks in each construction stage.

Construction stage	Deflection (mm)
0	3.1
1	4.9
2	6.2
3	7.8
4	9.3
5	10.8
6	11.6
7	12.2
8	13.1
9	11.5

Note. Construction stage 9 is the closure stage.

As shown in Figure 14, the compressive stress of the visa plate shows an uneven distribution, the maximum compressive stress at the bottom corner is 17 MPa, and the distribution of the compressive stress is related to the size and position of the prestress. The static bending extrusion strength of the Visa plate with the thickness of 21 mm is 25 MPa, and the selected Visa board can meet the requirements of force and deformation.

As can be seen from the left picture of Figure 15, in the cantilever construction, the top of the zero block pier is anchored, the flexible pier will retract from the upper part with the deformation of the zero block, the lower part expands outward with the reverse bending point, and the maximum deformation of the upper part is 9.3 mm. As can be seen from the picture on the right of Figure 15, when the flexible pier is deformed, the tensile stress at the root of the

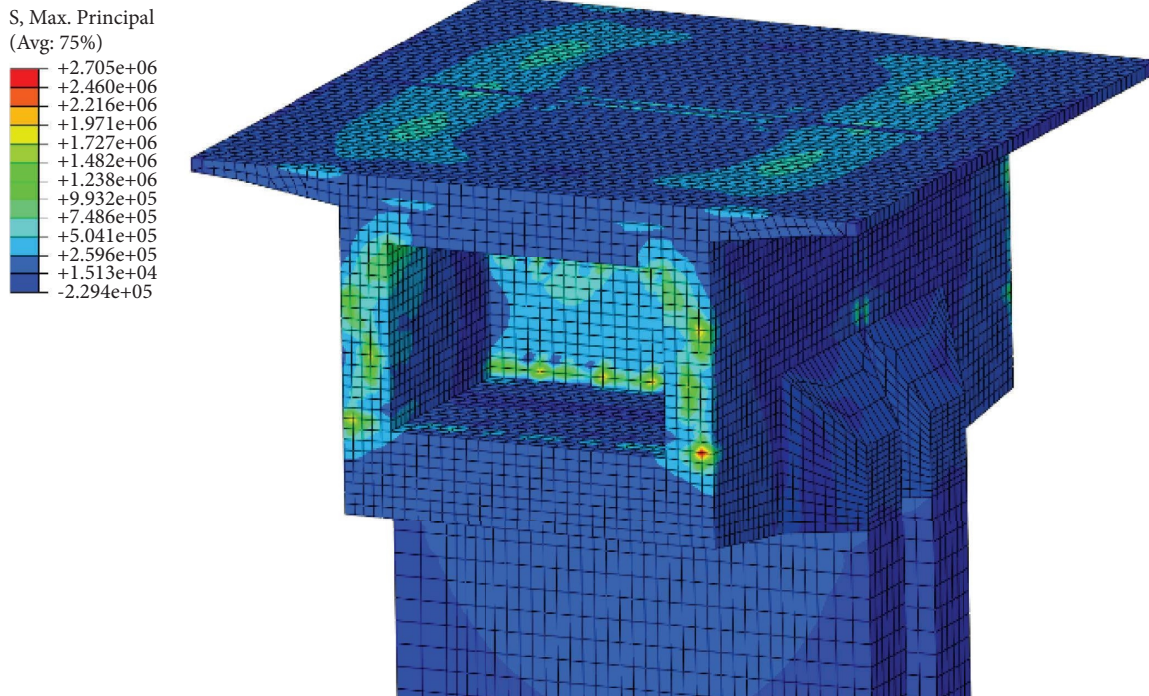


FIGURE 12: Cloud picture of the second maximum principal stress at the construction stage.

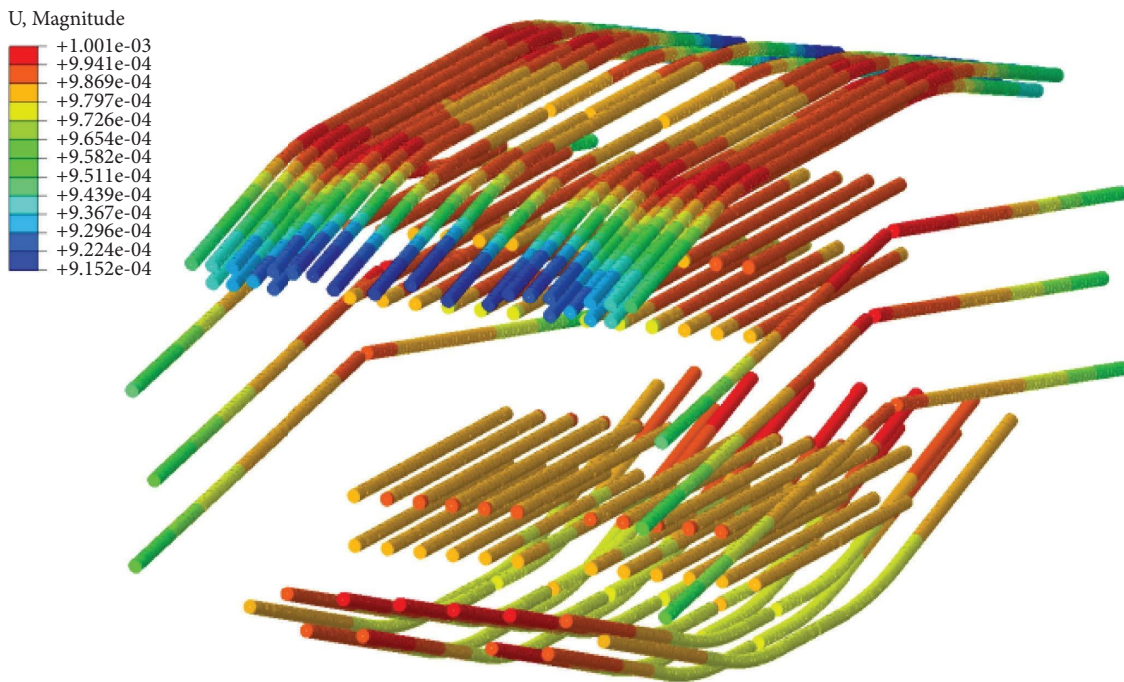


FIGURE 13: Cloud diagram of deformation of second steel bundle and steel bar in construction stage.

flexible pier is larger, because the internal prestress of the pier is not taken into account in the calculation, the result is only for reference and needs to be locally strengthened at the root of the two limbs.

Figure 16 shows the force and deformation of the connecting pier after the bridge is closed and the anchorage is removed. It can be seen from the figure that due to the

release of the constraint at the top of the pier, the loaded piles of the two single limbs are similar to the cantilever beam, and the inside of the single limb is subjected to tensile stress, the maximum tensile stress is about 2.7 MPa, and the maximum deformation of the limb is 33.5 mm. The flexible pier can release the deformation caused by the joint through its own deformation, so as to improve the stress conditions of the

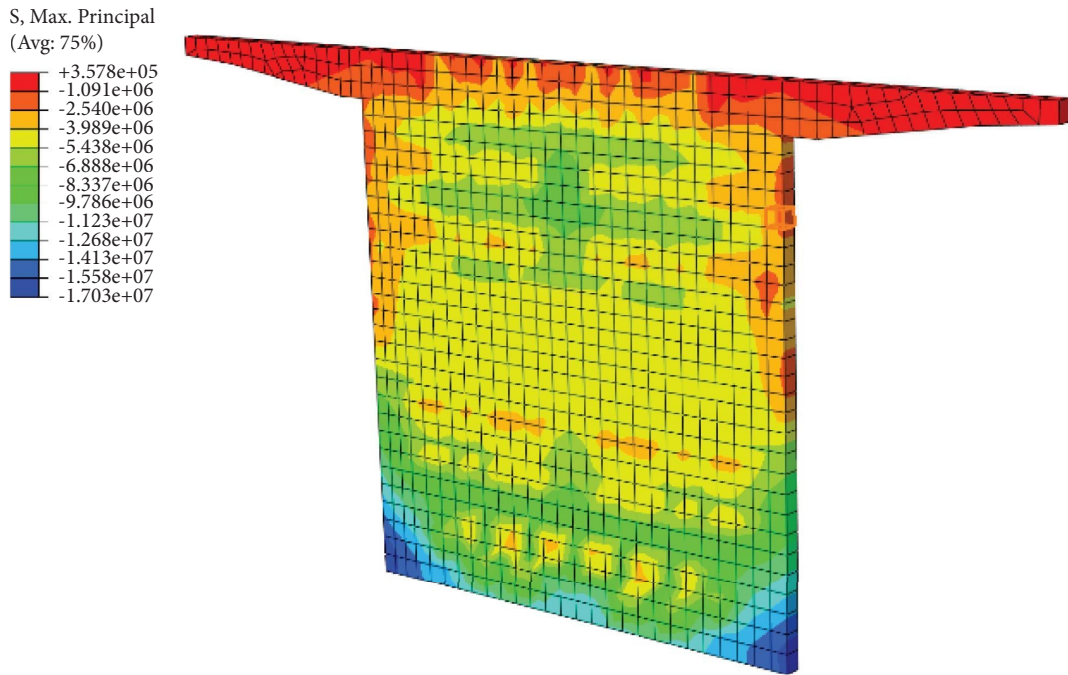


FIGURE 14: Compressive stress cloud diagram of the Visa plate.

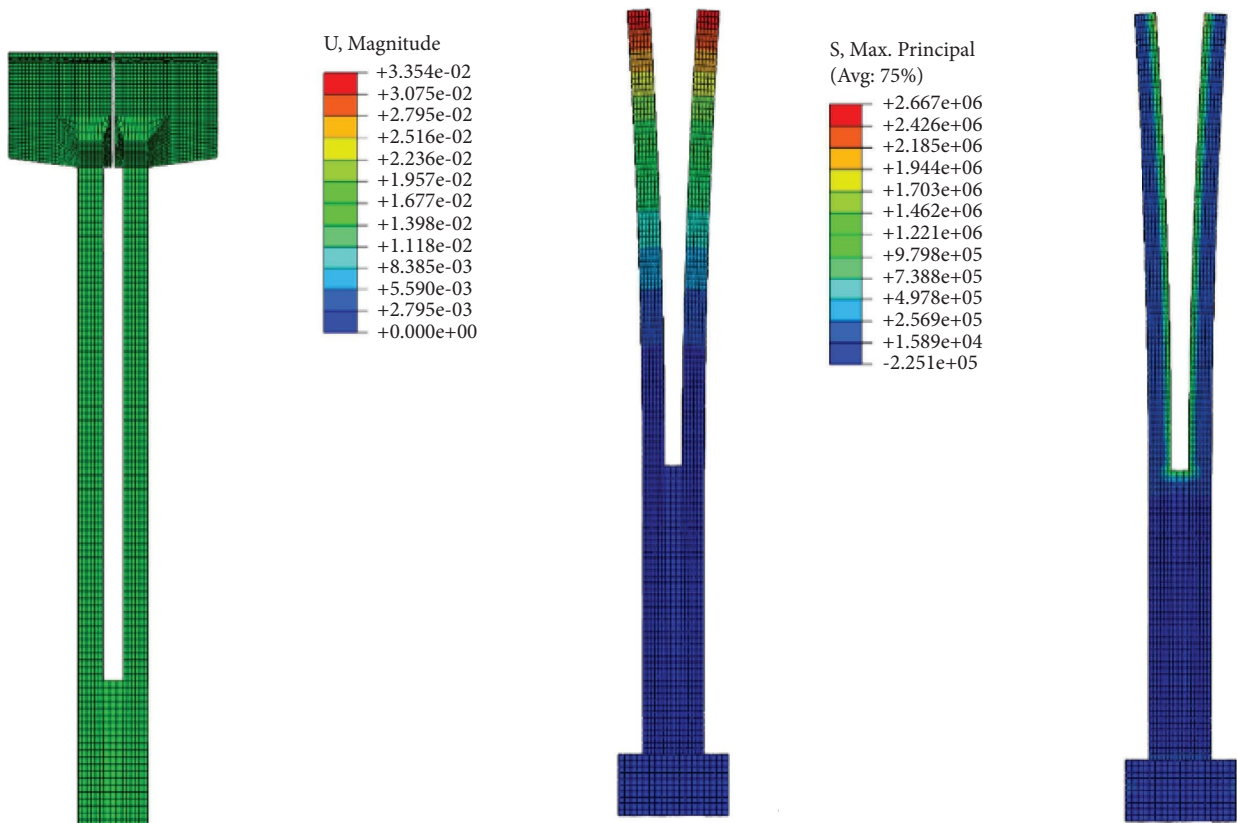


FIGURE 15: Deformation diagram of double-leg thin-walled piers under anchorage condition.

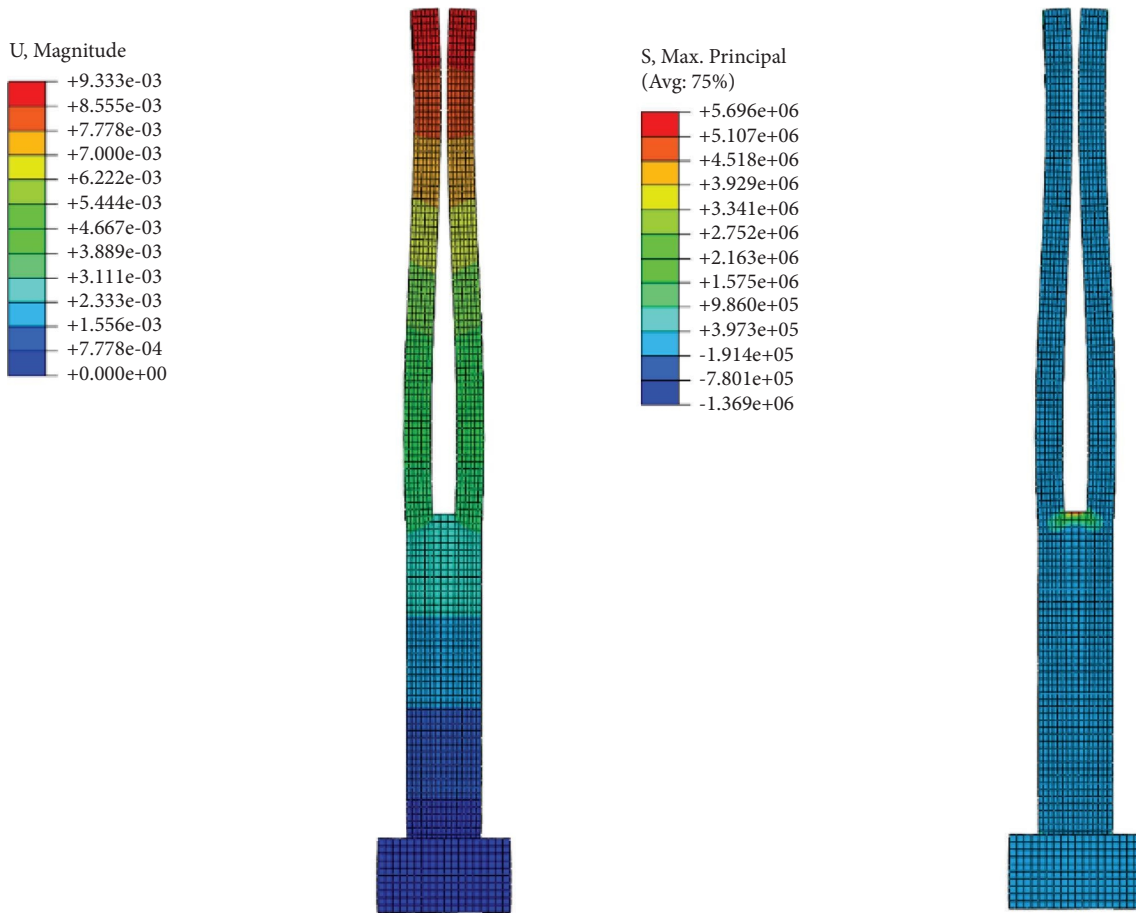


FIGURE 16: Deformation diagram of double-leg thin-walled piers under anchorage removal.

rigid frame bridge and reduce the additional internal force of the bridge. However, due to the existence of the tensile stress on the inside of the single limb, the pier will crack if it is not handled properly, so local reinforcement must be done when this type of pier is used.

3.3. Applying Seismic Time-History Load. The seismic area where the bridge is located is 8 degrees, the site is class III, the design reference period is 100 years, and the substructure and special position of the bridge are the key fortification parts. In order to simulate the seismic time-history load, based on the data of PEER (Pacific earthquake Engineering Research Center), the processed waveforms of seismic waves occurring near this area are obtained as shown in Figure 17:

When the earthquake intensity is lower than the earthquake intensity, the destructive effect of the frequent earthquake on the bridge structure is small. The acceleration of the common earthquake is 0.08 g and the gravity acceleration is defined as gravity acceleration. For the convenience of the study, the safe value is 10 m/s^2 , and the peak value of seismic acceleration is within 0.8 m/s^2 .

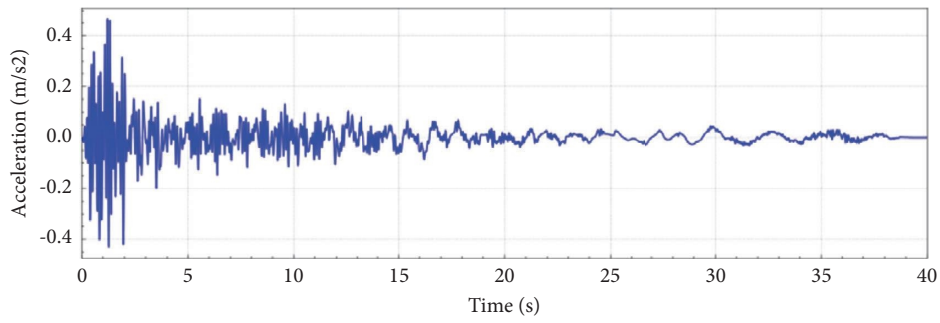
In this paper, on the basis of the time-history analysis of the common earthquake of the connecting pier, the time-history analysis is also done under the action of rare earthquake. The seismic wave used is the seismic wave

obtained after amplification and correction of common seismic waves, and the peak seismic acceleration reaches 4 m/s^2 , as shown in Figure 18.

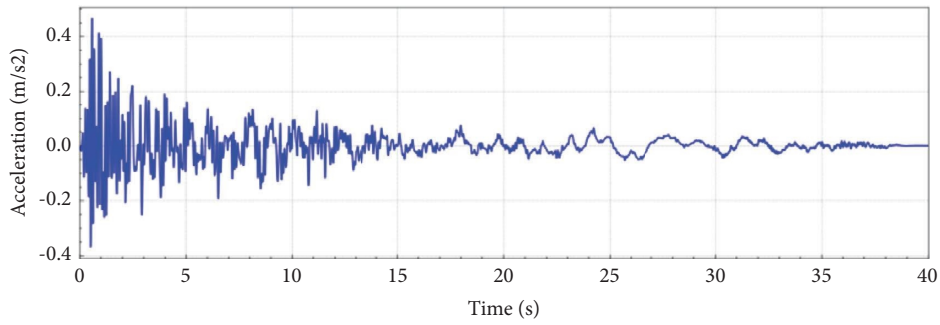
Under the stress state after the analysis of the ABAQUS construction stage, the model applies the acceleration time-history load in three directions: common earthquake and rare earthquake, carries on the time-history analysis, and obtains the time-history analysis result data.

3.4. Force Analysis Based on Rain Flow Counting Method. In the vertical direction of the double-leg thin-walled pier, the maximum principal stress data of three elements (as shown in the figure) are calculated by using the rain flow counting method, and the stress interval, average stress and cycle times can be obtained, as shown in Figure 19. The rain flow method is regarded as the most common cycle-counting method used in the irregular loading spectrum and is therefore adopted in this study [7].

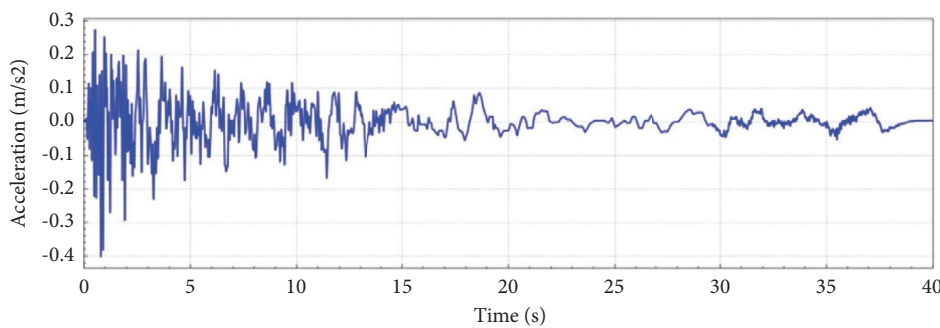
As shown in Figure 20, from the statistics of the rain flow count of the maximum principal stress in frequently encountered earthquakes, the maximum principal stress at position 1 and 3 of the connecting pier is larger, and the stress at position 2 is smaller, and the average stress of the maximum cycle number of the element at position 1 is about 2.9 MPa , the element at position 2 is about 1.24 MPa , and



(a)

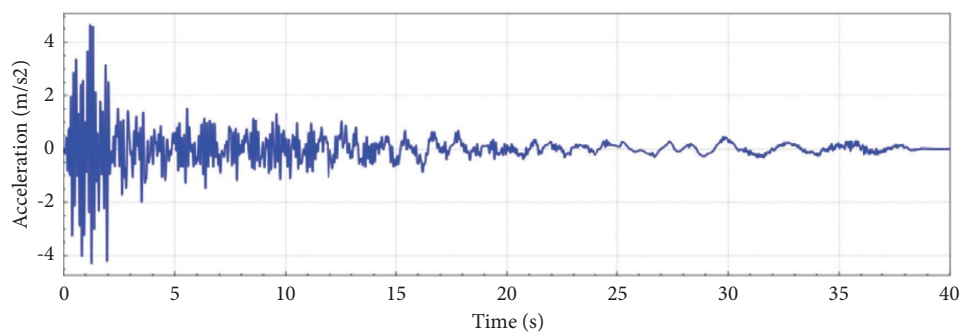


(b)



(c)

FIGURE 17: Frequently encountered seismic waves. (a) N-S seismic wave. (b) E-W seismic wave. (c) U-D seismic wave.



(a)

FIGURE 18: Continued.

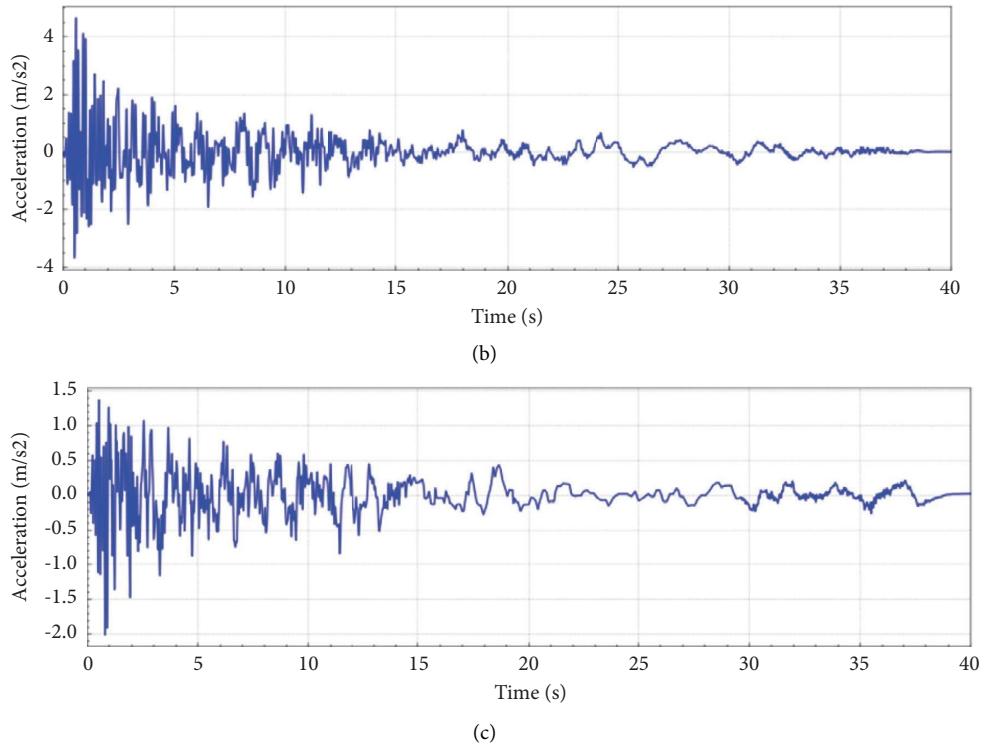


FIGURE 18: Rare seismic waves. (a) N-S seismic wave. (b) E-W seismic wave. (c) U-D seismic wave.

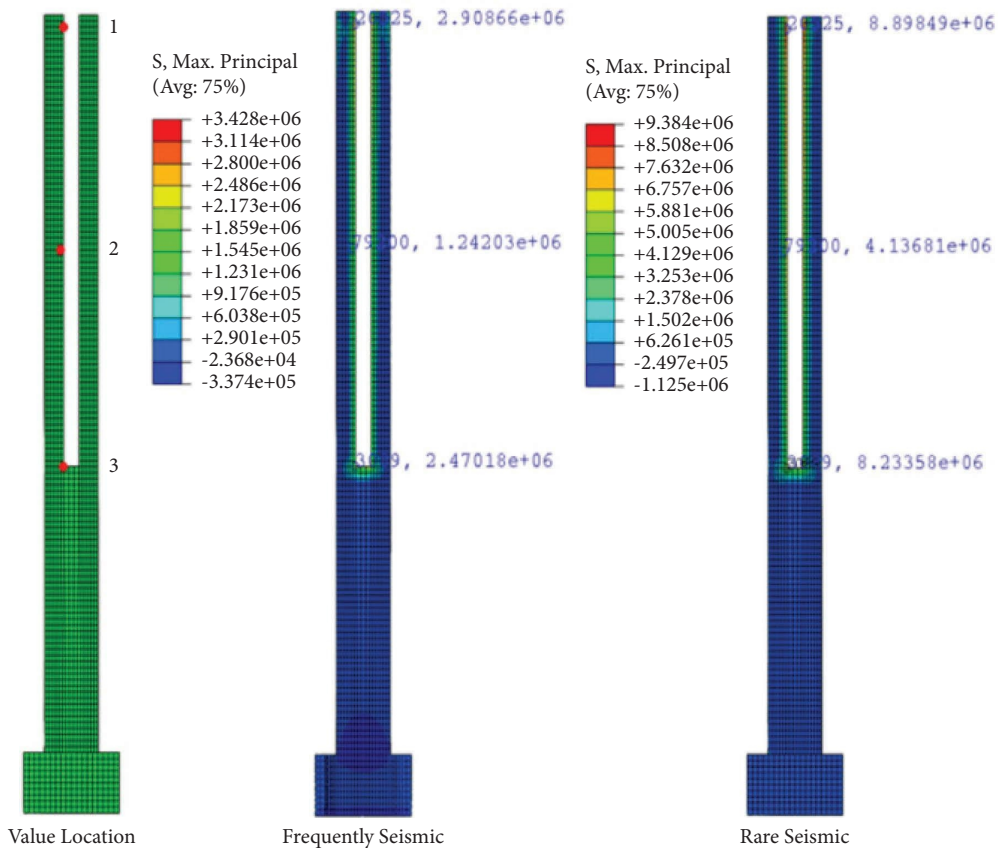


FIGURE 19: Calculation results of seismic spectrum.

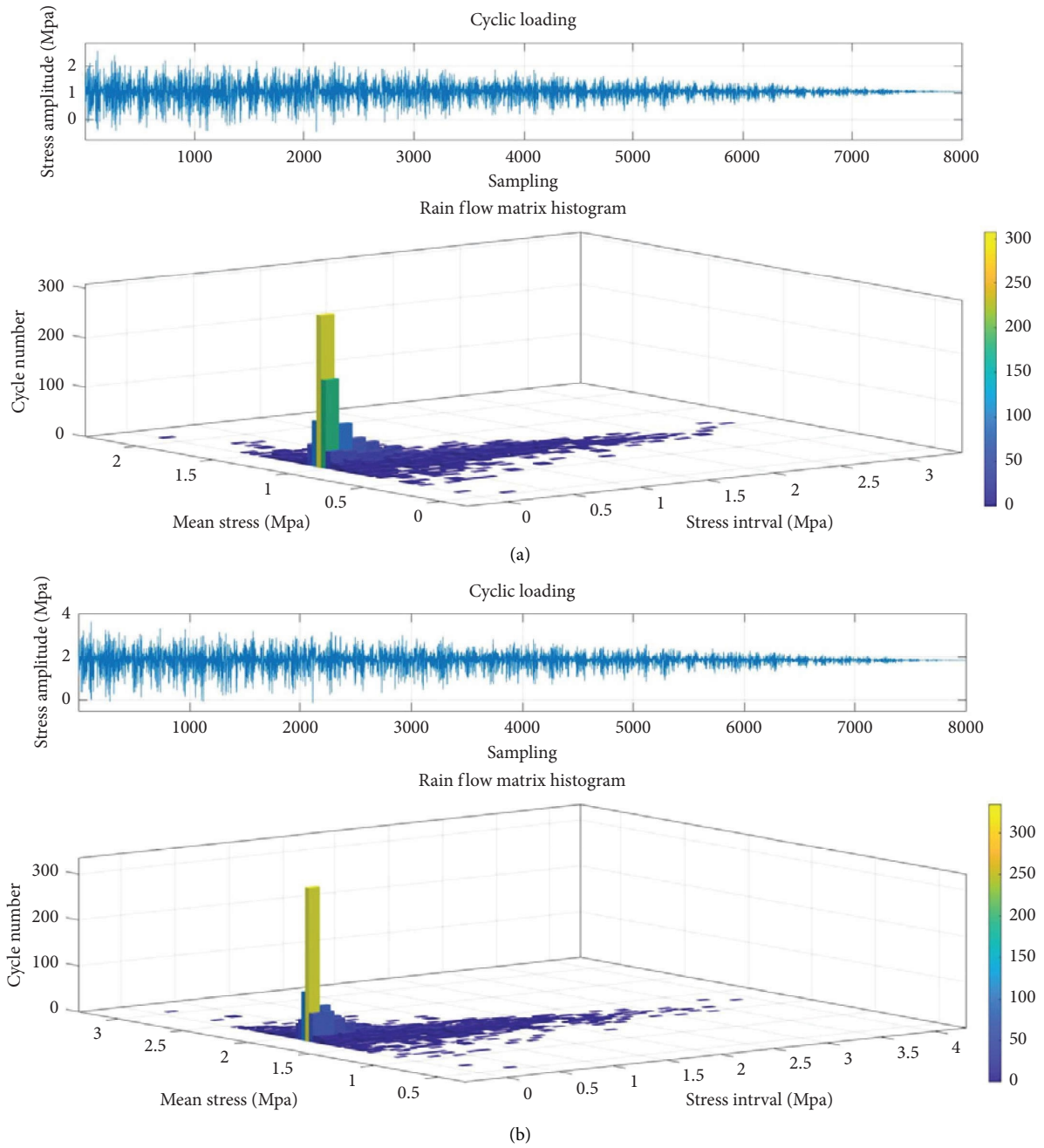


FIGURE 20: Continued.

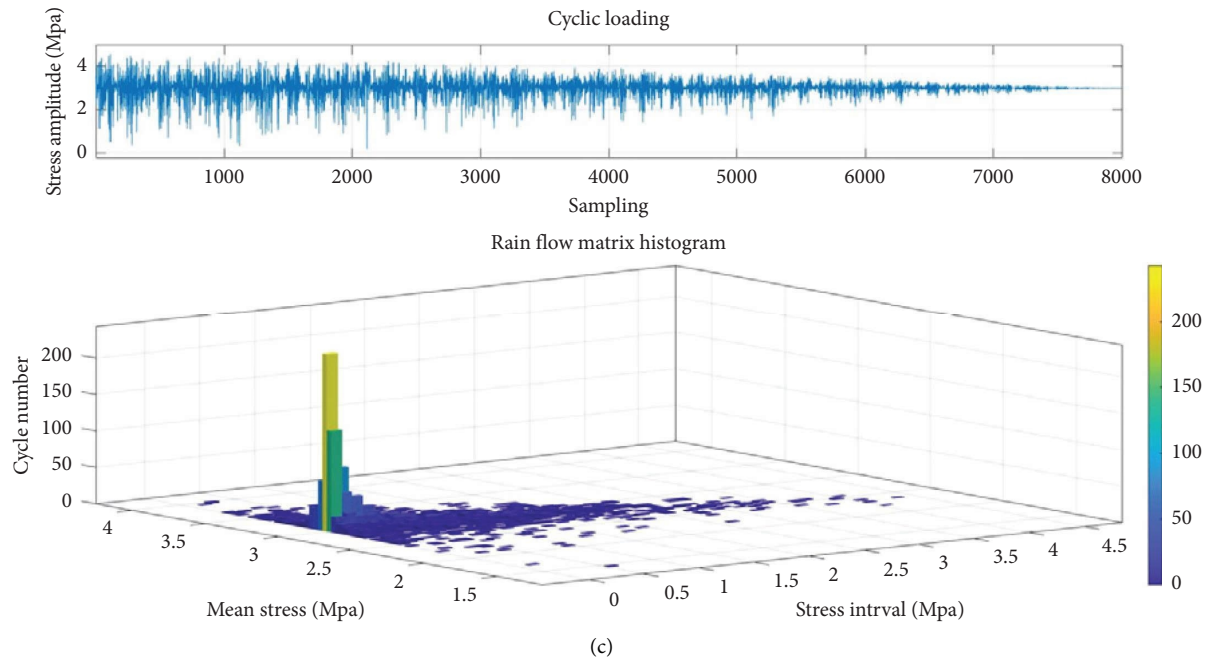


FIGURE 20: Statistics of rain flow count of maximum principal stress in frequently encountered earthquake units. (a) Rain flow count statistics of units at location 1. (b) Rain flow count statistics of units at location 2. (c) Rain flow count statistics at 3 locations.

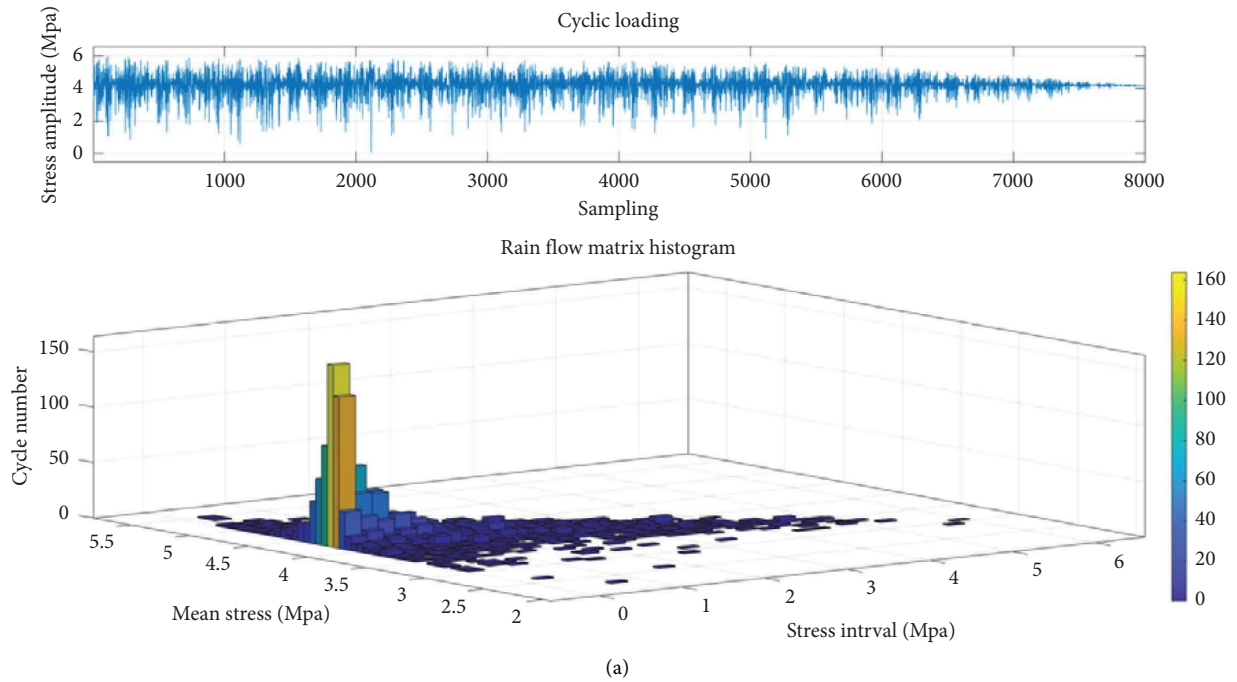


FIGURE 21: Continued.

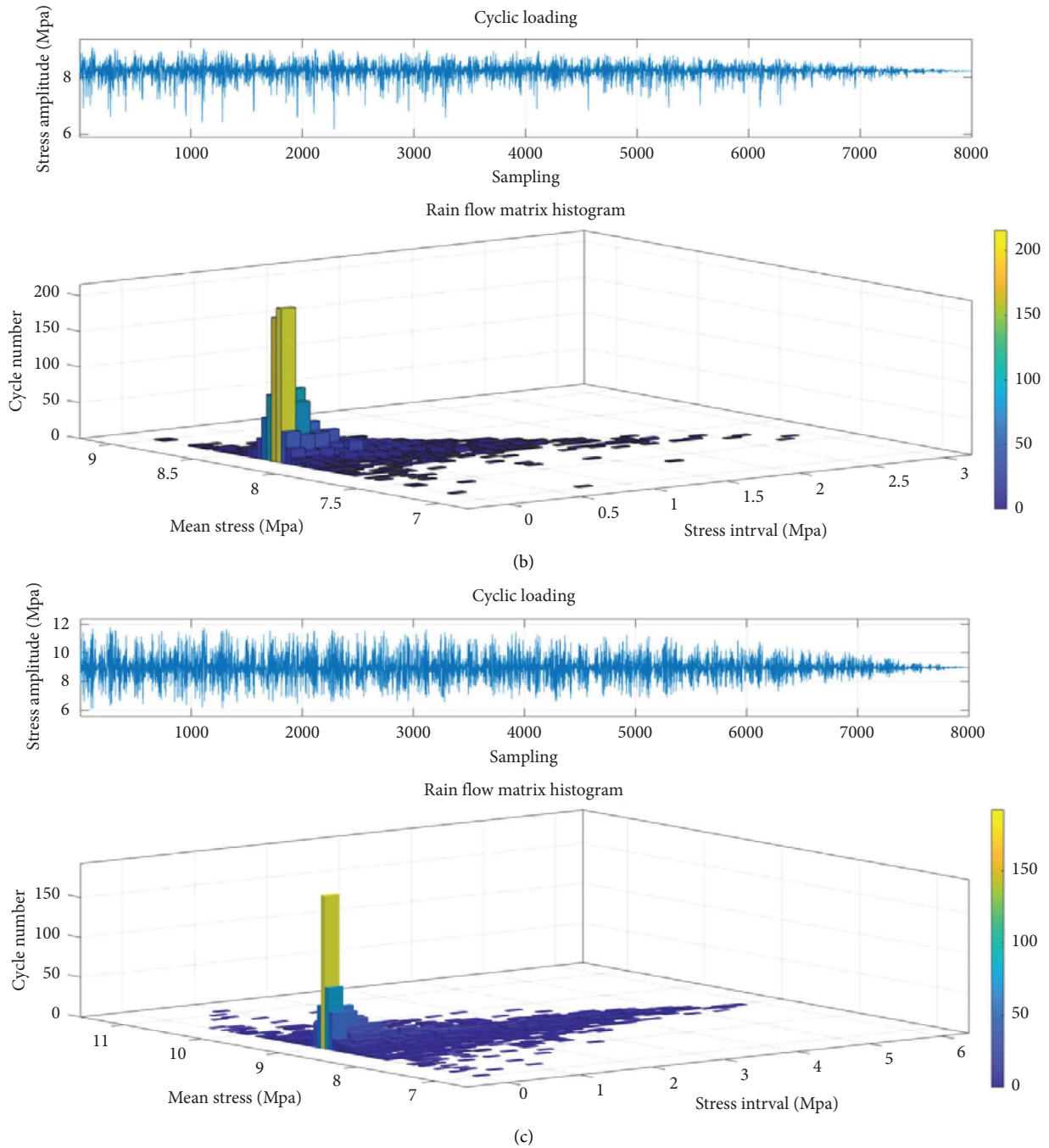


FIGURE 21: Statistics of rain flow count of maximum principal stress in rare earthquake units. (a) Rain flow count statistics of units at location 1. (b) Rain flow count statistics of units at location 2. (c) Rain flow count statistics at 3 locations.

that at position 3 is about 2.47 MPa, so under the action of common earthquakes, the concrete on the surface of the two limbs of the connecting pier will not produce structural cracks, and the pier can work normally.

As shown in Figure 21, from the rain flow count statistics of the maximum principal stress of rare earthquakes, the

distribution law of the maximum principal stress is similar to that of common earthquakes, but the value of principal stress increases greatly. The stress average value of the maximum cycle number of the element at location 1 is about 8.9 MPa, the element at location 2 is about 4.1 MPa, and the element at location 3 is about 8.23 MPa. The concrete on the surface of

both limbs of the connecting pier has been cracked, and the internal steel bar will play an important role in the bearing capacity.

4. Conclusion

The approach bridge of Quanzhou Bay Bridge on Fuzhou-Xiamen High-speed Railway is a multijoint rigid frame bridge without support. The top of the transfer pier is broken horizontally along the bridge, and the large deformation capacity of the double-limb thin-walled flexible pier can effectively release the deformation of the multijoint due to temperature change and other factors. In order to adopt the same cantilever cast-in-place construction technology as the middle pier in the construction, the zero block separated from the pier is temporarily anchored to form a whole, and the temporary anchorage is removed after the cantilever construction is closed.

Due to the complex force of the construction method, the bridge structure will undergo structural system transformation, so it is necessary to analyze the mechanical state of related components in the process of construction and system transformation in detail. In this paper, through the establishment of a high authenticity finite element model, the deformation and stress changes of the junction pier in each construction stage are calculated and analyzed, and its mechanical laws are summarized, so as to provide a reference for the future application of this type of pier.

Data Availability

The data used to support the findings of this study are included within the article.

Conflicts of Interest

The authors declare that they have no conflicts of interest.

Acknowledgments

This project was supported by the science and technology research and development plan of China Railway Corporation_K2018G017.

References

- [1] X. Yang, F. Lin, and M. Huang, "Analysis of the law of joint deformation for grouted mortise-tenon joint," *Advances in Civil Engineering*, vol. 2022, Article ID 2909993, 13 pages, 2022.
- [2] S. Mostafa Mousavi, B. Ataie-Ashtiani, and S. Mossa Hosseini, "Comparison of statistical and mcdm approaches for flood susceptibility mapping in northern Iran," *Journal of Hydrology*, vol. 612, 2022.
- [3] H. Guo, D. Zhou, and Y. He, "Trajectory control algorithm of flexible joint manipulator based on random matrix and screw theory," *Mathematical Problems in Engineering*, vol. 2022, Article ID 6073374, 12 pages, 2022.
- [4] C. Lesmana, H.-T. Hu, T.-C. Pan, and Z.-S. Lin, "Parametric study on nonlinear finite element analysis of prestressed reinforced concrete beam strengthened by fiber-reinforced plastics," *Mathematical Problems in Engineering*, vol. 2022, Article ID 9646889, 11 pages, 2022.
- [5] J. Jia, J. Gao, W. Wang, L. Ma, J. Li, and Z. Zhang, "An automatic generation method of finite element model based on bim and ontology," *Buildings*, vol. 12, 2022.
- [6] H. Zhao, Y. Ding, S. Nagarajaiah, and A. Li, "Longitudinal displacement behavior and girder end reliability of a jointless steel-truss arch railway bridge during operation," *Applied Sciences*, vol. 9, no. 11, p. 2222, 2019.
- [7] W. Meng, L. Xie, Y. Zhang, Y. Wang, X. Sun, and S. Zhang, "Effect of mean stress on the fatigue life prediction of notched fiber-reinforced 2060 Al-Li alloy laminates under spectrum loading," *Advances in Materials Science and Engineering*, vol. 2018, Article ID 5728174, 16 pages, 2018.

Research Article

Closure Scheme Analysis of 3×70 m Bearingless Integral Rigid Frame Bridge of Fuzhou Xiamen High-Speed Railway

Fangwen Weng ¹ and Xiangui Li ²

¹CCCC Second Harbor Engineering Company Ltd., Wuhan 430040, China

²Southeast Coastal Railway Fujian Company Ltd., Fuzhou 350013, China

Correspondence should be addressed to Fangwen Weng; sponerock@hbut.edu.cn

Received 6 September 2022; Revised 28 October 2022; Accepted 24 November 2022; Published 30 March 2023

Academic Editor: S. Mahdi S. Kolbadi

Copyright © 2023 Fangwen Weng and Xiangui Li. This is an open access article distributed under the Creative Commons Attribution License, which permits unrestricted use, distribution, and reproduction in any medium, provided the original work is properly cited.

The hydrodynamic problems associated with the construction of the sea-crossing bridge were proposed. The deep-water approach bridge on both sides of the main bridge of Fuzhou Xiamen high-speed railway adopts the bearingless prestressed concrete integral rigid frame bridge for the first time in the domestic railway bridge design. The rigid frame bridge applies the hanging basket cantilever construction, and there are several options for closure. Because the bridge structure system changes before and after closure, which will cause the redistribution of bridge internal force, the results of internal force redistribution will be different with the sequence and position of closure, and sometimes, there will be great changes. In order to select the optimal closure scheme, this article establishes the finite element model of the whole bridge and analyzes the whole construction process according to the working conditions and the mechanical state of the bridge before closure is obtained. Based on this state, eight closure schemes are analyzed and studied, which provides a sufficient mechanical basis for the determination of the final closure construction scheme.

1. Project Profile

1.1. Rigid Frame Bridge Introduction. On both sides of the main bridge of Quanzhou Bay Sea-crossing Bridge, there are some built continuous rigid frame bridges with one link of three spans and each span of 70 m. There are 9 continuous rigid frame bridges from pier 47 to 74 on the Fuzhou side, 11 continuous rigid frame bridges from pier 79 to pier 114 on the Xiamen side, and also another continuous rigid frame bridge of 2×70 m on the Xiamen side. The double-limb thin-walled pier is designed in the piers connecting the two ends of the continuous rigid frame bridge with other bridges and the two adjacent connecting piers of the continuous rigid frame bridge. The hollow pier is used in the middle of each pier, and the pier height is 27 m–51 m. The continuous rigid frame bridge adopts the cross-section form of a concrete variable cross-section box girder, which is a prestressed concrete integral rigid frame bridge without support. It is first used in domestic railway bridges, and the whole bridge does not have the bridge bearing.

According to the stress and construction characteristics of multispan multiconnected continuous rigid frame bridge, there are many times of structural system conversion, difficult construction alignment control, and the complex process in the construction process. Reasonable selection of the closure sequence of multispan multiconnected continuous beam construction is an important guarantee for structural quality and shape control. The advantages of such structural solution include better seismic performance and convenience in construction [1].

1.2. Technical Status of the Integral Rigid Frame Bridge without Bridge Bearing. Actually, the environment impact was simulated before the bridge construction in 1993 [2]. However, negligible change was predicted by the crude numerical model, which was newly developed at that stage. At present, the development of continuous rigid frame bridges in China and abroad tends to increase the span and joint length, and the research focuses are basically on the

construction optimization and monitoring of long-span and long-joint rigid frame bridges [3]. At present, there are no such cases of multiconnected continuous rigid frame without support in China and abroad, and the research on its complete set of construction technology is blank, most of which are simply repeated by single connection [4].

Semi-integral bridges have been widely used in German high-speed railways, such as the Erfot–Haller/Leipzig Railway Line and the Wendlingen–Ulmd Railway Line. The pier of semi-integral railway bridge is integrally connected with the superstructure, but the superstructure still sets the bridge bearing at the abutment. At present, the construction of this kind of bridge has been realized for the semi-integral railway bridges without structural expansion joints and rail expansion regulator within the length of 580 m [5].

The integral rigid frame bridge has no bridge and the side pier and the middle pier are consolidated with the main beam to form a rigid frame structure. The super- and substructures can cooperate, and the resistance of each part is evenly and fully, which realizes the overall stress of the structural system. The amount of material is greatly reduced, the structure is light and beautiful, good seismic performance, less maintenance, economy, and durability. Among the existing railway bridges in China, there is no precedent for the application of integral rigid frame bridge without bridge bearing.

2. Continuous Rigid Superstructure Closure Scheme

2.1. Overview of Mechanical Properties of Multiconnected Continuous Rigid Frame Bridge. The structure form of 3×70 m continuous rigid frame bridge is relatively novel, and the joint and joint connection position does not set bridge bearing. The junction pier is a double-legged pier, and the main beam at the top of the pier is divided, where expansion joints are set. During construction, both sides of the handover pier are temporarily consolidated, which facilitates the use of double-cantilever construction. It is conducive to reducing the construction difficulty and the use of temporary structures. After the completion of the construction, the structural system is transformed to remove the temporary consolidation [6].

The design and construction scheme of the transition pier is very characteristic, the main beam and pier are still consolidated, but the center of the pier is divided into two parts along the transverse. The construction made full use of the characteristics of the structure. Through the temporary anchoring structure to form an independent force structure, the construction method can be optimized. However, this design and construction scheme will also put forward higher requirements for the temporary anchorage technology, cantilever casting construction technology, construction control technology, construction process organization, closure sequence determination, and other aspects. In this article, the influence of different closure sequence on the mechanical properties of bridges is compared and analyzed.

The closure process of a continuous rigid frame bridge is not only the process of structural system transformation but

also the process of bridge completion in the final stage of cantilever construction. After closure, the bridge structure will change from the previous static structure to the statically indeterminate structure, and the internal force will be redistributed. Different closure sequences will lead to great differences in the redistribution of internal force, thus affecting the mechanical properties of the entire bridge.

2.2. Closure Construction Scheme. In this article, taking the Fuzhou side from no. 47 pier to no. 74 pier, a total of 9 links and 27 spans as the research objects for the comparison of the closure scheme, 8 closure schemes are analyzed and compared in order to fully understand the advantages and disadvantages of closure schemes.

In order to shorten the construction period, the middle pier of each joint and the adjacent joint transfer pier are simultaneously cantilevered. When the maximum cantilever state is reached, there are three closure joints in each joint. For the ease of distinction, each joint pier number is numbered in the order of 1, 2, and 3 from the Xiutu port to Quanzhou Bay (for example, joint port number A1 is A1-1, A1-2, A1-3), as shown in Figure 1.

With the center on the A5 joint, the closures were carried out simultaneously in the two directions of Xiutu Port Coast and Quanzhou Bay. The construction of transportation infrastructure is a vital step in boosting economic and social opportunities and often results in land use changes. According to the four principles of “first side span and then middle span,” “first middle span and then side span,” “alternate closure of side and middle span,” and “closure in turn,” the nine joint were divided into three construction bid sections (A1, A2, and A3 were bid Section 1; A4, A5, and A6 were bid Section 2; and A7, A8, and A9 were bid Section 3), and eight closure schemes were formulated. In each closure scheme, the prestressed tendons of the temporary cantilever beam are removed after the closure of the closure openings on both sides of the transfer pier. The side span closure beams are tensioned in two batches. The first batch is tensioned after the closure of the side span, and the second batch is tensioned after the removal of the temporary prestressed tendons. Three construction bid sections are shown in Figure 2.

When multiple beams are continuously connected, the piers are used as the intermediate supports. However, the distance between piers needs to be carefully calculated because it would affect the solidity of the bridge. The construction of a beam bridge essentially adds a significant structure in a form of a large steel or iron beam called a girder. The girder provides a stronger support to the concrete deck and transfers the load down to the foundation. Generally, there are two types of broadly used girders including I-beam girders and box girders [7]. The scheme one to scheme four in the eight kinds of the closure scheme take three sections as a whole construction, including 22 steps; scheme five to scheme eight will construct three sections simultaneously, including nine steps shown as follows.

The closure mode of scheme one is side and middle span alternate closure; the closure mode of scheme two is in turn

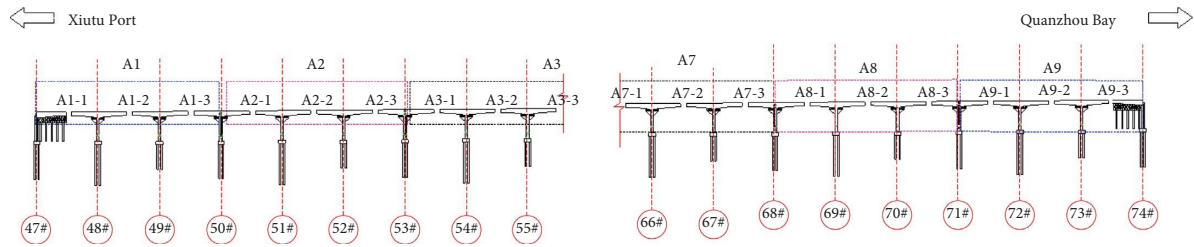


FIGURE 1: Number of each joint closure entrance.

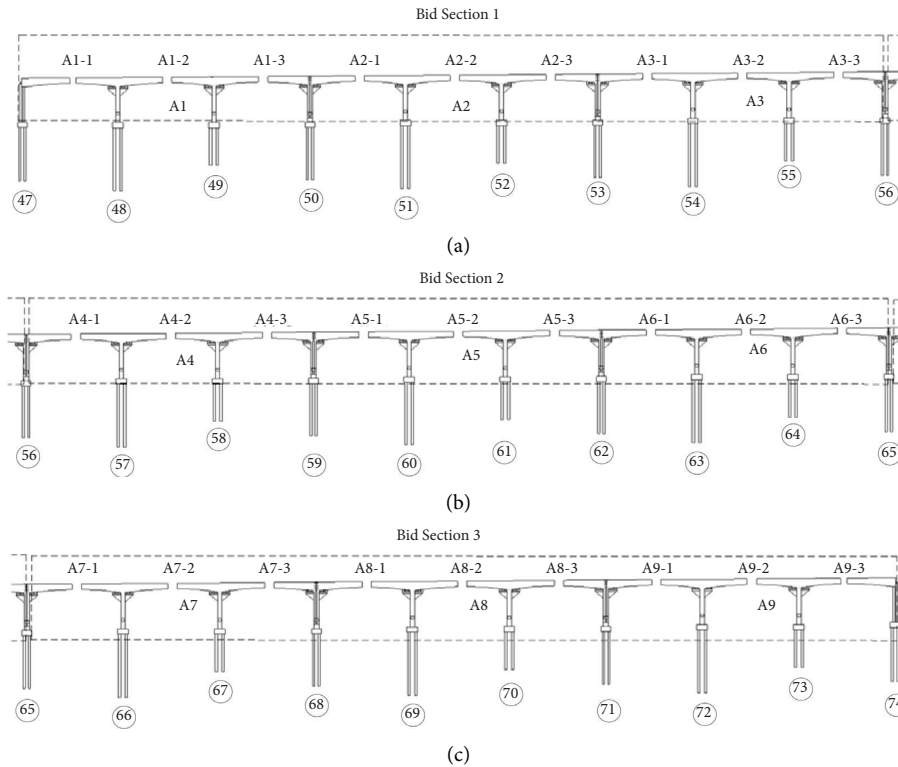


FIGURE 2: Three construction bid sections are (a) bid section 1, (b) bid section 2, and (c) bid section 3.

closure; the closure mode of scheme three is first middle span and then side span; the closure mode of scheme four is first side span and then middle span; the closure mode of scheme five is the simultaneous side and middle span alternate closure with three construction bid sections as a unit; the closure mode of scheme six is that three construction bid sections are taken as a unit to close at the same time; the closure mode of scheme seven is that the three construction bid sections are taken as a unit at the same time, first middle span and then side span; and the closure mode of scheme eight is that three construction bid sections are taken as a unit at the same time, and the side span is first and then the middle span.

It is proposed that the construction time of each closure section is 7 days, the removal time of temporary prestressed tendons is 2 days, and the tension time of the second batch of side span closure prestressed tendons is 2 days. Table 1 shows the maximum span number and closure time in the closure process of the 8 schemes.

3. Numerical Simulation Analysis of the Continuous Rigid Frame in the Construction Stage

A continuous rigid frame bridge cantilever construction process is very complicated and needs a high degree of internal force and deformation control. The internal force and deformation as the construction of the advance will be affected by many factors, and those factors include material elastic modulus, bulk density, temperature, shrinkage and creep, and external load [8]. These effects directly lead to the change of the internal force and deformation. Besides, there are also many structural system changes in the construction and structural system. Therefore, it is very necessary to conduct an accurate theoretical calculation and analysis before the construction.

The results of calculation and analysis can greatly guide the construction control, and the calculation model can also continue to play an important role in the construction

TABLE 1: The closure scheme duration and the maximum span number in the closure process.

Construction schemes	Closure construction period (days)	Maximum span number in the closure process	Timing of maximum spans
Scheme 1	114	7	A4-3 and A6-1 closure
Scheme 2	114	5	A4-3 and A6-1 closure
Scheme 3	114	7	A4-3 and A6-1 closure
Scheme 4	114	3	A5-2 closure
Scheme 5	43	7	A1-3, A3-1, A4-3, A6-1, A7-3, and A9-1 closure
Scheme 6	43	5	A1-3, A3-1, A4-3, A6-1, A7-3, and A9-1 closure
Scheme 7	43	7	A1-3, A3-1, A4-3, A6-1, A7-3, and A9-1 closure
Scheme 8	43	3	A2-2, A5-2, and A8-2 closure

monitoring, which can obtain dynamic feedback and decision-making in order to achieve the design purpose [9]. The final closure of the long-span continuous rigid frame is a structural system change, the final closure of the whole structure can produce dramatic change of internal force and deformation, and the final closure of the structure state (internal force and deformation) are the results of each construction stage accumulation. Therefore, for studying the mechanical state of the bridge structure during closure, it is necessary to analyze all the previous construction stages clearly. Before closure, each joint will undergo eight construction stages to form the maximum cantilever state before closure as shown in Figure 2, and the single joint as shown in Figure 3:

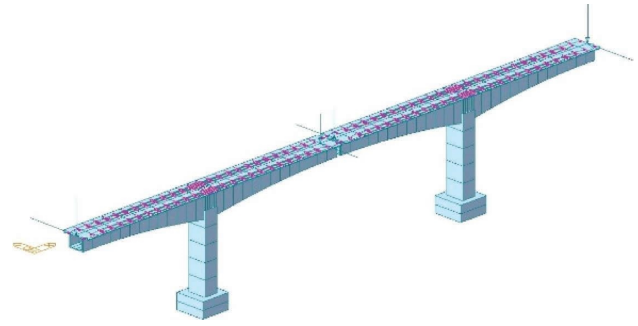


FIGURE 3: Phase VIII construction.

3.1. Establishment of the Finite Element Model. Piers for integral bridges can be of any type. If the inherent flexibility of a chosen type will accommodate structural movements, the piers may be built integrally with the superstructure or connected to it with anchor bolts. Otherwise, piers are designed as semirigid self-supporting substructures with movable bearings between them and the superstructure [10]. The finite element model adopts the beam element. In the bridge span direction, the variable section group provided by the program is used to generate variable section beams, and the beams and piers are consolidated. The beam pier corresponding node uses the master-slave node for rigid connection. The joints at the bottom of the pier are fixed boundary conditions with six degrees of freedom [11]. The loads in the construction process include dead weight, construction load, hanging basket weight, which is 75 tons, and the second-phase dead load. The influence of concrete shrinkage and creep is considered in calculation. The shrinkage and creep are calculated according to the code. The temperature load is taken according to the specification, and the temperature of the system is considered as $+15^{\circ}\text{C}$ or -15°C . The material parameters are shown in Table 2; the material parameters of a prestressed steel beam are shown in Table 3.

The number of prestressed steel beams is large, the shape is complex, and the conventional modeling method is time-consuming and laborious [12]. In the calculation, the interface program is developed to connect finite element software with three-dimensional modeling software. The spatial curve model of prestressed steel bundle can be

TABLE 2: Material characteristics of prestressed concrete.

Material properties	Values
Elastic modulus	36000 MPa
Weight by volume	26.5 KN/m
Thermal expansion ratio	0.00001
Poisson ratio	0.18
Prestressed concrete strength	$\geq 95\%$

established in 3D software and then directly imported into the finite element software through the interface program, which greatly improves the modeling efficiency of prestressed steel bundle. The whole finite element model is shown in Figure 4.

3.2. Results Analysis. The cantilever construction is carried out at the same time for the middle pier and the junction pier. The vertical deformation diagram and bending moment diagram of the structure under the maximum cantilever state are shown in Figures 5 and 6. The maximum span involved in the construction process of different closure schemes is 7 spans, and the influence of different closure schemes on other joint internal forces is similar to A4 and A5.

3.2.1. Contrastive Analysis of Internal Force of Each Closure Scheme. In the process of the construction and in the complete stage of the bridge, the beam sections in the position of the pier and closure are prone to bending cracks. The main beams at the junction pier, middle pier, and closure section are taken as stress statistical points to

TABLE 3: Properties of prestressed tendons.

Mechanical properties of prestressed reinforcement	Numerical magnitude
Elastic modulus (E_p)	195000 MPa
Duct deviation coefficient	0.0015
Relaxation coefficient of steel strands	0.3
Friction coefficient of prestressed duct	0.17
End-anchorage reinforcement recondensation	0.006 m
Controlled stretching stress of longitudinal steel strands	1395 MPa
Controlled stretching stress of lateral steel strands	1302 MPa
Controlled stretching stress of vertical steel strands	785 MPa

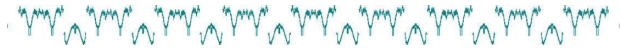
FIGURE 4: Nine-link 3×70 m continuous rigid frame 3D finite element model.

FIGURE 5: Vertical deformation diagram of the maximum cantilever state.



FIGURE 6: Bending moment diagram under the maximum cantilever state.

compare and analyze the stress in the construction process and in the complete stage of the bridge of different closure schemes, as shown in the figure.

Midas-Civil finite element software can output the normal stress at four positions of the upper and lower flange of the beam element section [13]. The maximum compressive stress and tensile stress (the compressive stress is negative and the tensile stress is positive) at four positions of the upper and lower flange are only counted when the beam element stress of different closure schemes is calculated, as shown in Figures 7 and 8.

The stress difference $\Delta\sigma$ is used to describe the bridge completion state and the stress deviation in the closure process between the schemes, as shown in the following formula:

$$\Delta\sigma = \sigma_{\max} - \sigma_{\min}. \quad (1)$$

In the formula, σ_{\max} represents the maximum stress of the beam element at a certain position in eight construction schemes and σ_{\min} represents the minimum stress of the beam element at a certain position in eight construction schemes.

The comparison results of the bridge completion state and maximum stress in the closure process of eight closure schemes are shown in Figures 9 and 10 and Tables 4 and 5.

Based on the above data analysis, it can be seen that

- (1) In the completed bridge state, there is little difference in the stress between different closure schemes, and both the pier and closure section present the full section compression state. The maximum stress difference $\Delta\sigma$ of the eight schemes is 0.42 MPa, which appears at the beam pier section of the midspan pier of the bridge link A4 (SA4-2-3).
- (2) During the closure process, the tensile stress occurs at the beam section of the middle pier and the junction pier, and the beam section of the closure section is in a compression state. Among them, the tensile stress of the beam section (SA4-2-3) at the middle span pier of scheme 1 and scheme 5 in the link A4 is the largest, 1.53 MPa and 1.68 MPa, respectively.
- (3) In the construction of different closure schemes, the maximum stress difference $\Delta\sigma$ is 1.04 MPa, which appears at the closure section pier of the link A4 span (SA4-1-2). In the process of closure, the maximum stress difference $\Delta\sigma$ is 0.78 MPa, which appears at the beam section midspan pier of the link A4 (SA4-2-3).

3.2.2. Comparative Analysis on Structural Deformation of the Bridge Completion State of Each Closure Scheme. In the construction process, the precamber is generally used to make the structure achieve reasonable completed bridge shape. In the case that the longitudinal slope and long-term deflection effect of the structure are not considered, it can be considered that the reasonable completed bridge shape of the structure is when the deflection of each point in the completed bridge state is 0. As the girder deflection at the pier is generally zero and the deflection at the closure is large, the deflection of the bridge at the A4 joint and A5 joint is taken as a comparative analysis of the parameters deviating from the reasonable completed bridge state under different closure schemes, as shown in Figure 11.

The average deflection D_{avg} at each deflection statistical point under the bridge completion state represents the deviation of bridge completion deflection from the reasonable bridge completion state of different schemes, which actually reflects the average camber of each statistical point in the construction process, as shown in the following formula:

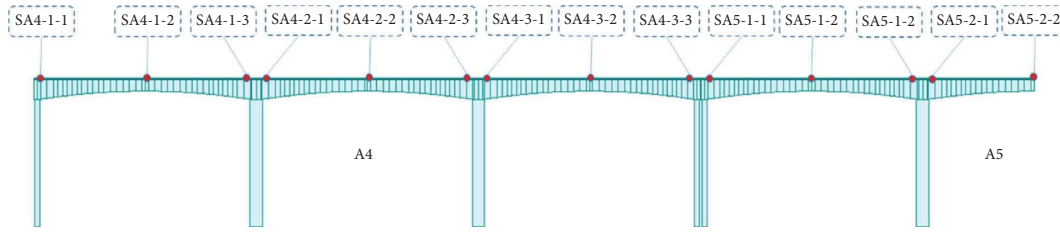


FIGURE 7: Beam element stress statistical point.

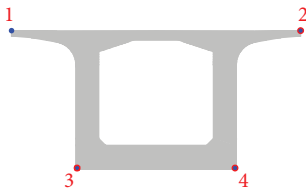


FIGURE 8: Finite element stress calculation output point.

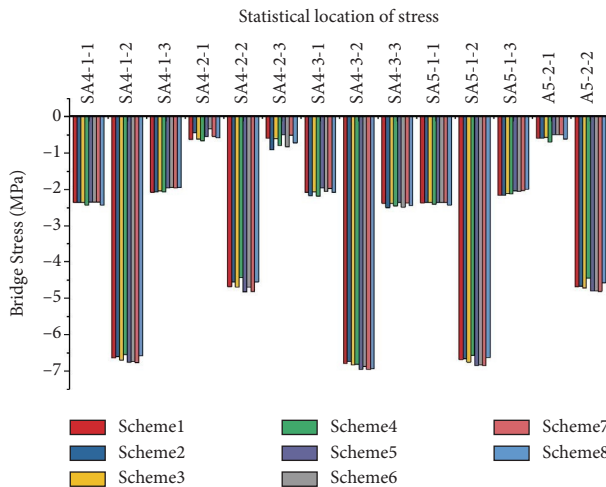


FIGURE 9: Comparison of beam element stress of each closure scheme in the bridge forming stage.

$$D_{avg} = \frac{|D_1 - 0| + |D_2 - 0| + \dots + |D_9 - 0|}{9} \quad (2)$$

In the formula, D_i is the deflection of 9 statistical points of deflection.

Based on the above data analysis as shown in Table 6 and Figure 12, it can be seen that

- (1) Scheme 4 and scheme 8, scheme 2 and scheme 6, scheme 1, scheme 3, scheme 5, and scheme 8 are relatively close in the bridge alignment
- (2) There is little difference between the maximum deflection and the maximum arch under different closure schemes. The maximum deflection of each closure scheme in the completed bridge state is about 20 mm, which all appear at the right position of the closure section of A4 joint third span (DA4-3-2). Except for scheme 4 and scheme 8, the maximum

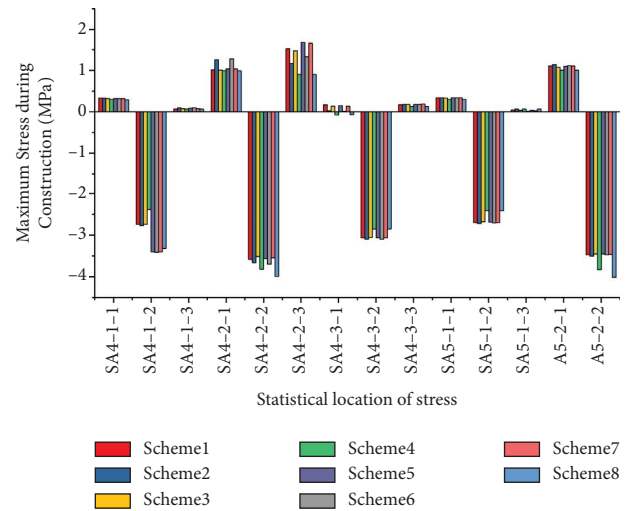


FIGURE 10: Comparative analysis of maximum stress of the beam element in the closure process of different closure schemes.

camber appears on the left side of the third span closure section, and the maximum cambers of other closure schemes in the bridge state all appear on the left side of the A4 middle span closure section (A4-2-1). The maximum camber of scheme 4 and scheme 8 is about 5 mm, and the maximum camber of other schemes is about 10 mm.

- (3) The D_{avg} value of average deflection of all closure schemes in the completed bridge state is not different from each other. Compared with other closure schemes, the scheme 4 and the scheme 8 are close to reasonable completed bridge shape. Scheme 4 has the lowest D_{avg} value of average deflection of 6 mm, while scheme 5 and scheme 7 have the largest D_{avg} value of 10.5 mm. The D_{avg} value difference between the maximum and minimum average deflections is 4.5 mm.
- (4) In conclusion, the difference of internal force and bridge shape between different closure schemes is small. There is little difference between the maximum stress of the main beam in the process of closure and the stress in the completed bridge state between different closure schemes. The maximum upper deformation, deflection, and D_{avg} value of average deflection between different closure schemes are within 5 mm.

TABLE 4: The bridge state and the stress difference between the schemes in the process of closure (MPa).

Construction scheme	Statistical number of beam element stress															
	SA4-1-1	SA4-1-2	SA4-1-3	SA4-2-1	SA4-2-2	SA4-2-3	SA4-3-1	SA4-3-2	SA4-3-3	SA5-1-1	SA5-1-2	SA5-1-3				
$\Delta\sigma$	0.08	0.23	0.13	0.33	0.39	0.42	0.22	0.23	0.13	0.07	0.29	0.17	A5-2-1	A5-2-2	0.20	0.36

TABLE 5: Maximum stress difference of the beam element in the closure process of different closure schemes (MPa).

Construction scheme	Statistical number of beam element stress													
	SA4-1-1	SA4-1-2	SA4-1-3	SA4-2-1	SA4-2-2	SA4-2-3	SA4-3-1	SA4-3-2	SA4-3-3	SA5-1-1	SA5-1-2	SA5-1-3	SA5-2-1	SA5-2-2
$\Delta\sigma$	0.04	1.04	0.04	0.29	0.48	0.78	0.25	0.25	0.06	0.05	0.31	0.05	0.13	0.57

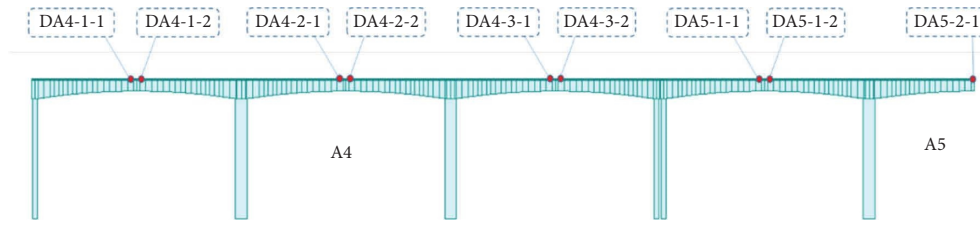


FIGURE 11: Deformation statistical point.

TABLE 6: Average deflection of each closure scheme in the bridge state (mm).

Closure schemes	D_{avg}
Scheme 1	9.8
Scheme 2	9.3
Scheme 3	9.8
Scheme 4	6
Scheme 5	10.5
Scheme 6	9.8
Scheme 7	10.5
Scheme 8	6.3

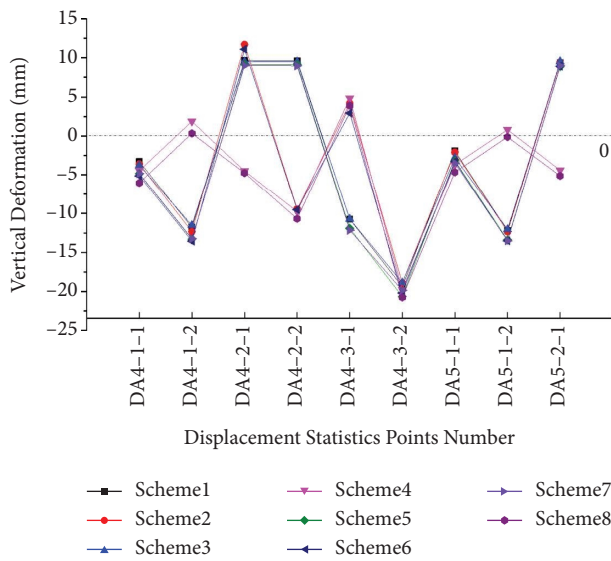


FIGURE 12: Deviation of the displacement statistical point.

3.2.3. *Stress Analysis of Each Closure Scheme under Ambient Temperature Change.* Studies attempting to relate environmental factors to bridge temperatures, and subsequently to bridge movements and stresses, indicate that the task is extremely complex [14]. Due to the temporary connection between the box girders on both sides of the junction pier, the force of the structure is different from that of the conventional continuous rigid frame. The more spans are in the closure process, the more obvious the effect of the structure is under the temperature change. The difference between temperature rise and temperature drop in the closure process is proposed to be 15°C. In the closure process of scheme 1, the maximum number of spans is 7 and the structural stress diagram under the effect of temperature rise

and temperature drop is shown in the figure. Table 7 and Figure 13 show the statistical results of maximum stress of main beams and piers of the link A4 and A5 during the construction stage of the maximum span number involved in the closure process of different closure schemes.

According to the Table 7, it can be seen that

- (1) Compared with the temperature rise of ambient temperature, the temperature drop of ambient temperature has a greater impact on the stress of structural piers and girders
- (2) The influence of ambient temperature on the stress of the girder and pier during construction is related to the maximum span number in the process of closure, but there is no direct proportional relationship between the maximum span number in the process of closure of different closure schemes and the maximum stress of girder and pier considering the effect of temperature. Among them, the effect of environmental temperature on scheme 1, scheme 3, scheme 5, and scheme 7 has a greater impact on the maximum stress of the bridge pier and girder than other closure schemes, and the risk of cracking of the bridge pier and girder is greater. The maximum span number of scheme 1, 3, 5, and 7 is 7, and the maximum stress of the bridge pier and main beam is about 6.5 MPa and 3.6 MPa, respectively. In scheme 2 and 6, the maximum span is 5 spans in the process of closure, and the maximum stress of the bridge pier and main beam is about 3.0 MPa and 2.4 MPa, respectively. The maximum span in scheme 4 and 8 is 3 spans, and the maximum stress of the bridge pier and main beam is about 4.5 MPa and 1.4 MPa, respectively.
- (3) The reason why the maximum stress of the pier in scheme 2 and scheme 6 is smaller than that in scheme 4 and 8 is that the side pier section is smaller than the middle pier section in scheme 4 and scheme 8 due to the temporary removal of prestress, and the maximum stress appears on the side pier. After the removal of all temporary prestress in scheme 2 and scheme 6, the maximum span number is 3. The maximum stress of the bridge pier in the process of closure is the same as that in scheme 4 and 6.
- (4) This article focuses on the comparison and selection of different closure schemes. In the analysis of the temperature effect, the ambient temperature is 15°C, and the bridge pier height is uniformly set at 40 m. In

TABLE 7: Each closure scheme considers/does not consider the maximum stress (MPa) of the main beam and pier under the action of temperature.

Closure schemes	Maximum span number in the closure process	Considering the effect of temperature		Not considering the effect of temperature	
		Bridge pier	Main beam	Bridge pier	Main beam
Scheme 1	7	6.1 (1.0)	3.6 (1.3)	2.8	1.3
Scheme 2	5	3.1 (0.9)	2.3 (0.6)	1.2	1.3
Scheme 3	7	6.1 (1.0)	3.6 (1.3)	2.7	1.3
Scheme 4	3	4.3 (2.6)	1.4 (1.3)	2.6	1.3
Scheme 5	7	6.5 (1.0)	3.9 (1.3)	2.8	1.3
Scheme 6	5	3 (0.9)	2.5 (0.6)	1.2	1.3
Scheme 7	7	6.6 (1.0)	3.9 (1.3)	2.7	1.3
Scheme 8	3	4.6 (2.7)	1.4 (1.3)	2.7	1.3

Note. The values in brackets refer to the structural stress at the corresponding position without considering temperature load.

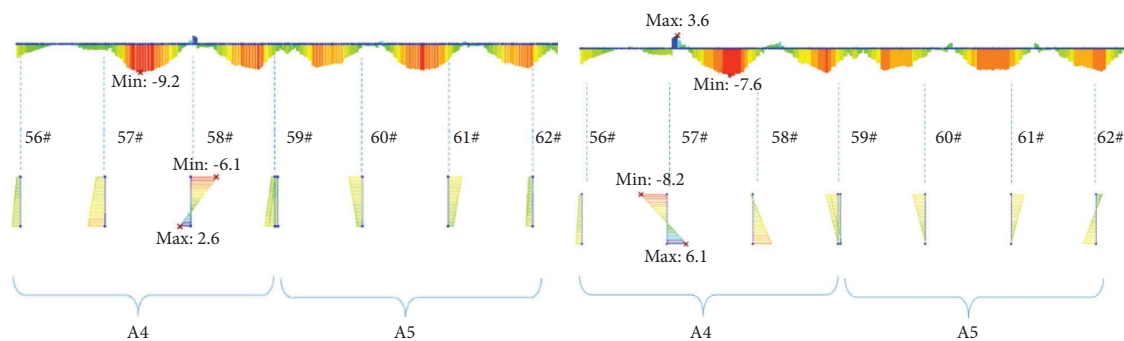


FIGURE 13: Stress diagram of the girder and pier under temperature rise and drop (MPa).

the checking calculation of structural cracking under the effect of temperature, the actual height of the bridge pier should be considered, and the temperature change at the bridge site should be further investigated.

4. Conclusion

The Quanzhou Bay Bridge of Xiamen High-speed Railway is a steel-concrete composite beam semifloating cable-stayed bridge whose approach bridges contains 9-link 3×70 m rigid frame bridges without bridge bearing. Because there are lots of spans, what the final closure scheme is set might lead to a big impact on the completed bridge. If the appropriate construction scheme is applied, it will be better for releasing the deformation of the beam body, reducing the additional internal force, improving the stress of the girder, and making use of the bridge. On the contrary, if a better construction scheme is not selected at this stage, more additional internal forces and deformation will be accumulated in the beam body, and they will superimpose on the beams together with the operation load resulting in the failure and cracking of the beam body and affecting the operation of the bridge. The results show that the displacement deformation decreases gradually with increasing elastic modulus of the soil around the anchor pier and increases with increasing Poisson's ratio. The change in elastic modulus mainly affects the relative shear displacement of the anchor pier and soil and the compressive

deformation of the soil at the front end of the anchor pier. Poisson's ratio has the greatest influence on the relative shear displacement of the anchor pier and soil. A larger anchor pier is not better; thus, it is wise to choose the economic design dimension. Theoretical and numerical simulation results are consistent, showing a linear growth trend.

In this article, 8 kinds of closure schemes are calculated and analyzed, and the following conclusions are drawn:

- (1) The differences of structural stress and bridge alignment in the process of closure are small. In the process of closure, the maximum difference of compressive stress, tensile stress, and bridge stress is 1.04 MPa, 0.78 MPa, and 0.42 MPa, and the difference of the D_{avg} value of the average deflection and statistical position of the bridge are within 5 mm.
- (2) The influence of ambient temperature on the maximum stress of the pier and girder during construction is more obvious. After considering the effect of temperature, schemes 1, 3, 5, and 7 have a greater risk of cracks in bridge piers and main beams, while scheme 4 and scheme 8 have a smaller maximum stress in the main beam in the process of closure than other schemes, so the risk of cracks is relatively small.
- (3) The difference between scheme 4 and scheme 8 mainly lies in the construction organization, and scheme 8 has three construction bid sections. When comparing scheme 4 and scheme 8, something

should be considered comprehensively such as construction period and construction organization.

- (4) Through the study of this article, the selection of the bridge closure construction scheme provides a sufficient basis.

Data Availability

The data used to support the findings of this study are included within the article.

Conflicts of Interest

The authors declare that they have no conflicts of interest.

Acknowledgments

This study was supported by the Project of Science and Technology Research and Development Plan of China Railway Corporation (K2018G017).

References

- [1] E. F. Deng, L. Zong, Y. Ding et al., "Seismic performance of mid-to-high rise modular steel construction-A critical review," *Thin-Walled Structures*, vol. 155, Article ID 106924, 2020.
- [2] B. Peeters and G. De Roeck, "One-year monitoring of the Z24-Bridge: environmental effects versus damage events," *Earthquake Engineering & Structural Dynamics*, vol. 30, no. 2, pp. 149–171, 2001.
- [3] Y. Sheng and O. Jinping, "Structural health monitoring and model updating of aizhai suspension bridge," *Journal of Aerospace Engineering*, vol. 30, 2016.
- [4] S. Deshan, L. Qiao, K. Inamullah, and Z. Xiaohang, "A novel finite element model updating method based on substructure and response surface model," *Engineering Structures*, vol. 103, 2015.
- [5] S. X. Rong and S. H. Yu, "The confirmation of closure jacking force in continuous rigid frame bridge," *Applied Mechanics and Materials*, vol. 638, 2014.
- [6] R. W. Li, F. S. Zhong, B. J. Xiao, D. G. Wei, and Y. Z. Jia, "Analysis on construction control of continuous rigid frame bridge in winter intermission," *Advanced Materials Research*, vol. 791–793, 2013.
- [7] H. D. Wright, H. R. Evans, and P. W. Harding, "The use of profiled steel sheeting in floor construction," *Journal of Constructional Steel Research*, vol. 7, no. 4, pp. 279–295, 1987.
- [8] Q. Zhu, Y. L. Xu, and X. Xiao, "Multiscale modeling and model updating of a cable-stayed bridge. I: modeling and influence line analysis," *Journal of Bridge Engineering*, vol. 20, 2014.
- [9] S. Masoud, G. R. Imbaro, J. A. McClain, and L. C. Brown, "Structural model updating using experimental static measurements," *Journal of Structural Engineering*, vol. 123, no. 6, 1997.
- [10] N. T. Davis, E. Hoomaan, M. Sanayei, A. K. Agrawal, and F. F. Jalinoos, "Integrated superstructure-substructure load rating for bridges with foundation movements," *Journal of Bridge Engineering*, vol. 23, no. 5, Article ID 04018022, 2018.
- [11] M. Y. Fattah, K. T. Shlash, and M. S. Al-Soud, "Pile-clayey soil interaction analysis by boundary element method," *Journal of Rock Mechanics and Geotechnical Engineering*, vol. 4, no. 1, 2012.
- [12] R. M. Antonio and M. Valdés, "Long-term behavior of continuous precast concrete girder bridge model," *Journal of Bridge Engineering*, vol. 5, no. 1, 2000.
- [13] M. R. Chowdhury and J. C. Ray, "Further considerations for nonlinear finite-element analysis," *Journal of Structural Engineering*, vol. 121, no. 9, pp. 1377–1379, 1995.
- [14] J. C. Reynolds and J. H. Emanuel, "Thermal stresses and movements in bridges," *Journal of the Structural Division*, vol. 100, no. 1, pp. 63–78, 1974.

Research Article

The Behavior of RC Beams Strengthened with Steel Fiber Concrete Layer by ANSYS Simulation

Thanh Quang Khai Lam  and Thi My Dung Do 

Faculty of Civil Engineering, Mien Tay Construction University, 20B Pho Co Dieu Street, Vinh Long, Vietnam

Correspondence should be addressed to Thanh Quang Khai Lam; lamthanhquangkhai@gmail.com

Received 24 August 2022; Revised 27 September 2022; Accepted 10 October 2022; Published 2 March 2023

Academic Editor: S. Mahdi S. Kolbadi

Copyright © 2023 Thanh Quang Khai Lam and Thi My Dung Do. This is an open access article distributed under the Creative Commons Attribution License, which permits unrestricted use, distribution, and reproduction in any medium, provided the original work is properly cited.

In this study, a double-layer reinforced concrete beam structure was created for the purpose of repairing reinforced concrete beams by pouring a layer of concrete on top of the reinforced concrete beam and then adding fibers to the concrete. Take into consideration the bearing capacity of these double-layer concrete beams as well as the effects that the input parameters have on the stress strain, the propagation of cracks in reinforced concrete beams. The study looks at double-layered reinforced concrete beams, with the steel fiber concrete placed on top of the one containing the normal concrete. This investigation led to the following relationships: load-compressive stress, tensile stress, and vertical displacement at the midpoint of the beam span, as well as a diagram showing how cracks spread in the beams. After getting the experimental results and comparing them with an ANSYS simulation, the diagram was used to figure out the loads at which the beams start to look cracked and the loads at which the beams are damaged. This study investigated the following six cases: how the addition of SFs affects the properties of concrete, the spacing of the stirrups at the ends of the beam should be looked into to see what effects it might have, how the number of tensile steel bars in the beam affects its properties, how the diameter of tensile steel bars affects their properties, how the diameter of compressed steel bars affects the results, and how the thickness of the SFC layer affects the properties of the material. Also, the things that were mentioned would have a big effect on how these double-layer beams in the design work.

1. Introduction

Steel fiber concrete is used quite commonly because they have increased load capacity, reduced the number of cracks, increased construction life, and have good impact resistance. A few studies on nanoconcrete with steel fibers (SFs) looked into the effects of concrete aggregation on increasing concrete tensile strength [1], the enhanced plasticity of concrete with SFs [2], and an observation design was also carried out to consider nanosilica effects on HPC strength at an early age [3], the fracture features of SFs' reinforced concrete beams [4]. A number of scholars have started referring to a series of studies on the RC beams with and without SFs; these studies have constructed a stress strain of the reinforced concrete (RC) beams with SF contents in concrete of 0%, 4%, and 8% by volume. This state determines the load of concrete beams

at which the beams begin to appear cracked and the load at which they begin to be damaged [5, 6].

A multi-layer reinforced concrete structure was created for the purpose of repairing reinforced concrete structures by pouring a layer of concrete on top or at the bottom of the reinforced concrete structures and then adding fibers to the concrete, such as multilayer shells, these studies investigated experimental and simulation analyses on stress strain, vertical displacement [7, 8]. In addition, the studies either looked at how cracks spread in composite beams with SFs' reinforcement or how strong composite beams are when bent [9, 10].

Both theoretical and practical investigations into the properties of layered reinforced concrete beams have been carried out by Iskhakov et al. Both a layer of SFs and a layer of HPC were used in the beams over the period of the study; however, neither material was prioritized over the other.

These studies have shown the formation and growth of cracks in concrete beams, the stress strain of the RC beams, and the practicability of two-layer concrete beams made of normal and fibered high-strength concrete [11, 12]. After these studies, continuous experimental analysis of full-scale two-layer RC beams [13, 14] and experimental investigation of continuous two-layer RC beams [15] were conducted, respectively.

Many studies and FEM analyses of the bending moment of the double-layered RC beam are also interested [16]. Based on the studies of Iskhakov et al., material modeling of SFs' reinforced concrete [17–19], and in which [20] the input parameters in the design of RC beams affecting the work of SFs' reinforced concrete beams were investigated. The authors of this research [21] conducted experiments on beams made of two layers of SFs' concrete. A layer of SFs' concrete was placed both below and on top of the layer of normal concrete in these beams. After that, a simulation of the beams using dimensions of 15 by 30 by 220 centimeters had to be carried out. The investigation into the impact on beams built of three layers of concrete of the same size will continue even with these findings. These three-layer beams each feature one layer of SFs' concrete on the top, one layer of SFs' concrete on the bottom, and a normal concrete (NC) layer that is ten centimeters thick in the middle of the beam. According to the results, the beams made of two layers of SFs' concrete degraded the least quickly, but the beams made of three layers of SFs' concrete degraded quite quickly. Studies of two-layer beams, laminated beams, and three-layer beams are included here. Some case studies of these studies are the following: the influence of geometrical cross-sectional parameters, strength, and deformability of the materials used on the stress strain of three-layered RC beams [22], FEM analysis of a three-layer concrete beam with composite reinforcement [23–28].

Flexural behavior of RC beams having various layers of conventional concrete and steel fiber reinforced concrete were investigated in [29]. The behavior of concrete beams strengthened with a SFRC layer was studied by the nonlinear finite element analysis using ANSYS software [30].

According to the research that was done on the multi-layer beams that were previously discussed, double-layer concrete beams that have SFs' concrete layers placed on top of the NC layer are commonly used in the repair of damaged concrete beams. However, there are still a great number of factors that need to be investigated. Within the scope of this article, the following factors should be investigated: the effects of modifying the beam's tensile steel bar number, diameter of steel bars in the tension zone, diameter of steel bars in the compression zone, the thickness of the SFs' concrete layer, and so on. It is important to take into account the effect that these factors have on the following relationships: load-compressive stress; tensile stress; vertical displacement (VD) in the middle of the beams' span; the propagation of cracks of beams, which determine the load at which the beams begin to crack; and determine the load at which the beams are damaged with beam dimensions of $15 \times 30 \times 220$ cm.

2. Materials and Methods

2.1. Design Model of Beam. The steel fiber concrete (SFC) layer that is a part of the double-layer SFs' reinforced concrete beam that is located in the compression zone indicates that it is placed on top of the NC layer. The dimensions of the beam are 15 by 30 by 220 cm. The concrete grade for the layer containing SFC is B30 (TCVN 5574-2018, Vietnamese standards), whereas the grade for the layer containing NC is B20. The thickness of the layer of SFC is 10 centimeters, the stirrups are spaced at $\phi 6$ at 200, the tensile steel bars are $2\phi 22$, and the compression steel bars are $2\phi 10$, and the volumetric percentage of SFs in the concrete is 2%. Concentrated stresses are applied to steel plates with dimensions of 10 by 14 by 6 centimeters.

The designs for the models of the double-layer concrete beams may be seen in Figure 1.

The strain gauge and VD measuring devices are shown in the diagram that may be seen in Figure 2.

2.2. Conducting Tests on Beams Made of Double Layer of RC. After the beams have been designed according to Section 2.1 and Figures 1 and 2, we go on to the next step, which is the creation of a 2-layer beam structure.

We construct the beam formwork and pour the concrete for the layers of the double-layer RC beams; after pouring the bottom layer, which is the NC layer, let the beams set for 24 hours before continuing to pour the SFC layer, as shown in Figure 3.

The concrete beams that were placed on top of the test pedestal are seen in Figure 4.

We set up ten tensiometers to measure strain, four devices to measure sliding strain between two layers of concrete, and three devices to measure vertical displacement, as shown in Figure 2.

We perform the beam bending test using two concentrated forces, draw the crack propagation diagram in the beam, and record both the strain values and the vertical displacement measurement value on the computer. In the process of this investigation, two beams were examined. Starting at 0 kN, the load was slowly increased until the beams were completely broken. The observations were then written down.

2.3. Modeling of a Double-Layer Concrete Beam Using Finite Element. Figure 5 shows the model of a double-layer RC beam that was constructed using ANSYS.

2.3.1. Element Types

Concrete: concrete simulation element—SOLID65 element

Steel reinforcement: used element of beam188

Choose the steel fiber model: a smeared model was used
Choose concrete cracking model: the smeared model for cracks in concrete

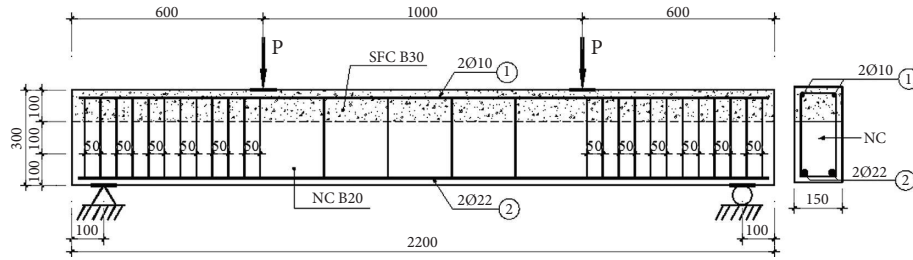


FIGURE 1: In the design, a double-layer concrete beam model is used.

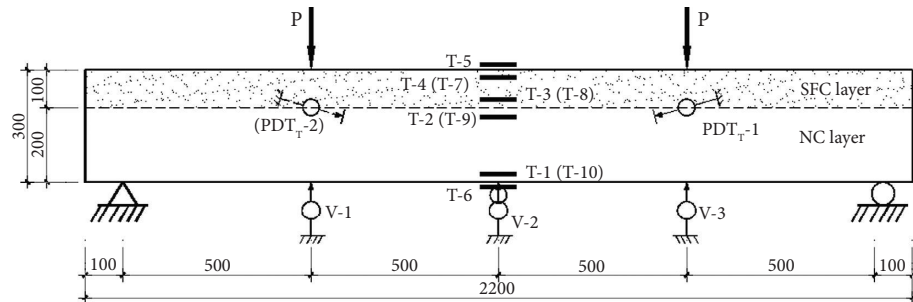


FIGURE 2: Double-layer beam measuring devices.



FIGURE 3: The design of the formwork and the beam concrete layers.



(a)

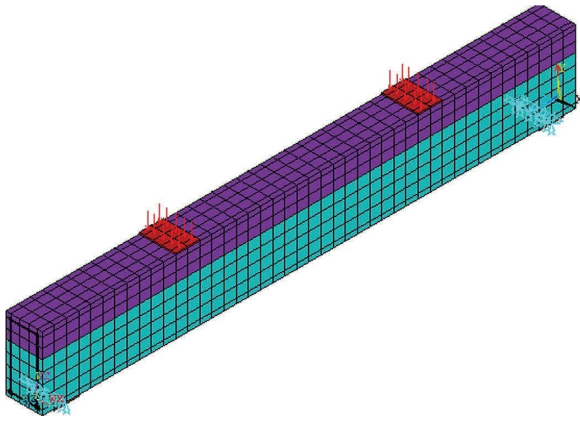


(b)

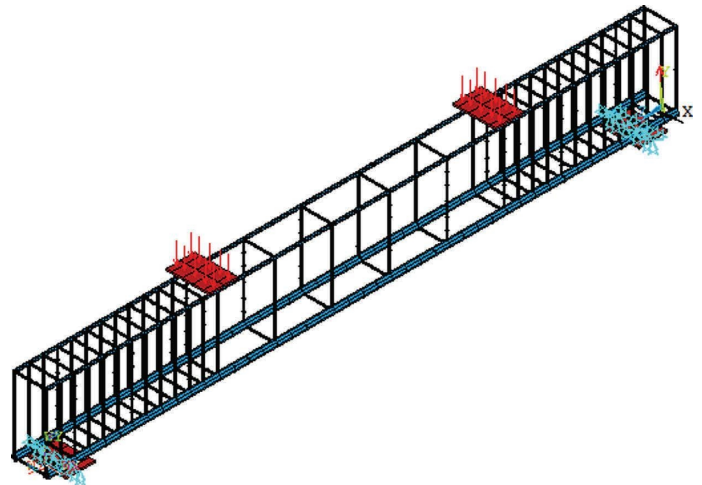


(c)

FIGURE 4: Test pedestal with measuring equipment and concrete beams: (a) measurement instruments for beams; (b) beams made of concrete were placed on the test pedestal; (c) connection of the measuring devices to the computer.



DOUBLE LAYERS STEEL FIBER CONCRETE BEAM



SANDWICH STEEL FIBER CONCRETE BEAM

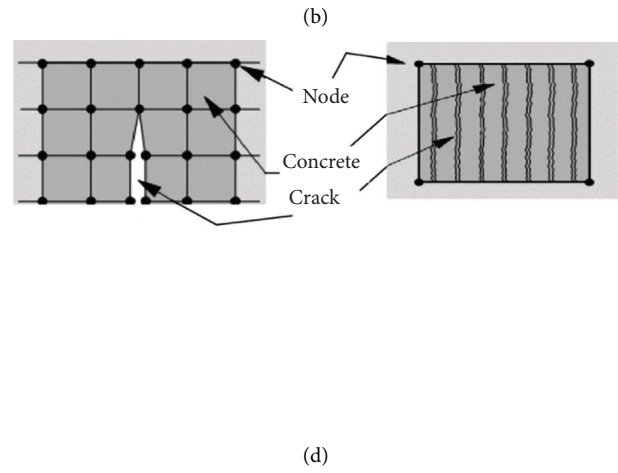
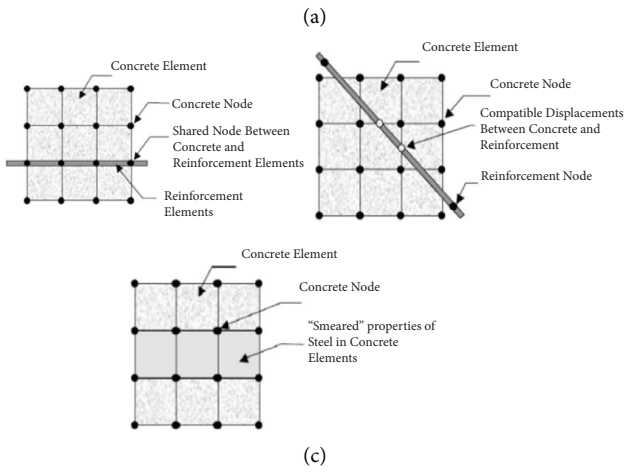


FIGURE 5: Continued.

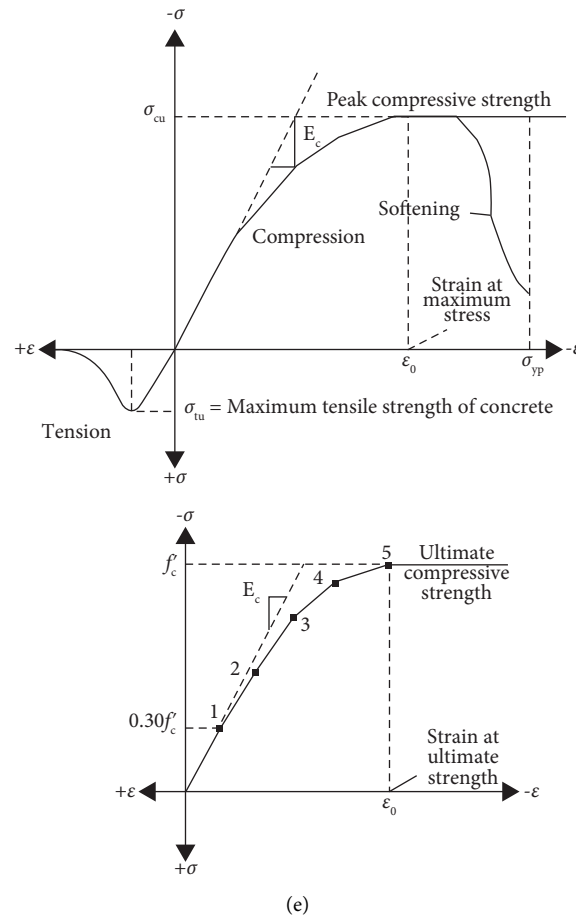


FIGURE 5: ANSYS model of a beam constructed with two layers of concrete: (a) a model of a beam made of double-layered concrete; (b) the model of the steel bars including the boundary condition and the load; (c) steel fiber model in concrete [25]; (d) concrete cracking model [25]; (e) typical uniaxial compressive and tensile stress-strain curve for concrete [25].

Concrete stress-strain model through tensile and compression: Kachlakev model was used

Destructive standards: the destructive standard of Willam and Warnke was used

3. Results and Discussion

In Figure 6, the results of crack formation and development in tested concrete beams (EXP) are presented for each load level that was applied to the beam. These results may be observed for each individual load level.

Using ANSYS software, we were able to model the effect of crack formation and development in a concrete beam, and the results are shown in Figure 7.

Figure 8 shows the results of the simulation carried out by ANSYS, which examined the VD that occurred in the midpoint of the RC beams' span.

In Figures 6 and 7, the experimental and ANSYS simulation methods both produce cracks in beams in a way that is similar in terms of how they start and how they progress. The VD value in the midpoint of the span of the beam in Figure 8 is 2 millimeters different, which is a very small difference between two different calculation methods. This is

due to the fact that the experimental method is also affected by the conditions of the measuring equipment, environment, and so on, and the test value is typically 30–50% higher than other analytical methods. As a result of this, it is possible to conduct more studies into the input factors that affect the stress strain in RC beams.

The following are the input parameters of a double-layerSFs' RC beam. These values will have an effect on the stress strain as well as the cracks in the beams.

3.1. Investigating How the Addition of SFs Affects the Properties of Concrete. In ANSYS, nonlinear materials are taken into consideration when the SFs' content in concrete is increased from 0% to 2% and 5%, the stirrup spacing at the ends of the beam is $\phi 6a50$, and the stirrup spacing in the middle of the beam is $\phi 6a200$. In addition to this, the tensile steel bars are $2\phi 22$, while the compressed steel bars are $2\phi 10$; the thickness of the layer made of steel fiber concrete is 10 centimeters, while the thickness of the layer made of normal concrete is 20 centimeters.

Color spectra of beam stresses and vertical displacement are shown in Figure 9.

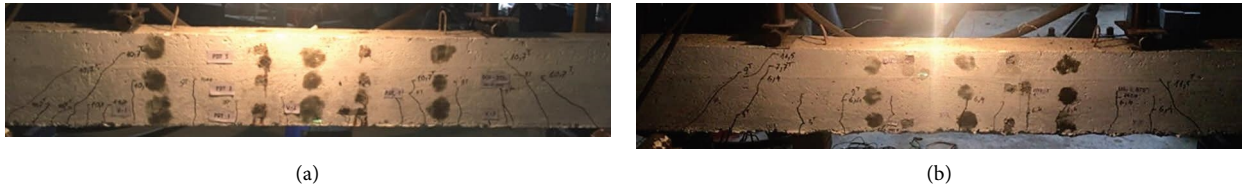


FIGURE 6: Observed cracks in the concrete beams: (a) there were cracks in the concrete beam (Beam 1); (b) there were cracks in the concrete beam (Beam 2).

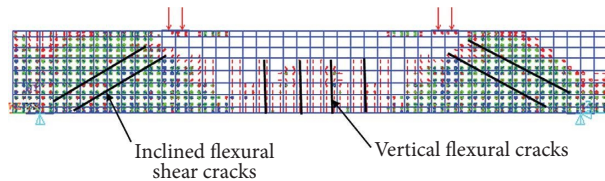


FIGURE 7: ANSYS simulation showing cracks in a concrete beam.

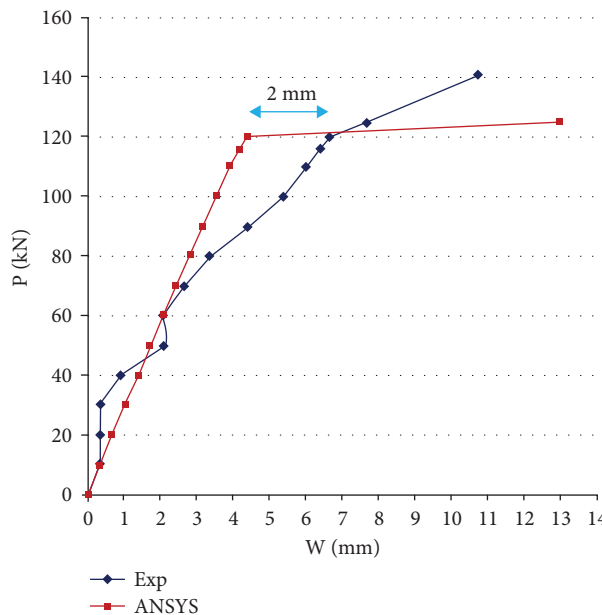


FIGURE 8: A vertical displacement could be seen in the middle of the span where the beam was installed.

As seen in Figure 9(a), the highest VD occurs in the midpoint of the beams' span and decreases as it reaches the supports. The color spectrum of stresses in Figure 9(b) reveals that the tensile stress is located below the beam, with its maximum value in the middle of the span; the compressive stress, on the other hand, is located at the top section of the beam, as well as the influence zone between the two concentrated forces. This shows that the ANSYS element model is suitable for the working conditions of a beam.

Figure 10 shows how beams start to crack when there is a change in the SFs' content of the concrete.

When the SFs' content in RC is zero, all of the concrete layers that make up the beam are NC layers. As a result, cracking occurs first in the area with the highest tensile

stress, which is under the beam, and then spreads to the compressive zone. The load starts to break even if its value has not changed when the percentage of SFs' content in the concrete is raised by 2%. When the percentage of SFs in concrete is raised by 5%, the load starts to crack and goes from 8 kN to 9 kN. Because of this, when bending concrete beams with SFs' concrete layers in the compression zone, the effect of reducing the number of cracks and making the beam stronger has not been seen.

As can be seen in Figure 11, the percentage of SFs in the concrete starts to change, which ultimately leads to the failure of the beams.

According to what is represented in Figure 11(a), when there is no SFs' content in the concrete at all, the beam starts to fail at a load of 116 kN, and fractures occur practically

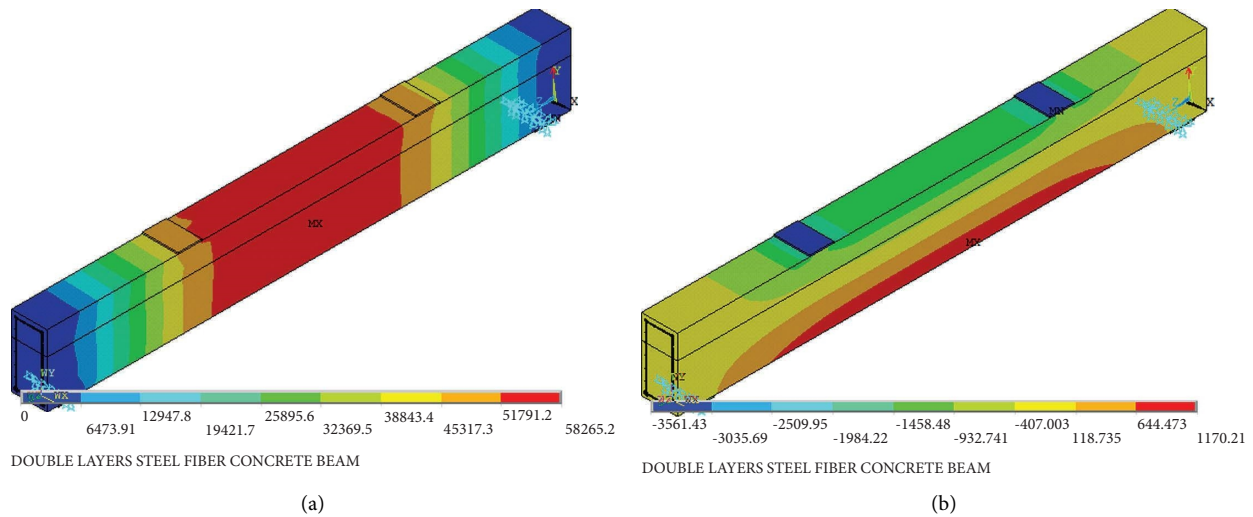


FIGURE 9: ANSYS's color spectrum of the beam's vertical displacement and stresses: (a) spectrum of color showing vertical displacement; (b) the spectrum of colors showing the stresses.

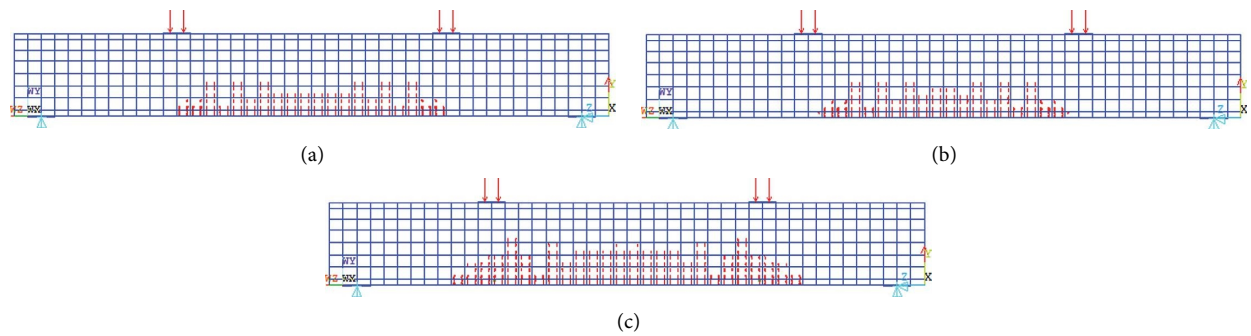


FIGURE 10: In ANSYS, cracks appear in the beams: (a) cracks begin to appear in the beam ($P_{crack} = 8 \text{ kN}$), $\mu = 0$; (b) cracks begin to appear in the beam ($P_{crack} = 8 \text{ kN}$), $\mu = 2\%$; (c) cracks begin to appear in the beam ($P_{crack} = 9 \text{ kN}$), $\mu = 5\%$.

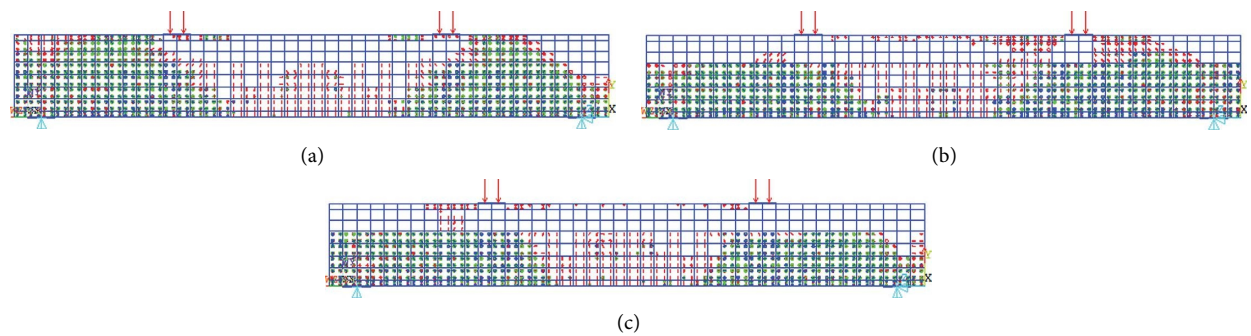


FIGURE 11: In ANSYS, beams quickly start to suffer from damage: (a) damage to the beam begins to appear ($P_{max} = 116 \text{ kN}$), $\mu = 0$; (b) damage to the beam begins to appear ($P_{max} = 125 \text{ kN}$), $\mu = 2\%$; (c) damage to the beam begins to appear ($P_{max} = 116 \text{ kN}$), $\mu = 5\%$.

everywhere throughout the concrete beam. The beam damage load also increases to 125 kN as the SFs' content increases up to 2% (Figure 11(b)), and the cracks reduce in comparison to beams with 0% fiber content. However, fractures largely occurred in the NC layer, although they were not entirely fractured in the up direction. When the SFs content is increased to 5% (Figure 11(c)), the beam's bearing

capacity does not keep going up compared to the concrete with 0% SFs' content. Instead, it just reduces the number of cracks that happen; large cracks have not yet formed in the top SFs concrete layer.

At the middle of the span of the RC beam, the relationships between: load and compressive stress, tensile stress, and VD are shown in Figure 12.

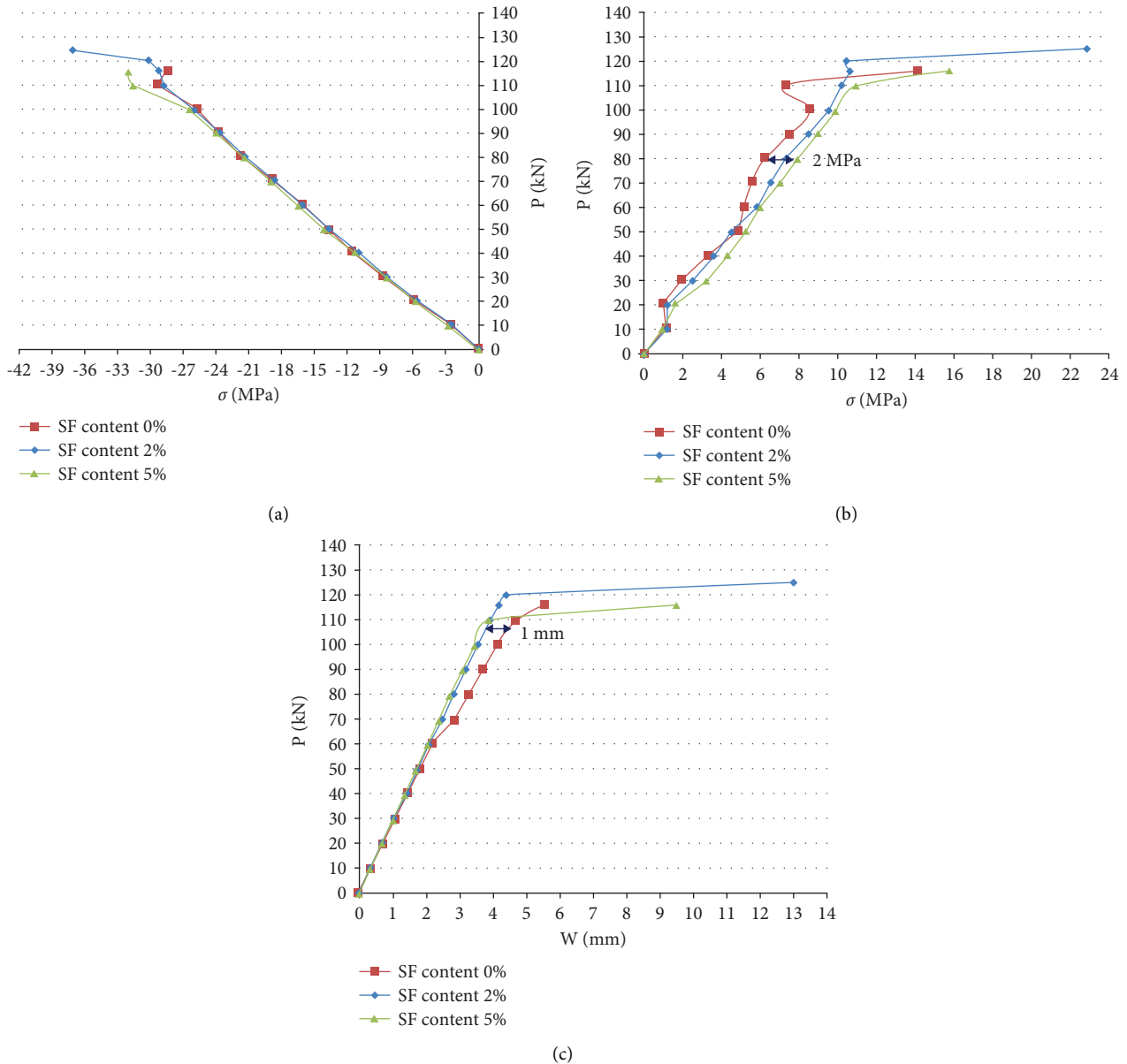
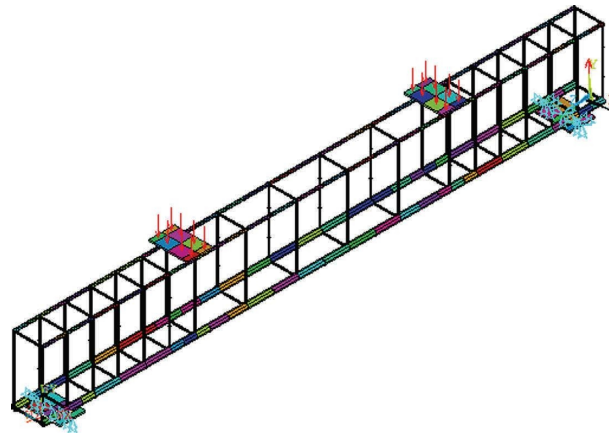


FIGURE 12: Relationship between load and stress, as well as between load and vertical displacement (effect of SFs): (a) relationship between load and compressive stress, (b) relationship between load and tensile stress. (c) the relationship between load and VD.

The SF content in the concrete is changed in Figure 12(a). However, this does not have any effect on the compressive stress of the beam. There is, nonetheless, a change in the tensile stress; however, this variation is around 2 MPa in magnitude (Figure 12(b)). The VD in the middle of the beam span will begin to grow when the applied load on the beam is greater than 60 kN. In addition, the vertical displacement is greater than the other fiber content by approximately one millimeter when the SFs' content in the concrete is zero. At the same load level of 116 kN, the beam is damaged by the NC layer below the SFs' content of 0% and 5% when the SFs' content in the concrete is too high. This causes the SFC layer to have a high strength, which in turn results in the high strength of the SFC layer. The

percentage of SFs that can be included in concrete ranges from 0% to 4%.

3.2. *The Spacing of the Stirrups at the Ends of the Beam Should Be Looked into to See What Effects It Might Have.* A beam with a SF content in the concrete of 2%, stirrup spacing at beam ends modified from $\phi 6a50$ to $\phi 6a100$, stirrups spaced at $\phi 6a200$ in the middle of span, tensile steel bars are $2\phi 22$, and compression steel bars are $2\phi 10$. The use of nonlinear materials in ANSYS's numerical simulation analysis reveals that the thickness of the SFC layer is $H = 10$ cm, whereas the thickness of the NC layer is 20 cm. This information is presented in Figure 13.



SANDWICH STEEL FIBER CONCRETE BEAM

FIGURE 13: The distance between the stirrups at the ends of the beam has been increased to 100 millimeters.

When the distance between the stirrups at the ends of the beam is increased to 100 millimeters, as shown in Figure 14, beams will begin to crack and will be destroyed.

Increasing the stirrup spacing at the ends of the beam to 50 millimeters causes the beam to begin cracking at 8 kN in Figure 10(b), increasing the stirrup spacing to 100 millimeters causes the beam to crack but does not affect the load level in Figure 14(a), the beam begins to deteriorate at 125 kN in Figure 14(a), and the beam begins to deteriorate at 125 kN in Figure 10(b) (Figures 11(b) and 14(b)). On the other hand, there are less than fifty millimeters worth of fractures in the beam that has stirrup spacing of one hundred millimeters. In none of these beams did cracks show up in the layer of SFC that was being used.

Within the middle of the span of a SFC beam, Figure 15 shows the load-compressive stress, tensile stress, and VD relationships.

When compared to stirrup spacing of 50 mm, the results of Figure 15 show that increasing the stirrup spacing at the ends of the beam from $\phi 6a50$ to $\phi 6a100$ results in a compressive stress that is greater than 1.5 MPa (Figure 15(a)) and a tensile stress that is less than 1.5 MPa (Figure 15(b)). As a result of this, it is not recommended to install an excessive number of bars at the ends of beams. There is also no influence from the VD that occurs in the midpoint of the beams' span (Figure 15(c)). Based on the results of this study, the best distance between stirrups is 100 millimeters, and the design $\phi 6a100$ is used to study a number of other parameters in double-layer RC beams.

3.3. Conducting Research on How the Number of Tensile Steel Bars in the Beam Affects Its Properties. Beam with a 2% SFs' content in concrete, stirrup spacing at the ends of the beam is $\phi 6a100$, stirrup spacing in the middle of span is $\phi 6a200$, tensile steel bars are changed from $2\phi 22$ to $3\phi 22$, compressed steel bars are $2\phi 10$, SFC layer thickness is $H = 10$ cm, NC layer thickness is 20 cm, and nonlinear materials are considered in the ANSYS numerical simulation analysis. This information is presented in Figure 16.

As shown in Figure 17, when the number of tensile steel bars is reduced or increased, the beams begin to crack and sustain damage.

The beam begins to fracture when the number of tensile steel bars in the beam is raised to $3\phi 22$, and it starts to be damaged later on. When the number of tensile steel bars in the beam is $2\phi 22$, the beam begins to crack at 8 kN, which increased to 1 kN later, and when the beam began to be damaged, it was 125 kN and 135 kN for the $3\phi 22$ beam, an increase of 10 kN. When the number of tensile steel bars in the beam is $3\phi 22$, the beam begins to crack at 135 k. The crack gets smaller as the number of tensile steel bars in the beam gets higher; in Figures 14 and 17, the beams only begin to crack in the NC layer of the beam without developing cracks in the SFC layer. This is because the SFC layer is stronger than the NC layer.

Figure 18 shows the load-compressive stress, tensile stress, and VD relationships in the midpoint of the span of a SFC beam.

The compressive stress between $2\phi 22$ and $3\phi 22$ does not change much when the load is raised from 0 to 60 kN in the zone of compressive stress (Figure 18(a)). However, when this 60 kN load is reached, the difference is 1.5 MPa. At a load of 110 kN, the difference in stress in the tensile zone is equal to 4 megapascals (MPa). This difference is larger when the applied load is increased (Figure 18(b)). The difference in VD is growing; the value of the difference in VD is 1.1 mm when the force is set at 120 kN (Figure 18(c)). Because of this, the fact that there are more steel bars in the tensile zone shows that these elements work to lower the tensile stress.

3.4. Conducting Research on How the Diameter of Tensile Steel Bars Affects Their Properties. The stirrup spacing is $\phi 6a100$ at both ends of the beam, and it is $\phi 6a200$ in the middle of the beam. When nonlinear materials are included in the ANSYS numerical simulation analysis, the tensile steel bars are changed to $2\phi 18$ and $2\phi 28$, the compression steel bars are changed to $2\phi 10$, the thickness of the SFC layer is $H = 10$ cm, and the thickness of the NC layer is 20 cm.

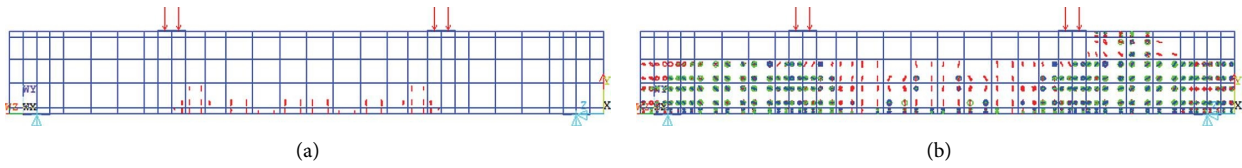


FIGURE 14: When the stirrup spacings are modified, cracks begin to appear in the beams, and the beams suffer damage: (a) cracks begin to appear in the beam ($P_{crack} = 8 \text{ kN}$), $\phi 6a100$; (b) damage to the beam begins to appear ($P_{max} = 125 \text{ kN}$), $\phi 6a100$.

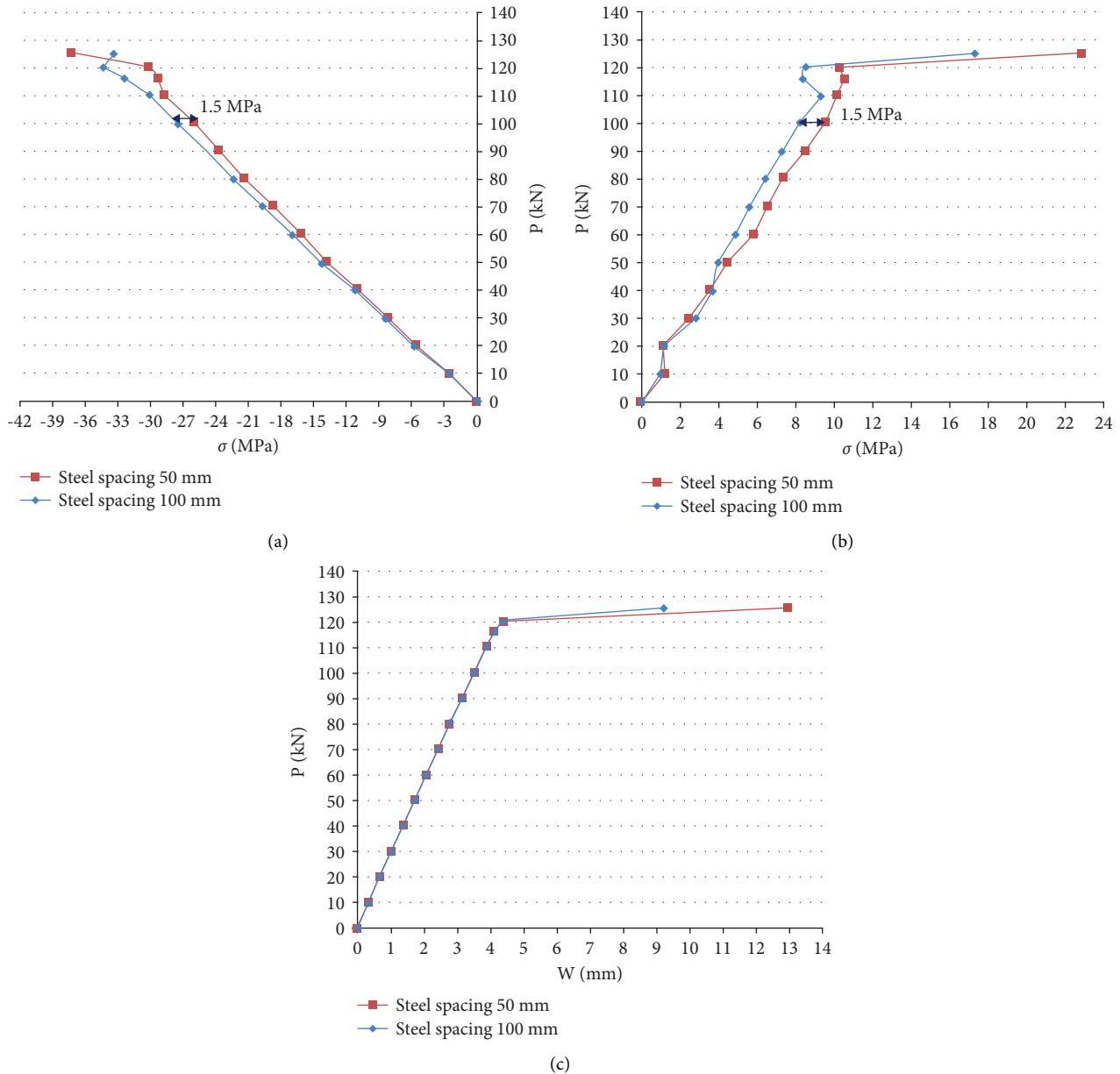
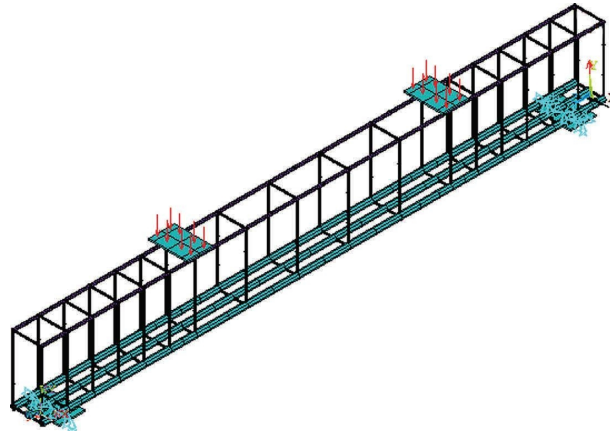


FIGURE 15: Relationship between load and stress, as well as between load and vertical displacement (effect of stirrups): (a) relationship between load and compressive stress, (b) relationship between load and tensile stress. (c) the relationship between load and VD.

Beams will begin to crack and get damaged if there is a change in the diameter of the tensile steel bars, as shown in Figure 19.

In Figures 14(a), 19(a), and 19(b), cracks form first in the NC layer, and the value of the cracking load does not vary much when there is not a significant change in the diameter



SANDWICH STEEL FIBER CONCRETE BEAM

FIGURE 16: Beam that has had the number of tensile steel bars dropped to $3\phi 22$.

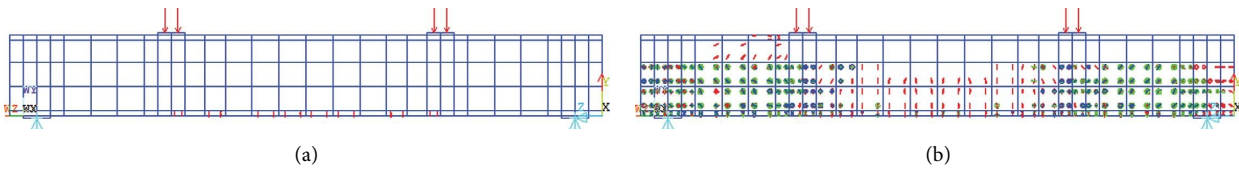


FIGURE 17: When the number of tensile steel bars was increased, the beams began to break and suffer damage as a result: (a) cracks begin to appear in the beam ($P_{crack} = 9\text{ kN}$), $3\phi 22$; (b) damage to the beam begins to appear ($P_{max} = 135\text{ kN}$), $3\phi 22$.

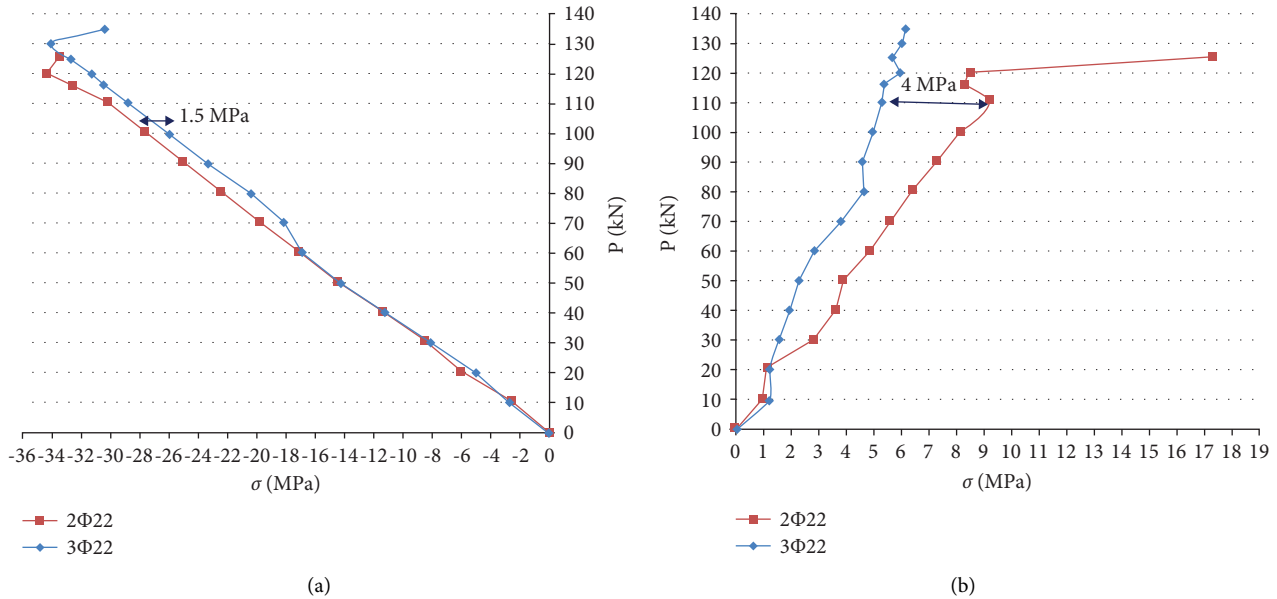


FIGURE 18: Continued.

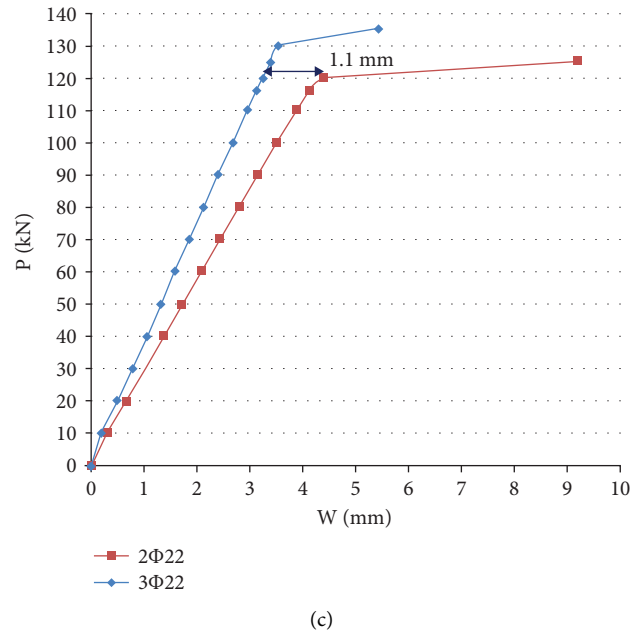


FIGURE 18: Relationship between load and stress, as well as between load and vertical displacement (effect of the number of tensile steel bars): (a) relationship between load and compressive stress, (b) relationship between load and tensile stress. (c) the relationship between load and VD.

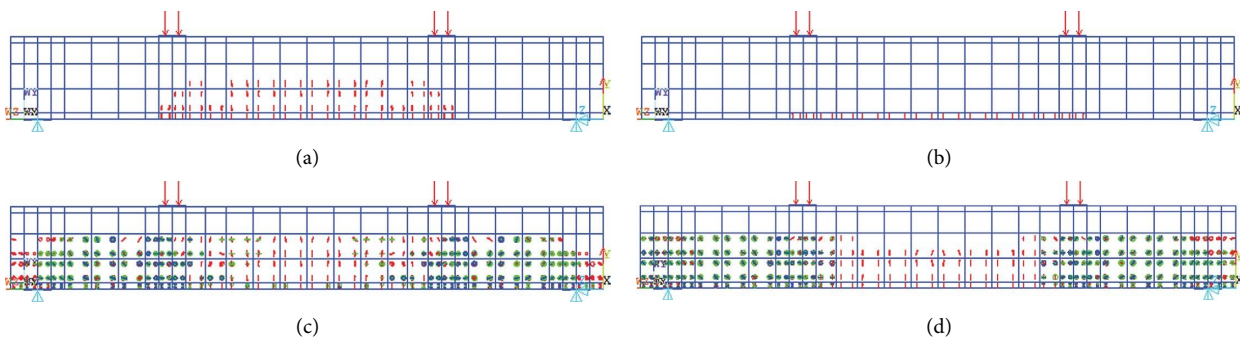


FIGURE 19: Because of a change in the diameter of the tensile steel bars, beams have begun to crack and have been damaged: (a) cracks begin to appear in the beam ($P_{\text{crack}} = 8 \text{ kN}$), $2\phi 18$; (b) cracks begin to appear in the beam ($P_{\text{crack}} = 10 \text{ kN}$), $2\phi 28$; (c) beam beginning to show signs of damage ($P_{\text{max}} = 90 \text{ kN}$), $2\phi 18$; (d) beam beginning to show signs of damage ($P_{\text{max}} = 130 \text{ kN}$), $2\phi 28$.

of the tensile steel bars. Beam $2\phi 18$ has a limit of 90 kN, beam $2\phi 22$ has a limit of 125 kN, and beam $2\phi 28$ has a limit of 130 kN. However, the limit of damaged beams varies (Figures 14(b), 19(c), and 19(d)). But when the beams are broken, only the NC layer cracks and not the SFC layer that is on top of it.

In the midpoint of the span of a SFC beam, Figure 20 shows the load-compressive stress, tensile stress, and VD relationships.

Although there is a difference in tensile stress of 3.2 MPa between $2\phi 18$ and $2\phi 28$, the stress in the compression zone does not vary much when the diameter of the tensile steel bars is modified (Figure 20(a)). When the diameter of the tensile steel bars is modified, however, the tensile stress dramatically rises (Figure 20(b)). The difference in tensile stress between $2\phi 22$ and $2\phi 28$ is 3.2 MPa, and the difference in tensile stress between $2\phi 18$ and $2\phi 22$ is 5.3 MPa. As a direct result of this, when the diameter of

the tensile steel bars is made bigger, the stress works better.

3.5. Conducting Research on How the Diameter of Compressed Steel Bars Affects the Results. Taking into consideration nonlinear materials in ANSYS numerical simulation analysis, the beam with a SF content in concrete of 2%, stirrups spacing at the ends of the beam is $\phi 6a100$, stirrups spacing in the middle of the beam is $\phi 6a200$, tensile steel bars are $2\phi 22$, compressed steel bars modified from $2\phi 10$ to $2\phi 16$, the thickness of the SFC layer is $H = 10 \text{ cm}$, and the thickness of the NC layer is 20 cm.

As shown in Figure 21, as the diameter of the compressed steel bars varies, cracking and damage to the beams begin to occur.

When the diameter of the compressed steel bars is increased in Figures 14 and 21, the bearing capacity of the

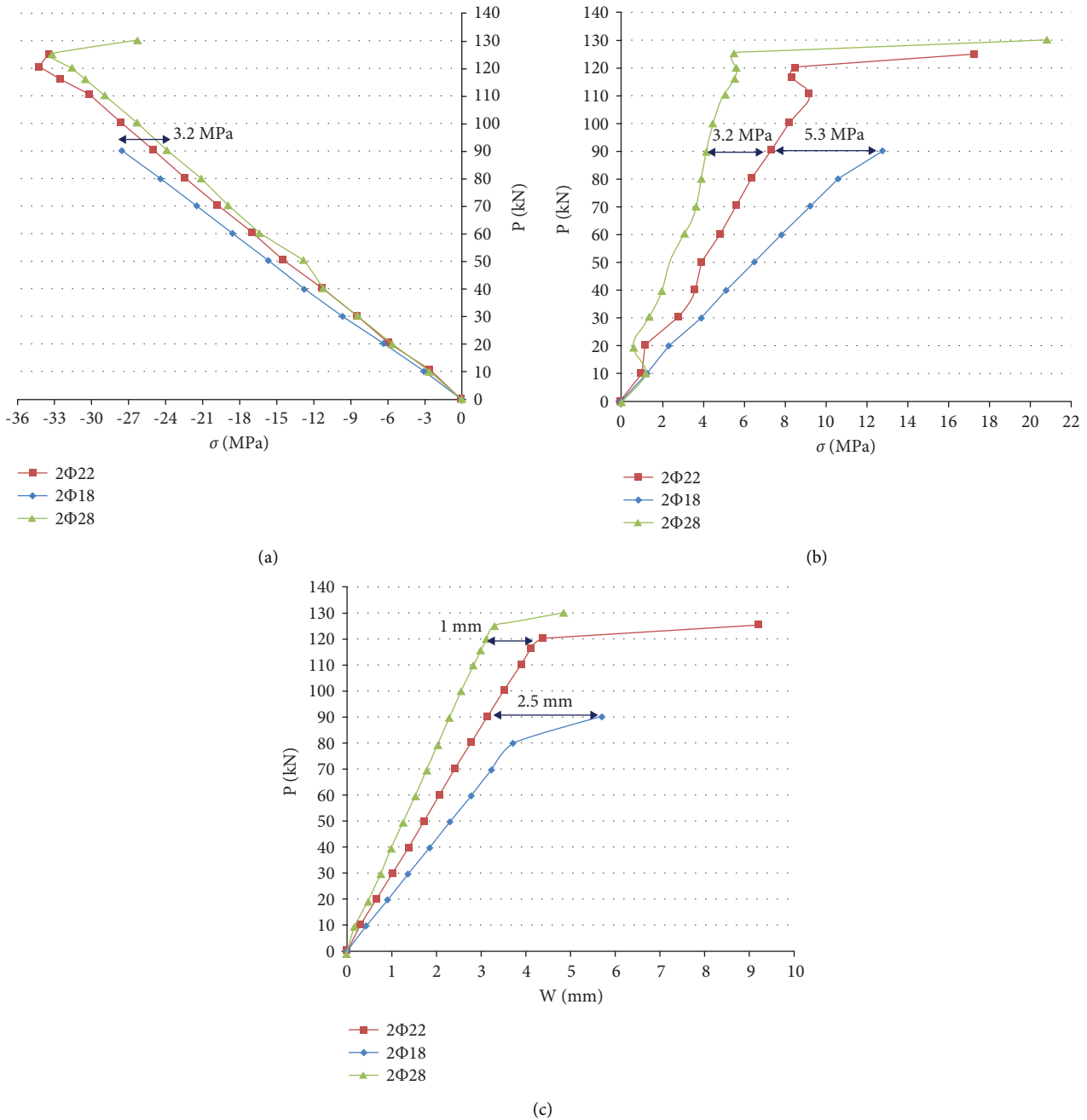


FIGURE 20: Relationship between load and stress, as well as between load and vertical displacement (effect of the diameter of tensile steel bars): (a) relationship between load and compressive stress, (b) relationship between load and tensile stress. (c) the relationship between load and VD.

beam also increases. Furthermore, when the load is increased from 2φ10 to 2φ16, the beam begins to crack at 8 kN to 9 kN and begins to damage at 125 kN to 131 kN. The layer of SFC that is located above the one being worked on is still in its early stages.

The relationships between load and compressive stress, tensile stress, and VD are shown in Figure 22 for a SFC beam in the middle of the span of the beam.

When the diameter of the compressed steel bars in Figure 22 is modified, there is a smaller change in the compressive stress and VD. However, there is a modification in the tensile stress. However, the difference in

tensile stress is relatively small, having a value of 0.8 MPa. Because of this, when the diameter of the compressed steel bars in a bending beam is changed, it is less likely to change the amount of stress and the vertical movement of the beam.

3.6. *Conducting Research on How the Thickness of the SFC Layer Affects the Properties of the Material.* The beam with 2% SFs' content in concrete, stirrup spacing of φ6a100 at the ends and φ6a200 in the middle, 2φ22 tensile steel bars and 2φ10 compressed steel bars, SFC layer thickness of $H = 10$ cm

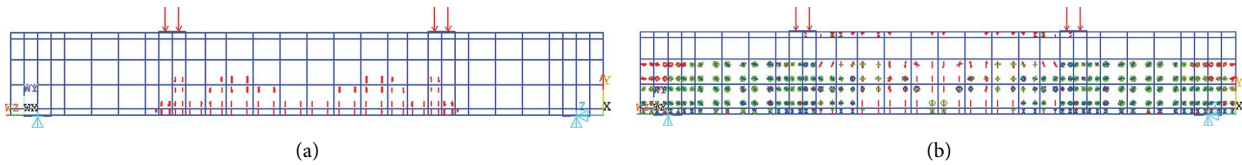


FIGURE 21: When the diameter of the compressed steel bars varied, cracking and damage began to appear in the beams: (a) cracks begin to appear in the beam ($P_{crack} = 9 \text{ kN}$), $2\phi 16$; (b) damage to the beam begins to appear ($P_{max} = 131 \text{ kN}$), $2\phi 16$.

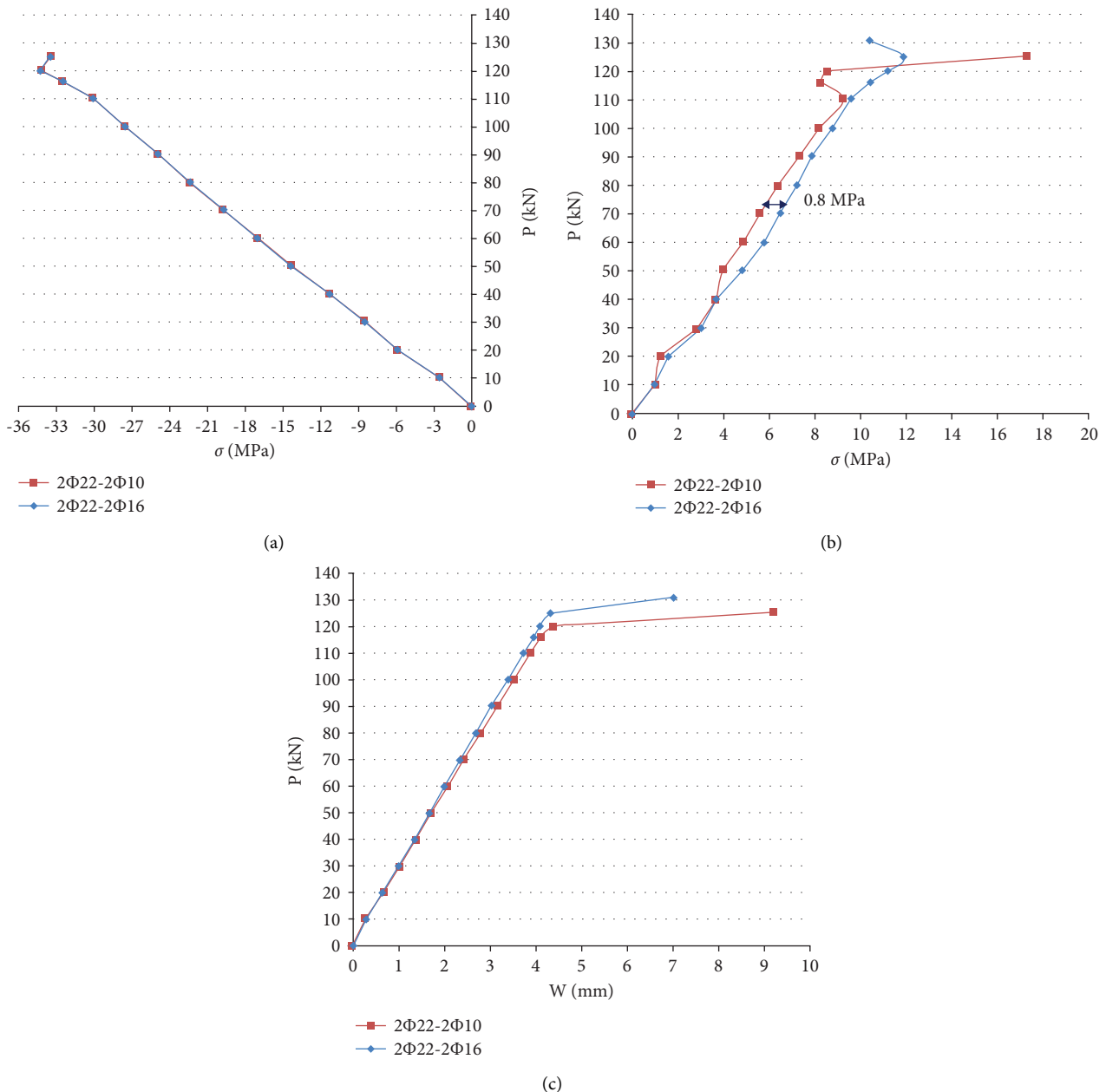


FIGURE 22: Relationship between load and stress, as well as between load and vertical displacement (effect of the diameter of compressed steel bars): (a) relationship between load and compressive stress, (b) relationship between load and tensile stress. (c) the relationship between load and VD.

modified to $H = 7 \text{ cm}$ and $H = 14 \text{ cm}$, and nonlinear materials taken into account in an ANSYS numerical simulation analysis.

Beams start to crack and suffer damage if there is a modification in the thickness of the SFC layer, as shown in Figure 23.

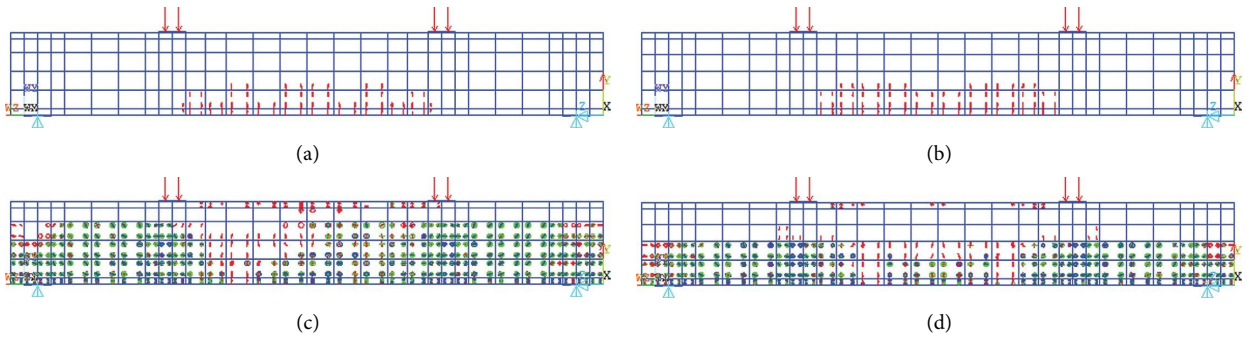


FIGURE 23: When the thickness of the steel fiber layer changed, the beams immediately began to crack and were damaged: (a) cracks begin to appear in the beam ($P_{crack} = 8 \text{ kN}$), $H = 7 \text{ cm}$; (b) cracks begin to appear in the beam ($P_{crack} = 8 \text{ kN}$), $H = 14 \text{ cm}$; (c) beam beginning to show signs of damage ($P_{max} = 125 \text{ kN}$), $H = 7 \text{ cm}$; (d) beam beginning to show signs of damage ($P_{max} = 128 \text{ kN}$), $H = 14 \text{ cm}$.

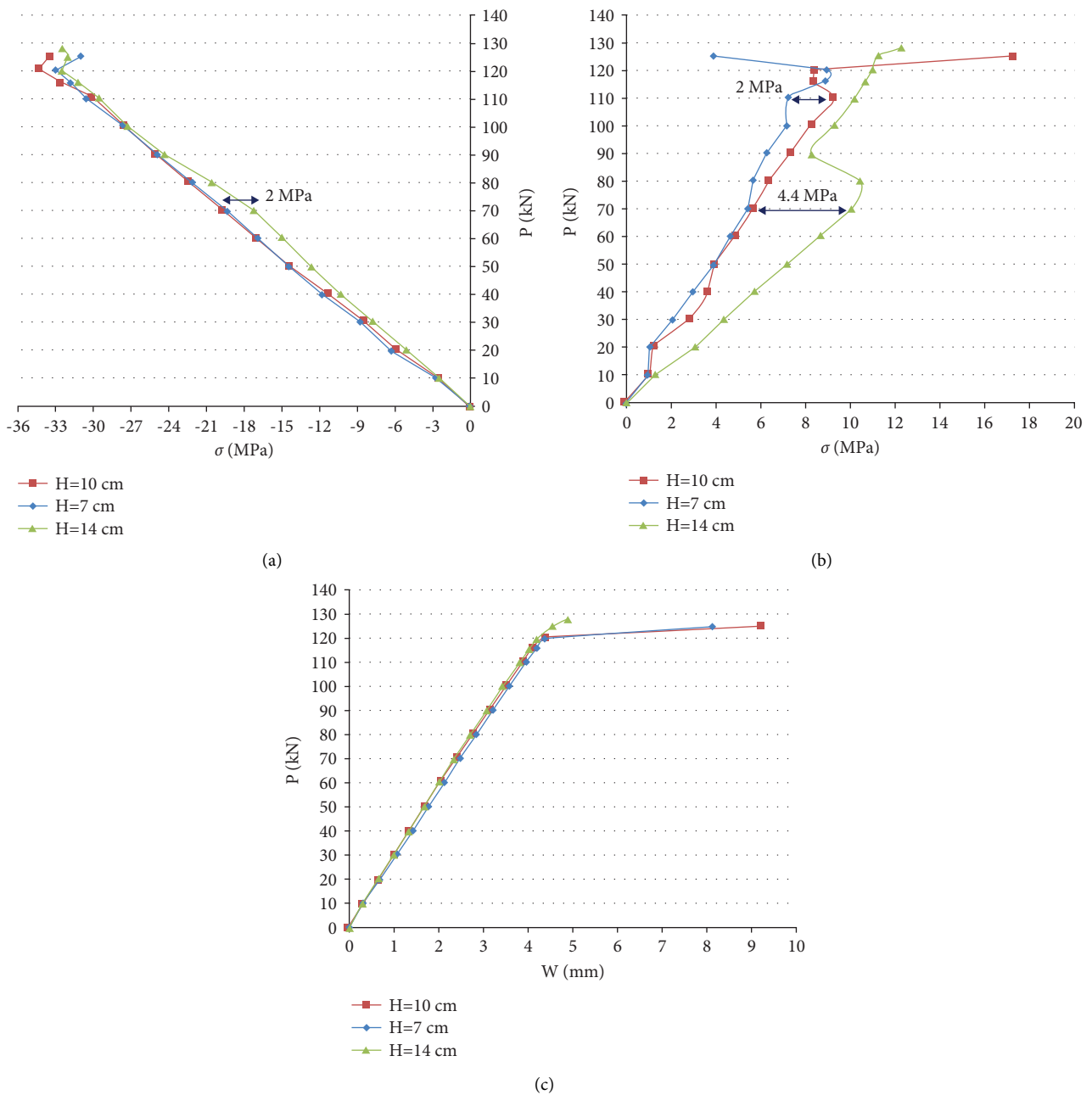


FIGURE 24: Relationship between load and stress, as well as between load and vertical displacement (effect of the thickness of the SFC layer): (a) relationship between load and compressive stress, (b) relationship between load and tensile stress. (c) the relationship between load and VD.

In Figure 23, increasing the thickness of the SFC layer from 7 centimeters to 14 centimeters results in no change in beam section size, an increase in beam bearing capacity from 125 kN to 128 kN and a significant reduction in the number of cracks in concrete beams; in both cases, the most cracked beams are in NC layers. Layers of SFC have been shown to cut down on the number of cracks in RC beams by a lot.

Figure 24 shows the load-compressive stress, tensile stress, and VD relationships in the midpoint of the span of a SFC beam.

Changing the thickness of the SFC layer in Figure 24 has little effect on compressive stress; the difference between beams is 2 MPa (Figure 24(a)). However, the tensile stress changes with stress, with the highest difference being 2 MPa between the beams with $H=7$ cm and $H=10$ cm, 4.4 MPa between the beams with $H=10$ cm and $H=14$ cm, and a smaller change in the VD in the middle of the span.

4. Conclusions

The following are some of the conclusions that may be derived from the results of the study:

- (1) We were able to show that the number of cracks in bending beams may be greatly decreased by using a RC layer reinforced with SFs. Because it is affected by the maximum allowable steel content in the concrete, the beam will be damaged at the very least when the SFs' content of the concrete is raised by 5%. This is because the beam is affected by the maximum allowable steel content.
- (2) When the distance between the stirrups at the ends is modified, it is found that the beam works more effectively when the distance between the stirrups grow to 100 millimeters. This is because the amount of steel in the concrete has reached the legal limit.
- (3) The ability of the beams to support weight greatly improves when both the number of tensile steel bars and the diameters of those bars are increased, which also reduces the risk that cracks will form. The influence of tensile stress is large in this case as a result of an increase in the number of steel bars in the tensile zone as well as the diameter of those steel bars.
- (4) The figures for compressive stress and VD do not vary much when the thickness of the SFC layer is modified, but the tensile stress does rise.
- (5) It has been shown that the input parameters of double-layer SFC beams have an effect on the performance of the beams. Because of this research, the important parameters could be changed to either limit or encourage certain values that are better for building SFC beams with multiple layers.

Abbreviations

FE: Finite element
 NC: Normal concrete
 NCL: Normal concrete layer

SFC: Steel fiber concrete
 SFCL: Steel fiber concrete layer.

Data Availability

The data used to support the findings of this study are included within the article.

Conflicts of Interest

The authors declare that there are no conflicts of interest regarding the publication of this paper.

References

- [1] V. T. Ngo, T. Q. Khai Lam, T. M. Dung Do, and T. C. Nguyen, "Nano concrete aggregation with steel fibers: a problem to enhance the tensile strength of concrete," *E3S Web of Conferences*, vol. 135, Article ID 03001, 2019.
- [2] V. T. Ngo, T. Q. K. Lam, T. M. D. Do, and T. C. Nguyen, "Increased plasticity of nano concrete with steel fibers," *Magazine of Civil Engineering*, vol. 1, no. 93, pp. 27–34, 2020.
- [3] V. T. Ngo, T. T. Bui, T. Q. K. Lam, T. T. N. Nguyen, and V. H. Nguyen, "Experimental evaluation of nano silica effects to high performance concrete strength in early age," *IOP Conference Series: Materials Science and Engineering*, vol. 869, no. 3, p. 869, Article ID 032011, 2020.
- [4] S. Anandan, S. Islam, and R. A. Khan, "Effect of steel fibre profile on the fracture characteristics of steel fibre reinforced concrete beams," *Journal of Engg. Research*, vol. 10, no. 2, pp. 105–124, 2019.
- [5] T. Q. Khai Lam, D. D. Thi My, V. T. Ngo, T. Chuc Nguyen, and T. Phuoc Huynh, "Numerical simulation and experiment on steel fiber concrete beams," *Journal of Physics: Conf. Ser.*, vol. 1425, no. 1, Article ID 012007, 2019.
- [6] A. Fatih, K. M. Metin, Y. Canan, A. Kamuran, and D. Adem, "Experimental investigation of reinforced concrete beams with and without steel fiber under explosive loading," *Indian Journal of Engineering and Materials Sciences*, vol. 14, pp. 419–426, 2007.
- [7] T. Q. K. Lam and T. M. D. Do, "Analysis of nonlinear material and steel fiber content in the double layers concrete shell," *AIP Conference Proceedings*, vol. 2283, p. 2020, Article ID 020008, 2020.
- [8] T. M. D. Do, T. Q. K. Lam, T. T. N. Nguyen et al., "Initial parameters affecting the multilayer doubly curved concrete shell roof," *Advances in Civil Engineering*, vol. 2021, Article ID 7999103, 18 pages, 2021.
- [9] A. Gokmen, "Buckling analysis of delaminated composite beams," *Indian Journal of Engineering and Materials Sciences*, vol. 20, pp. 276–282, 2013.
- [10] A. Soto and F. M. Tehrani, "An investigation of crack propagation in steel fiber-reinforced composite beams," *Periodica Polytechnica: Civil Engineering*, vol. 62, no. 4, pp. 956–962, 2018.
- [11] I. Iskhakov and Y. Ribakov, "A design method for two-layer beams consisting of normal and fibered high strength concrete," *Materials & Design*, vol. 28, no. 5, pp. 1672–1677, 2007.
- [12] I. Iskhakov and Y. Ribakov, "Two-layer beams from normal and fibered high strength concrete," *Modern Methods and Advances in Structural Engineering and Construction (ISEC-6)*, vol. 21, 2011.

- [13] I. Iskhakov, Y. Ribakov, K. Holschemacher, and T. Mueller, "Experimental investigation of full scale two-layer reinforced concrete beams," *Mechanics of Advanced Materials and Structures*, vol. 21, no. 4, pp. 273–283, 2014.
- [14] I. Iskhakov, Y. Ribakov, and K. Holschemacher, "Experimental investigation of continuous two-layer reinforced concrete beams," *Structural Concrete*, vol. 18, no. 1, pp. 205–215, 2017.
- [15] I. Iskhakov, Y. Ribakov, K. Holschemacher, and S. Kaeseberg, "Experimental investigation of prestressed two layer reinforced concrete beams," *Structural Concrete*, vol. 22, pp. 238–249, 2019.
- [16] M. M. A. Pratama, R. K. Suhud, P. Puspitasari, F. I. Kusuma, and A. B. N. Rahma Putra, "Finite element analysis of the bending moment-curvature of the double-layered graded concrete beam," *IOP Conference Series: Materials Science and Engineering*, vol. 494, p. 494, Article ID 012064, 2019.
- [17] B. Thomee, K. Schikora, and K. Bletzinger, "Material modeling of steel fiber reinforced concrete," *Computers and Concrete*, vol. 3, no. 4, pp. 197–212, 2006.
- [18] T. L. Teng, Y. A. Chu, and B. C. Shen, "Penetration resistance of steel fiber reinforced concrete containment structure to high velocity projectile," *Computers and Concrete*, vol. 5, no. 6, pp. 509–524, 2008.
- [19] P. Ramadoss and K. Nagamani, "A new strength model for the high-performance fiber reinforced concrete," *Computers and Concrete*, vol. 5, no. 1, pp. 21–36, 2008.
- [20] T. M. D. Do and T. Q. K. Lam, "Nonlinear analysis of multi-layer steel fiber reinforced concrete beams," *Journal of Construction, Vietnam*, vol. 4, pp. 58–63, 2021.
- [21] T. M. D. Do and T. Q. K. Lam, "Design parameters of steel fiber concrete beams," *Magazine of Civil Engineering*, vol. 2, no. 102, 2021.
- [22] V. D. Tho and E. A. Korol, "Influence of geometrical parameters of the cross section, strength and deformability of the materials used on stress-strain state of three-layered reinforced concrete," *IOP Conference Series: Materials Science and Engineering*, vol. 661, no. 1, p. 661, Article ID 012121, 2019.
- [23] D. T. Vu, E. Korol, Y. Kustikova, and H. H. Nguyen, "Finite element analysis of three-layer concrete beam with composite reinforcement," *E3S Web of Conferences*, vol. 97, Article ID 02023, 2019.
- [24] A. Ayman and M. Sayed, "Nonlinear static analysis of reinforced concrete framed buildings - a case study on Cairo earthquake," *Journal of Engg. Research*, vol. 4, no. 4, 2016.
- [25] T. Q. K. Lam, T. M. D. Do, V. T. Ngo, T. T. N. Nguyen, and D. Q. Pham, "Concrete grade change in the layers of three-layer steel fibre reinforced concrete beams," *Journal of Achievements in Materials and Manufacturing Engineering*, vol. 1, no. 102, pp. 16–29, 2020.
- [26] T. M. D. Do and T. Q. K. Lam, "Design parameters of double layers steel fiber concrete beams," *Lecture Notes in Civil Engineering*, vol. 130, pp. 299–321, 2021.
- [27] T. M. D. Do, T. Q. K. Lam, V. T. Ngo, and T. T. N. Nguyen, "Two-layered steel fiber concrete beam with concrete grade change in layers," *Resilient Infrastructure*, vol. 202, pp. 427–443, 2021.
- [28] T. M. Dung Do and T. Q. Khai Lam, "Cracks in single-layer and multi-layer concrete beams," *Transportation Research Procedia*, vol. 63, pp. 2589–2600, 2022.
- [29] H. Mertol, "Farklı gçlbksbked," *Journal of Polytechnic*, vol. 25, no. 1, pp. 273–280, 2021.
- [30] N. Elmezaini and M. Ashour, "Nonlinear analysis of concrete beams strengthened with SFRC layer," *Journal of Engineering Research and Technology*, vol. 2, no. 3, pp. 181–188, 2015.

Research Article

Shield Cutting Pile-Group Implementation Effects on the Superstructure

Chi Zhang,¹ Shiju Ma ,² Yuancheng Guo,¹ Mingyu Li,¹ and Kui Fu³

¹School of Civil Engineering, Zhengzhou University, Zhengzhou, China

²School of Civil Engineering, Zhengzhou Institute of Technology, Zhengzhou, China

³China Railway 18th Bureau Group First Engineering Co. LTD, Baoding, Hebei, China

Correspondence should be addressed to Shiju Ma; mashiju2010@126.com

Received 21 July 2022; Revised 18 August 2022; Accepted 24 August 2022; Published 27 September 2022

Academic Editor: S. Mahdi S. Kolbadi

Copyright © 2022 Chi Zhang et al. This is an open access article distributed under the Creative Commons Attribution License, which permits unrestricted use, distribution, and reproduction in any medium, provided the original work is properly cited.

The shield tunneling method is widely used in urban subway construction. However, as the layer stress state changes during shield tunnel construction, layer displacement and surface deformation occur accordingly. This study tries to investigate the settlement and deformation of the masonry structure in shield cutting the composite foundation of group piles in a shield tunnel project at Zhengzhou Metro Line 5. To understand the distribution characteristics and changing rules of building settlement during the process of shield cutting group piles composite foundation passing through the masonry structure, a thorough analysis of the ground surface settlement and building settlement, including on-site measured, was conducted. The results show that piles go down through a composite foundation during shield cutting. The cumulative maximum settlement and maximum differential settlement of the masonry structure were concentrated at the intersection of the tunnel axis and the building. The longitudinal distribution of the cumulative settlement of the south and north wall of the masonry structure changes continuously with the change of the position of the shield excavation surface. That behavior may cause the building to be tilted and deformed and cause the structure to undergo rigid rotation and twisting deformation. Based on the composite pile foundation project of the Shield Tunnel Cutting Group in a specific section of Zhengzhou Metro Line 5, this paper analyzes the surface settlement and foundation settlement data of the building caused by the construction of the shield. It obtains the changes of the surface settlement and the settlement of the foundation of the building. No other changes have been made to the existing cracks in the external walls of the building. At the same time, because of the low angle between the longitudinal axis of the masonry structure and the tunnel axis (22°) and the positive effect of the ring beam and column of the structure in the building, it is clear that the construction of this project has little effect on the upper building, thus showing improved control.

1. Introduction

With the rapid development of the urban subway system, an increasing number of tunnels are being built in China. However, tunneling deforms the surrounding soil and adjacent structures, such as buildings, existing tunnels, and buried pipelines. Therefore, minimizing the interference of the tunnel construction process on nearby structures has been the focus of engineers and researchers in the field of geotechnical engineering. Usually, this kind of displacement

and deformation can be completed in a short time, and this kind of rapid deformation is very destructive to the superstructure. Many scholars have investigated the damage to the upper structures caused by shield tunnel construction. In terms of theory, Burland and Wroth [1] and Burland et al. [2] proposed a classification standard of damage level of masonry structure based on the concept of ultimate tensile strain. They applied it to the influence of tunnel excavation on upper buildings. Boscardin and Cording [3] and Boone [4] treat buildings as elastic beams and then propose a

method to define the failure level by angular distortion and horizontal strain. Burland [5] and Clarke and Laefer [6] proposed a method to define the failure level by the horizontal strain and deflection ratio. In terms of field measurement, Dimmock and Mair [7] compared and analyzed the bending deformation and strain of the building caused by shield construction and the deformation and strain of the surface based on the measured data and concluded that the stiffness of the upper building has a corrective effect on the settlement caused by the tunnel. Camós et al. [8] observed buildings' settlement, deformation, and damage through shield tunnel construction. They found that the vertical and horizontal displacement of the ground is often reduced because of the existence of buildings.

Underground pile foundations are dense in cities with crowded buildings. If the distance between the pile foundation and the shield is too close, tunneling may cause uneven settlement, deformation of the structure, and cracks in the building [9]. Zhang et al. [10] studied the impact of the shield tunnel crossing underneath a river on bridge piles under the working conditions without rainfalls and concluded that the scheme of erecting up temporary inverted arches and grouting under-the-bridge piles for water plugging was feasible and that the grouting effect was critical to the construction of under-the-bridge undercutting piles.

With the development of the urban underground space, the cases of shield tunnel digging under or adjacent to the existing pile foundations of buildings are increasing. Tunnel construction inevitably redistributes the initial soil stress and causes surface settlement, tilting, curvature change, horizontal displacement, and discontinuous deformation that may affect the adjacent pile foundations, resulting in potential safety hazards for the structure to bring constructions. Breth and Chambosse [11] and Frischmann et al. [12] studied and analyzed the ground subsidence caused by tunnel excavation. Forth and Thorley [13] believed that the main reason for the reduction of pile side friction resistance caused by shield construction was the vertical displacement of the stratum towards the tunnel. Miliziano et al. [14] used two-dimensional numerical simulation methods to study the impact of tunnel construction on adjacent buildings in terms of numerical analysis. Giardina et al. [15], Giardina et al. [16], and Giardina et al. [17] established two-dimensional and three-dimensional finite element models to evaluate the damage degree of adjacent masonry structures caused by surface settlement caused by tunnel construction under different working conditions. Burd et al. [18] established a three-dimensional finite element model of tunnel-soil-building integration considering the weight and stiffness of the building. The results of their study showed that the interaction between the soil and the structure would reduce the damage degree to the building. Underground structures, especially tunnels, are very common, especially in urban areas [19]. Nevertheless, studies that investigate the influence of the underground structures on the dwelling structures are very sporadic. Furthermore, to the best of our knowledge, there is no study that analyzes the settlement and deformation of the masonry structure in shield cutting the composite foundation of group piles in a shield tunnel.

Furthermore, we propose cost-effective methods for real-time tracking and control of building settlement. Therefore, the main goal of this study is to better understand the interaction between underground and surface masonry structures, i.e., the investment effect of a tunnel in masonry construction meetings. Also, the paper suggests some cost-effective monitoring and mitigation measures. The rest of the paper is organized as follows: Section 2 provides a brief description of the stud case, Section 3 describes the most common methods for monitoring settlements, Section 4 details the monitoring and analysis of construction settlements for the case this study took into consideration, Section 5 describes surface settlements and the most critical areas, and Section 6 discusses the consequences of settlements on building stability. Finally, the main conclusions and recommendations from this study are presented in Section 7.

2. Engineering Situation

Shield cutting soil-cement group piles composite foundation in Zhengzhou Metro Line 5 passes through the building project. The mileage of the left line of the pile cutting construction section is DK13+662.558~DK13+711.322 (685 rings~715 rings, the length is about 48.764 m), and the tunnel forms an angle of 22° with the plane of the existing house, as shown in Figure 1.

There are about 224 agitating piles intruded by the shield. The length of the shield cutting pile is about 2.6~3.7 m. The outer diameter of the segment is 6.2 m, the inner diameter is 5.5 m, the wall thickness is 0.35 m, and the width of the lining ring is 1.5 m. The segment material is C50 concrete, and the segment assembly method adopts staggered seam assembly. The building is a 7-story masonry structure with a semi-basement, and the foundation form is a strip foundation. The foundation is treated with a cement-soil pile composite foundation. The pile length is 11.5 m, the pile diameter is 0.5 m, and the spacing between the piles is 0.95 m. The exterior of the building is shown in Figure 2.

3. Settlement Control Measures

As shown in Figure 3, two “gaps” need to be mainly controlled during shield construction, namely clearance between shield and shield tail and clearance between cutter and shield, to reduce the adverse impact on the masonry structure and foundation during the construction process of the shield machine cutting piles.

This paper uses three “Clay shock” grouting methods, synchronized grouting, and secondary reinforcement grouting to control the surface settlement and building settlement.

3.1. Clay Shock Method. Eight radial grouting holes with a diameter of 12 mm are arranged along the circumference of the shield body at the middle shield position in the shield machine (Figure 4). Grouting is carried out synchronously to the outside of the shield machine shell, which is the gap between the shield body and the outer soil body. Grouting can form a reliable sealing water-blocking clay grouting layer

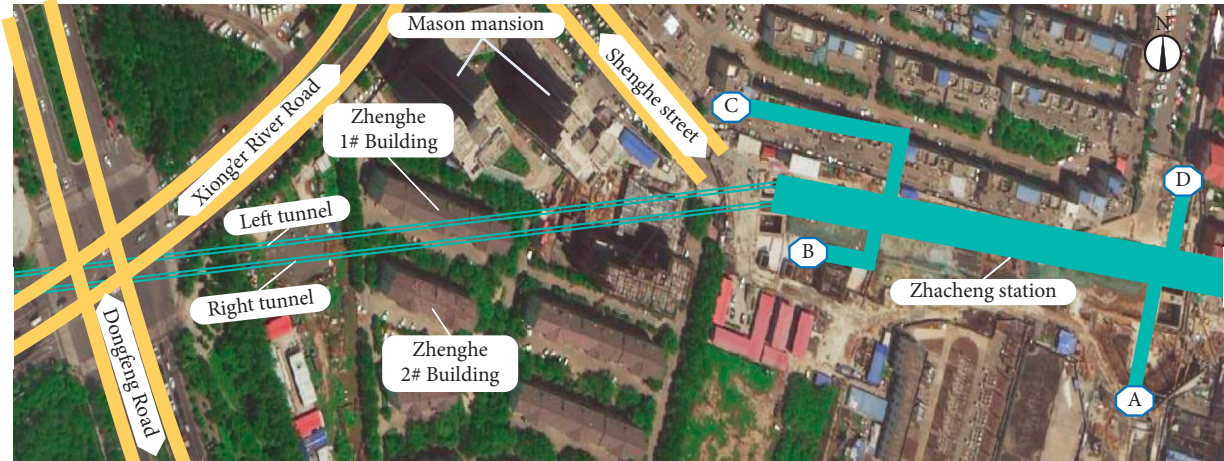


FIGURE 1: Plan view of shield tunnel cut pile passing through masonry structure.



FIGURE 2: The appearance of a masonry structure.

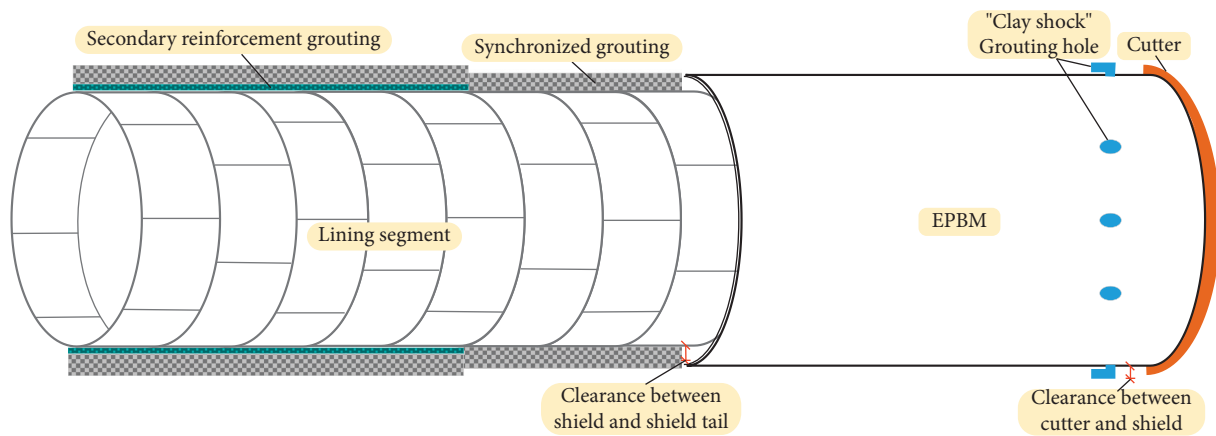


FIGURE 3: Schematic diagram of formation subsidence control principle.

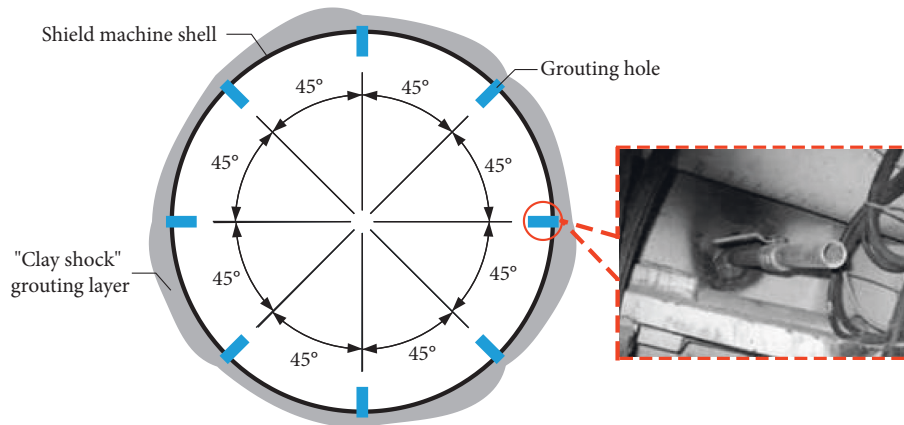


FIGURE 4: The layout of grouting holes in the shield machine shell.

around the shield machine, filling the gap between the shield and the stratum and effectively controlling the amount of soil subsidence during excavation. The injection process of “Clay shock” grouting is controlled as follows: the “Clay shock” grouting starts at the first ten rings of passing the building. Before the shield machine starts to advance, inject A liquid first and then B liquid. Prevent pipe blockage caused by the mixing of water glass with clay slurry.

The grouting pressure is 0.2~0.4 MPa. “Clay shock” grouting is synchronized with propulsion, and the grouting speed should be adjusted according to the propulsion speed. Inject 1.26 m^3 of mixed solution (140% of the theoretical value) into each ring. The ratio of “Clay shock” grouting is shown in Table 1.

3.2. Synchronized Grouting. When the lining structure is separated from the shield tail, fill the building gap between the shield machine shell and the lining structure on time and prevent the composite foundation from sinking rapidly in a short period. The synchronous grouting measures at the shield machine’s shield tail are taken. The theoretical building gap caused by advancing the single-ring segment is $1.5 \times \pi \times (6.442 - 6.22) / 4 = 3.57 \text{ (m}^3\text{)}$, and the initial setting time of the slurry was about 4 hours. The actual grouting volume is 150%~200% of the theoretical building space of each ring segment, i.e., the synchronous grouting volume for each advancing ring is 8 m^3 , and the pressure at the pumping outlet is generally controlled at 0.3~0.4 MPa. The slurry pressure should also be adjusted and controlled according to ground and building settlement. The slurry ratio is shown in Table 2.

3.3. Secondary Reinforcement Grouting. To reduce the late settlement of the soil after the shield machine and reduce the waterproof pressure of the tunnel, secondary reinforcement grouting is carried out after the segment is separated from the 6th to 8th rings of the shield tail. Moreover, a double slurry composed of cement slurry and water glass is selected to quickly fill the gap between the grouting layer remaining in the synchronous grouting and form a certain strength. The ratio of the double slurry is shown in Table 3.

The grouting sequence is injected according to the method of “first dome, then two waists, and two waists are symmetrical.” After filling one ring, the grouting of the next ring is carried out. The standard of filling is that no water flows out after the lifting hole of the ring is opened. The secondary grouting pressure is controlled at $\neq 0.5 \text{ Mpa}$.

4. Settlement Measurement

According to the requirements of “Technical Specifications for Urban Rail Transit Engineering Monitoring” [20, 21] and “Urban Rail Transit Engineering Measurement Specifications” [22, 23], combined with the actual project site overview and building characteristics, three surface subsidence monitoring sections, namely DB1, DB2, and DB3, were set up. The measuring points of the building foundation settlement are arranged clockwise along the corner of the building, numbered JG1~JG19. There are 19 measuring points in total. See Figure 5~7 for the relative positional relationship between the building and the tunnel and the layout method of monitoring points.

5. Surface Settlements

The surface subsidence process caused by shield construction is divided into five stages: stage I is before the shield reaches the monitoring section. In stage II, the shield passes through the monitoring section. Stage III is the shield tail prolapse monitoring section. In stage IV, shield cut pile group composite foundation passed. Stage V is the subsequent subsidence stage. The DB1 monitoring section is located at the cross-section of the 685 rings of the left-line tunnel. The shield cutter head of the left-line tunnel cuts into the composite foundation and starts to cut piles. It can be seen from Figure 8 that, in stage I, each monitoring point of the DB1 monitoring section showed slight uplift, and the maximum uplift value appeared on the right line tunnel outline. In stage II (III), the measuring point DB1-1 on the center of the left tunnel and the measuring point DB1-2 on the outline of the left tunnel appeared to sink because of shield excavation and pile cutting. In contrast, the centerline of the right tunnel and the corresponding measuring points

TABLE 1: The ratio of “Clay shock” grouting.

Material name	Proportion	Dosage (m ³)	Volume weight (kg/m ³)	Coagulation time (s)	Viscosity (dPa·s)
Liquid A: special bentonite liquid Liquid B: water glass mixture	20:1	“Clay shock” powder 400 kg, 40 Baumé degree, water glass dosage 70 kg, water 846 kg	2600	4.5 s start to cement, 20 s initial setting.	300~500

TABLE 2: Synchronous grouting slurry ratio table.

Cement (kg)	Fly ash (kg)	Bentonite (kg)	Sand (kg)	Water (kg)
170	400	800	750	450

TABLE 3: Secondary grouting slurry ratio table.

Material name	Material parameters	Proportion	Coagulation time (s)	28 days strength (Mpa)
Cement Water glass	P.O 42.5 Baumé degree: 30~35, modulus: 2.8~3.1	Water: Water glass: Cement slurry = 3:1:1 (volume ratio)	30	2.6

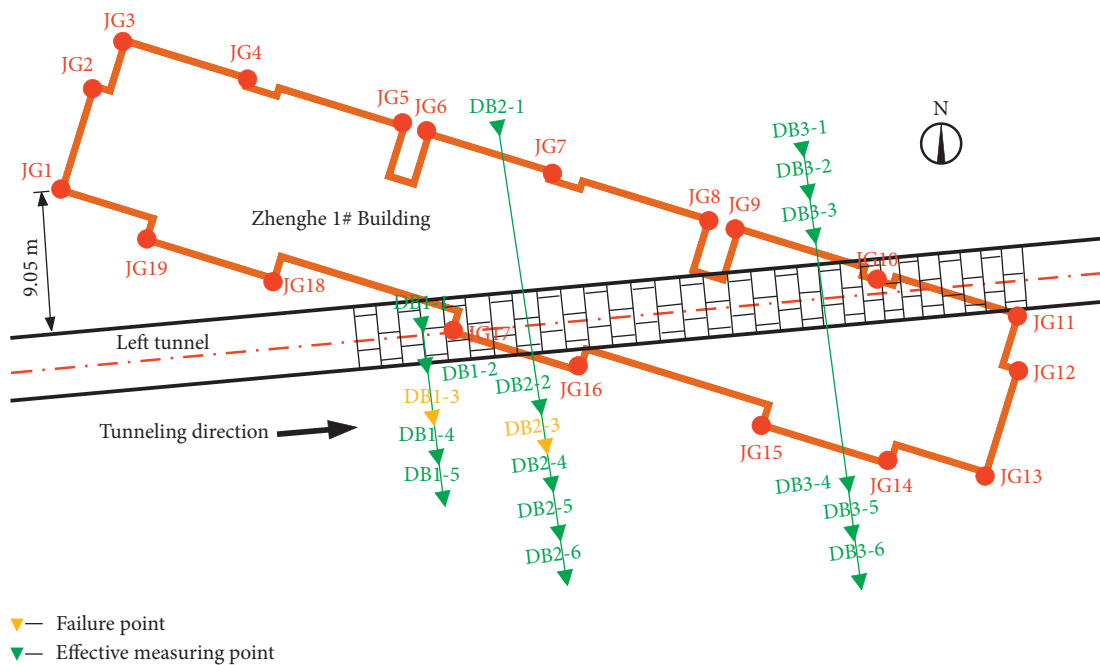


FIGURE 5: The relative position between building and tunnel and the plan of monitoring instruments.

DB1-4 and DB1-5 on the outline of the tunnel on the right line is uplifted. It is because of synchronous grouting and the “Clay shock” method when the shield cuts piles. The extruded soil effect caused the pile body that was not damaged by the shield to bulge slightly upwards, which triggered the ground surface to bulge. In stage IV, all measuring points of this monitoring section subside. The settlement law and settlement amount of the measuring points on the centerline and outline of the left tunnel are generally consistent, and the settlement value is greater than that of the measuring points on the right tunnel. In stage V, the monitoring points of the DB1 monitoring section first subsided and then gradually

rose. Finally, the subsidence was stable until the shield tail protruded for 15 days. The maximum occurred at the centerline of the left tunnel, and the subsidence value was -9.0 mm.

As shown in Figure 9, before the shield reaches the DB2 monitoring section, i.e., stage I, each measuring point of this monitoring section is slightly uplifted. Nevertheless, the maximum uplift point appears at the two monitoring points, DB2-1 and DB2-2, closest to the building, which is different from the maximum uplift position of the DB1 monitoring section. In stage II (III), affected by the existing cement-soil group pile composite

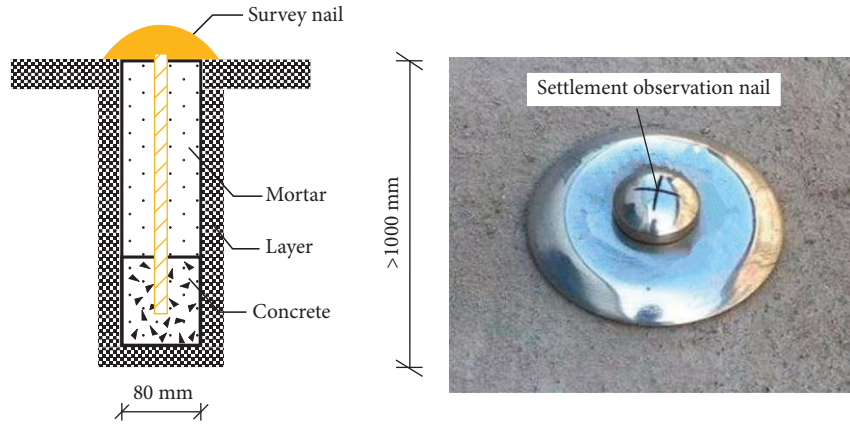


FIGURE 6: Buried method and physical map of surface subsidence measuring points.

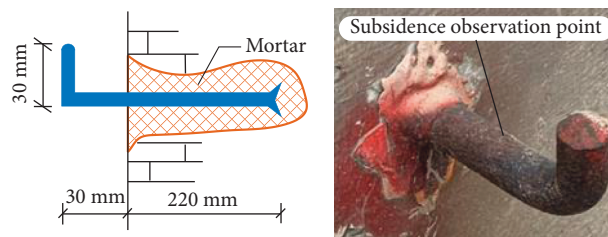


FIGURE 7: Layout method and physical map of building foundation settlement monitoring points.

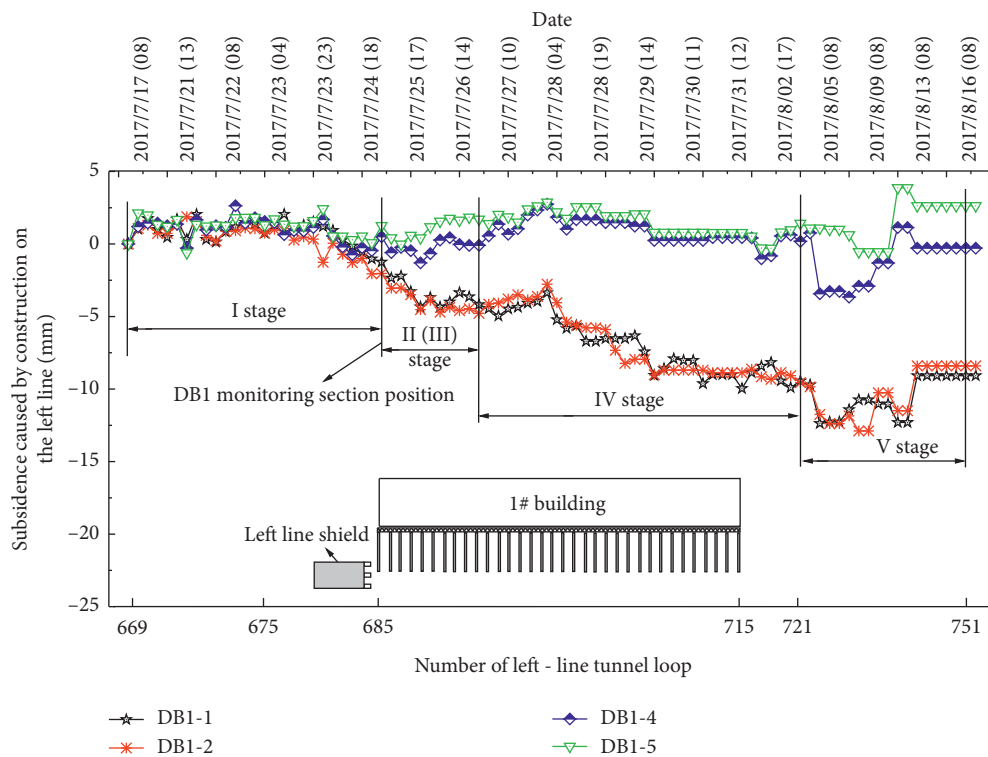


FIGURE 8: Monitoring time-history curve of surface subsidence of section 1.

foundation, the changes of each measuring point of the DB2 monitoring section at this stage are small, except for the DB2-2 measuring point that is closer to the centerline of the left line of the tunnel, which sinks slightly. In

addition, all other measuring points have uplifted, and the uplift value is not large. In stage IV, the shield tail was separated from the monitoring section and continued to cut piles. All monitoring points were affected by the

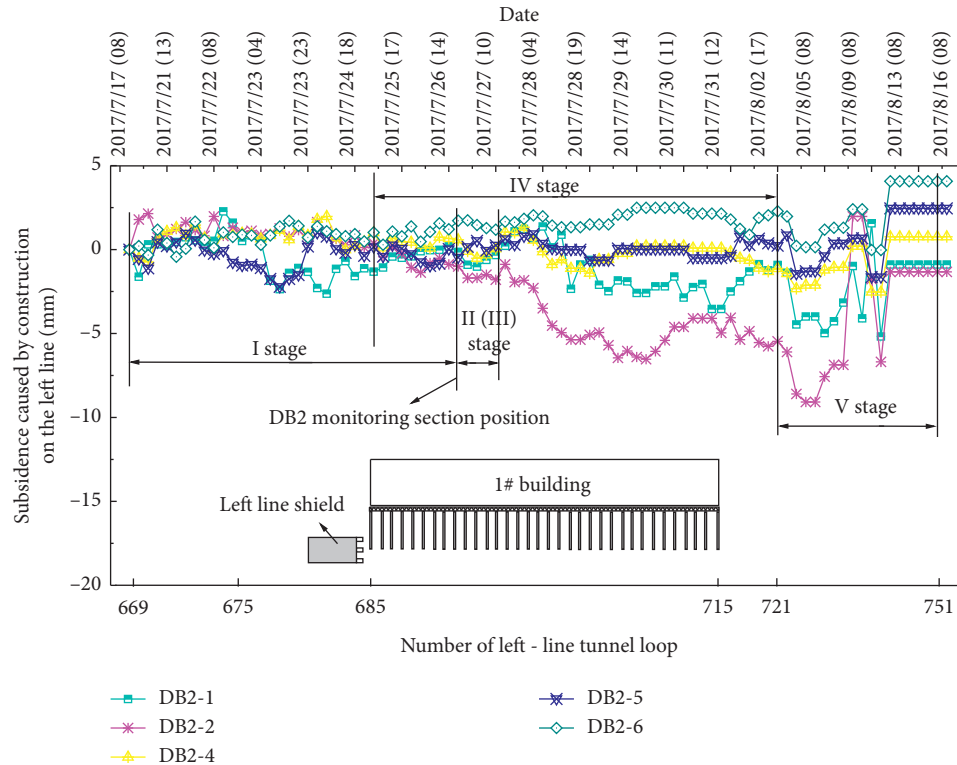


FIGURE 9: Monitoring time-history curve of surface subsidence of section 2.

construction disturbance of shield cutting and pile cutting, and they sank. The maximum settlement occurs near the intersection point of the left-line tunnel cutting into the building. The settlement value is -6.5 mm. In the stage, each measuring point of the surface settlement presents a “W” shape, closely related to the secondary grouting amount of the shield and the grouting amount of “Clay shock” grouting. The position of the maximum settlement value at this stage is the DB2-2 measuring point, the settlement value is -9.0 mm, and the settlement value of this measuring point after stabilization is -0.89 mm.

As shown in Figure 10, the monitoring points DB3-1, DB3-2, and DB3-3 subsided in stage I. The maximum subsidence occurred at the monitoring point DB3-1, with a value of -3.5 mm. The monitoring points of DB3-4, DB3-5, and DB3-6 are slightly uplifted, the maximum uplift value is $+2.4$ mm, and the maximum uplift point is the DB3-4 measurement point. It is caused by the uneven settlement of the building caused by the construction of the left shield line cutting piles. In stage II, as the shield cutting piles are excavated through the DB3 monitoring section, the monitoring points closer to the left line of the tunnel have the largest settlement.

In contrast, the measuring points arranged on the south side of the right line of the tunnel are slightly uplifted. In stage III, apart from the gradual sinking of the DB3-3 measuring point, the DB3-1 and DB3-2 measuring points were affected by the simultaneous grouting and secondary grouting and presented an uplift. In contrast, the DB3-4 and DB3-5 on the south side of the building were uplifted. DB3-6

monitoring point side changes gently, indicating that grouting effectively controls the surface settlement and building inclination caused by tunnel pile cutting. Stage IV includes stages I, II, and III, and hence, no analysis is done.

6. Effects on Building

6.1. Building Response. As shown in Figures 11 and 12, the settlement time-history curves of the north and the south wall of the building show that the settlement value of each settlement measurement point of the south wall is slightly larger than that of the north wall. However, the variation range of each settlement measurement point of the south wall is smaller than that of the north wall. Before the left line of the shield reaches the building, each measuring point on the north wall presents a bulge, and the maximum bulge value is $+5.59$ mm, which is located at the JG5 measuring point of the south wall is slightly sunk, and the maximum settlement is -2.21 mm. It is located at the JG1 measuring point (i.e., the southwest corner of Building 1). The left-line cutter head of the shield cuts into the pile group composite foundation until the shield tail escapes away from the composite foundation. Cutting the pile group composite foundation on the left line, measuring the building’s settlement above the left line of the tunnel outline, and measuring the south wall’s JG17 and JG16 points are all parts of the process. The most dangerous locations are JG10 and JG11 measuring points on the North Wall, whereas JG17 and JG16 measuring points on the

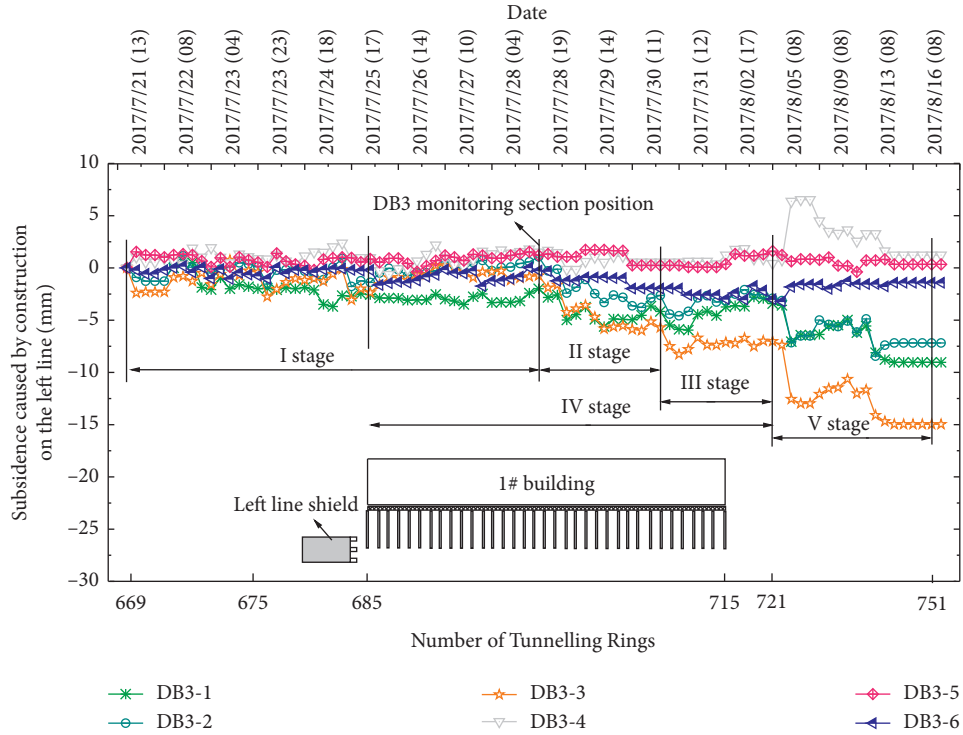


FIGURE 10: Monitoring time-history curve of surface subsidence of section 3.

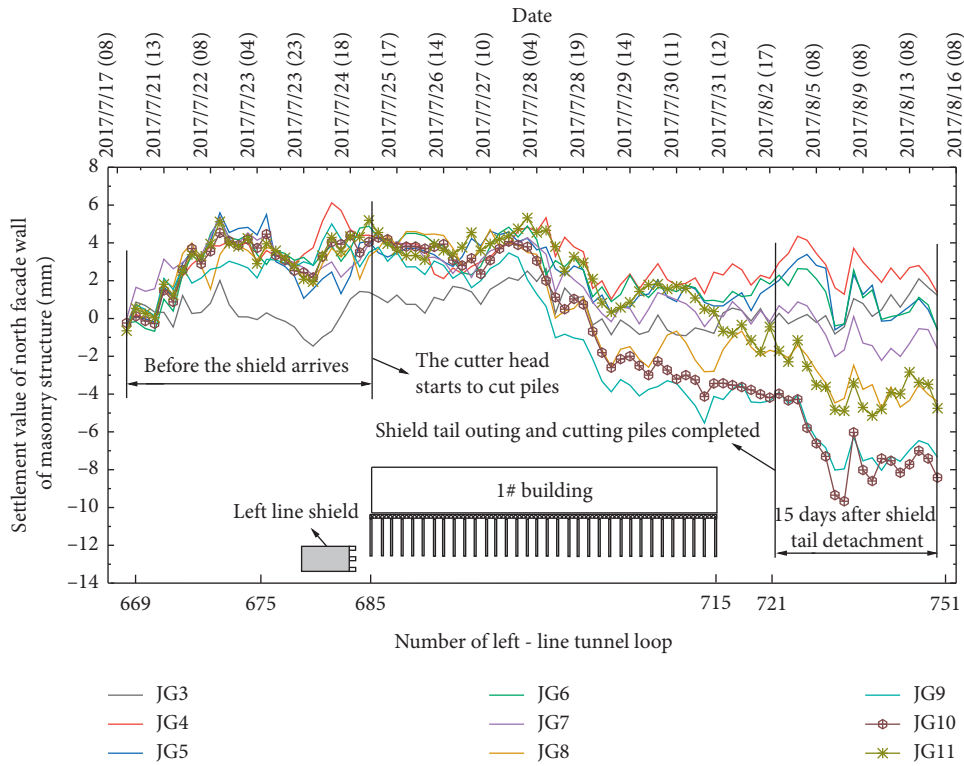


FIGURE 11: Settlement time-history curve of north facade wall of the building.

South Wall have settlement variation ranges of +3.49 mm ~ -5.79 mm, +4.3 mm ~ -2.53 mm, respectively. 15 days after the shield tail of the left line was protruded, the settlement values of the measuring points

JG17 and JG16 on the south wall were -8.66 mm and -10.98 mm, respectively, and the settlement values of the measuring points JG10 and JG11 on the north wall were -9.63 mm and -7.76 mm, respectively.

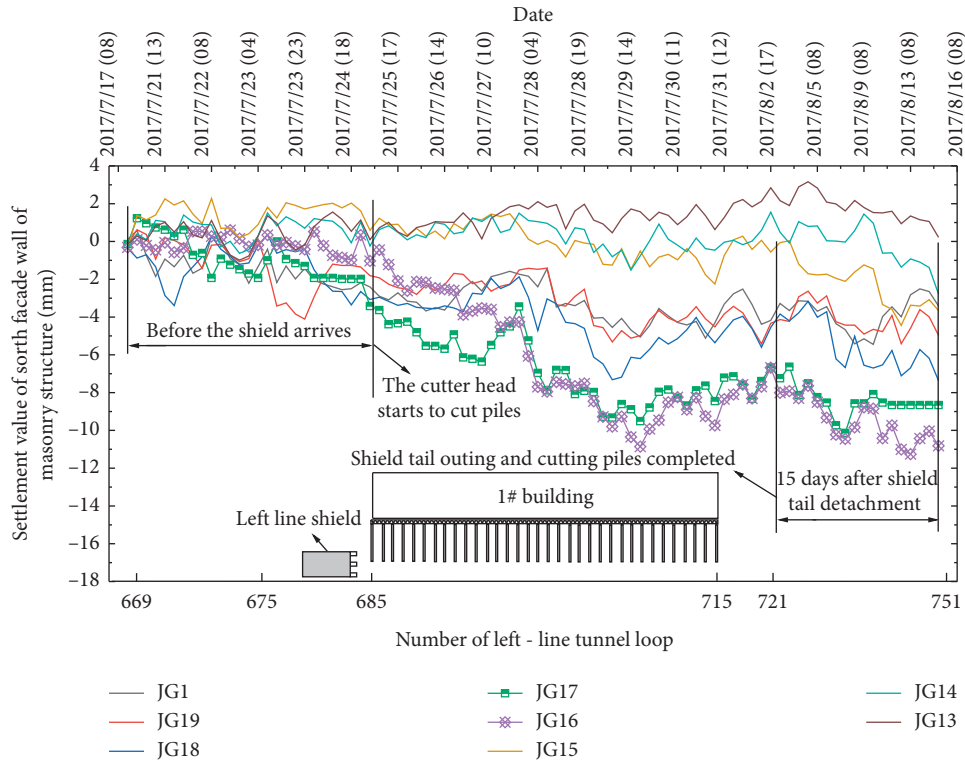


FIGURE 12: Settlement time-history curve of south facade wall of the building.

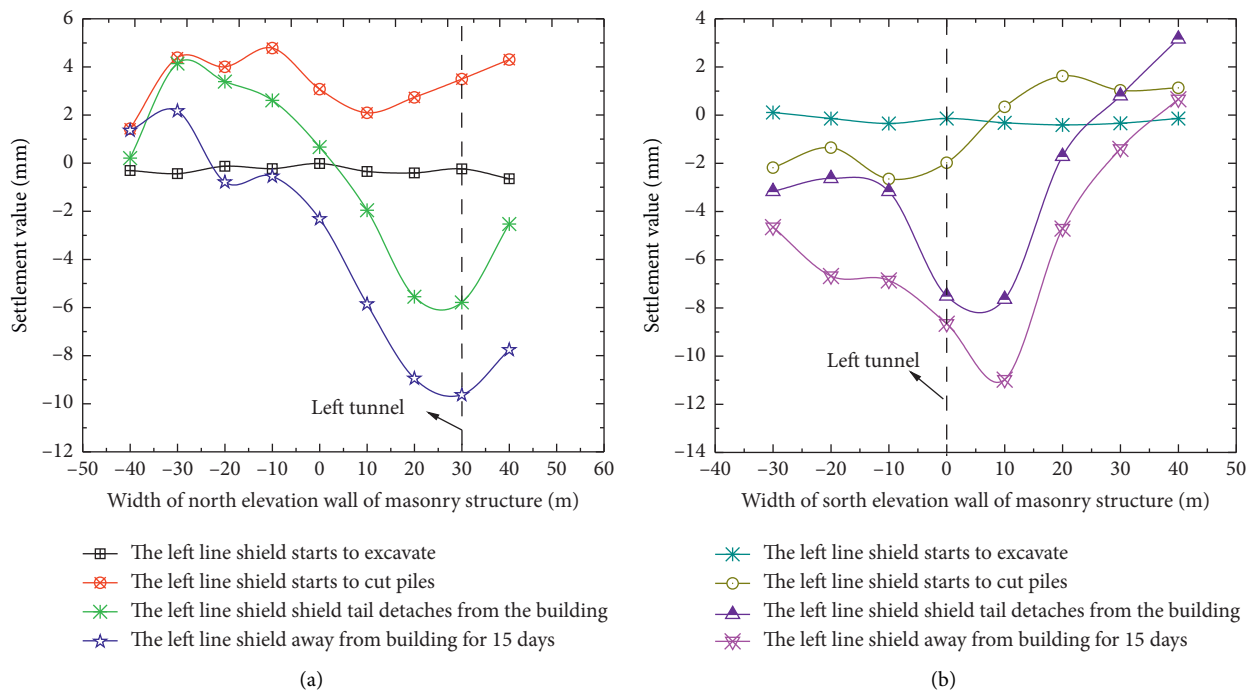


FIGURE 13: The settlement curve: (a) north facade and (b) south facade wall of the building at the critical moment.

Figure 13 shows the characteristic curves of the settlement distribution at the critical moment of the north and south walls of the building. It can be seen from the figures that the influence range of the shield tunnel construction on the ground settlement and the building settlement is

different. The former is the tunnel axis 1.5 D. The latter involves the entire building. When the shield construction causes the settlement of one side of the building, the rigid building will rotate, resulting in the overall tilt of the building. Comparing Figures 13 and 14(a), it can be seen that



FIGURE 14: Cracks (a) between the wall and outside apron slope and (b) on the basement floor.



FIGURE 15: Cracks on the first floor of the masonry structure.

the excavation construction of shield cutting piles causes the building as a whole to incline to the south, because the maximum settlement value position occurs at the oblique intersection of the tunnel and the building space.

6.2. Building Damage Assessment. As shown in Figures 14 and 15, when the shield construction of the left line is far away from 1# building for 15 days, the crack survey of the building structure shall be carried out above the building. The technical construction measures for sediment settlement are effective.

A crack with a length of 1.2 m and a width of 1.0~1.5 cm appeared between the wall at the northwest corner of the masonry structure and the scattered concrete water. A uniform crack with a length of 1.6 m and a width of 0.6 cm appeared on the ground in the northeast corner of the basement. A vertical crack with a length of 0.8 m and a width of 0.15 cm appeared on the first-floor wall at the southwest corner of the masonry structure.

According to “Code for Design of Building Foundation” (GB50007) [21] and “Standard for Appraisal of Dangerous Buildings” (JG J125) [22] and Limiting Tensile Strain Method (Limiting Tensile Strain Method), structural damage was analyzed. For measuring points JG1-1 and JG1-3, the differential settlement is 4.6 mm, and the slope is $i = 0.2\%$. For measuring points JG1-11 and JG1-13, the differential settlement is 5.8 mm, and the slope is $i = 0.3\%$. For measuring points JG1-16 and JG1-07, the differential settlement is 10.7 mm, and the slope is $i = 0.6\%$. The ultimate tensile strain of the masonry structure is 7%.

7. Conclusions

Based on the theory of ultimate tensile strain to control building deformation, crack investigation and building damage assessment are carried out after construction, which confirms the effectiveness of building settlement control technology and innovative measures proposed in this research. The maximum value of surface settlement caused by shield construction occurs near the tunnel’s axis on the left line. Because of the existence of the existing buildings, the surface settlement is relatively gentle for some time after shield construction. With the completion of the shield cutting group pile composite foundation, the surface settlement is larger than the building settlement. In the shield-cutting pile group composite foundation, the cumulative maximum settlement and the maximum differential settlement of masonry structure are concentrated at the intersection of the tunnel axis and building. The masonry structure is subjected to complex forces. In addition to the inclined deformation caused by differential settlement, the structure also has rigid rotation and distortion.

When the shield cutting piles construction, it is more beneficial to control the settlement and deformation of the house by stabilizing the pressure of the soil bin, increasing the amount of synchronous grouting and increasing the rotational speed of the cutter head. After the shield tail is separated from the house, the construction parameters should not be greatly adjusted, the cutter head pressure and Jack thrust should be appropriately increased, and the cutter head torque, cutter head speed, synchronous grouting amount, and tunneling speed should be kept unchanged, which is more conducive to controlling the settlement of the house. The settlement of ground surface and buildings can be effectively controlled using the “Clay shock” method and synchronous grouting during shield cutting piles construction. Secondary reinforcement grouting is carried out after the segment is separated from the 6th to 8th rings of the shield tail. The grouting sequence of each ring is injected according to the method of “first arch, then two waists, and two waists are symmetrical,” which can effectively control the settlement after construction.

The subsequent settlement after construction is mainly affected by secondary grouting and the amount of “Clay shock” grouting. The maximum settlement monitoring point is the DB3-3 monitoring point, and the maximum settlement value after stabilization is -14.97 mm. The strength characteristics of the north wall and the south wall of the building are different. From the settlement curve formed after the shield was removed from the building for 15 days, it can be seen that the south wall approximately exhibits the force characteristic of the cantilever beam, while the north wall approximately exhibits the mechanical characteristics of the beam support. The whole process of building the shield tunnel causes the uneven settlement of the building, tilting of the building, and twisting deformation of the building.

Data Availability

The data used to support the findings of this study are available from the corresponding author upon request.

Conflicts of Interest

The authors declare no conflicts of interest.

Acknowledgments

The remarkable assistance from China Railway 18th Engineering Bureau Group First Engineering Co., Ltd, is highly appreciated.

References

- [1] J. B. Burland and C. Wroth, “Settlement of buildings and associated damage,” in *Proceedings of the Settlement of Structures*, pp. 611–654, London, England, January 1975.
- [2] J. B. Burland, B. B. Broms, and V. F. De Mello, “Behaviour of foundations and structures,” in *Proceedings of the 9th International Conference on Soil Mechanics and Foundation Engineering*, pp. 495–546, Tokyo, Japan, 1978.
- [3] M. D. Boscardin and E. J. Cording, “Building response to excavation-induced settlement,” *Journal of Geotechnical Engineering*, vol. 115, pp. 1–21, 1989.
- [4] S. J. Boone, “Ground-movement-related building damage,” *Journal of geotechnical engineering*, vol. 122, no. 11, pp. 886–896, 1996.
- [5] J. Burland, “Assessment of risk of damage to buildings due to tunnelling and excavations,” in *Proceedings of the 1st International Conference on Earthquake Geotechnical Engineering*, Tokyo, Japan, 1995.
- [6] J. A. Clarke and D. F. Laefer, “Evaluation of risk assessment procedures for buildings adjacent to tunnelling works,” *Tunnelling and Underground Space Technology*, vol. 40, pp. 333–342, 2014.
- [7] P. S. Dimmock and R. J. Mair, “Effect of building stiffness on tunnelling-induced ground movement,” *Tunnelling and Underground Space Technology*, vol. 23, no. 4, pp. 438–450, 2008.
- [8] C. Camós, C. Molins, and O. Arnau, “Case study of damage on masonry buildings produced by tunneling induced settlements,” *International Journal of Architectural Heritage*, vol. 8, no. 4, pp. 602–625, 2014.
- [9] P. Li, Y. Lu, J. Lai, H. Liu, and Ke Wang, “A comparative study of protective schemes for shield tunneling adjacent to pile groups,” *Advances in Civil Engineering*, vol. 2020, Article ID 6964314, 16 pages, 2020.
- [10] X. G. Zhang, L. Ju, and F. Li, “Analysis on and countermeasures for mining tunneling of line 14 of Beijing Metro crossing underneath existing bridge piles,” *J. Tunnel Construction*, vol. 35, no. 7, pp. 692–697, 2015.
- [11] H. Breth and G. Chambosse, “Settlement behavior of buildings above subway tunnels in Frankfurt clay,” in *Proceedings of the Conference on Settlement of Structures*, pp. 329–336, London, England, 1974.
- [12] W. W. Frischmann, J. E. Hellings, G. Gittoes, and C. Snowden, “Protection of the mansion house against damage caused by ground movements due to the docklands light railway extension,” *Proceedings of the Institution of Civil Engineers - Geotechnical Engineering*, vol. 107, no. 2, pp. 65–76, 1994.
- [13] R. Forth and C. B. Thorley, “Hong Kong Island line-predictions and performance,” in *Proceedings of the Geotechnical Aspects of Underground Construction in Soft Ground*, pp. 677–682, Rotterdam, Netherlands Europe, 1996.
- [14] S. Miliziano, F. Soccodato, and A. Burghignoli, “Evaluation of damage in masonry buildings due to tunnelling in clayey soils,” in *Proceedings of the Geotechnical Aspects of Underground Construction in Soft Ground*, pp. 335–340, 2002.
- [15] G. Giardina, M. A. N. Hendriks, and J. G. Rots, “Numerical analysis of tunnelling effects on masonry buildings: the influence of tunnel location on damage assessment,” *Advanced Materials Research*, vol. 133–134, pp. 289–294, 2010.
- [16] G. Giardina, M. A. N. Hendriks, and J. G. Rots, “Damage functions for the vulnerability assessment of masonry buildings subjected to tunneling,” *Journal of Structural Engineering*, vol. 141, no. 9, Article ID 04014212, 2015.
- [17] G. Giardina, M. A. N. Hendriks, and J. G. Rots, “Sensitivity study on tunnelling induced damage to a masonry façade,” *Engineering Structures*, vol. 89, pp. 111–129, 2015.
- [18] H. J. Burd, G. T. Houlsby, C. E. Augarde, and G. Liu, “Proceedings of the Institution of Civil Engineers,” *Geotechnical Engineering*, vol. 143, no. 1, pp. 17–29, 2000.
- [19] M. Ghorbani, M. Sharifzadeh, S. Yasrobi, and M. Daiyan, “Geotechnical, structural and geodetic measurements for conventional tunnelling hazards in urban areas – the case of

- Niayesh road tunnel project,” *Tunnelling and Underground Space Technology*, vol. 31, pp. 1–8, 2012.
- [20] L. Wang, S. Xu, J. Qiu et al., “Automatic monitoring system in underground engineering construction: review and prospect,” *Advances in Civil Engineering*, vol. 2020, Article ID 3697253, 16 pages, 2020.
- [21] J. Yan, X. Liu, X. Bai et al., “Research on surface subsidence of long-span underground tunnel,” *Advances in Civil Engineering*, vol. 2021, Article ID 6643892, 13 pages, 2021.
- [22] Z. Chen, C. Qin, J. Tang, and Y. Zhou, “Experiment research of dynamic stray current interference on buried gas pipeline from urban rail transit,” *Journal of Natural Gas Science and Engineering*, vol. 15, pp. 76–81, 2013.
- [23] Y. Xu, P. Deng, R. Wang et al., “Influences of GPS point coordinate selection on Metro intersection area control network,” *IOP Conference Series: Materials Science and Engineering*, vol. 780, Article ID 062050, 2020.

Research Article

Convergence Study of Variational Space-Time Coupled Least-Squares Frameworks in Simulation of Wave Propagation in Viscoelastic Medium

M. A. Saffarian ¹, A. R. Ahmadi,² and M. H. Bagheripour ³

¹Civil Engineering Department of Shahid Bahonar University of Kerman, Kerman, Iran

²Mechanical Engineering, Kerman Graduate University of Technology, Kerman, Iran

³Civil Engineering, Shahid Bahonar University of Kerman, Kerman, Iran

Correspondence should be addressed to M. A. Saffarian; amin.saffarian@eng.uk.ac.ir

Received 13 June 2022; Revised 13 July 2022; Accepted 7 August 2022; Published 13 September 2022

Academic Editor: S. S. Mahdi Kolbadi

Copyright © 2022 M. A. Saffarian et al. This is an open access article distributed under the Creative Commons Attribution License, which permits unrestricted use, distribution, and reproduction in any medium, provided the original work is properly cited.

There are many novel applications of space-time decoupled least squares and Galerkin formulations that simulate wave propagation through different types of media. Numerical simulation of stress wave propagation through viscoelastic medium is commonly carried out using the space-time decoupled Galerkin weak form in site response problem, etc. In a recent investigation into accuracy of this formulation in simulating elastic wave propagation, it was shown that the diffusive and dispersive errors are greatly reduced when space-time coupled least squares formulation is used instead in variational form. This paper investigates convergence characteristics of both formulations. To this end, two test cases, which are site response and impact models for viscoelastic medium, are employed, one dominated by dispersive and the other by diffusive numerical error. Convergence studies reveal that, compared to the commonly used space-time decoupled Galerkin and the coupled least squares formulation has much lower numerical errors, higher rates of convergence, and ability to take far larger time increments in the evolution process. In solving such models, coefficient matrices would require updating after each time step, a process that can be very costly. However large time steps allowed by ϵ LS are expected to be a significant feature in reducing the overall computational cost.

1. Introduction

Vibration energy dissipation, damping, is involved in many fields of mechanics problems. Mostly, reducing response amplitudes of flexible or solid bodies is important to be considered for engineering subjects. Employment of the elasticity theory to simplify the analysis proves to be inconsistent with the accurate behavior of materials, because most engineering materials have much dependency on their intrinsic properties due to internal friction. In mechanical problem, investigation of damping has a main role in smart mechanical tools, response free fieldout and, structures such as tall building and high way bridges [1]. A number of researchers investigated damping property effect of rubber-sand mixture material underlain by the structures to reduce peak of acceleration, displacement, and shear stress at their bases [2–4].

The study in [5] first introduced a famous approach called *viscous damping* that had been obtained from rheology science. This was competent idealization to describe locally vague material properties which dissipated vibration energy by means of their internal friction. Other idealization is mentioned that the damping matrix assumed to be consisted of linear combination of mass and stiffness matrices. In this model, undamped systems can be used for the analysis of damped systems effortlessly.

Overall, damping is divided into two main classes: (1) damping in discrete systems including SDOF and MDOF systems and (2) damping in continuous systems. Usually, the first is in conjunction with ordinary differential equations (ODEs), extracted from dynamic equilibrium equations, and the second is related to partial differential equations (PDEs), such as wave differential equation. The authors of [4, 6, 7]

worked on viscoelastic problems in different damping models.

There have been studies on one-dimensional viscoelastic analysis of axial wave propagation through rod with various damping models. The authors of [8–10] demonstrated realistic behavior of viscous damping for analyzing actual dynamic systems.

From before to recently, wave propagation simulation considering energy dissipation has been a desirable and attractive topic to research of viscoelastic problem all over the world. There are two major computational methods to analyze viscoelastic dynamic problems, with discrete or continuous systems; (a) time-domain methods, in which the most general computational approaches are included, and (b) frequency-domain methods, which are favorable for linear or equivalent linear problems, extensively computed by mean of finite difference, boundary elements, and finite element methods along with the isogeometric and meshless variations. The study in [11, 12] investigated the earthquake response of surcharged soil layers using Hybrid Frequency Time Domain (HFTD) approach. They used and developed transfer function method, which is categorized into frequency domain analyses, for viscoelastic soil medium on which equivalent mass is surcharged. The study in [13] compared responses 1D viscoelastic horizontally layered soil model and 2D one and observed no significant difference between them.

In time-domain analyses, the solution is known for all points of the spatial domain at a given time t_0 and the objective is to determine the solution at time $t_0 + \Delta t$. The formulation needed for this evolution can be cast in a space-time decoupled or a space-time coupled computational framework. The decoupled Galerkin formulation is widely utilized in study of wave equations, as they appear in many engineering disciplines. Here, coefficient matrices representing discrete spatial distribution of medium's property form a set of ordinary time-dependent equations, which are then solved over a given time span using difference-based techniques such as Newmark- β or Wilson- θ methods [14]. Many improvements have been done to the decoupled formulations [15–17]. Even though the semi-discrete finite elements approach has led to significant improvements in simulation of elastic wave propagation, problems with high frequency loading and sharp temporal gradients still present a significant challenge.

Space-time coupled formulations have been successfully applied in studying time-dependent problems [18]. In this framework, finite element interpolation is performed over an $m + 1$ -dimensional computational domain with m being the number of spatial dimensions. The study in [19] was the first to carry out study over the coupled domain. As demonstrated in [20], in the study of elastic wave propagation due to impact, the decoupled Galerkin yields unsatisfactory results and a space-time coupled discontinuous Galerkin scheme was introduced in order to reduce the dispersive error in this problem. The author of [21] in PhD thesis proposes a discontinuous scheme with least squares stabilizers; this method requires auxiliary variables and, like other discontinuous schemes, upwinding parameters have to be tuned to a particular problem at hand.

Instead of using discontinuous formulations and dealing with complications of proper upwinding scheme, the study in [22] has suggested a comprehensive framework for casting the problem in a space-time coupled least squares framework with higher continuity elements. This framework presents means of convergence through a combination of element length, order of interpolation, and global smoothness. In an error analysis of the wave equation, a quadratic rate of convergence for the wave equation was predicted by [23]. The rate is with respect to element characteristic length, with approximation defined over the coupled domain. However, in context of finite element, it was established that higher smoothness is needed to obtain such rates.

Reference [24] proposed new nonsymmetric variational formulations which are employed to parallelize computations on MIMD-parallel computer for viscoelastic problems based on the continuous and discontinuous Galerkin method. In the study therein, the three-parameter Malvern model described viscoelastic pattern. Promising results were achieved for discontinuous Galerkin method with respect to continuous Galerkin method.

Reference [25] developed temporal decoupling of discontinuous Galerkin space-time finite element method, which is formulated by [26], which is applied only to parabolic differential equation, heat diffusion equation. Continuous Galerkin form in space and discontinuous Galerkin form in time were adopted for second-order wave equations including elastodynamic problem with and without Kelvin–Voigt and Maxwell–Zener, viscoelasticity. Acceptable results were extracted for moderately high-order (up to degree 7) temporal and spatial-temporal approximation. Their method, decoupling procedure, produced a set of boundary value problems that need to be solved for each time interval.

The most popular methods in the engineering practice are the finite and the spectral element methods. They present known advantages (deal with complex geometries, material nonlinearities, etc.) and drawbacks (numerical damping and dispersion, spurious reflections at artificial truncation boundaries). Although various numerical strategies exist to limit spurious reflections (e.g., absorbing boundary conditions or boundary layers), the boundary element method (BEM) remains a very effective approach for dynamic problems in spatially-extended regions (idealized as unbounded), especially so since the advent of fast BEMs such as the fast multiple method (FMM) used in this work. [27].

This macroelement allows one to model soil-footing geometric (uplift) and material (soil plasticity) nonlinearities that are coupled through a stiffness degradation model. Footing uplift is introduced by a simple non-linear elastic model based on the concept of effective foundation width, whereas soil plasticity is treated by means of a bounding surface approach in which a vertical load mapping rule is implemented [28]. Performance criteria are generally displacement-based in the performance-based design approach. Quality requirements in the approach to performance-based design are typically based on displacement. Firstly, keeping this displacement within an acceptable limit ensures the main purpose of planning to have sufficient strength and stiffness. In multistorey commercial and residential structures, coupled

walls are a typical type of shear wall. Through a fusion of the coupling beam's frame action and the wall pier's flexural action, a coupled shear wall system resists lateral forces [29]. Carbon textile is considered an alternate material due to its corrosive resistance property, high tensile strength, and being perfectly elastic. Prestressing is also the only realistic way to utilize fully ultra-high tensile strength in carbon textile material [30].

In a recent paper [31], it was shown that numerical errors can be significantly reduced if the problem is cast in a space-time coupled least squares finite element framework. As an extension to that work, in this paper, convergence characteristics of damped wave equation are studied for the decoupled Galerkin and coupled least squares formulations. In this investigation, since numerical errors are a combination of dispersive and diffusive types, two test cases were designed: one of them is site response model and the other is impact model, each dominated by one of the two error types. Using exact solution, convergence through spatial and temporal refinements and the effects of interpolation and global smoothness on the computational process are studied here.

The remainder of this manuscript is organized as follows: The mathematical model describing viscoelastic wave propagation is presented first followed by the decoupled Galerkin and coupled least squares weak formulations. The succeeding section presents two test cases; one simulates impact and the other base motion. Convergence studies are presented and overall patterns are deduced. This is followed by a discussion on findings and concluding remarks. This study tried to investigate about the relations of variational space-time coupled least squares frameworks using wave propagation in viscoelastic medium, while other research works concentrated on some aspect of this concept.

2. Mathematical Model

Propagation of viscoelastic waves in a one dimensional homogeneous medium can be modeled with

$$\rho \frac{\partial^2 u}{\partial t^2} = E \frac{\partial^2 u}{\partial x^2} + \eta \frac{\partial^3 u}{\partial t \partial x^2}, \quad (1)$$

where E and η respectively are the elastic and viscous modulus; ρ denotes mass density; and $u = u(x, t)$ is the displacement field over space-time domain $\Omega = \mathcal{X} \times \mathcal{T}$ defined by intervals $x \in \mathcal{X} = [0, L]$ and $t \in \mathcal{T} = [0, T]$.

This model (1) together with suitable boundary and initial conditions constitute the strong formulation of viscoelastic wave propagation in one dimension.

The exact solution to (1) can be approximated by $u^h(x, t)$ as

$$u(x, t) \approx u^h = \mathbf{N} \cdot \Phi, \quad (2)$$

where superscript h signifies characteristic length in the finite element mesh over the spatial domain \mathcal{X} . \mathbf{N} is the row vector of the approximating shape functions and Φ represents the degrees of freedom vector 4. This approximation leads to the residual function

$$R(u) = \rho \frac{\partial u^2}{\partial t^2} - E \frac{\partial u^2}{\partial x^2} - \eta \frac{\partial u^3}{\partial t \partial x^2}, \quad (3)$$

which is subsequently utilized to develop variation-based integral statements that can be used to determine Φ in (2).

Next, two different integral-based computational frameworks, namely the space-time coupled least squares and the space-time decoupled Galerkin are generated for (3). Numerical experiments are then conducted to compare computational errors and convergence rates in each of the frameworks.

Viscoacoustic seismic modeling is much cheaper, but at the tradeoff of using incomplete physics. The algorithm contains two viscoacoustic forward modeling steps; the first is the same as the traditional viscoacoustic modeling, while the second propagation is generated using a residual error source, which is derived by comparing the viscoacoustic and viscoelastic wave equations in the form of stress-particle velocity formulations. The corrected P -wave particle velocities can be obtained by adding the wavefield from the second simulation step to the original (the first simulation step) viscoacoustic wavefield. Only P waves are modeled. The overall cost is about twice that of viscoacoustic modeling, but it is significantly less than a viscoelastic propagation, because there are fewer calculations, and we can use a coarser grid and larger time steps for the same accuracy [32].

2.1. Space-Time Coupled Least Squares Formulation.

Solutions from space-time coupled least squares formulation (cLs) are a linear combination of two dimensional shape functions formed over $(x - t)$ space; i.e. $u(x, t) = \mathbf{N}(x, t) \cdot \Phi$. The least square error functional is defined as

$$\mathcal{J} = \int R^2(u) d\Omega, \quad (4)$$

which is bounded, nonnegative, and quadratic by construction. First variation of \mathcal{J} yields the least squares minimization statement.

$$\delta \mathcal{J} = \int_{\mathcal{T}} \int_{\mathcal{X}} \mathbf{Q}^T \mathbf{Q} A dx dt \cdot \Phi = 0, \quad (5)$$

where

$$\mathbf{Q} = \left(\rho \frac{\partial^2}{\partial t^2} - E \frac{\partial^2}{\partial x^2} - \eta \frac{\partial^3}{\partial t \partial x^2} \right) \mathbf{N}. \quad (6)$$

Solution vector Φ that satisfies the minimization statement given in (5) is the best approximation to u that may be found in solution space spanned by basis $\mathbf{N}(x, t)$.

Note that the least squares weak form, (5), requires global continuity of \mathcal{C}^1 over both space and time computational domains. In all computations carried out here, space-time elements are constructed from tensor product of two cubic ordered \mathcal{C}^1 elements [33].

The representation of viscoelastic media in the time domain becomes more challenging with greater bandwidth of the propagating waves and number of travelled wavelengths. With the continuously increasing computational

power, more extreme parameter regimes become accessible, which requires the reassessment and improvement of the standard memory variable methods to implement attenuation in time-domain seismic wave propagation methods [34].

2.2. Space-Time Decoupled Galerkin Formulation. Space-time decoupled Galerkin formulation (*dGa*) is the most commonly used computational framework in study of viscoelastic vibrations. The space-time decoupled Galerkin weak form of (1) can be derived by letting $u(x, t) = \mathbf{N}(x) \cdot \Phi(t)$, leading to a set of time dependent ordinary differential equations, i.e.,

$$\left(\mathbf{M} \frac{d^2}{dt^2} + \mathbf{C} \frac{d}{dt} + \mathbf{K} \right) \cdot \Phi = \mathbf{0}, \quad (7)$$

where $\mathbf{M} = \int_x \rho \mathbf{N}^T \mathbf{N} A dx$ is the mass matrix, $\mathbf{C} = \int_x \eta d\mathbf{N}^T / dx d\mathbf{N} / dx A dx$ is the damping matrix, and $\mathbf{K} = \int_x E d\mathbf{N}^T / dx d\mathbf{N} / dx A dx$ is the stiffness matrix.

The highest order of derivative appearing in the definition of each coefficient matrix is unity; hence, utilization of linear C^0 finite elements provides the minimum global continuity requirement in *dGa* computations.

The set of linear ordinary differential equations in (7) is evolved through time using the unconditionally-stable Newmark- β integration. The method assumes linear acceleration profile; i.e., the displacement is cubic in time. This order of interpolation in time is equivalent to the cubic distribution employed in approximation of displacement in temporal direction. However, in the *cLs* framework, continuity of displacement and velocity are strictly enforced, whereas in the Newmark method continuity of displacement and velocity are controlled by a shift in continuity of velocity defined as averaged acceleration across the time-increment.

3. Numerical Experiments

In studying the computational characteristics of *dGa* and *cLs*, dynamic response predictions made by the weak forms (7) and (5) of (1) are compared to exact solution. Test cases are designed to allow for separate studies in connection with dispersive and diffusive numerical errors. Errors in displacement and stress distributions over the first few cycles of wave reflection and propagation are measured; and are utilized to identify convergence characteristics of each computational framework.

3.1. Evaluation Tools. For evaluating the merits and drawbacks of each formulation, means of convergence and measurement of numerical error are defined as follows.

3.1.1. Error Measurement. Since the exact solutions are available in all case studies, relative error is measured using $\%Error = 100 \times \sum_i D_i / \sum_i E_i$ where $D_i = \Delta_i (d_i + d_{i+1}) / 2$ is the weighted average difference and $E_i = \Delta_i (e_i + e_{i+1}) / 2$ is the weighted average exact value. Here, $d_i = |a_i - e_i|$, a_i is the

approximate value, and e_i is the exact value at the i^{th} time point of time segment Δ_i .

3.1.2. *h*-Convergence. In any finite element computational process, errors can be reduced by increasing the number of approximating elements (*mesh refinement*), i.e., *h*-Convergence. In studies conducted here uniform spatial meshing is employed, i.e., a uniform mesh of n elements is defined over the spatial domain of length L with $h = L/n$. In all *dGa* studies, n is taken from the set \mathbb{N}_{Ga} and in *cLs* studies from the set \mathbb{N}_{Ls} , where

$$\mathbb{N}_{Ga} = \{12, 24, 48, 96, 192, 384\}, \quad (8)$$

$$\mathbb{N}_{Ls} = \{12, 24, 48\}. \quad (9)$$

Note that the sequence uses a growth factor of 2. Hence, the characteristic length h is halved in each refinement.

3.1.3. *R*-Convergence. It is also possible to reduce numerical error using smaller time increments, or *R*-refinement. Here, time increment Δt is kept constant and it is set equal to a fraction of the reference time increment $\hat{\Delta}t$; i.e., $\Delta t = \hat{\Delta}t/R$; where, $\hat{\Delta}t = h/c$ and $c = \sqrt{E/\rho}$ is the axial stress wave propagation speed in domain Ω with zero damping. Defining mesh speed as the ratio of characteristic length to time-increment's size, i.e., $\mathcal{V} = h/\Delta t$, R may be regarded as the ratio of mesh speed to the stress wave speed, i.e., $R = \mathcal{V}/c$.

In *dGa* studies, *R*-convergence is applied by halving time increment's duration, starting with $R = 1$; which in turn doubles the number of time steps required for evolving the solution over the specified time span, \mathcal{T} . In *cLs* studies values of $R < 1$ are also considered for the sake of speeding the computational process.

Time increment factor, R , is selected from sets \mathbb{R}_{Ga} and \mathbb{R}_{Ls} in *dGa* and *cLs* convergence studies, respectively.

$$\mathbb{R}_{Ga} = \{1, 2, 4, 8, 16, 32\}, \quad (10)$$

$$\mathbb{R}_{Ls} = \{0.1, 0.25, 0.5, 0.75, 0.8, 0.9, 1, 2, 4\}. \quad (11)$$

Note that \mathbb{R}_{Ga} sequence has a growth factor of 2; i.e., in *dGa* *R*-convergence studies time increment is halved in each refinement, with $\Delta t = \hat{\Delta}t/32$ being the smallest time increment. Also note that \mathbb{R}_{Ls} set contains values less than unity as well. For $R < 1$ mesh speed is less than stress wave's speed, i.e., $\mathcal{V} < c$. This allows for larger time increments to be taken; which translates to fewer number of evolution steps needed to reach a given final time.

3.1.4. *p*-Convergence. Minimum polynomial order required by *dGa* weak form (7) is unity with C^0 global continuity; and for *cLs* weak form (5), a bicubic polynomial with C^1 continuity in both space and time is the minimum requirement. Possibility of reducing the approximation error through polynomial-order increase or *p*-convergence is also investigated here.

Finite elements used here are Lagrange-based hierarchical elements [33].

3.1.5. τ -Convergence. In particular, since the coupled formulation allows for temporal discretization as well as the usual spatial discretization over each time slab (*space-time domain over a time increment*), possibility of reducing the error through temporal meshing or τ -convergence is also investigated for the least squares formulation. Here, the computational domain is meshed over the time increment, where three cases are considered by dividing Δt to $\{1, 2, 4\}$ divisions.

3.2. Test Models. In general, numerical errors have dispersive and diffusive (dissipative) characteristics [31]. Each of the two test models employed here exhibits dominance of one type of numerical error. The first test case, Impact (*Imp.*), simulates the response of a relatively stiff medium to

a constant load, where dispersive numerical error is dominant. Diffusive error is dominant in the second test case, Base-motion (*Bms.*), which simulates response of a relatively flexible medium to an imposed harmonic displacement boundary condition. Relative stiffness in each case refers to stress wave speed; which is 1000m/s for *Imp.* and it is 60m/s for base motion case. Errors are measured using the computed displacement u or stress $\sigma = E\epsilon = E\partial u/\partial x$ where ϵ is the strain field.

3.2.1. Impact: Model Specifications. The medium considered is a rod of unit area and unit length. Mass density and elastic modulus are $\rho = 1000\text{ kg/m}^3$ and $E = 1\text{ GPa}$, respectively; hence, the wave speed in this model $c = 1000\text{ m/s}$. The rod is fixed at $x = 0$ and loaded with point load $P = 1$ at $x = 1$ for $0 \leq t \leq T$.

Closed form solution to (1) based on conditions stated here will be

$$u(x, t) = \sum_{n=1,3,\dots} \frac{2e^{-\beta} L \hat{\epsilon} (m \cos(m/2) - 2 \sin(m/2)) \sin(mz/2L) (e^\gamma \lambda + \lambda + (e^\gamma - 1) \eta m n)}{m^2 \sqrt{n^2 (\eta^2 m^2 - 16EL^2 \rho)}} + z \hat{\epsilon}, \quad (12)$$

where $\hat{\epsilon}$ is the applied strain at the loaded end and

$$\begin{cases} \beta = \frac{\pi t (\lambda + \eta m n)}{8L^2 \rho} & \gamma = \frac{\pi \lambda t}{4L^2 \rho}, \\ m = n\pi & \lambda = \sqrt{\pi^2 \eta^2 n^4 - 16EL^2 n^2 \rho}. \end{cases} \quad (13)$$

3.2.2. Site Response Model: Model Specifications. In seismic numerical simulations of wave propagation, it is very important for us to consider surface topography and attenuation, which both have large effects (e.g., wave diffractions, conversion, amplitude/phase change) on seismic imaging and inversion. An irregular free surface provides significant information for interpreting the characteristics of seismic wave propagation in areas with rugged or rapidly varying

topography, and viscoelastic media are a better representation of the earth's properties than acoustic/elastic media [35].

In this model, $L = 10\text{m}$, elastic modulus $E = 7.5\text{ MPa}$, and weight density $\rho g = 20\text{kN/m}^3$, where $g = 9.81\text{m/s}^2$. The model is at rest prior to imposition of harmonic displacement at $x = 0$. Boundary and initial conditions can be stated as, $u(0, t) = A \sin(\omega t)$ and $\partial u/\partial x(L, t) = u(x, 0) = \partial u/\partial t(x, 0) = 0$. The displacement condition $u(0, t)$ has amplitude of $A = 0.01\text{ m}$ and frequency of $\omega = 2\pi f$, with $f = 10\text{ Hz}$. Furthermore, since C^1 finite elements are employed in studying (5), the stress free boundary condition $\partial u/\partial x|_{(x=L,t)} = 0$ is imposed explicitly; a feature that is not available in computations based on the C^0 -dGa formulation. A closed form solution of (1) subjected to boundary and initial conditions stated here, may be found through separation of variables technique, yielding

$$u(z, t) = A \sin(\omega t) + \sum_{n=1,3,\dots} \frac{4\alpha A ((-1)^n - 1) \sin(mz/2L) e^{-\beta}}{\lambda m (E^2 m^4 - 8\alpha E m^2 \omega + \omega^2 (16\alpha^2 + \eta^2 m^4))} \left(\begin{array}{l} me^\gamma (2E^2 m^2 n + \omega^2 (\eta m (\eta m n - \lambda) - 8EL^2 n \rho)) \\ -2E^2 m^3 n + 2\lambda \omega e^\beta (\sin(\omega t) (4\alpha \omega - E m^2) + \eta m^2 \omega \cos(\omega t)) - m \omega^2 (\eta m (\lambda + \eta m n) - 8EL^2 n \rho) \end{array} \right), \quad (14)$$

where $\alpha = L^2 \rho \omega$ and the remaining parameters are as defined in (13).

3.2.3. Damping Ratio. All studies are carried out by considering damping ratio $\xi = \eta/\eta_c$, where critical damping for a homogeneous axial rod is

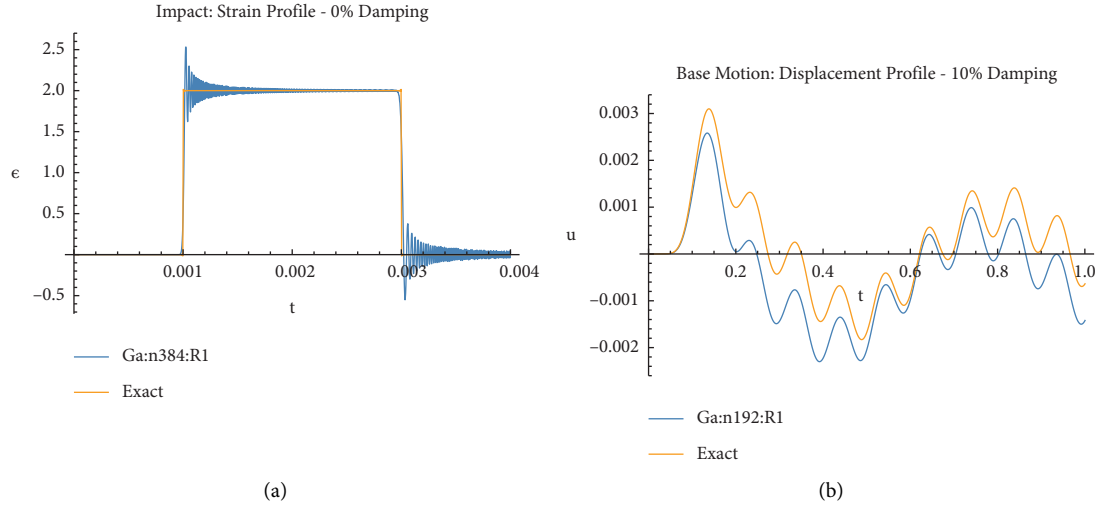


FIGURE 1: Solution profiles for impact and base-motion test cases. (a) *Imp.* strain profile at the boundary. (b) *Bms.* displacement profile at the free end.

$$\eta_c = \frac{4\sqrt{\rho EL}}{\pi}. \quad (15)$$

Values of ξ considered here are $\xi \in \{0.01, 0.1, 0.5, 1.0\}$.

3.2.4. Solution Characteristics and Profiles. In definition of the impact problem (*Imp.*), a constant force is applied at the free end of a relatively stiff rod, producing a constant-stress wave which reflects from the fixed boundary and interacts with the incoming imposed wave. The result is an oscillating rectangular wave with sharp temporal gradient, the sharpness of which depends on the amount physical damping present in the system. Numerical simulation of undamped impact case [31] shows that the dominant error is dispersive in nature and it is most significant at the fixed boundary, as shown in Figure 1(a). Fictitious oscillations observed here decrease naturally with increase in system damping; i.e., depending on amount of damping present in the system, the square profile of the stress wave will assume smoother corners, thereby reducing the oscillatory overshoots. In definition of the base motion (*Bms.*) test case, medium is relatively flexible and low frequency harmonic displacement is imposed at the base of a long rod. The overall motion is harmonic with smooth gradients in time. In this setup, the dominant numerical error is of diffusive nature; and it increases with increase in system's damping. Figure 1 shows the diffused profile of computed displacement from a study using 384-element mesh with $R = 1$.

In general, numerical error from any computational model is a combination of both diffusive and dispersive types. Convergence characteristics and computational time of both formulations for each dominant error type are examined next.

3.3. *h*- and *R*-Convergence. As noted earlier, the dominant numerical error is of dispersive type in case of impact and of diffusive type in case of base-motion disturbance. Numerical studies indicate that regardless of the framework employed, increasing damping has contradictory effects on dispersive

and diffusive errors. For impact loading, note from Figure 2 that, given the same computational resources, errors are much smaller in cases that have higher damping values.

Note that physical viscosity reduces dispersive error; this is because the sharp corners of the rectangular pulse in undamped case, shown in Figure 1(a), which are responsible for solution dispersion, are smoothed in direct proportion to physical damping present in the system, hence reducing the dispersion. On the other hand, since viscosity is diffusive in nature, it increases the numerical error of diffusive type; i.e., given the same computational resources, in the case of base-motion disturbance, where diffusive-type numerical error is dominant, increase in damping increases the computational error (Figure 3).

Comparing *cLs* and *dGa* *h*-curves in sub-figures of Figures 2 and 3 shows a difference of at least an order of magnitude in numerical error. The *R*-convergence curves demonstrate that *dGa* solutions can be improved upon when smaller time increments are employed; however, as can be noted from Figures 2(a) and 3(a) for *dGa:n12* curves, insufficient spatial meshing, and, as will be shown later, insufficient global continuity inhibit the *R*-convergence process.

3.3.1. *h*- and *R*-Convergence Rates. Effectiveness of *h* and *R* refinements can be assessed by measuring the rate at which such refinements reduce the computational error. *h*-convergence rates based on mesh refinements defined in (8) and (9) are computed by comparing the ratio of errors from two consecutive refinements to the ratio of their corresponding degrees of freedom. Similarly, in computing *R*-convergence rates, in accordance to (10) and (11), the ratio of numerical errors from two *R*-refinements is compared to the ratio of corresponding *R*-values. It is found that except for the computed stresses in *Bms.* case, rate of *h*-convergence for all other cases is at most linear in *dGa* and at most quadratic in *cLs* frameworks; i.e., by halving *h* the accuracy will at most double in *dGa* and quadruple in *cLs* computations. Furthermore, *R*-convergence rate in *dGa* studies is also at most linear; i.e., halving time increment's size will at

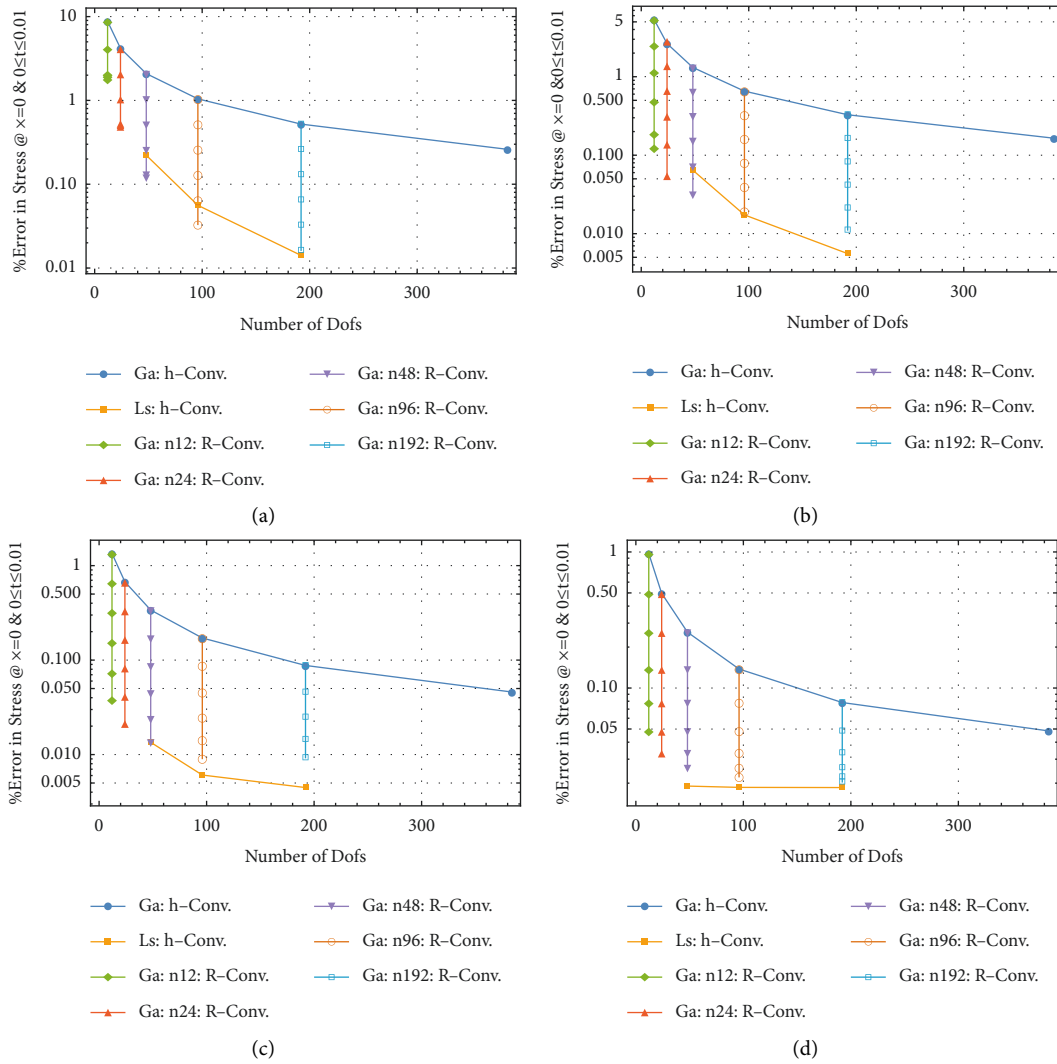


FIGURE 2: Decrease in computational errors with increase in damping ratio for *Imp.* disturbance. (a) *Imp.* stress convergence, $\xi = 0.01$. (b) *Imp.* stress convergence, $\xi = 0.1$. (c) *Imp.* stress convergence, $\xi = 0.5$. (d) *Imp.* stress convergence, $\xi = 1$.

most double the accuracy. *R*-convergence in *cLs* framework will be discussed separately. For all *Imp.* studies presented in Figure 2 except the critical damping case (2d) the convergence rate varies between 3.3 and 4.4 for *cLs* and between 1.3 and 2 for *dGa* cases. Errors in *Bms.* studies are high and difficult to reduce. Uniform mesh refinements and time increment reduction seem to yield at most a linear convergence rate in both *dGa* and *cLs* studies. A closer look at the solution reveals the error's source in each case (Figure 4).

As can be seen from Figure 4(a), the error in *cLs* computations is confined to the starting cycle, which disappears quickly as time passes. This error is due to inconsistency between the zero initial velocity and the nonzero velocity condition at time zero coming from the imposition of displacement function $A \sin(\omega t)$ at $x = 0$. Since the error is spatially and temporally confined, uniform space-time mesh refinement is not the best approach for removing this error; a simple mesh grading that refines the region close to the disturbed boundary resolves the issue, as shown in Figure 5(a). Considering *dGa* test cases presented in

Figure 3, the nonconvergent *h*-refinement at $R = 1$ would have actually diverged if the unconditionally stable Newmark- β method was not employed for evolving the solution. Source of this error in *dGa* simulation is due to lack of boundary conditions at the free end. Figure 4(b) displays the violation of free-stress condition at $x = L$; which increases with mesh refinement. Error plots also indicate that using higher values of R , i.e., smaller time increments along with sufficient spatial meshing reduce the errors significantly, as shown in Figure 3. However, the fictitious strain profiles shown in Figure 4(b) can be suppressed if similar to *cLs* computations; C^1 finite elements are employed in *dGa* study of this ill posed problem. Figure 5(b) shows the *h*- and *R*-convergence curves from *dGa*: C^1 computations and *h*-convergence curves from *dGa*: C^0 and *cLs*: C^1 computations. Among test cases considered here, *Bms.* has shown the slowest rates of convergence, especially in *cLs* computations. However, comparing Figures 3(b) and 5(b) clearly shows that imposition of stress-free condition yields convergence rates that are consistent with other *dGa* studies.

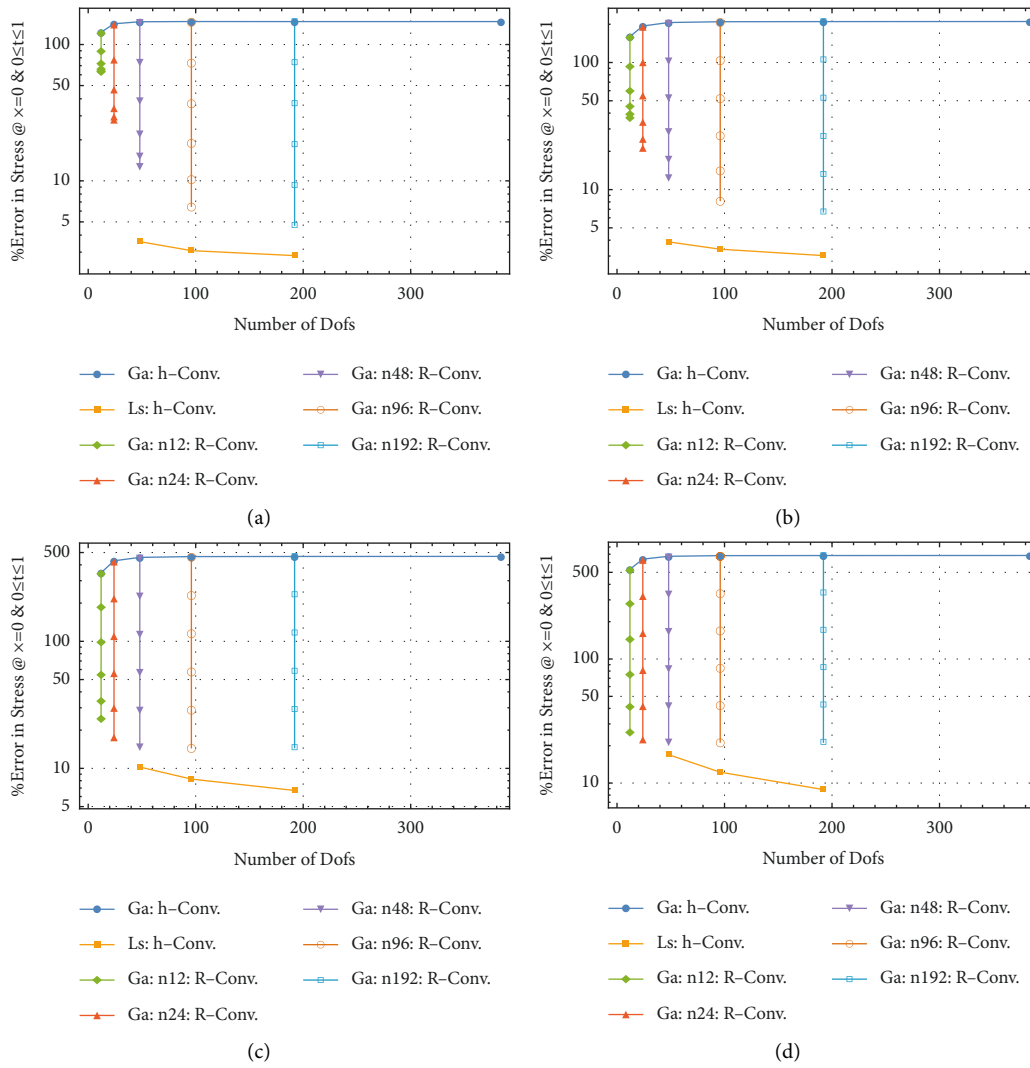


FIGURE 3: Increase in computational errors with increase in damping ratio for *Bms.* disturbance. (a) *Bms.* stress convergence, $\xi = 0.01$. (b) *Bms.* stress convergence, $\xi = 0.1$. (c) *Bms.* stress convergence, $\xi = 0.5$. (d) *Bms.* stress convergence, $\xi = 1$.

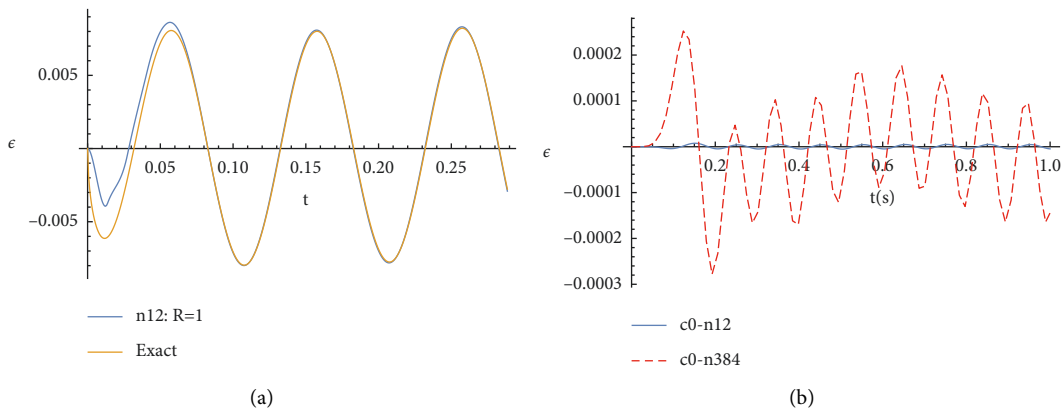


FIGURE 4: *Bms.* strain profiles: sources of inconsistent convergence, as shown in Figures 3(a) and 3(b). (a) *cLs* computed strain at $x = 0$. (b) *dGa* fictitious strain at free boundary $x = L$.

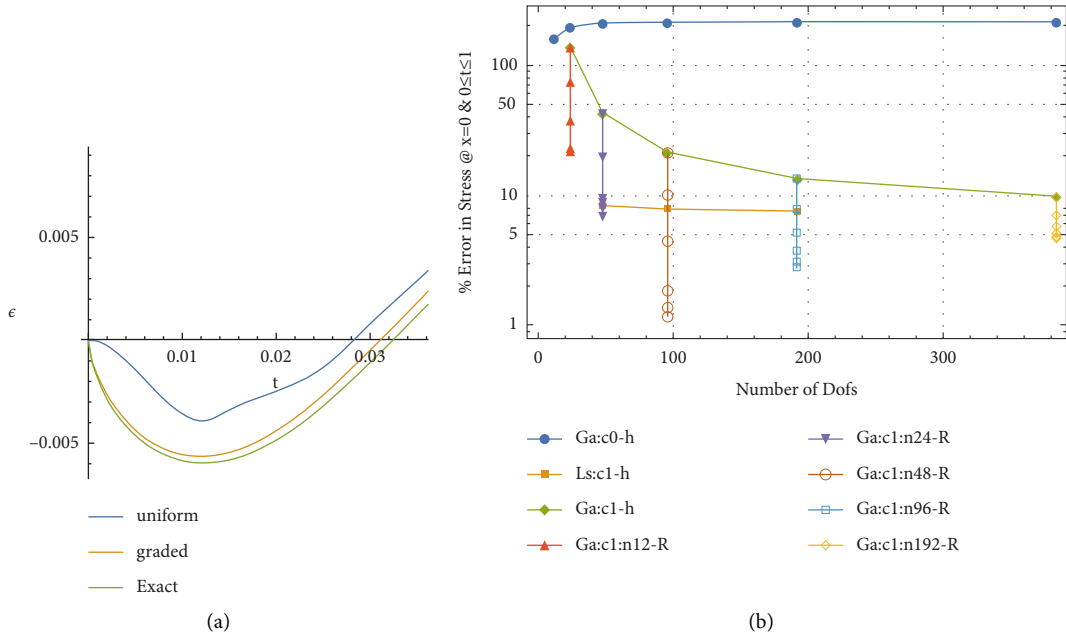


FIGURE 5: *Bms.* Effects of non-uniform meshing and C^1 elements on convergence— $\xi = 0.1$. (a) *cLs*: n12: *R1* strain profile. (b) *dGa*: C^1 and C^0h - and *R*-convergence of stress.

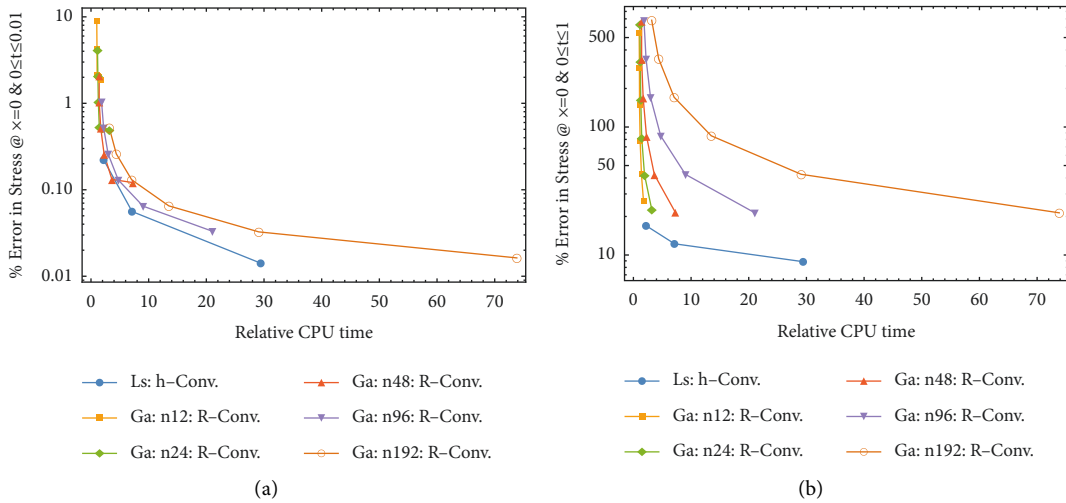


FIGURE 6: Error versus relative CPU time. (a) *Imp.* stress convergence, $\xi = 0.01$. (b) *Bms.* stress convergence, $\xi = 1$.

Furthermore, using C^1 elements, the errors are pushed down significantly through *R*-refinement.

3.3.2. *CPU Usage.* The two formulations of *cLs* and *dGa* studied here pass through different sets of computational steps; a meaningful comparison of the two would be accuracy versus cost; with cost being the CPU time used in each study. Furthermore, since highest errors in *Imp.* studies occur at lower damping and in *Bms.* studies at higher damping values, two representative graphs, one for *Imp.* and one for *Bms.*, are presented in Figure 6. Each *dGa* curve shows the relative computational time spent in each *R*-convergence study and the *cLs* *h*-convergence study.

It can be noted that *cLs* produces least error for least amount of CPU used, regardless of the error type.

3.4. *p*-Convergence. Minimum polynomial order required by *dGa* formulation is one and for *cLs*, it is three. Increasing *p* is known to increase computational accuracy in boundary value problems. In studies conducted here, increasing *p* in spatial interpolation is found to affect *R*-convergence of stress away from the reflecting boundary in *dGa* case, which could also be realized at lower number of degrees of freedom if C^1 elements are used.

Comparison of Figures 7(a) and 7(b) to Figure 2(a) shows that error in stresses computed away from the reflecting boundary cannot be reduced through *R*-refinement; i.e., reducing time increment's size does not reduce the error. However, this issue can be remedied by increasing the order of polynomial, *p*, from one to three, as shown in Figure 8(a) or simply using C^1 finite elements at *p* = 3, which requires less *Dofs* for the same accuracy, as shown in Figure 8(b).

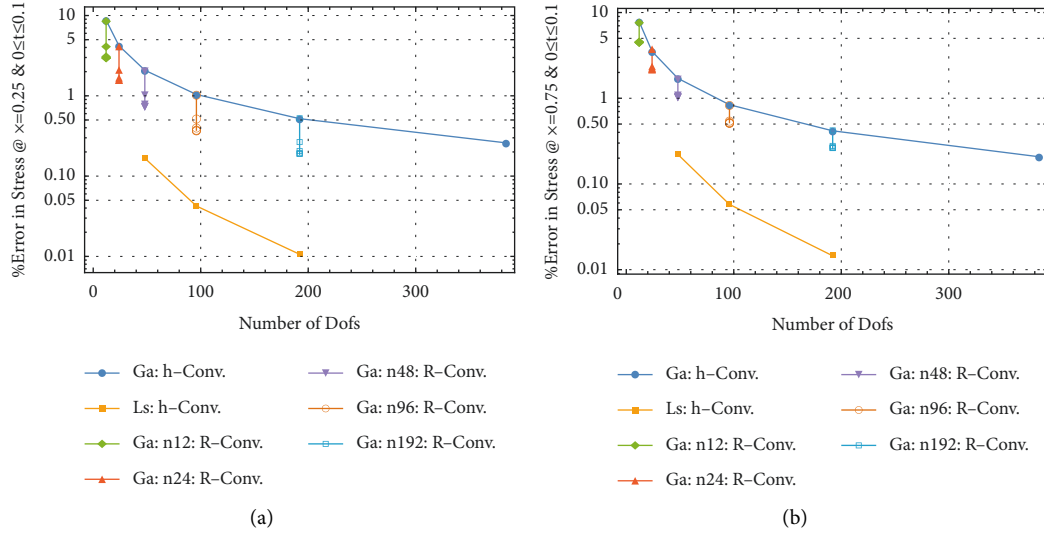


FIGURE 7: *Imp.* stress convergence at points away from boundaries: C^0 - $p = 1$, $\xi = 0.01$. (a) *Imp.* H - and R -stress convergence @ $x = 0.25$. (b) *Imp.* H - and R -stress convergence @ $x = 0.75$.

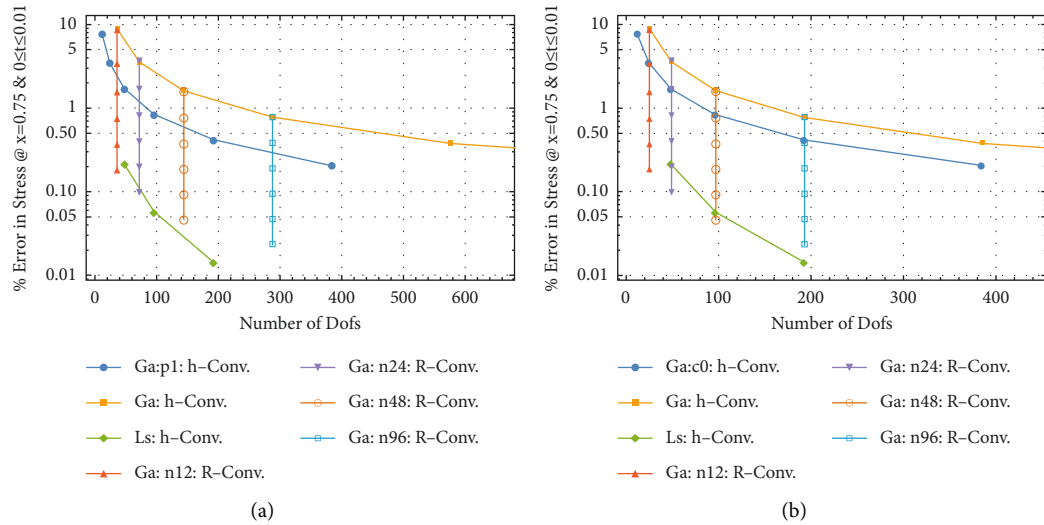


FIGURE 8: *Imp.* improved R -convergence of stress at $x = 0.75$ and $\xi = 0.01$. (a) *Imp.* H - and R -stress convergence: C^0 - $p = 3$. (b) *Imp.* H - and R -stress convergence: C^1 - $p = 3$.

In cLs studies, increasing p in space does not change the error present in computations, regardless of space-time meshing used. However, increasing p in time's direction can make the evolution divergent. The issue is best demonstrated by Figure 9. Here, for $R = 0.1$, i.e., large time increment of $\Delta t = 10\hat{\Delta}t$, the cLs : h -convergence curve shows hyperconvergence, whereas increasing p in either direction (x or t) has no benefit to the process and in fact can cause divergence in case of crude spatial meshing when polynomial's order is increased in time.

3.5. R - and τ -Convergence in cLs Framework. In the space-time least squares process duration of each time increment is equal to the space-time slab's size in temporal direction. Duration of the time increment Δt is controlled by R , i.e.,

$\Delta t = \hat{\Delta}t/R$. When $R = 1$ mesh speed equals the undamped wave speed; and in dGa studies, solutions were found to improve for $R > 1$, i.e., finer meshing in time. Obviously when $R < 1$, the error increases and h -convergence in dGa would have higher error compared to $R = 1$ curve. However, the coupled nature of space and time in cLs formulation allows for hyper- h -convergence to take place for large time steps.

Furthermore, since over each time increment the space-time slab can be meshed in the temporal direction, a series of studies into benefits of temporal meshing are also presented. Here, Δt is meshed uniformly to study τ -convergence in cLs formulation.

3.5.1. R -Convergence. Based on R -values listed in (11), cLs : R -convergence for both test cases was investigated. Figure 10

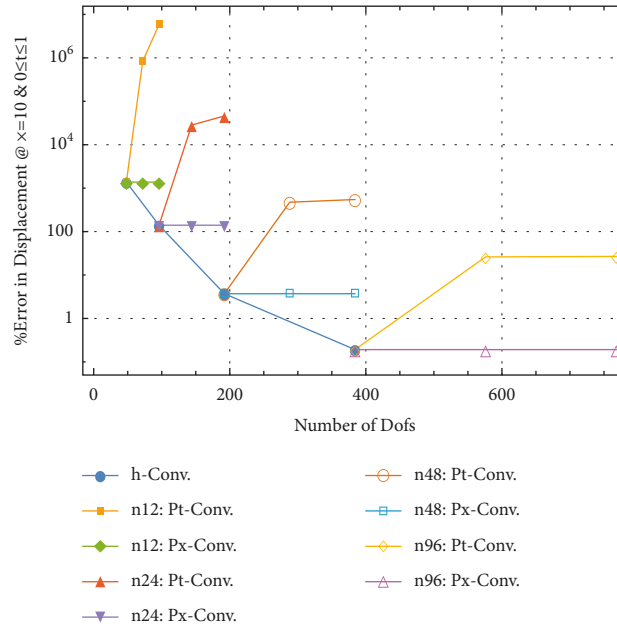


FIGURE 9: *Bms.* cLs p -convergence in space and time, $R = 0.1$ and $\xi = 0.1$.

indicates that for values of $R > 1$, i.e., smaller time increments, little if any improvement is seen for the extra computational effort spent in stepping through the extra number of time increments. This is in contrast to R -convergence in the dGa -framework, which shows linear rate of convergence in most cases.

An important point to note here is that errors in computations with values of R close to one are almost the same as those computed using $R = 1$. Also, note that for $R = 0.1$ significant error exists when crude spatial-mesh is employed, however, h -convergence shows hyper-rates that reduce the error quickly. Convergent process for $R < 1$ is a significant characteristic of cLs framework since it reduces the computational cost significantly by taking large time increments. Convergence for $R < 1$ is not necessarily monotonic, as shown in Figures 10(a) and 10(c), but for the significantly low value of $R = 0.1$ h -convergence is monotonic and hyper and requires ten times less number of evolution steps as compared to Dof -equivalent $R = 1$ computations.

3.5.2. τ -Convergence. Over the space-time domain, h -refinement means increasing the number of divisions in spatial direction. Similarly, τ -refinement implies an increase in the number of divisions in temporal direction over a given time slab with Δt duration. Three uniform temporal divisions of $\tau \in \Delta t / \{1, 2, 4\}$ were considered for τ -convergence study.

As can be observed from Figure 11(a), τ -refinement does not improve the solution if $R = 1$. For $R < 1$, the τ -refinement shows hyper-convergence in improving a crude solution, as shown in Figure 11(b). However, note that τ -refinement applied to spatial meshes with $R = 0.1$ cannot improve the solution beyond the accuracy offered by $R = 1$ for the same spatial meshing. Therefore, τ -refinement does not offer any advantage in cLs framework; in fact, far more

resources would be needed when more than one division is used in temporal direction of space-time slab.

4. Discussion

Accurate simulation wave propagation through media is an important issue. Test cases simulating impact (*Imp.*) and base motion (*Bms.*), with respective dominance in dispersive and diffusive error types, were employed to investigate convergence characteristics of dGa and cLs weak formulations of damped wave (1). To this end, standard refinements were applied and numerical errors were plotted against the degrees of freedom (*Dofs*) used by refined models. Furthermore, since dGa and cLs pass through completely different sets of computational steps, graphs of error versus total CPU time were also generated. Based on these studies, several general remarks can be made with regard to accuracy and convergence characteristics of cLs and dGa computational frameworks.

Depending on the numerical error type, being dispersive or diffusive, mechanical damping present in the system affects computational accuracy differently. Dispersive errors are higher for lower damping values and diffusive errors are higher for higher damping values. This characteristic is true for both dGa and cLs.

The *Bms.* problem is ill posed in dGa - C^0 framework as shown in Figures 3 and 4(b); employment of C^1 finite elements removes the issue and increases the accuracy in dGa - R convergence significantly as shown in Figures 5(b) and 8. Rate of h -convergence is at most linear for dGa and at most quadratic for cLs. A quadratic rate predicted by [23] can not be realized in dGa because of its decoupled constitution. Rate of R -convergence is at most linear for dGa and is hyper h -convergence for small values of R in cLs framework.

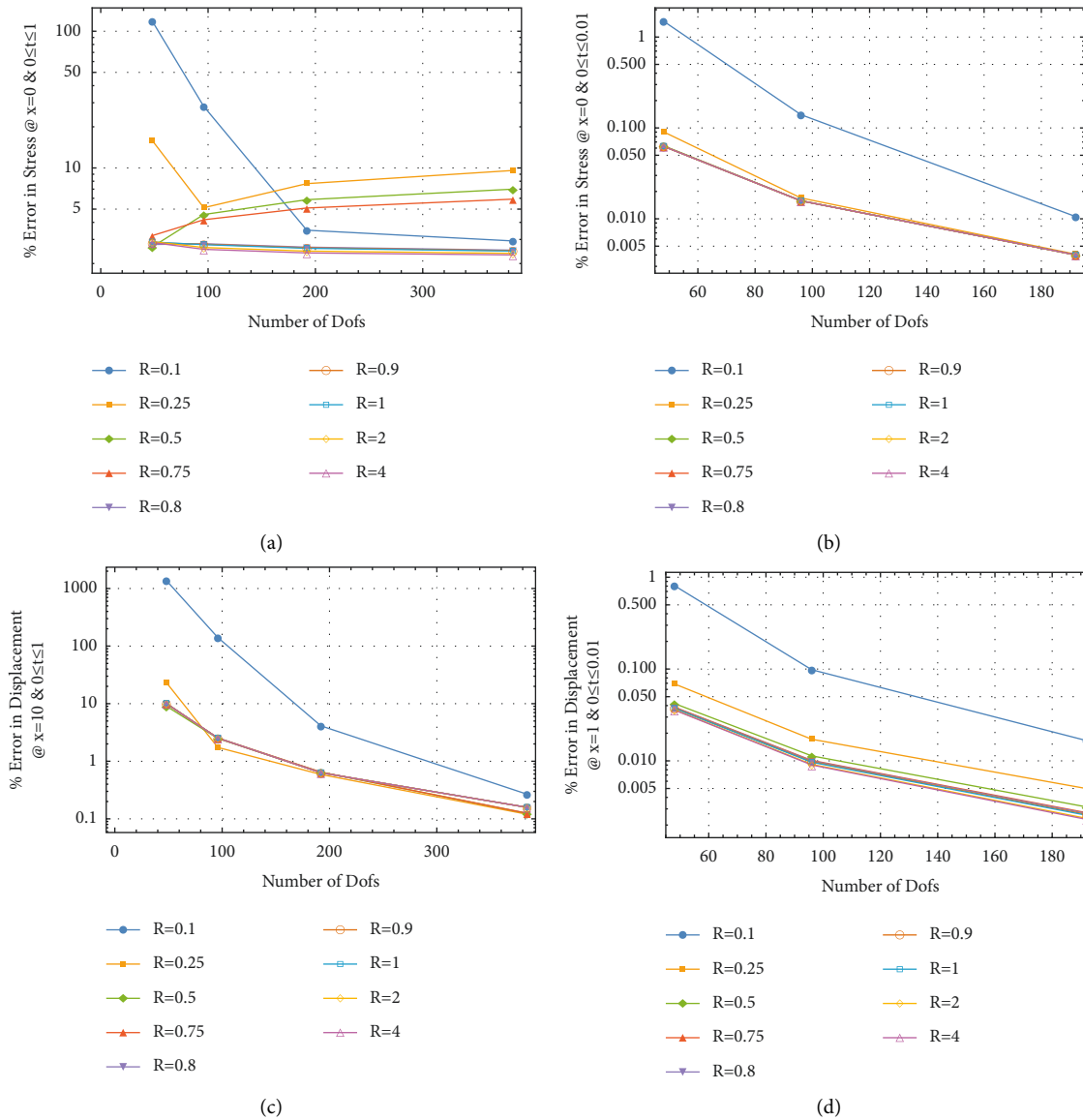


FIGURE 10: cLs R -convergence of stress and displacement for *Bms.* and *Imp.*— $\xi = 0.1$. (a) *Bms.* R -stress convergence. (b) *Imp.* R -stress convergence. (c) *Bms.* R -displacement convergence. (d) *Imp.* R -displacement convergence.

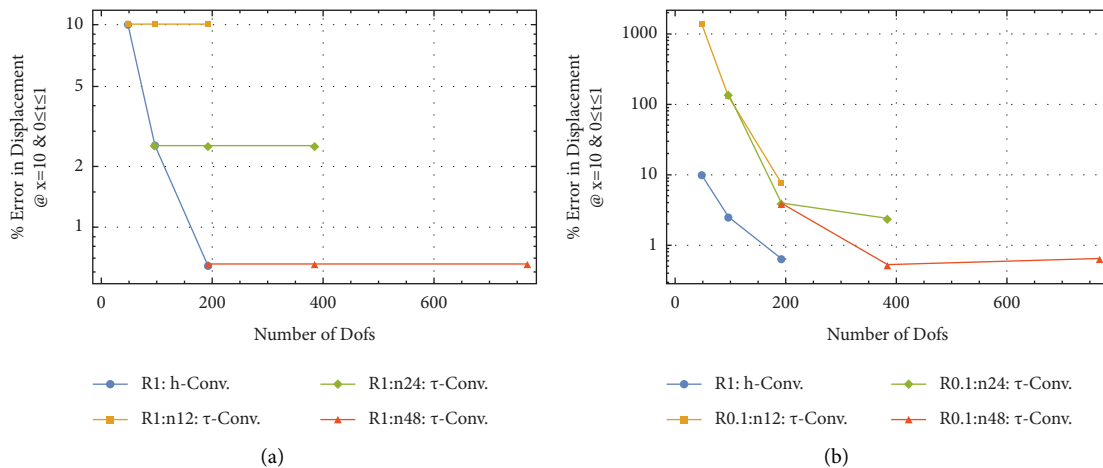


FIGURE 11: *Bms.* cLs: h - and τ -displacement convergence— $\xi = 0.1$. (a) τ -convergence at $R=1$. (b) τ -convergence at $R=0.1$.

5. Conclusions

Even though space-time coupled framework has been promoted by different researchers, the extra dimension of the computational domain makes it unappealing and hence not commonly utilized in study of real world problems. The focus of this research has been to investigate the computational characteristics of cLs and compare them to those of dGa for viscoelastic wave (1). The first is the space-time coupled least squares (cLs) formulation, which was recently employed for solving the undamped wave equation [31]. The second is the widely utilized space-time decoupled Galerkin (dGa) formulation along with the unconditionally stable Newmark- β method. Comparisons were made based on accuracy versus *Dofs* as well as accuracy versus CPU time spent. Two test cases, each susceptible to a particular type of numerical error, i.e., dispersive or diffusive, were studied and some general conclusions on computational characteristics of the methods were made.

R -convergence in cLs has little or no effect for R values around one and $R > 1$; however, for small values, e.g., for $R = 0.1$ for which the time increments are ten times larger, h -convergence is of high rate and stable Figure 10. It was established that for $R = 1$ numerical errors from dGa computations are in general one to two orders of magnitude larger than error in cLs results for the same number of *Dofs*, as shown in Figures 2 and 3. Results from dGa studies require significantly smaller time increments, e.g., $R = 32$, yields comparable accuracy to cLs at $R = 1$. Convergence rate is not the same for all spatial points; this was seen in *Imp.* problem where increasing R has no effect in lowering error in stress profile predicted by dGa at points away from the reflecting boundary, as shown in Figure 7. p -convergence in dGa and cLs has little to no effect on numerical accuracy, as shown in Figure 8(a). However, it has significant effect in dGa framework where R -convergence, for points away from the boundaries, was shown to be inhibited when $p = 1$. In the cLs framework, increasing p from its minimum value of three in the spatial direction has no effect on accuracy. However, increasing p in temporal direction makes the evolutionary process divergent as shown in Figure 9. τ -convergence in cLs, where space-time slabs are refined in temporal direction, shows no improvement on computational accuracy as shown in Figures 11(a) and 11(b). CPU time used by each framework while improving computational accuracy was constructed for cases with highest numerical error. Comparison shows cLs requires less time than dGa to reach a certain level of accuracy.

It was found that mechanisms which allow for refinements over the coupled domain in cLs are not necessarily beneficial to the process; e.g., τ refinement where time increment Δt is meshed was shown to be counterproductive as shown in Figure 11. Also contrary to dGa, where reducing Δt (or increasing R) can reduce the error at a linear rate, cLs shows negligible gain in accuracy for $R > 1$, as shown in Figure 10, hence rendering the process costly.

Convergence rates were found to be at most linear in dGa formulation from the h - and R -convergence studies. This rate does not change with higher p -level or higher global

continuity; however, employment of C^1 elements was found to be essential in applying free end condition in base-motion test case. Except for a meshing issue in study of *Bms.* case, h -convergence rates in cLs studies were at most quadratic for $R = 1$. While taking smaller time increments, i.e., $R > 1$ was found to be without merit, large time steps, in particular $R = 0.1$ was found to be stable with hyper- h -convergence allowing for reasonably refined spatial mesh evolving at $R = 0.1$ to have comparable accuracy to the 10 times slower evolution of the same spatial mesh at $R = 1$. However, it should be noted that while evolution of the solution over large time increments of $R = 0.1$ appears to be stable for cases considered here, it would most likely fail if discontinuities exist, e.g., multimaterial interface.

Coefficient matrices of dGa formulation are constructed over the one-dimensional domain x ; the resulting system of equations is then evolved in time according to Δt . The cLs coefficient matrix is formed over the two-dimensional domain (x, t) which requires relatively more computational resources than dGa. However, it was observed that the extra demand by cLs is offset by the need of dGa for very small time steps; i.e., for comparable accuracy $\Delta t_{cLs} \gg \Delta t_{dGa}$, i.e., dGa requires time steps with more orders of magnitude compared to cLs to yield the same accuracy. It should be noted that, for very small time increments, round-off errors can become a significant source of error. In continuation of this work, nonlinear models are considered.

Data Availability

Requests for access to these data should be made to the corresponding author at amin.saffarian@eng.uk.ac.ir.

Conflicts of Interest

The authors declare that there are no conflicts of interest regarding the publication of this paper.

References

- [1] C. Wu, H. Wang, J. Zhao, X. Jiang, Q. Yanjun, and B. Yusupo, "Prediction of viscoelastic pavement responses under moving load and nonuniform tire contact stresses using 2.5-d finite element method," *Mathematical Problems in Engineering*, vol. 2020, Article ID 1029089, 2020.
- [2] S. Brunet, J. C. de la Llera, and E. Kausel, "Non-linear modeling of seismic isolation systems made of recycled tire-rubber," *Soil Dynamics and Earthquake Engineering*, vol. 85, pp. 134–145, 2016.
- [3] K. Pitilakis, S. Karapetrou, and K. Tsagdi, "Numerical investigation of the seismic response of RC buildings on soil replaced with rubber-sand mixtures," *Soil Dynamics and Earthquake Engineering*, vol. 79, pp. 237–252, 2015.
- [4] L. Gaul, "The influence of damping on waves and vibrations," *Mechanical Systems and Signal Processing*, vol. 13, no. 1, pp. 1–30, 1999.
- [5] J. Rayleigh, *Theory of Sound*, Dover Publications, New York, 1877.
- [6] Z. Liang, G. Lee, G. F. Dargush, and J. Song, "Structural damping: applications in seismic response modification,"

- Advances in Earthquake Engineering*, CRC Press, Boca Raton, FL, USA, 2011.
- [7] C. M. A. Vasques, R. A. S. Moreira, and J. D. Rodrigues, "Viscoelastic damping technologies - Part I: modeling and finite element implementation," *Journal of Advanced Research in Mechanical Engineering*, vol. 1, no. 2, pp. 76–95, 2010.
 - [8] S. Yuksel and U. Dalli, "Longitudinally vibrating elastic rods with locally and non-locally reacting viscous dampers," *Shock and Vibration*, vol. 12, no. 2, pp. 109–118, 2005.
 - [9] X. c. Zhao, Y. j. Lei, and J. p. Zhou, "Strain analysis of nonlocal viscoelastic Kelvin bar in-tension," *Applied Mathematics and Mechanics*, vol. 29, no. 1, pp. 67–74, 2008.
 - [10] J. Garcia-Barruetabena, F. Cortes, and J. M. Abete, "Dynamics of an exponentially damped solid rod: analytic solution and finite element formulations," *International Journal of Solids and Structures*, vol. 49, no. 3-4, pp. 590–598, 2012.
 - [11] M. A. Saffarian and M. H. Bagheripour, "Seismic response analysis of layered soils considering effect of surcharge mass using HFTD approach. Part I: basic formulation and linear HFTD," *Geomechanics and Engineering*, vol. 6, pp. 517–530, 2014.
 - [12] M. A. Saffarian and M. H. Bagheripour, "Seismic response analysis of layered soils considering effect of surcharge mass using HFTD approach. Part II: nonlinear HFTD and numerical examples," *Geomechanics and Engineering*, vol. 6, pp. 531–544, 2014.
 - [13] C. G. Sun and C. K. Chung, "Assessment of site effects of a shallow and wide basin using geotechnical information-based spatial characterization," *Soil Dynamics and Earthquake Engineering*, vol. 28, no. 12, pp. 1028–1044, 2008.
 - [14] O. Zienkiewicz, "A new look at the Newmark, Houbolt and other time stepping formulas: a weighted residual approach," *Earthquake Engineering & Structural Dynamics*, vol. 5, no. 4, pp. 413–418, 1977.
 - [15] H. Hilber and T. Hughes, "Collocation, dissipation and overshoot for time integration schemes in structural dynamics," *Earthquake Engineering & Structural Dynamics*, vol. 6, no. 1, pp. 99–117, 1978.
 - [16] T. Hughes, "Analysis of transient algorithms with particular reference to stability behavior," *Computational methods for transient analysis*, pp. 67–155, 1983.
 - [17] H. Hilber, T. Hughes, and R. Taylor, "Improved numerical dissipation for time integration algorithms in structural dynamics," *Earthquake Engineering & Structural Dynamics*, vol. 5, no. 3, pp. 283–292, 1977.
 - [18] B. Bell and K. Surana, "A space-time coupled p-version least-squares finite element formulation for unsteady fluid dynamics problems," *International Journal for Numerical Methods in Engineering*, vol. 37, no. 20, pp. 3545–3569, 1994.
 - [19] J. Argyris and D. Scharpf, "Finite elements in time and space," *Nuclear Engineering and Design*, vol. 10, no. 4, pp. 456–464, 1969.
 - [20] G. Hulbert and T. Hughes, "Space-Time finite element methods for second order hyperbolic equations," *Computer Methods in Applied Mechanics and Engineering*, vol. 84, no. 3, pp. 327–348, 1990.
 - [21] M. Coronado, *Finite Element Methods for Viscoelastic Fluid Flow Simulations: Formulations and Applications*, Ph.D. Thesis, RICE University, Houston, Texas, 2009.
 - [22] K. Surana, J. Reddy, and S. Allu, "The k-version of finite element method for initial value problems: mathematical and Computational Framework," *International Journal for Computational Methods in Engineering Science and Mechanics*, vol. 8, no. 3, pp. 123–136, 2007.
 - [23] J. Rauch, "On Convergence of the finite element method for the wave equation," *SIAM Journal on Numerical Analysis*, vol. 22, no. 2, pp. 245–249, 1985.
 - [24] A. Idesman, R. Niekamp, and E. Stein, "Continuous and discontinuous Galerkin methods with finite elements in space and time for parallel computing of viscoelastic deformation," *Computer Methods in Applied Mechanics and Engineering*, vol. 190, no. 8-10, pp. 1049–1063, 2000.
 - [25] H. T. Banks, M. J. Birch, M. P. Brewin et al., "High order space-time finite element schemes for acoustic and viscodynamic wave equations with temporal decoupling," *International Journal for Numerical Methods in Engineering*, vol. 98, no. 2, pp. 131–156, 2014.
 - [26] T. Werder, K. Gerdes, D. Schotzau, and C. Schwab, "hp-discontinuous Galerkin time stepping for parabolic problems," *Computer Methods in Applied Mechanics and Engineering*, vol. 190, no. 49-50, pp. 6685–6708, 2001.
 - [27] E. Grasso, *Modelling Visco-Elastic Seismic Wave Propagation: A Fast-Multipole Boundary Element Method and its Coupling with Finite Elements*, Ph.D. Thesis, Paris Est school, Paris, France, 2012.
 - [28] R. Figini, R. Paolucci, and C. Chatzigogos, "A macro-element model for non-linear soil–shallow foundation–structure interaction under seismic loads: theoretical development and experimental validation on large scale tests," *Earthquake Engineering & Structural Dynamics*, vol. 41, no. 3, pp. 475–493, 2012.
 - [29] V. Singh and K. Sangle, "Analysis of vertically oriented coupled shear wall interconnected with coupling beams," *HighTech and Innovation Journal*, vol. 3, no. 2, pp. 230–242, 2022.
 - [30] D. Ngo and H. Nguyen, "Experimental and numerical investigations on flexural behaviour of prestressed textile reinforced concrete slabs," *Civil Engineering J*, vol. 7, no. 6, pp. 1084–1097, 2021.
 - [31] M. Saffarian, A. Ahmadi, and M. Bagheripour, "Highly accurate space-time coupled least-squares finite element framework in studying wave propagation," *SN Applied Sciences*, vol. 2, no. 4, pp. 664–710, 2020.
 - [32] P. Guo, G. McMechan, and L. Ren, "Modeling the viscoelastic effects in P-waves with modified viscoacoustic wave propagation," *Geophysics*, vol. 84, no. 6, pp. T381–T394, 2019.
 - [33] K. Surana, S. Petti, A. Ahmadi, and J. Reddy, "On p-version hierarchical interpolation functions for higher-order continuity finite element models," *International Journal of Computational Engineering Science*, vol. 02, no. 04, pp. 653–673, 2001.
 - [34] M. van Driel and T. Nissen-Meyer, "Optimized viscoelastic wave propagation for weakly dissipative media," *Geophysical Journal International*, vol. 199, no. 2, pp. 1078–1093, 2014.
 - [35] X. Liu, J. Chen, Z. Zhao, H. Lan, and F. Liu, "Simulating seismic wave propagation in viscoelastic media with an irregular free surface," *Pure and Applied Geophysics*, vol. 175, no. 10, pp. 3419–3439, 2018.

Research Article

Numerical and Large-Scale Laboratory Study of Rock Column Groups in Sandy Soil Behavior Improvement

Ali Yousefi Samangani  and Reza Naderi

Civil Engineering Department, Shahrood University of Technology, Shahrood, Iran

Correspondence should be addressed to Ali Yousefi Samangani; aliyosefi90@yahoo.com

Received 24 May 2022; Revised 9 June 2022; Accepted 21 June 2022; Published 1 August 2022

Academic Editor: S. Mahdi S. Kolbadi

Copyright © 2022 Ali Yousefi Samangani and Reza Naderi. This is an open access article distributed under the Creative Commons Attribution License, which permits unrestricted use, distribution, and reproduction in any medium, provided the original work is properly cited.

The use of stone columns as one of the effective methods in improving soil behavior can increase soil bearing capacity. One of the common methods in improving poor soil is the use of stone columns. Stone columns are considered one of the suitable options to improve the bearing capacity of loose cohesive and granular soils, which, in addition to reducing soil subsidence, is also considered an effective, economical, and environmentally friendly method in structures built on soil. Considering the financial and human losses caused by the construction of various buildings on poor soils, the importance of developing improvement methods in weak and unsuitable soils is essential. On the other hand, sandy soils are always considered an unsuitable soil sample in design. Therefore, in the present study, we use group stone columns to improve the behavior of a sandy soil sample. When a sample of soft sandy soil is exposed to loading due to its sandiness, we see an increase in soil subsidence and thus a decrease in its load-bearing capacity. In order to obtain practical and useable results in practice, in addition to numerical studies, we conduct a laboratory study to investigate the effect of rock columns on improving sandy soil performance. In sandy soil armed with 4 rock columns, the comparison of the results obtained from the numerical and laboratory model to the displacement of 2 mm is completely consistent with each other, and with increasing displacement, we see a difference between the numerical and laboratory results, so that for a 6 mm displacement, we see an 8% difference in numerical and laboratory results. The final sample capacity in the numerical and laboratory study in this case is 6730 N and 6192 N, respectively.

1. Introduction

To arrange the stone columns (single arrangement, triangular arrangement, and quadrangular arrangement), geometric characteristics of the stone columns (height, diameter of the column, center-to-center distance of the columns, and percentage of sandy soil density) are considered the main variables in the study. It should be noted that, in order to apply the results of the present study, in addition to performing a numerical study in finite element software, the samples will also be studied in a laboratory. In the process of designing the foundation of structures on different soils, bearing capacity and soil subsidence are considered the two main criteria considered by engineers and designers so that the construction of structures on soft and weak soils causes destructive subsidence and the instability of the structure. Therefore, it is

necessary to develop methods for improving weak and unsuitable soils. On the other hand, sandy soils, especially in coastal areas, due to the poor mechanical properties of the soil, have always been considered an unsuitable soil sample in the design, and the need for improvement in this type of soil is urgently needed. Therefore, the present study, by using group stone columns, will seek to improve the behavior of a sample of sandy soil (Firoozkooh sandy soil). In fact, the present study will seek to improve sandy soil using group stone columns. Soil improvement is a process in which an increase in soil quality is observed. In other words, in the process of soil improvement, the mechanical and resistance parameters of the soil increase. In order to improve the behavior of sandy soils, the present study will deal with numerical and laboratory modeling of the group of rock columns as one of the appropriate tools for improving poor soils.

Among the various methods of deep vibration, we can name the method of stone or sand columns and the method of adding various dominant elements. In different conditions, according to the characteristics of the land for the construction of the structure and also according to the time and economic factors, the optimal method for improving poor soil can be selected. Currently, the stone column method is applied in a wide range of soil types, especially weak soils. As a simple and complete definition of a rock column, it can be said that the replacement of a part of weak soil by compacted vertical columns consisting of granular materials in a regular and completely permeable set in soil layers is called rock or sand columns. Figure 1 shows the geometric characteristics of group stone columns along with a sample of a single rock column in the soil bed. In this figure, H is the height of the rock column, L is the height of the loose soil layer, S is the center-to-center distance of the rock columns, and D is the diameter of the rock column. Determining the mentioned parameters in each issue optimally can have a significant effect on increasing soil efficiency and reduce destructive settlements in the soil. In these conditions, by reducing the possible damage due to soil weakness, the stability of the structure will be provided. Figure 1 shows the arrangement and number of individual stone columns used to form the group of stone columns. Therefore, it can be seen that group stone columns can have triangular arrangement (triple), square (quadruple), and rhombus (quadruple and not triple).

2. Literature and Research Background

The vibrating rock column method is an extension of the floating vibration method, which was introduced in Europe in 1930 as an economical method for compacting granular soils. In the vibration compaction method, loose granular soils, due to applied vibrations, lose their previous arrangement and settle in their densest state. The vibrating rod then vibrates into the soil with a jet of pressurized water. The soil particles in the vicinity of the vibrating rod are separated from each other, and the effective stress between them is zero. These particles are in the densest possible position due to the movements of the vibrating rod and their weight. Given that the grains are placed next to each other without applying special stress, the obtained density will be stable (Figure 2). It should be noted that, depending on the height of the rock column and based on the depth of the rock bed, the column can be supported with the end located in the rock bed or floating with the free end of the column in the ground, according to or Figure 2 to be implemented [3].

Shear failure due to the occurrence of cuts in rock columns and surrounding soils is considered one of the most important factors in the failure of lands reinforced with rock column group. Determining appropriate methods to increase resistance and prevent this failure requires accurate knowledge of the behavior of the reinforced soil and the parameters affecting it. Puncture of a stone column occurs when the length of the column is not long enough to transfer the load to the depth. Based on experimental observations, in short stone columns (length-to-diameter ratio less than 6),



FIGURE 1: Sample of a stone column made in laboratory conditions [1].

swelling occurs along the entire length of the column, and the column is punched in the clay. This pattern of deformation occurs more frequently in adjacent columns (columns with a high replacement surface ratio). The tall columns are significantly deformed in the upper part, while the lower part remains unchanged. This indicates that the lack of load transfer to the floor in tall columns will not cause puncture rupture and the occurrence of other rupture conditions such as swelling or cutting. Therefore, the length-to-diameter ratio of about 6 is considered the critical length of the rock column in the design [4]. The rupture will occur conically in the form of a general shear failure. Under these conditions, column deformation in various forms such as lateral expansion, punching, shear, and bending has been observed, but the failure of the rock column group is a general shear failure [5]. Failure due to buckling in the side columns of a group is possible when the column length is less than the critical length.

Extensive laboratory and numerical studies have been performed to calculate the critical length. The results of studies show that, in calculating the critical length of the column, the amplitude of strain in the column is dependent on the diameter of the foundation and is not related to the diameter of the column [6]. Yang et al. [7] examined the numerical model and the laboratory model of stone columns in nonplastic silt materials. The numerical model included the three-dimensional finite element model of the group of stone columns, and the laboratory model included centrifuge experiments with and without stone columns. The results of laboratory models confirmed the obtained numerical results, and both types of analyses showed a reduction in soil mass deformation when using stone columns. In 2014 [8], Castro studied a series of two-dimensional and three-dimensional finite element analyses to evaluate the performance of a group of stone columns under a rigid foundation. The results of this research showed that the number and arrangement of stone columns have the least effect on changes in the load-settling curve. He also showed that, in order to estimate the reduction of subsidence and the critical length of stone columns, the group of stone columns located under the foundation can be replaced with a stone column with an equivalent surface in the center of the

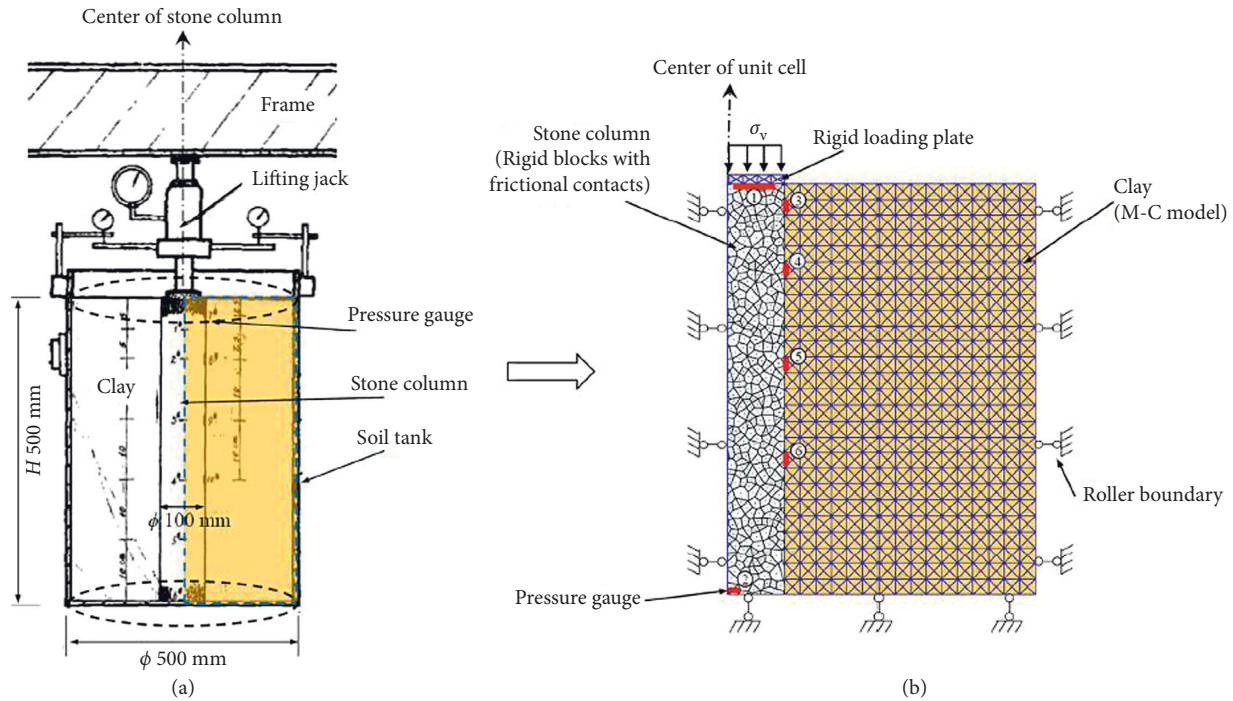


FIGURE 2: Conceptualization of the model from the experimental model to the numerical model. (a) Two-dimensional DEM-FDM model in UDEC [2]. (b) Experimental settings used.

foundation. In 2015, Mohapatara et al. [9] investigated the behavior of granular columns reinforced with geosynthetic fibers under a large-scale direct shear test. In the research of these researchers, sandy soil was used instead of ordinary solidified clay due to the simplicity of sample making. According to the results, it was observed that the presence of geosynthetic coating increases the bearing capacity of granular columns, but after rupture, the resistance to the surface of unreinforced granular columns decreases, and the mode of rupture of reinforced granular columns was of the flexural type, while the unreinforced column was broken in the form of shear, and also the effect of the grain column group was better than the single column with the same cross section.

Tan and Chen performed a two-dimensional numerical study on a rock column in a clay layer using a paired DEM-FDM model similar to the one proposed by Indratna et al. [10]. Tan and Chen used the Universal Distinctive Element Code (UDEC), a 2D-DEM program developed primarily to demonstrate the behavior of discontinuous materials (such as seamstones and aggregate columns) exposed to static or dynamic forces. In UDEC, distinct blocks behave as rigid or deformable elements, which also allows the simulation of continuous materials. Tan and Chen simulated columnar aggregates at UDEC as convex (polygonal) discrete blocks randomly generated based on Veronese veins, while Mohr-Coulomb can be considered as a proper constitutive law (Figure 2). The advantage of this method implemented in UDEC is that the complex interaction between the grain column and the surrounding soil can be simulated in a single model without the need for supervised nodes to pair the DEM-FDM model. The numerical results were in good

agreement with the experimental data of the laboratory, which indicates the potential of this proposed modeling method for further numerical studies to continue to improve the understanding of the behavior of columnar systems. However, this modeling framework offers significant limitations in terms of total free space ratio and relative density modeling. Using the Veronese block system, stone columns are produced in a zero-porosity packing arrangement, which represents a much denser compaction condition than stone columns. In addition, it is common in DEM models for micromechanical contact parameters to differ from those obtained from laboratory experiments. Therefore, appropriate calibrations are needed to ensure that the contact parameters model the reproduction of the behavior of the granular material. Next, a simple strain model is simulated. Hence, a full-scale three-dimensional DEM model can improve the understanding of the complex behavior of stone columns [11].

2.1. Research Methods. The modeling performed in the present study will be done in the form of numerical modeling and large-scale (physical) laboratory modeling. In numerical modeling using Abacus finite element software, rock column groups with different arrangement, number, and diameter of rock columns in sandy soil will be studied under load [12]. Also, in order to perform physical modeling in the laboratory environment, the necessary equipment for physical modeling of stone columns will be made, and loading will be done by a hydraulic Jack. In fact, the samples will be made in the laboratory and loaded first [13]. In physical modeling in the laboratory, after the construction of the device, circular stone

columns with different diameters, in different geometric arrangements and for different percentages of soil density, will be loaded by a hydraulic Jack [14]. During the experiment, two measurement tools will be used [15]. One of these tools will be used to measure displacement and the other to record and measure the load on the soil sample. In numerical modeling using Abacus finite element software, stone columns with different geometry and geometric arrangement in sandy soil, under the application of an axial force, will be studied. Finally, the most appropriate arrangement and geometric parameters of the rock column, which leads to the most optimal response of the soil mass under load, are introduced, and the results obtained from laboratory study and numerical modeling will be compared (Figure 3).

Introducing the studied samples, as mentioned so far, geometric characteristics, the arrangement of stone columns, and soil compaction percentage are considered variable parameters in the present study. Therefore, the studied models will be formed based on these variables [16]. Therefore, in the following, we will introduce the variables of the present study in detail. The basic variables in this study include the physical and mechanical properties of the various components [17]. The diameter of stone columns (d) is considered one of the variables of the present study. Therefore, three diameters of 60, 90, and 120 mm will be used as the diameters of the stone column. The height-to-diameter ratio of the stone columns (L/d) studied in the present study will be considered equal to 3, 5, and 7, and then the most appropriate height-to-diameter ratio based on the results obtained will be selected. Depending on the size of the proposed diameters, the length of the stone columns will be based on Table 1.

According to the introduced variables, 162 different modeling modes ($2 \times 3 \times 3 \times 3 \times 3$ modes) will be studied and evaluated in the present research in a software and laboratory environment. Table 2 presents the selected cases evaluated in the present study along with the acronym.

2.2. Laboratory Study. In order to perform laboratory studies, it is necessary to manufacture samples and test equipment. Therefore, in the following, we will pay attention to the details of making the device and making stone columns in the laboratory environment, along with introducing other types of required equipment and tools. Due to the fact that, in the present study, laboratory modeling is considered on a large scale, it is necessary to make a test box to estimate the behavior of the substrate in certain dimensions. In order to perform experiments on group stone columns with the desired arrangement, it is necessary to make the necessary equipment for testing; for this purpose, equipment similar to the equipment is provided [18], including a large metal box [19]. The dimensions of the test box mold made in the present study are $90 \times 120 \times 120$ cm. It should be noted that, after the construction of the device with the desired dimensions and considering that according to studies the wedge created under the foundation is spread to a distance of about 2 to 2.5 times the width of the foundation from the center of the foundation to the surrounding area, border conditions will not affect the results of large-scale experiments. Figure 4 shows the

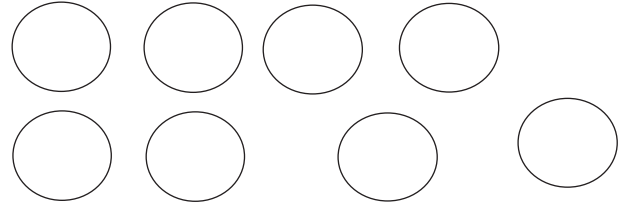


FIGURE 3: Geometric arrangement of stone columns studied in the present study.

TABLE 1: The length of the stone columns studied in the present study.

D (mm)	L/d = 3	L/d = 5	L/d = 7
60	180	300	420
90	270	450	630
120	360	600	840

TABLE 2: Introduction of the studied modes in the present study.

No.	Abb	D (cm)	H/D	Geo	Density (%)
1	4SC ₆₋₅₋₀₋₂	6	5	4	0
2	4SC ₆₋₅₋₀₋₃	6	5	4	0
3	4SC ₆₋₅₋₃₅₋₂	6	5	4	35
4	4SC ₆₋₇₋₀₋₂	6	7	4	0
5	4SC ₆₋₇₋₀₋₃	6	7	4	0
6	4SC ₁₂₋₅₋₀₋₂	12	5	4	0
7	4SC ₁₂₋₅₋₀₋₃	12	5	4	0
8	4SC ₁₂₋₅₋₃₅₋₂	12	5	4	35
9	4SC ₁₂₋₇₋₀₋₂	12	7	4	0
10	4SC ₁₂₋₇₋₀₋₃	12	7	4	0
11	3SC ₆₋₅₋₀₋₂	6	5	3	0
12	3SC ₆₋₅₋₀₋₃	6	5	3	0
13	3SC ₆₋₅₋₃₅₋₂	6	5	3	35
14	3SC ₆₋₇₋₀₋₂	6	7	3	0
15	3SC ₆₋₇₋₀₋₃	6	7	3	0
16	3SC ₁₂₋₅₋₀₋₂	12	5	3	0
17	3SC ₁₂₋₅₋₀₋₃	12	5	3	0
18	3SC ₁₂₋₅₋₃₅₋₂	12	5	3	35
19	3SC ₁₂₋₇₋₀₋₂	12	7	3	0
20	3SC ₁₂₋₇₋₀₋₃	12	7	3	0
21	1SC ₆₋₅₋₀₋₀	6	5	1	0
22	1SC ₆₋₅₋₃₅₋₀	6	5	1	35
23	1SC ₆₋₇₋₀₋₀	6	7	1	0
24	1SC ₁₂₋₅₋₀₋₀	12	5	1	0
25	1SC ₁₂₋₅₋₃₅₋₀	12	5	1	35
26	1SC ₁₂₋₇₋₀₋₀	12	7	1	0

foundation simulator designed for laboratory studies in the present study. The loading system includes loading frame, load handling system, loading plate, and data collection system. The data collection system consists of a computer, data entry system, displacement meter, and dynamometer [20].

The test procedure is similar to the procedure performed in reference [21], which is described in detail in the following. Three-ton Jack is installed in order to apply load and displacement sensors and dynamometer in order to record the amount of displacement and force applied to the loading plate. The loading process is based on displacement control, and its speed is selected as 1 mm/min. It should be noted that the conditions for stopping the application of load to the



FIGURE 4: Pi simulator for large-scale and load plate tests with displacement and dynamometer sensors.

samples, reaching the settling rate in the samples to the extent of 50 mm, are considered [22]. Also, the loading plate is positioned so that its center is on the center of the stone pillar. The ratio of height to diameter of the studied stone columns is considered to be equal to 3, 5, and 7, and then the most appropriate ratio of height to diameter will be selected based on the results obtained. In the present study, each experiment was repeated twice to ensure the accuracy of the experiments performed. It is important to note that, before making the samples, the inner walls of the test box (device) were well impregnated with oil to minimize the friction of sandy soil with the surfaces of the device under test [23].

Figure 4 shows how the displacement sensor and dynamometer are connected on the loading screen. In this study, in order to apply load on the studied stone columns, a circular steel loading plate has been used. A hydraulic Jack is applied to the center of the loading plate, and two displacement sensors record the amount of displacement recorded on the steel plate [24]. Also, by installing a dynamometer sensor at the point of contact of the Jack with the steel plate, the amount of force applied to the steel plate can be controlled and measured.

2.3. Material Specifications. The soil studied in the present study is Firoozkooh sandy soil. Therefore, stone columns enclosed in sandy soil will be studied and tested. The

characteristics of the studied sandy soils are presented in Table 3.

2.4. Construction of Stone Columns. There are different methods for making stone columns. In this study, to make stone columns, a plastic sheath (thin-walled pipe) with different diameters was used, and during the construction of the model, at each stage, according to the specific weight of the column, the required sand was poured, and compaction operations were performed. And graveling was done. Figure 5 shows the steps of making a stone column. Table 4 presents the characteristics of the sand used to build the stone columns.

3. Numerical Study

The Mohr–Coulomb rupture model is a complete elasto-plastic model of the simplest and most widely used models in geotechnical analysis. This is because of the small number of variables without the need for complex experiments. In the Mohr model, the Mohr–Coulomb rupture criterion is used as the yield surface, and the law of flow in the shear state is assumed to be independent. In using this model, it should be noted that some basic aspects of soil behavior, such as the dependence of stiffness on the path and the history of stress

TABLE 3: Introducing the characteristics of the studied sandy soil.

Parameter	Numerical value
Dry specific gravity	16 kN/m ²
Saturation specific gravity	18 kN/m ²
Dry internal friction angle	40 degrees
Internal friction angle of saturation	36 degrees
Adhesion	0
Modulus of elasticity	40 MPa
Specific density	2.65
Poisson ratio	0.3
Maximum porosity ratio	0.6
Minimum porosity ratio	0.3

TABLE 4: Introducing the specifications of sand used to build stone columns.

Parameter	Numerical value
Dry specific gravity	16 kN/m ²
Saturation specific gravity	19 kN/m ²
Dry internal friction angle	41 degrees
Internal friction angle of saturation	37 degrees
Adhesion	0
Modulus of elasticity	100 MPa
Specific density	2.6
Poisson ratio	0.2
Maximum porosity ratio	0.75
Minimum porosity ratio	0.35



FIGURE 5: Steps of making a stone column in the laboratory.

and strain in it, have been omitted [13]. In order to model sandy soil and improve it by using stone columns with the desired specifications, the capabilities of Abacus finite element software will be used. In order to apply the load, a single load is used. The magnitude of the applied load will be a maximum of 3 tons. In geotechnical engineering, Mohr–Coulomb theory is used to determine the shear strength of soil and rock at different levels of effective stress, and in structural engineering, this theory is used to determine the load and fracture angle of concrete and similar materials. In addition, the Coulomb friction hypothesis is used to obtain the

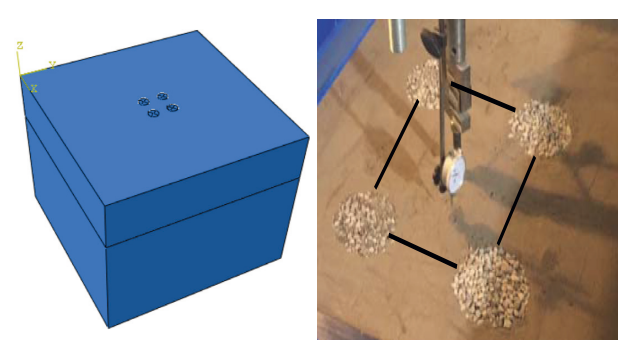


FIGURE 6: Sandy soil model reinforced with 4 stone pillars.

combination of normal and shear stresses that cause failure. The molar circle determines the main stresses that cause this combination and the angle of their action plane. If the failure of material occurs according to the Columbus friction hypothesis, the angle of the displacement line at the point of failure will be equal to the angle of friction. According to this property, the strength of the material can be calculated by comparing the external mechanical work resulting from external displacement and loading as well as the internal mechanical work resulting from stress and strain at the fracture line. According to the principle of energy conservation, the sum of these values must be zero. This makes it possible to calculate the structural failure load. One development of the Mohr–Coulomb model is the description of fractures isolated by combining Columbus's law of friction with Rankine's principle. The fracture criterion shows the linear coupling obtained from the shear strength diagram of the material against the normal stress applied to it. This criterion is defined as equation (1):

$$\tau = \sigma \tan(\varphi) + c. \quad (1)$$

3.1. Analysis of Results. In order to evaluate the performance of the group of rock columns in improving the behavior of sandy soil, in both experimental and numerical studies, different responses were recorded under a fixed and specific axial load and compared with each other in different modes. The analysis and interpretation of the results are made in such a way that the direct impact of each variable on the final response of the soil system dominated by the rock column is

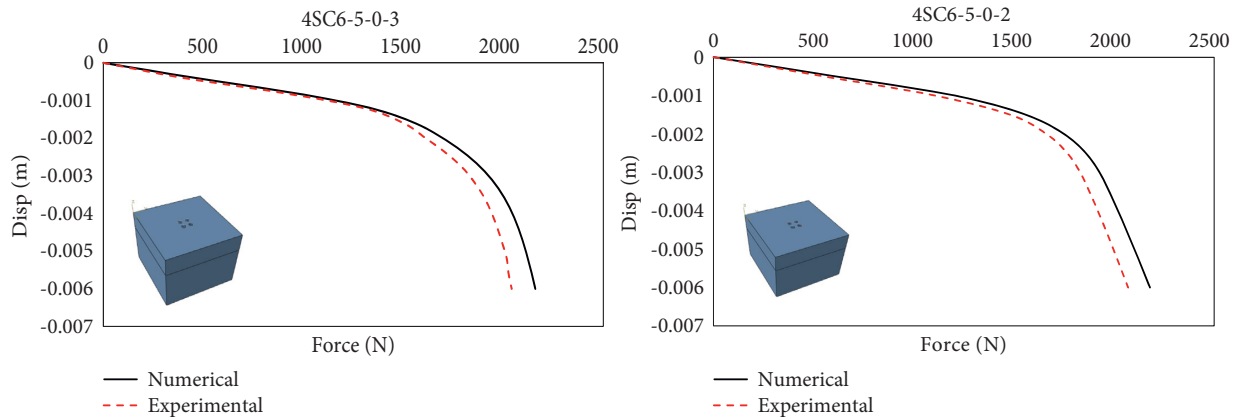


FIGURE 7: Conditional force-displacement diagram for 4SC6-5-0-2 and 4SC6-5-0-3 models in both numerical and laboratory modes.

understandable. The first answer studied in the present study is the comparison of force-displacement diagrams related to 26 selected models in both numerical and laboratory modes. According to the force-displacement diagram, the maximum bearing capacity and the maximum displacement created in the studied models can be compared with each other. It should be noted that, in naming the studied samples, the number before SC indicates the number of stone columns, and the numbers after SC indicate the diameter of the stone column, the ratio of height to diameter of the stone column, the percentage of soil density, and the distance from the center to the center of the column, respectively. The stones are from each other. Figure 6 shows the dominant soil with 4 stone columns in the software environment and in the laboratory environment. Also, in Figure 6, the force-displacement diagram of the sample 4SC6-5-0-2 is presented in both numerical and laboratory modes.

According to Figure 7, the results obtained from the numerical and laboratory study are in good agreement with each other, which indicates the acceptable accuracy of the modeling process in the software environment. Due to the fact that the load is applied statically and controlled by displacement, it is observed that, for a displacement of 6 mm, the final capacity of the sample is obtained based on a numerical study equal to 2179 Newtons, while the final capacity of the sample in 2070 Newton laboratory studies has been obtained. In this case, the difference between the results of numerical and laboratory studies on the 4SC6-5-0-2 model is equal to 5%. Figure 7 shows the force-displacement diagram of 4SC6-5-0-3 in both laboratory and numerical modes. Adaptation of numerical and laboratory results indicates the desired accuracy of the research process. In this case, the sandy soil is reinforced with 4 stone columns with a square arrangement. The diameter of the columns is 6 cm, the ratio of height to the diameter of the columns is equal to 5, and the distance from the center to the center of the stone columns is equal to 3. According to the results presented in Figure 7, for a displacement of 6 mm, the final sample capacity calculated from the numerical and laboratory analysis is 2159 and 2041 N, respectively. The difference between the results obtained from numerical and laboratory studies on the 4SC6-5-0-2 model is equal to 5.46%.

Figure 8 shows the force-displacement diagram for 4SC6-5-35-2 in both laboratory and numerical modes. In this case of modeling, we see the adaptation of numerical and laboratory results. The soil sample in this case consists of sandy soil with 4 stone columns with a square layout. In this sample, the diameter of the stone columns is 6 cm, and the height to diameter ratio of the columns is 5, the distance from the center to the center of the columns. The rock is considered to be equal to 2, and the soil density percentage is equal to 35%. Based on the results presented in Figure 8, it can be seen that the final sample capacity in the numerical and laboratory study for 6 mm displacement is estimated to be 2141 and 2012 newtons, respectively. The difference between the results obtained from numerical and laboratory studies on the 4SC6-5-35-2 model is equal to 6.02%. Figure 8 shows the force-displacement diagram of the 4SC6-7-0-2 sample in both laboratory and numerical modes. In this mode of modeling, there is an acceptable agreement between numerical and laboratory results. The soil sample in this case consists of sandy soil with 4 stone columns with a square layout. In this sample, the diameter of the stone columns is 6 cm, and the height to diameter ratio of the columns is 7, the distance from the center to the center of the columns. Stone is considered equal to 2, and soil without density is considered. Based on the results presented in Figure 8, it can be seen that the final capacity of the sample in the numerical and laboratory study for 6 mm displacement is estimated to be 2806 and 2609 N, respectively. The difference between the results of numerical and laboratory studies on this model is equal to 7%.

Figure 9 shows the force-displacement diagram of the 4SC6-7-0-3 sample in both laboratory and numerical modes. The soil sample studied in this case consists of sandy soil with 4 stone columns with a square arrangement. In this sample, the diameter of the stone columns is 6 cm, and the height to diameter ratio of the columns is 7, the distance from the center to the center of the columns. Rock is equal to 3, and soil without density is considered. The results show that the difference in bearing capacity in this case is based on two categories of numerical and laboratory studies equal to 7%. The final sample capacity in the numerical and laboratory study for a displacement of 6 mm is estimated at 2614 and 2431 N, respectively. Figure 9 shows the force-

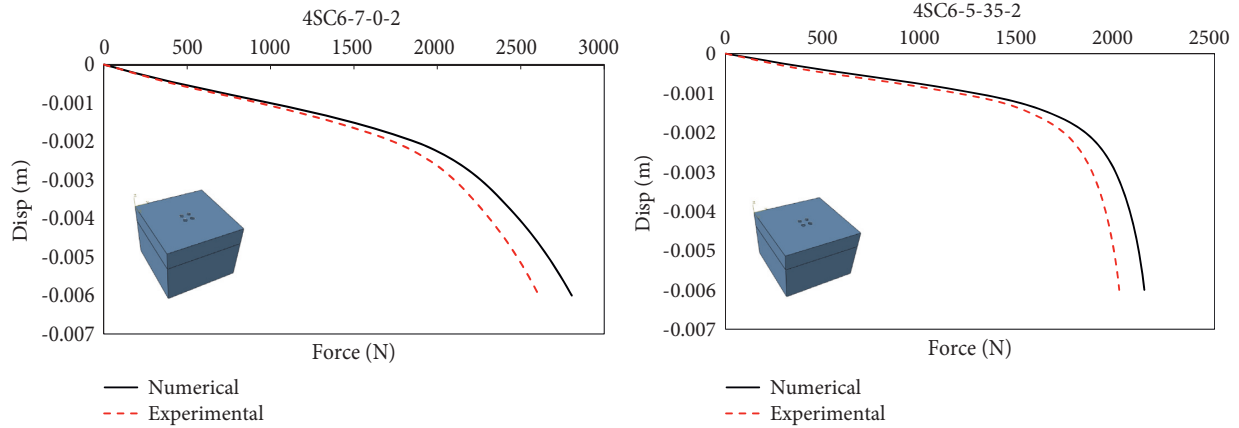


FIGURE 8: Force-displacement diagrams related to 4SC6-5-35-2 and 4SC6-7-0-2 models in both numerical and laboratory modes.

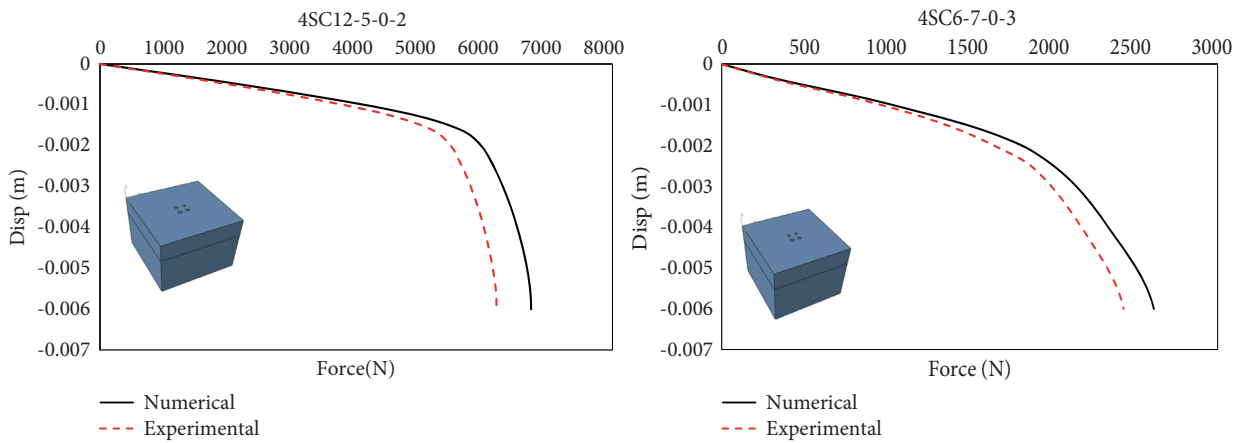


FIGURE 9: Force-displacement diagram related to models 4SC6-7-0-3 and 4SC12-5-0-2 in both numerical and laboratory modes.

TABLE 5: Numerical comparison of bearing capacity of numerical and laboratory models related to reinforced sandy soil samples.

Model	Numerical final load capacity (newton)	Final laboratory bearing capacity (newton)	Results difference (%)
4SC ₆₋₅₋₀₋₂	2179	2070	5
4SC ₆₋₅₋₀₋₃	2159	2041	5.46
4SC ₆₋₅₋₃₅₋₂	2141	2012	6.02
4SC ₆₋₇₋₀₋₂	2806	2609	7
4SC ₆₋₇₋₀₋₃	2614	2431	7
4SC ₁₂₋₅₋₀₋₂	6730	6192	8
4SC ₁₂₋₅₋₀₋₃	6860	6517	5
4SC ₁₂₋₅₋₃₅₋₂	6946	6543	5.8
4SC ₁₂₋₇₋₀₋₂	6746	6206	8
4SC ₁₂₋₇₋₀₋₃	9043	8410	6.9

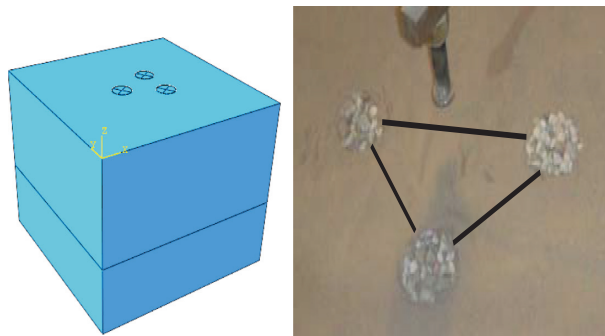


FIGURE 10: Sandy soil model reinforced with 3 stone pillars.

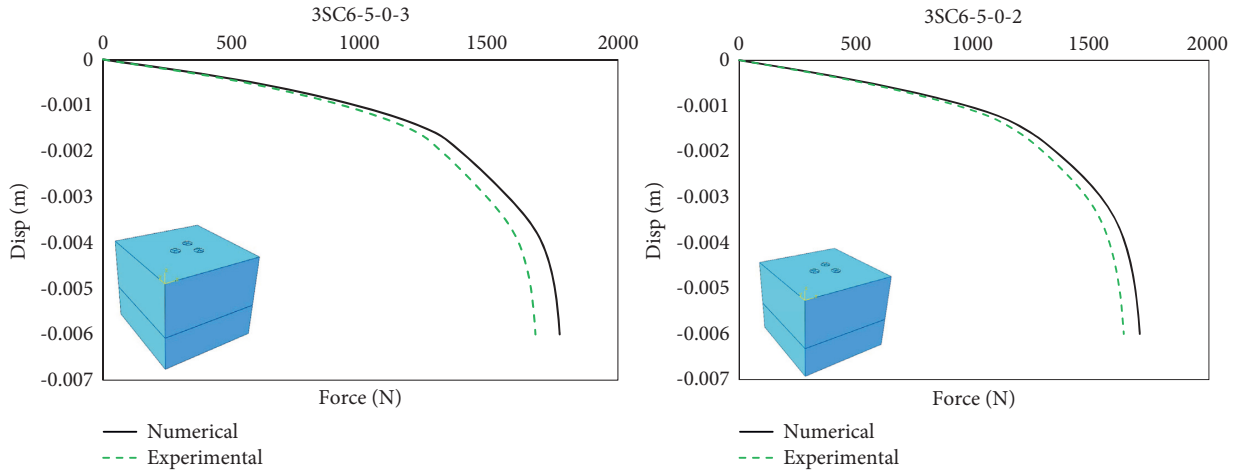


FIGURE 11: Force-displacement diagram related to 3SC6-5-0-2 and 3SC6-5-0-3 models in both numerical and laboratory modes.

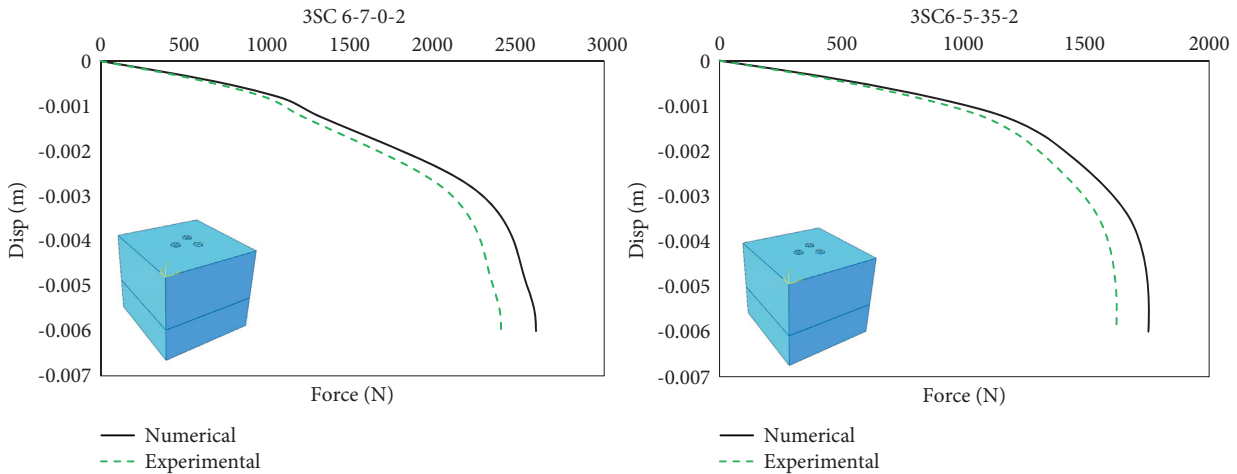


FIGURE 12: Force-displacement diagram related to models 3SC6-5-35-2 and 3SC6-7-0- in both numerical and laboratory modes.

displacement diagram of the 4SC12-5-0-2 sample in both laboratory and numerical modes. From the comparison of the results obtained from the numerical and laboratory model to the displacement of 2 mm completely on each other and consistent with increasing displacement, we see a difference between numerical and laboratory results so that, for a displacement of 6 mm, we will see an 8% difference in numerical and laboratory results. The final sample capacity in the numerical and laboratory study in this case is 6730 and 6192 N, respectively (Table 5).

Figure 10 shows the dominant soil with 3 stone columns in the software environment and in the laboratory environment. Also, in Figure 10, the force-displacement diagram related to sample 3 SC6-5-0-2 is presented in both numerical and laboratory modes.

Figure 11 shows the results of the numerical and laboratory study on sample 3 SC6-5-0-2. The obtained results indicate acceptable compatibility of laboratory and numerical results with each other, which indicates the acceptable accuracy of the modeling process in the software environment. It can be seen that, for a displacement of 6 mm, the final sample capacity is based on a numerical study of 1705 N, while the final sample

capacity is obtained in laboratory studies at 1637 N. In this case, the difference between the results obtained from numerical and laboratory studies on the 3SC6-5-0-2 model is equal to 3.9%. Figure 11 shows the results of the numerical and laboratory study on sample 3 SC6-5-0-3. It can be seen that, for a displacement of 6 mm, the final sample capacity is based on a numerical study of 1773 newtons, while the final sample capacity is obtained in laboratory studies at 1679 newtons. In this case, the difference between the results of numerical and laboratory studies on the 3SC6-5-0-3 model is 5.3%.

Figure 12 shows the results of the numerical and laboratory study on sample 3 SC6-5-35-2. It can be seen that, for a displacement of 6 mm, the final sample capacity is based on a numerical study of 1752 N, while the final sample capacity in laboratory studies is 1620 N. In this case, the difference between the results of numerical and laboratory studies on the 3SC6-5-0-3 model is 7.53%. Figure 12 shows the results obtained from the numerical and laboratory study on sample 3 SC6-7-0-2. It can be seen that, for a displacement of 6 mm, the final sample capacity is based on a numerical study of 2594 newtons, while the final sample capacity is obtained in laboratory studies at 2386 newtons. In

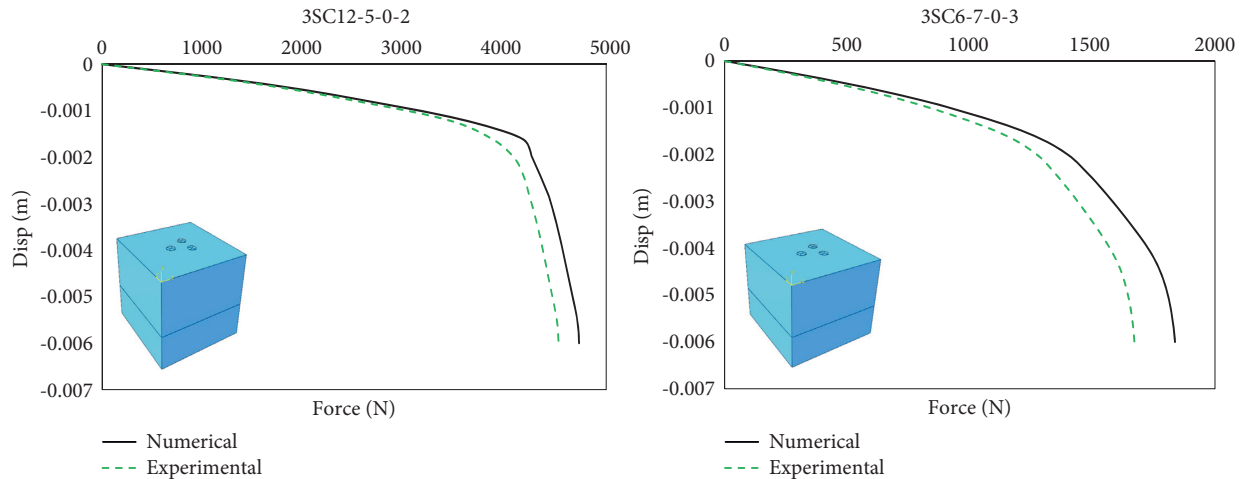


FIGURE 13: Force-displacement diagram related to model 3SC6-7-0-3 in both numerical and laboratory modes.

this case, the difference between the results obtained from numerical and laboratory studies on the 3SC6-7-0-2 model is equal to 8%.

Figure 13 shows the results of the numerical and laboratory study on sample 3 SC6-7-0-3. It can be seen that, for a displacement of 6 mm, the final sample capacity is based on a numerical study of 1837 newtons, while the final sample capacity is obtained in laboratory studies at 1671 newtons. In this case, the difference between the results obtained from numerical and laboratory studies on the 3SC6-7-0-2 model is equal to 9%. Figure 13 shows the results of the numerical and laboratory study on sample 3 SC12-5-0-2. It is observed that, for a displacement of 6 mm, the final sample capacity is obtained based on a numerical study equal to 4731 N, while the final sample capacity is obtained in laboratory studies at 4527 N. In this case, the difference between the results obtained from numerical and laboratory studies on the 3SC6-7-0-2 model is equal to 4.3%.

4. Discussion and Conclusion

The use of stone columns can be done individually or in groups. Due to the high volume of studies on the performance of individual rock columns, the present study sought to investigate the performance of group rock columns in improving the behavior of sandy soils. The soil sample studied in this study was sandy soil (Firoozkooh sandy soil), and also, in order to achieve real laboratory results, the experiments were performed as large-scale experiments. After this step, based on the results of experiments, numerical modeling will be performed using Abacus finite element software. Stone columns will be studied and evaluated in groups in different numbers and arrangements. The studied modes are in the form of a triangular triple group and a quadruple square group. The Mohr–Columb theory is a theory for describing the reaction of materials such as soil and concrete against normal shear stress. In most classical engineering materials, part of the shear failure cap somehow follows this theory. The scope of application of Mohr–Columb theory is for materials that have a much

higher compressive strength than their tensile strength. The stone columns will be studied and evaluated as a group in different numbers and arrangements (triangular triple group, square quadruple group, and single arrangement). For the distance of stone columns in the group, the distance from the center to the center of the stone columns is 2, 2.5, and 3 times the diameter of the stone column. Sand soil density in the present study bed soil (Firoozkooh sand soil) was studied in two compaction states without density and with a density of 35%. In sandy soil reinforced with 3 stone pillars, it is observed that, for a displacement of 6 mm, the final sample capacity is obtained based on a numerical study equal to 4731 N, while the final sample capacity is obtained in laboratory studies of 4527 N.

Data Availability

Requests for access to these data should be made to the corresponding author's e-mail address: aliyosefi90@yahoo.com.

Conflicts of Interest

The authors declare that there are no conflicts of interest regarding the publication of this paper.

Authors' Contributions

Ali Yousefi Samangani contributed to FEM controlling, simulation controlling, results evaluation, and paper writing. Reza Naderi contributed to literature review, FEM simulation, and draft writing.

Acknowledgments

The authors would also like to show their gratitude to Dr. Amir Bazrafshan (Civil Engineering Dept., Shahrood University of Technology, Iran) for sharing his pearls of wisdom with them during the course of this research.

References

- [1] M. Etezad, "Geotechnical performance of group of stone columns," PhD Thesis, Concordia University, Montreal, Canada, 2007.
- [2] S. M. Seyed Kolbadi, N. Hassani, S. M. Seyed-Kolbadi, and M. Mirtaheeri, "Analyzing parametric sensitivity on the cyclic behavior of steel shear walls," *Shock and Vibration*, vol. 2021, Article ID 3976793, 10 pages, 2021.
- [3] A. Zahmatkesh and A. J. Choobbasti, "Investigation of bearing capacity and settlement of strip footing on clay reinforced with stone columns," *Australian Journal of Basic and Applied Sciences*, vol. 4, no. 8, pp. 3658–3668, 2010.
- [4] B. Pulko and B. Majes, "Analytical method for the analysis of stone-columns according to the Rowe Dilatancy theory," *Acta Geotechnica Slovenica*, vol. 3, no. 1, pp. 37–45, 2006.
- [5] M. Krishna and M. R. Madhav, "Engineering of ground for liquefaction mitigation using granular columnar inclusions: recent developments," *American Journal of Engineering and Applied Sciences*, vol. 2, no. 3, pp. 526–536, 2009.
- [6] A. P. Ambily and S. R. Gandhi, "Behavior of stone columns based on experimental and FEM analysis," *Geotechnical and Geoenvironmental Engineering*, vol. 133, 2007.
- [7] J. Castro, "Numerical modelling of stone columns beneath a rigid footing," *Computers and Geotechnics*, vol. 60, pp. 77–87, 2014.
- [8] S. R. Mohapatra, K. Rajagopal, and J. Sharma, "Direct shear tests on geosynthetic-encased granular columns," *Geotextiles and Geomembranes*, vol. 44, no. 3, pp. 396–405, 2016.
- [9] X. Tan, M. Zhao, and W. Chen, "Numerical simulation of a single stone column in soft clay using the discrete-element method," *International Journal of Geomechanics*, 2018.
- [10] M. Kolbadi, "Review on nonlinear behavior assessment of reinforced concrete frames by carbon fiber reinforced polymers under blast loading," *Cur Trends Civil & Structures Engineering*, vol. 2, no. 5, 2019.
- [11] S. N. Malarvizhi, K. Ilamparuthi, and S. Bhuvaneshwari, "Behavior of geogrid encased stone column and stone column stabilized soft clay bed," in *Proceedings of the 6th International Conference on Physical Modelling in Geotechnics*, Hong Kong, China, August 2006.
- [12] J. Hughes and N. Withers, "Reinforcing of soft cohesive soils with stone columns," *Ground Engineering*, vol. 7, no. 3, pp. 42–49, 1974.
- [13] S. M. Seyed Kolbadi, N. Hassani, S. M. Seyed-Kolbadi, and M. Mirtaheeri, "Analyzing parametric sensitivity on the cyclic behavior of steel shear walls," *Shock and Vibration*, vol. 2021, Article ID 3976793, 10 pages, 2021.
- [14] D. McKelvey, V. Sivakumar, A. Bell, and J. Graham, "Modelling vibrated stone columns in soft clay," *Proc. Institution of Civil Engineers - Geotechnical Engineering*, vol. 157, no. 3, pp. 137–149, 2004.
- [15] W. Hu, D. M. Wood, and W. Stewart, "Ground improvement using stone column foundations: result of model tests," in *Proceedings of the Int. Conf. on Ground Improvement Techniques*, pp. 247–256, CI-Premier, Singapore, 1997.
- [16] S. Murugesan and K. Rajagopal, "Geosynthetic-encased stone columns: numerical evaluation," *Geotextiles and Geomembranes*, vol. 24, no. 6, pp. 349–358, 2006.
- [17] W. Hu, *Physical modeling of group behavior of stone column foundations*, Ph.D. dissertation, Univ. of Glasgow, Glasgow, U.K, 1995.
- [18] B. McCabe, J. McNeill, and J. Black, "Ground improvement using the vibro-stone column technique," in *Proceedings of the Transactions of the Institution of Engineers of Ireland*, Galway, January 2007.
- [19] M. A. Hassan, M. A. M. Ismail, and H. H. Shaalan, "Numerical modeling for the effect of soil type on stability of embankment," *Civil Engineering Journal*, vol. 7, pp. 41–57, 2022.
- [20] A. Zahmatkesh and J. Ch. Choobbasti, "Settlement evaluation of soft clay reinforced with stone columns using the equivalent secant modulus," *Arabian Journal of Geosciences*, vol. 5, no. 1, pp. 103–109, 2012.
- [21] B. Mc Cabe, J. McNeill, and J. A. Black, "Ground improvement using the vibro stone column technique," in *Proceedings of the Institution of Engineers of Ireland*, Galway, January 2007.
- [22] W. Mingming, C. Jianyun, W. Liang, and S. Bingyue, "Discussion of "hydrodynamic pressure on gravity dams with different heights and the westergaard correction formula"," *International Journal of Geomechanics*, vol. 22, no. 8, 2022.
- [23] N. E. I. Boumekik, M. Labed, M. Mellas, and A. Mabrouki, "Optimization of the ultimate bearing capacity of reinforced soft soils through the concept of the critical length of stone columns," *Civil Engineering Journal*, vol. 7, no. 9, 2021.
- [24] J. Lu, Z. Yang, K. Adlier, and A. Elgamal, "Numerical analysis of stone column reinforced silty soil," in *Proceedings of the 15th Southeast Asian geotechnical conference*, Bangkok, Thailand, November, 2004.

Research Article

Evaluation of the Seismic Behavior Based on the Performance of Special Steel Moment Frames by Modified Energy Method and Force Design Method

Ramin Bagherzadeh, Abolfazl Riahi Nouri , Mohammad Sajjad Massoudi, Mohammad Ghazi, and Farzan Haddad Shargh

Department of Civil Engineering, West Tehran Branch, Islamic Azad University, Tehran, Iran

Correspondence should be addressed to Abolfazl Riahi Nouri; riahinouri.abolfazl@wtiau.ac.ir

Received 14 May 2022; Revised 2 June 2022; Accepted 8 June 2022; Published 8 July 2022

Academic Editor: S. Mahdi S. Kolbadi

Copyright © 2022 Ramin Bagherzadeh et al. This is an open access article distributed under the Creative Commons Attribution License, which permits unrestricted use, distribution, and reproduction in any medium, provided the original work is properly cited.

Although conventional methods in seismic design consider such parameters as force, displacement, and ductility, the behavior of a significant number of structures that have been designed and experienced earthquakes shows that the existing criteria are insufficient and more comprehensive ones should be used. In this regard, the energy-based design method may be considered one of the suitable solutions. This method is based on creating a balance between the input and output energy of structures. It is possible to have a more appropriate estimate of the energy input as well as dissipated energy by the structure and use it in the design of the structure. In the modified energy method that has been used in this study, control of items such as the creation of a soft story, establishment of the Strong-Column Weak-Beam concept, the uniform distribution of loads in the members, the nonconcentration of force and local damage, and simultaneous drift control of the structure with the optimal distribution of plastic hinges have been considered. Also, modifications have been made to the energy balance equation. In this paper, 8-, 16-, and 24-story frames with lateral force resisting system of special steel moment frame have been modified by energy method and compared by the design force method of AISC code. Performance level criteria of the ASCE41-17 code have been applied in the design, and the $P - \Delta$ effects have also been considered in the nonlinear analysis. The results show that, for the frame which is designed by the energy method, the plastic hinges are created in the upper stories and beams; however, in the frame designed by the LRFD method, several plastic hinges are formed in the columns of the upper stories, and a local mechanism is created. Also, in 8- and 16-story structures, the weight of the structure which is designed by the energy method is less than that obtained by the LRFD method. The results also showed that, in contrast to the energy method, the relationships presented in the codes regarding the Strong-Column Weak-Beam rule cannot prevent local and undesirable mechanisms in severe earthquakes.

1. Introduction

Current seismic codes for building design often utilize a force or a displacement-based approach in their implementation. In a force-based approach, a structure is designed to ensure that it possesses sufficient strength to resist the maximum forces imparted to it by gravity and earthquake. In a displacement-based approach, the structure is proportioned to achieve a specified performance level based on the target displacement, defined by strain or drift limits, under a specified level of seismic intensity. A third approach, which is

gaining popularity in the earthquake engineering community, is the energy-based approach. In this approach, a design is considered satisfactory if the capacity of a structure to absorb or dissipate energy exceeds its energy demand from an earthquake. Seismic resistance of structures in conventional seismic design methods is considered appropriate when the deformation capacity or resistance limit of the structure is more than the demand of the design earthquake. This is despite the fact that a large portion of the damage which is caused by earthquakes is the result of inelastic cycles. Noting that the energy entering the structure is directly

dependent on its cyclic behavior, the energy concept can be considered an effective tool in seismic-resistant design.

In 1956, Housner, for the first time, applied the concept of energy to study the seismic behavior of structures. Despite the simple relations proposed by Housner, his approach opened the way for the future development of the energy method in the seismic design of the structures. He showed that the spectral velocity curve of structures is stable for most earthquakes over a wide range of periods [1]. In 1988, Akiyama also explored seismic design according to the concept of energy. Akiyama proposed a relation for calculating the input energy per unit mass as a function of the period of the structure [2]. In 1998, Fakhri Niasar and Ghafory Ashtiany stated that the energy parameter is comprehensive and includes all characteristic parameters related to an earthquake. They proposed that, due to the scalar nature of the energy, it is required to collect the amounts of energy related to the various components of the earthquake record, rather than considering the energy of one component of the earthquake record alone [3]. In another investigation conducted in 2000 by Ghafory Ashtiany and Maleki, the seismic energy was studied in several reinforced concrete moment frame structures, and some relationships were proposed for the maximum input energy per unit mass of the structure [4].

In 2003, Ruzi explored the energy concept in seismic design and stated that the dependence of the effect of seismic loading and structural strength on conventional seismic design methods could be a shortcoming [5]. In studies conducted by Mollaioli and Decanini in 2001 and Ye in 2009, the effects of the hysteretic model and the slope of the postyield area in the structure's behavioral model on the input energy spectrum were studied. They concluded that the input energy spectrum was not significant; in this case, if the slope of the postyield area became more, it would reduce the drift and the more uniform distribution of inelastic deformations, leading to more uniform damage [6, 7]. In 2007, Ghodrati Amiri et al. studied the impacts of damping and a strong shock of the earthquake on elastic input energy. They concluded that the input energy to the structure increases by an increase in the strong shock of the earthquake [8]. In 2011, Haddad Shargh and Hosseini studied the optimal stiffness distribution at the height of the building to minimize the seismic input energy. They showed that, for medium-sized structures (up to about 22 stories), the optimal stiffness distribution could be considered parabolic; however, for taller structures, the optimal stiffness distribution at height is similar to a bell-shaped curve. [9].

In 2015, Havaei and Mobedi studied the effects of cradle motion due to the yielded column on the response of steel structures [10]. In 2016, Bemanian and Shakib evaluated the nonlinear behavior of a dual steel moment frame-shear wall system under a set of earthquakes and concluded that the dual steel moment frame-shear wall system could be a suitable system for absorbing a high level of input energy [11]. In 2018, Vahdani et al. studied the impacts of damping as well as ductility on the input energy spectrum. They concluded that changing the ductility coefficient was more influential than changing the damping ratio on the relative input energy spectrum [12]. In 2020, Ucar calculated the

input energy in MDOF systems using the input energy responses of ESDOF systems according to each mode of the system. He studied 3-, 5-, and 8-story reinforced concrete frames to NTHAs under eleven earthquakes and found that direct input powers of the ESDOF systems could be effectively used to calculate the input energy in the MDOF system [13]. Tran and Adhikari, in 2021, also used the energy-based seismic design process (EBSDF) to estimate the SDF and then compared it to the resistance-based SDF. They used the energy method to quantify the performance of the building system [14]. Meanwhile, Baqherzadeh et al., in 2022, using the combination of the energy method and whale meta-heuristic optimization (E-WOA) algorithm to optimize steel moment frames, showed that using the E-WOA method improves the plastic hinge distribution and seismic energy dissipation. The structure's weight was also reduced [15].

The main goal of the present study is to apply the energy method to balance the input-output energy of the structure in the special steel moment frame design. In the proposed energy method, the design of the members is carried out by equalizing the structure's input energy and the energy which is dissipated in the plastic hinges. The system's dissipated energy is the result of the energy dissipated at all hinges formed on the frame. In the equilibrium relations, the effects of gravity loads and the higher modes on the energy entering the structure are seen. Based on this balance of energy, the minimum required bending moments of the beams are obtained; based on that, the beams will be designed. The columns will be also designed according to the maximum required capacity and the control of constraints such as Strong-Column Weak-Beam and soft and weak story. By considering all results together, a proper comparison has been made between the responses in the linear and nonlinear regions of the diagram. These relationships have been investigated in special steel moment frames with a different number of stories. The study models are special moment frames of 8, 16, and 24 stories. The story drift and the beam deformations are controlled based on AISC2016 [16]. Furthermore, a pushover analysis is carried out with constant gravity loads and incremental lateral loads. Then, the structure is analyzed nonlinearly with a uniform distribution, and the structures are controlled at four functional levels in the target displacement. The control criteria for this stage are taken from the ASCE41-17 code [17]. The required codes are written in MATLAB [18], and the static linear and nonlinear modeling analyses are carried out in SAP2000 [19]; these two programs are linked.

2. Modified Energy-Based Design Method in Steel Frames

The concept of the energy-based design method is founded on the assumption that the amount of energy required to push a given structure to reach the target displacement equals the maximum input energy of the earthquake, which is approximated by $1/2\gamma M \times S_v^2$ [20, 21].

In the new energy method presented in this paper, the following modifications have been applied to improve the results:

- (1) The damping effect of hysteresis cycles has been considered in equilibrium.
- (2) The effects of different modes have been seen in the input energy of the earthquake.
- (3) A correction factor called γ , which is the ratio of the energy absorbed by the inelastic system to that of the equivalent elastic system, has been considered in the algorithm.
- (4) Target displacement is considered as displacement in equilibrium.
- (5) The $P - \Delta$ effect has been considered in calculating the base shear.

The energy balance equation proposed by Lee and Goel is as follows [20, 21]:

$$E_e + E_p = \frac{1}{2} \gamma M S_v^2, \quad (1)$$

where E_e and E_p are, respectively, the elastic and plastic components of the energy needed as the structure is pushed up to the target drift. γ is the correction factor, M is the total structure's seismic weight, and S_v is the design pseudovelocity. The researchers have stated that γ is associated with the natural period of the structure. Also, the period of the structure can have an important impact on the input energy of the ground motion [22].

Figure 1 represents the relationship between the base shear (CW) and the corresponding drift (Δ) for an elastic, as well as an elastoplastic system. Equation (1) can be written as

$$\gamma \frac{1}{2} C_{eu} W \Delta_e = \left(\frac{1}{2} C_y W (2\Delta_{\max} - \Delta_y) \right). \quad (2)$$

Equation (2) can be summarized as follows:

$$\frac{\gamma \Delta_e}{\Delta_y} = \frac{(2\Delta_{\max} - \Delta_y)}{\Delta_e}, \quad (3)$$

where $\Delta_e = R_\mu \Delta_y$ and $\Delta_{\max} = \mu_s \Delta_y$. By considering these values in equation (3), one gets the following:

$$\gamma = \left(\frac{2\mu_s - 1}{R_\mu^2} \right). \quad (4)$$

In relation to (4), μ_s is the structure's ductility coefficient, R_μ is the reduction coefficient of ductility, which is related to μ_s , and Δ_y is the yield displacement of the system. In this study, the relationships which have been presented by Newmark and Hall [23], as shown in Table 1, are used.

For multi-degree-of-freedom systems, all vibration frequencies are effective in calculating the seismic input energy [24]. The input energy of multi-degree-of-freedom systems can be written according to (5) [24]:

$$E = \sum_{n=1}^N \Gamma_n^2 E_{SDOF,n}. \quad (5)$$

Γ_n , the modal participation factor for the mode n , is calculated from equation (6):

$$\Gamma_n = \frac{L_n}{M_n^*} \quad L_n = \phi_n^T M l \quad M_n^* = \phi_n^T M \phi_n, \quad (6)$$

where ϕ_n is the vector of the eigenvalues and M refers to the mass matrix. According to the following equation, the input energy of a system is calculated as one degree of freedom, $E_{SDOF,n}$ [24].

$$E_{SDOF,n} = \frac{1}{2} \gamma M_n^* V_{\max,n}^2 = \frac{1}{2} \gamma M_n^* S_{v,n}^2 = \frac{T_n^2}{8\pi^2} \gamma M_n^* S_{a,n}^2, \quad (7)$$

where $S_{v,n}$ and $S_{a,n}$ refer to the spectral velocity and the spectral acceleration of each mode obtained from the elastic response spectrum. T_n is the n th mode period. In dissipation systems with a decreasing behavior in deformation cycles, there are major cycles that control the input energy of these systems.

Akiyama [2] revealed that the elastic energy for a single degree of freedom (SDOF) could be written as equation (8) with acceptable accuracy:

$$E_e = \frac{1}{2} V_y \Delta_y = \frac{1}{2} M \left(\frac{T_e}{2\pi} \frac{V_y}{W} g \right), \quad (8)$$

where V_y refers to the yield base shear, Δ_y indicates the yield displacement limit, T_e is the structure's period, g denotes the gravitational acceleration, and W is the weight of the structure.

The frame's yield mechanism is assumed as represented in Figure 2. Frame's plastic deformation occurs after the structure reaches the yield point.

According to Hazner's assumption, the energy which enters the structure is equal to the sum of elastic and plastic energy [25]. According to equation (9), Leelataviwat et al. [26] proposed an energy-based approach to the performance-based design in which the need for drift control was eliminated at the end of the design. The concept of energy balance is shown in Figure 3.

$$E_e + \eta E_p = \lambda E, \quad (9)$$

where E refers to the input energy to the structure, E_e is the elastic energy, and E_p is the energy dissipated by plastic hinges. λ and η are the damping coefficients and the behavior of the curve representing the deformation cycle of the structure, respectively.

The value λ was considered equal to $\lambda = 1/1 + 3\xi + 1.2\sqrt{\xi^2}$ by Akiyama [2]; ξ is the damping of the structure.

In this paper, equation (9) has been used to modify plastic energy, and equation (1) has been applied to modify the earthquake's input energy. Finally, the modified energy balance equation is as follows:

$$E_e + \eta E_p = \gamma E. \quad (10)$$

To define η according to Figures 4(a) and 4(b), the effects of earthquake reciprocating behavior on sections can be seen through equation (11) [27]:

$$\eta = \frac{A_P}{A_F} = \frac{A_P}{A_F} \left(\frac{A_F}{A_{RPP}} \right)^{-1}. \quad (11)$$

This relationship is defined for the quantification of the energy dissipation capacity of structural systems with

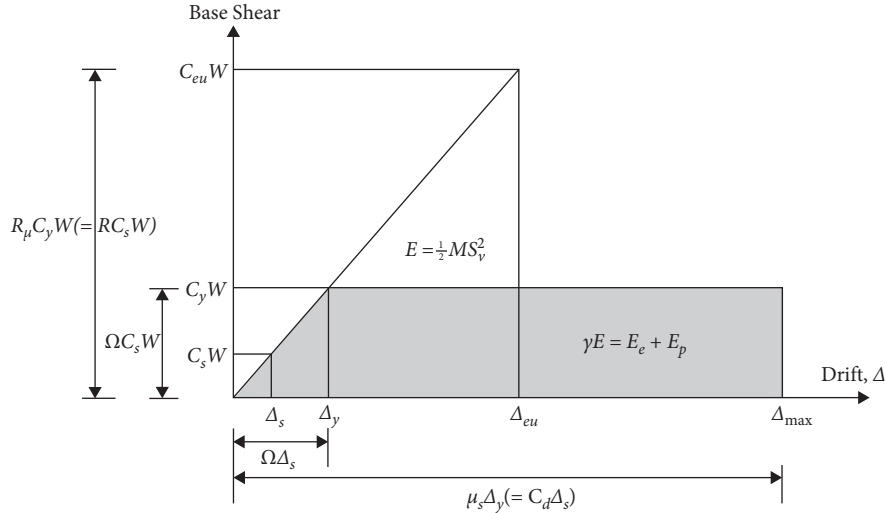


FIGURE 1: Structural idealized response and energy balance concept [22].

TABLE 1: Ductility reduction factor and the corresponding structural period range.

Period range	Ductility reduction factor
$0 \leq T \leq T_1/10$	$R_\mu = 1$
$T_1/4 \leq T \leq T_1/10$	$R_\mu = \sqrt{2\mu_s - 1} (T_1/4T)^{2.315 \log(1/\sqrt{2\mu_s - 1})}$
$T_1/4 \leq T \leq T_1'$	$R_\mu = \sqrt{2\mu_s - 1}$
$T_1' \leq T \leq T_1$	$R_\mu = T\mu_s/T_1$
$T_1 \leq T$	$R_\mu = \mu_s$
$T_1 = 0.57 \text{ sec } T_1' = T_1 (\sqrt{2\mu_s - 1} / \mu_s) \text{ sec}$	

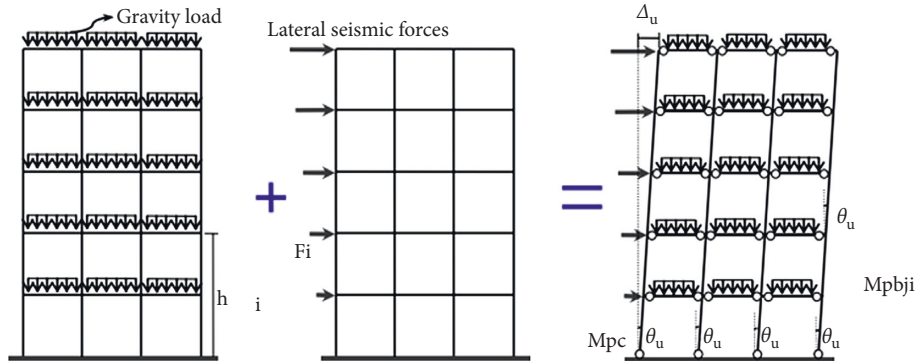


FIGURE 2: A frame's yield mechanism [24].

reduced hysteresis cycles. As can be seen, the A_F and A_{RPP} values are constant, and η coefficient is a function of A_p .

According to Figure 4(b), the real hysteresis rings of structures are not complete; this means that they are reduced or compressed in some areas. For such structures, to calculate inelastic strain energy, according to Figure 4(a), the energy dissipation capacity is overestimated. Therefore, to improve the energy-based plastic method for designing structural frames, the effect of reducing the area enclosed to the structural hysteresis cycle must be considered. In Figure 4, A_p is the area enclosed by the reduced hysteresis cycle. A_{RPP}/A_F can be written as follows [27]:

$$\frac{A_F}{A_{RPP}} = \frac{(\mu - 1)(1 - r)}{\mu(1 + r\mu - r)}. \quad (12)$$

In this relation, r is the slope of the second part of the ratio of hardness, and μ is the ductility factor ($\mu = \Delta_{\max}/\Delta_y$), where Δ_{\max} refer to the maximum displacement and Δ_y indicates the yield point. The consumed energy in each plastic hinge is determined based on the type of its cyclic behavior. In this research, the Takada model has been applied as follows [27]:

$$\xi_H = \frac{2}{\pi} \frac{A_p}{A_{RPP}} \Rightarrow \frac{A_p}{A_{RPP}} = \frac{\pi}{2} \xi_H \Rightarrow \eta = \frac{\pi\mu(1 + r\mu - r)}{\mu(\mu - 1)(1 - r)}, \quad (13)$$

where ξ_H is hysteretic damping. For the type of cycle and the effect of periodicity, Dwairi et al. [27] presented the damping equation according to (14):

$$\xi_H = C \left(\frac{\mu - 1}{\pi\mu} \right) \Rightarrow \eta = C \cdot \frac{(1 + r\mu - r)}{2(1 - r)}. \quad (14)$$

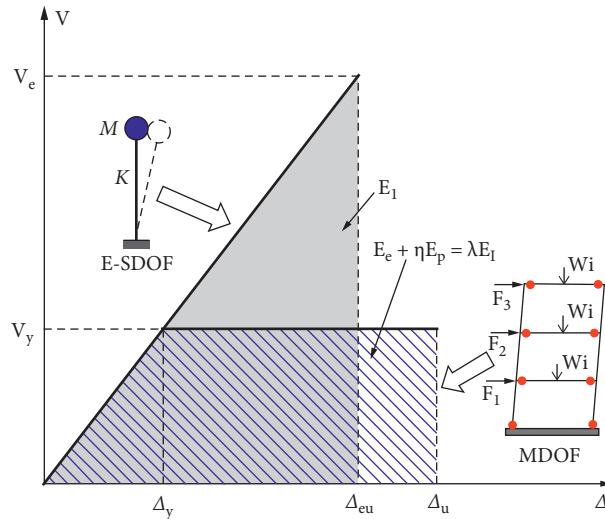


FIGURE 3: The concept of energy balance [26].

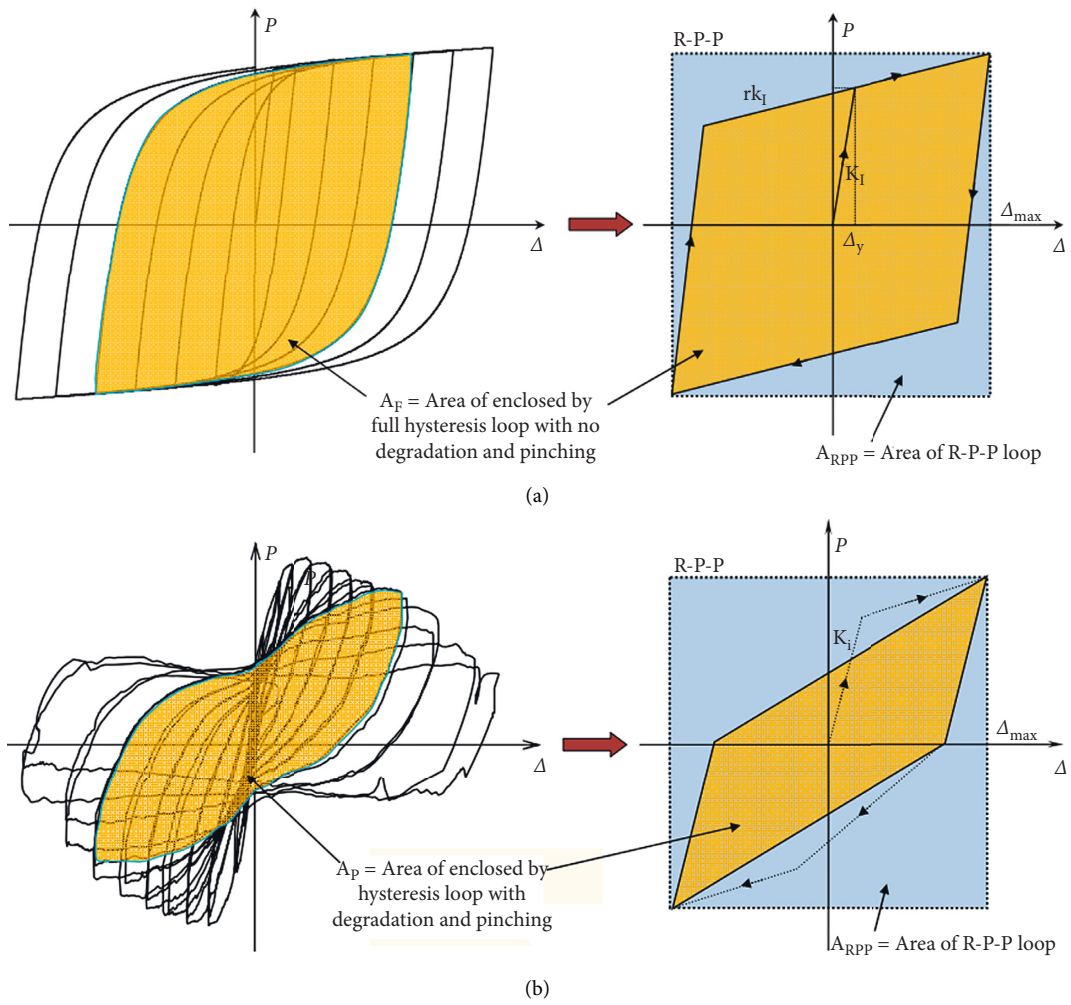


FIGURE 4: Effects of earthquake reciprocating behavior on sections [27]. (a) The hysteresis cycle and its equivalent model. (b) Reduced hysteresis and its equivalent model.

In this relation, the value of C was suggested based on equation (15) and the elastoplastic model:

$$C = \begin{cases} 0.85 + 0.6(1 - T_{eff}), & \text{for } T_{eff} < 1s, \\ 0.3, & \text{for } T_{eff} \geq 1s, \end{cases} \quad (15)$$

$$E_p = \frac{\gamma E - E_e}{\eta} = \left(\lambda \cdot \sum_{n=1}^N \Gamma_n^2 \left(\frac{T_n^2}{8\pi} M_n^* S_{a,n}^2 \right) - \frac{1}{2} M \cdot \left(\frac{T_e}{2\pi} \frac{V_y}{W} g \right)^2 \right) \cdot \eta^{-1}. \quad (16)$$

The rotation related to the plastic area of the frame (θ_p) will be equal to the difference existing between the total elastic and plastic rotation of the frame and the elastic rotation. In this paper, nonlinear static analysis is performed to accurately determine θ_p . Also, the rotation of a point on the curve whose slope changes is considered as the value of the elastic rotation.

The energy obtained from equation (16) must be dissipated by the plastic hinges shown in Figure 3, which is equal to

$$E_p = \left((m+1)M_{pc} + 2 \sum_{j=1}^m \mu_j \sum_{i=1}^n \beta_i M_{pbr} \right) \theta_p, \quad (17)$$

where M_{pbr} refers to the reference moment of the plastic beam at the j th opening, M_{pc} indicates the plastic moment of the base of the columns on the first story, m represents the number of frame openings, n stands for the number of frame stories, and β_i is the coefficient of the resistance distribution

$$V_y \left(\frac{\sum_{i=1}^n W_i h_i^{k+1}}{\sum_{i=1}^n W_i h_i^k} \right) \theta_p + \sum_{i=1}^n W_i \frac{\theta_p^2 h_i}{2} = \left(\gamma \cdot \sum_{n=1}^N \Gamma_n^2 \left(\frac{T_n^2}{8\pi} M_n^* S_{a,n}^2 \right) - \frac{1}{2} M \cdot \left(\frac{T_e}{2\pi} \frac{V_y}{W} g \right)^2 \right) \cdot (\eta)^{-1}, \quad (19)$$

where K is equal to

$$\begin{aligned} K &= 0.5T + 0.75, \\ \text{if } T \leq 0.5 &\longrightarrow k = 1, \\ \text{if } T \geq 2.5 &\longrightarrow k = 2. \end{aligned} \quad (20)$$

In the base shear relation, as calculated by the energy method, the effects of $P - \Delta$ are not considered. To apply the effects of $-\Delta$, we can use its value by adding its value to the lateral loads of equation (21).

$$F_i^p = F_i + \Delta F_i = \alpha_i V_y + W_i \theta_u, \quad (21)$$

where ΔF_i is the additional lateral load due to gravity loads, F_i refers to the seismic force at the level i , W_i is the weight of the story level, θ_u is the angle of the rotation of the story, and α_i is the ratio of the lateral force, which is distributed at the story level to the base shear.

where T_{eff} is the main rotation of the structure.

According to equations (1), (7), (8), and (10), the total plastic energy a structure must dissipate during an earthquake for a given system with multidegrees of freedom is equal to

of the beams (the value of which is mentioned below) on the 1st story. Also, $\mu_j = l_r/l_j$ is the reference moment coefficient of the beams, which equals the ratio of the length of the reference opening to the length of the j th opening.

After yield, the external forces should be in equilibrium with the internal ones. By equating the energy dissipated in the plastic state with the external one, which is done by lateral forces and gravitational loads, we can act according to equation (18):

$$E_p = V_y \left(\frac{\sum_{i=1}^n W_i h_i^{k+1}}{\sum_{i=1}^n W_i h_i^k} \right) \theta_p + \sum_{i=1}^n W_i \frac{\theta_p^2 h_i}{2}. \quad (18)$$

To obtain the frame's base shear with a suitable estimation, the input energy of the dissipated earthquake (by equation (16)) can be equal to the work which is done by external forces (on plastic hinge), which includes lateral and gravitational loads according to equation (19).

By solving the quadratic equation of equation (19), the base shear value will be obtained. Once the base shear is determined, the design force of each level is obtained.

To calculate the beam's M_{pbr} , the columns plastic moment, M_{pc} , must be properly estimated. This appropriate value is determined by imposing the prevention of the formation of soft-story failure in the first story. For this purpose, plastic hinges at the top and bottom of the first-story columns are assumed. The story columns' plastic moment capacity is determined to prevent the formation of this failure state according to Figure 5.

$$M_{pc} = 1.1 \left(\frac{V_y h_1 + W h_1 \theta_p}{2(m+1)} \right). \quad (22)$$

The parameters of this relation have been introduced before, and the factor 1.1 is the overstrength factor to account for possible overloading due to strain hardening [28].

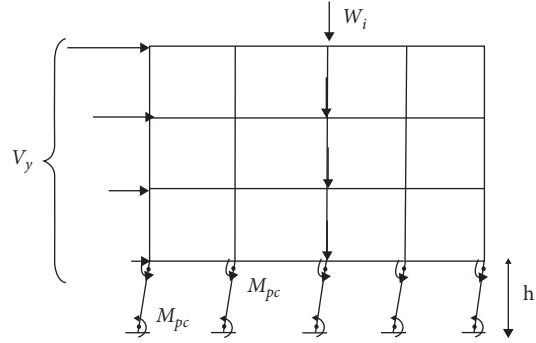


FIGURE 5: Soft-story failure mode.

The coefficient of resistance distribution, β_i , plays a significant role in structures' seismic response. This coefficient depends on the structures' hardness as well as lateral strength along the height. β_i must be properly selected to match the forces exerted during the earthquake. It also ensures that the incoming energy is dissipated in the structure, thus preventing damage from being concentrated on one story. Numerous numerical analyses have been previously conducted to obtain the best resistance distribution of the beams. The aim was to obtain a function that could well express the shear resulting from different earthquakes. As an initial approximation, the relative distribution of shear force at height during an earthquake can be approximated by the distribution of static shear force at height, as calculated from (23). Its value is equal to [29]

$$\beta_j = \left(\frac{V_i}{V_y} \right)^{1/2}, \quad (23)$$

where V_i and V_y are static shear in the i th level and the highest story level, respectively. The value of 1/2 is obtained using the least-squares method from the results which are obtained from several nonlinear dynamic analyses [29]. By establishing the equation of relations (17) and (18) and getting its unknowns, the value of M_{pbr} is obtained; then, based on that value, the design moment of the beams is calculated, as represented as follows:

$$\varphi M_{pbij} \geq \mu_j \beta_i M_{pbr}, \quad (24)$$

where φ refers to the resistance coefficient, and it is calculated based on AISC2016 [17]. M_{pbij} indicates the beam's plastic moment in the i th story and the j th opening.

3. Nonlinear Static Analysis

The finite element planar model related to the three steel frames described above was established by applying the SAP2000 software [20]. The finite element model is shown in Figures 6 and 7 (taking the 8-story steel frame as an example). The frame sections are adopted for all beams and columns. Each of the beams and columns includes only one element with two nodes. All steel frames are well connected. The column base is fixed too.

The finite element planar model was established completely, and then the related pushover analyses were carried out. The hinge P-M3 was then applied for the simulation of the frame columns' material nonlinearity. Also, the use was made of the hinge M3 to simulate the frame beams nonlinearity. The constitutive relation related to the hinge P-M-M can be seen in Figure 7. The vertical coordinate shows the bending moments, while the horizontal one represents the rotation. Plastic hinges' mechanical behavior can be determined according to ASCE41-17 [18]. In the pushover analysis, the material strength uses the average values, and the lateral force applies the inverted triangular distribution pattern.

For the nonlinear static method, the general relationship of the deformation force, as represented in Figure 8, can be used. The effects of strain hardening are considered by assuming a slope, which is equal to 3% of the slope of the elastic part. Details of this figure are given in ASCE41-17 [18].

The pushover analysis was done in accordance with ASCE41-17 [18]. To apply the combination of gravity loads and lateral load distribution patterns, in the combination of gravity and lateral loads, the upper and lower limits of gravity load effects, Q_G , were calculated from the relations (25) and (26).

$$Q_G = 1.1(Q_D + Q_L), \quad (25)$$

$$Q_G = 0.9Q_D, \quad (26)$$

where Q_D and Q_L are the effective seismic dead and live loads, respectively.

In the section related to examples and numerical results, to compare the results, all two methods were analyzed and examined based on nonlinear static analysis.

In the optimization process, target displacement for each of the candidate designs is computed by applying equation (27) to conduct the pushover analysis.

$$\delta_t = C_0 C_1 C_2 S_a \frac{T_e^2}{4\pi^2} g, \quad (27)$$

where C_0 , C_1 , and C_2 factors are determined on the basis of ASCE41-17 [18]. The structural effective fundamental period is shown by T_e , and the ground motion acceleration is indicated by g . Also, S_a denotes the spectral acceleration

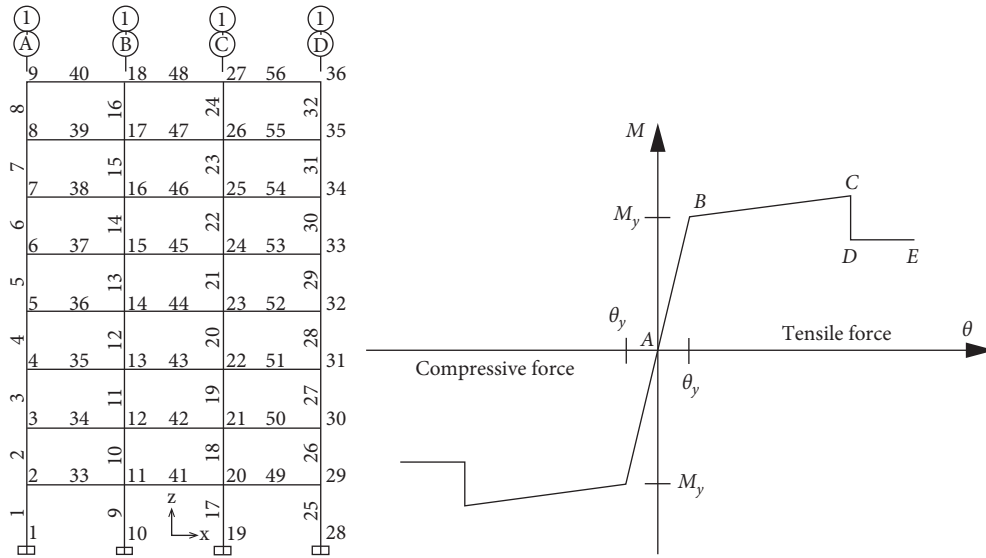


FIGURE 6: The 8-story steel frame's finite element planar model.

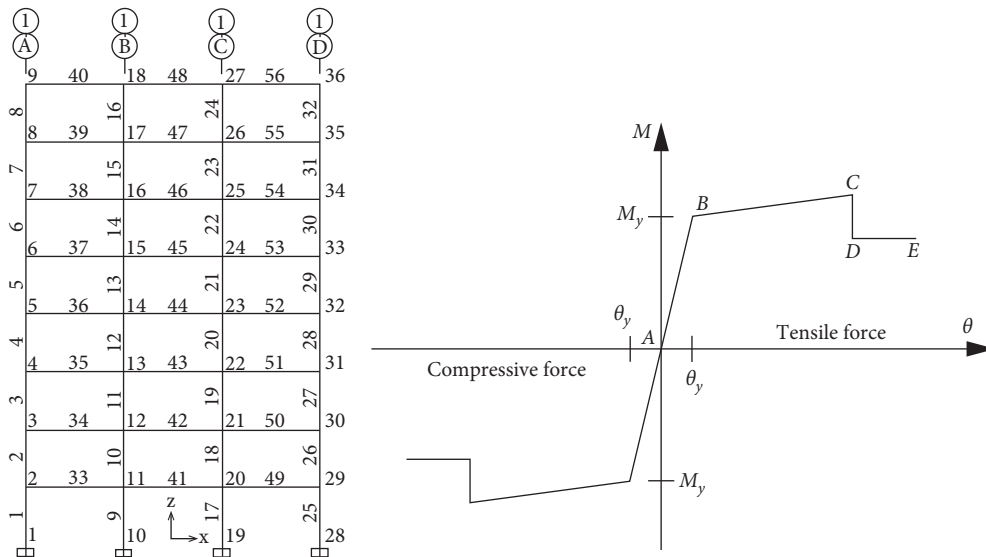


FIGURE 7: Constitutive relation of the hinge P-M-M.

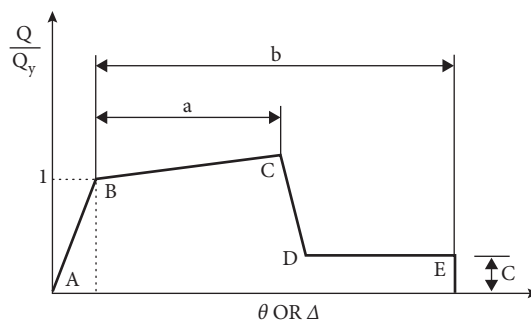


FIGURE 8: General force-deformation curve for members and components.

which is estimated according to the ASCE41-17 code [18]. The analysis is according to the assumption that the roof target displacement is equal to 0.004, 0.007, 0.025, and 0.05,

relative to the structure's total height. Each of these values represents the performance levels of OP, IO, LS, and CP. Control of the story drift is done for all functional levels;

however, the members' permissible rotation is checked for the last three target movements.

After performing a nonlinear analysis and getting the required results, the constraints are checked as follows:

- (a) For beams, according to the slenderness ratio, the constraint related to the member's rotation is controlled through equation (28).

$$\theta_{beam} \leq \theta_{all}^i \quad i = OP, IO, LS, CP. \quad (28)$$

In this relation, θ_{all}^i is equivalent to the rotation of the beam at its end, and θ_{beam} is the permissible displacement in ASCE41-17 [18], according to the desired level of performance.

For columns, based on the displacement of the control, the permissible rotation must be controlled by relation (29). According to the control force, the control of the force ratio in the final stage of the analysis related to the column capacity should be done based on equation (30).

$$\theta_{column} \leq \theta_{all}^i \quad i = OP, IO, LS, CP, \quad (29)$$

$$\frac{P_c}{\phi P_n} + \frac{M_c}{\phi M_n} \leq 1. \quad (30)$$

In this relation, P_c and ϕP_n refer to the axial force and the nominal capacity of the column, respectively. Further, M_c and ϕM_n indicate the columns' present bending moment and nominal capacity, respectively. θ_{column} is also permissible displacement in ASCE41-17 [17] according to the desired performance level.

Story drift constraint can be controlled according to relation (31):

$$\Delta_{interstory}^i \leq \Delta_{allinterstory}^i, \quad (31)$$

where $\Delta_{interstory}^i$ is the story drift based on the desired performance level and $\Delta_{allinterstory}^i$ refers to the allowable story drift in OP to CP performance levels.

Strong-Column Weak-Beam constraint is defined as shown in relation (32):

$$\frac{\sum M_{Pcolumn}}{\sum M_{Pbeam}} \geq 1. \quad (32)$$

Based on this relation, $M_{Pcolumn}$ and M_{Pbeam} refer to the plastic moment of the columns and beams, respectively.

The flowchart of the modified energy method is shown in Figure 9.

4. Numerical Examples

4.1. Introducing Steel Frame Models and Controlling Structural Design Criteria. In the present study, three two-dimensional 8-, 16-, and 24-story frames were modeled to compare different design methods. The number of spans, the length of each span, and the height of the stories were 5, 5, and 3 meters, respectively. The dead and live loads on the stories were 5000 and 2000 kg/m, respectively. All sections used in the

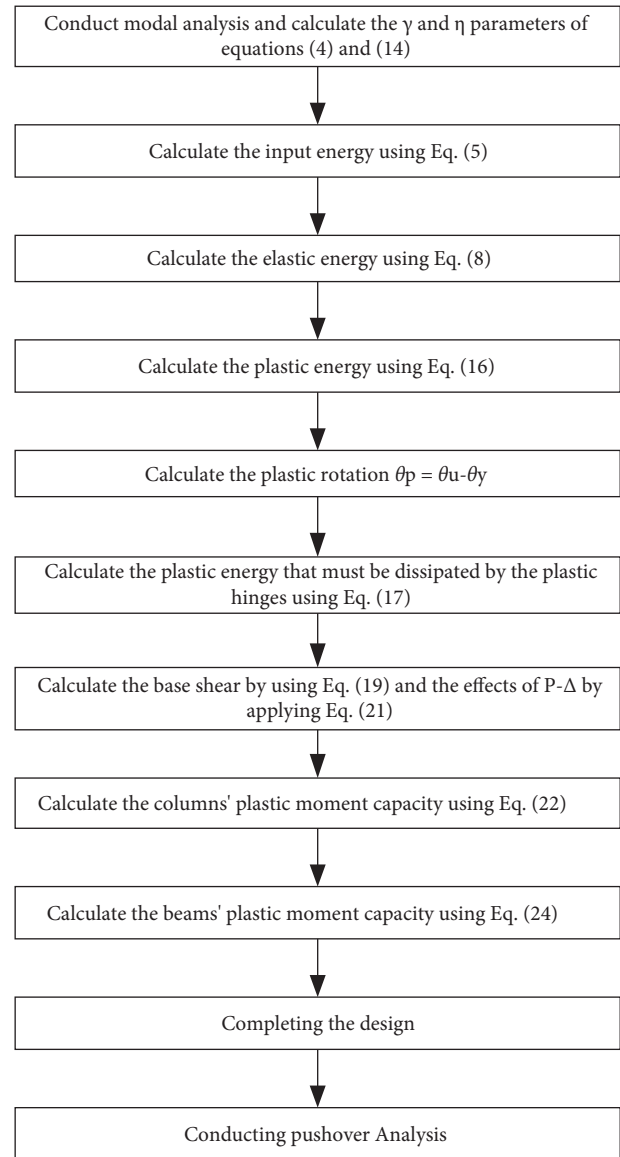


FIGURE 9: Flowchart of the modified energy method.

modeling were selected from W-shaped sections of the AISC database [17]. The important point that has been observed in the selection of sections was that all selected sections had seismic compression conditions. The specifications of the steel materials modeled in this paper are as described in Table 2.

Seismic loading in the static analysis of structures was done based on ASCE7-16 [29]. For designing by the LRFD method, the design location of the frames in an area with the soil class D (an area with a very high relative risk) was assumed, and residential use was considered for the buildings. According to ASCE 7-16 standards [29], the coefficient $S_1 = 0.63$ and the coefficient $S_s = 1.5$ were considered. A permissible relative displacement control of 0.02 was used for the structures. The modeling and design of the frame were carried out using the LRFD method by applying the SAP2000 software [19].

In structural models, the lateral load-resistant system is a special steel moment frame, and all nodal connections of the structures are rigid.

TABLE 2: Specifications of the steel materials.

$W = 7850 \text{ kg/m}^3$	Unit weight of the material volume
$E = 2.0e + 10 \text{ kgf/m}^2$	Modulus of elasticity
$\nu = 0.3$	Poisson's ratio
$F_y = 24e + 6 \text{ kgf/m}^2$	Stress yield of steel materials
$F_u = 37e + 6 \text{ kgf/m}^2$	Ultimate tensile stress of steel materials

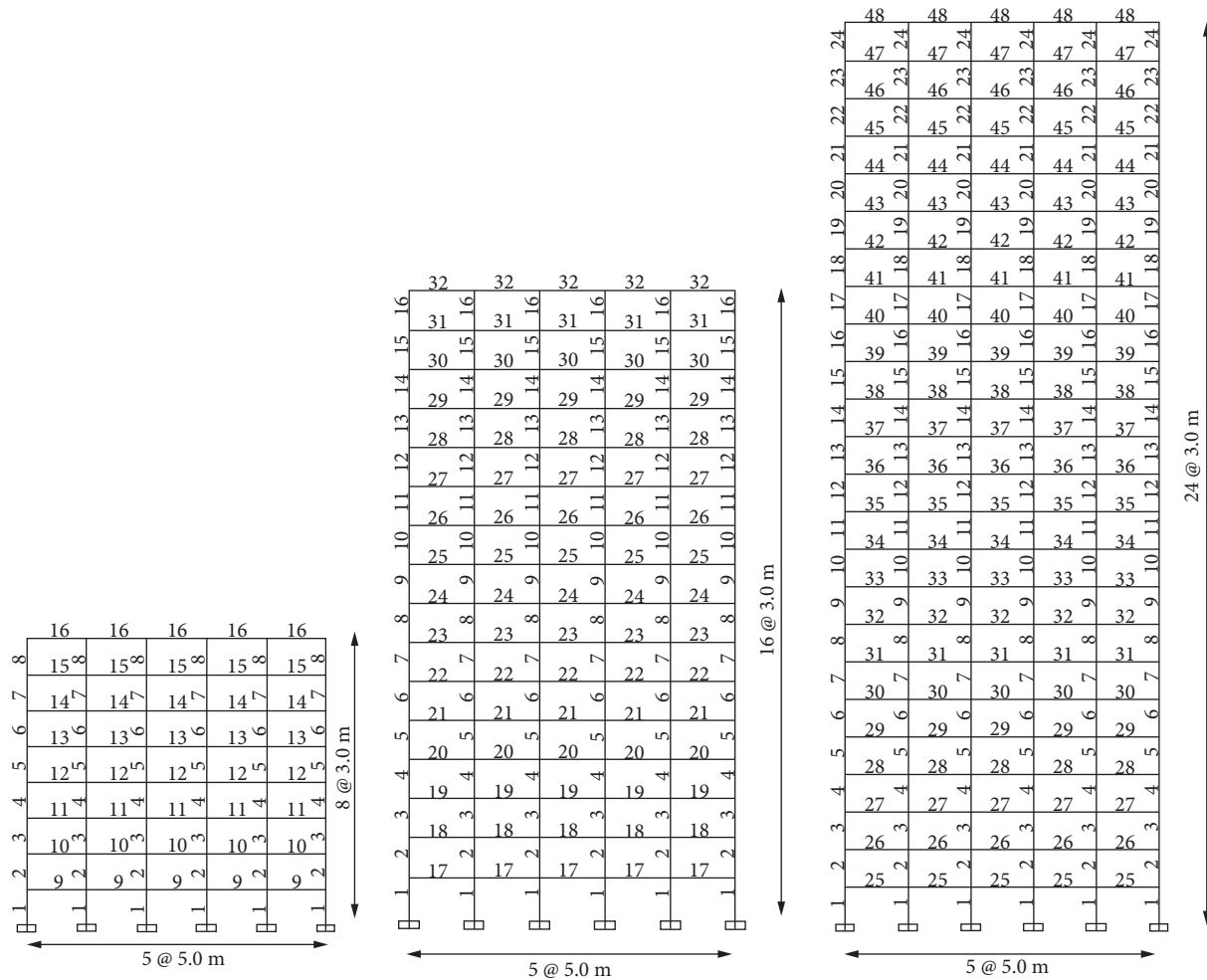


FIGURE 10: Typology of the designed models of 8-, 16-, and 24-story structures.

The codes related to the energy method have been written in the MATLAB software [18]. The nonlinear static analyses of the frames were performed in the SAP2000 software [18], and SAP2000 software [19] was linked to the MATLAB software [18]. Different types of sections are shown in Figure 10. Also, the section specifications of the two methods are represented in Tables 3 to 5.

The results related to the energy and LRFD methods in shifting the target locations IO, LS, and CP were obtained. The results of shifting the target location LS are presented as the design results obtained through these methods. Also, the final result is presented for all three examples according to Tables 3–5 for the LRFD and energy methods.

4.2. Controlling the Results of Frame Analyses. After designing the structure in accordance with the AISC 2016 standard [16] and performing all controls required by the codes, the ratio of the minimum, maximum, and average stress of members and the ratio of the capacity of beams to columns are shown in Tables 6–8.

One of the most important controls performed on a special moment frame or a highly ductile moment frame is the Strong-Column Weak-Beam control. According to this rule, the plastic hinge should be formed first in the beams; then, the structure can withstand further deformation without any reduction of strength. As can be seen from the above tables, the capacity of the beams to the

TABLE 3: Final design results of energy and LRFD methods in 8-story structures.

		Type number and cross section assigned to each of the beams and columns of the frame								Design methods			
		10	9	8	7	6	5	4	3	2	1		
13													
W12×79	W14×74	W14×74	W14×74	W16×36	W24×84	W27×102	W27×102	W30×148	W30×148	W30×148	W36×160	LRFD	
W21×50	W21×55	W24×55	W24×55	W21×55	W24×76	W30×90	W27×84	W30×90	W30×108	W33×118	W33×130	Energy	
									16	15	14		
									W10×54	W10×54	W12×79	LRFD	
									W14×37	W18×40	W21×44	Energy	

TABLE 5: Final design results of energy and LRFD methods in 24-story structures.

	Type number and cross section assigned to each of the beams and columns of the frame														Design methods					
	10	11	12	13	14	15	16	17	18	19	20	21	22	23		24				
W40 × 372	W40 × 372	W40 × 372	W40 × 372	W40 × 372	W40 × 397	W40 × 397	W40 × 397	W40 × 397	W40 × 397	W40 × 397	W40 × 397	W40 × 397	W40 × 431	W40 × 431	W40 × 431	W40 × 431	W40 × 431	W40 × 431	W40 × 431	LRFD
W40 × 372	W40 × 503	W40 × 503	W40 × 503	W40 × 503	W40 × 503	W40 × 503	W40 × 503	W40 × 503	W40 × 503	W40 × 503	W40 × 503	W40 × 503	W40 × 593	W40 × 593	W40 × 593	W40 × 593	W40 × 593	W40 × 593	W40 × 593	Energy
26	25	24	24	23	23	21	21	20	20	19	18	18	17	17	16	16	15	15	14	14
W18 × 86	W18 × 86	W21 × 93	W27 × 114	W27 × 114	W30 × 148	W30 × 148	W30 × 148	W33 × 169	W33 × 263	W33 × 263	W33 × 263	W33 × 263	W33 × 263	W33 × 263	W33 × 263	W33 × 263	W33 × 263	W33 × 263	W33 × 263	LRFD
W21 × 68	W21 × 68	W21 × 55	W33 × 130	W33 × 130	W40 × 149	W40 × 149	W40 × 183	W40 × 211	W40 × 211	W40 × 211	W44 × 230	W44 × 230	W44 × 262	W44 × 262	W44 × 290	W44 × 290	W44 × 324	W44 × 324	W44 × 324	Energy
39	38	37	36	36	34	34	33	32	32	31	31	30	30	30	29	29	28	28	27	27
W16 × 77	W16 × 77	W18 × 76	W18 × 76	W18 × 76	W18 × 76	W18 × 76	W18 × 76	W18 × 76	W18 × 76	W18 × 76	W18 × 76	W18 × 76	W18 × 76	W18 × 76	W18 × 76	W18 × 76	W18 × 86	W18 × 86	W18 × 86	LRFD
W21 × 62	W21 × 62	W24 × 62	W24 × 62	W24 × 62	W24 × 62	W24 × 62	W21 × 68	W21 × 68	W21 × 68	W21 × 68	W21 × 68	W21 × 68	W21 × 68	W21 × 68	W21 × 68	W21 × 68	W21 × 68	W21 × 68	W21 × 68	Energy
				48	47	47	46	45	45	44	44	43	43	42	42	41	41	40	40	40
			W12 × 58	W12 × 58	W12 × 58	W12 × 58	W12 × 58	W12 × 58	W12 × 58	W16 × 77	W16 × 77	W16 × 77	W16 × 77	W16 × 77	W16 × 77	W16 × 77	W16 × 77	W16 × 77	W16 × 77	LRFD
			W16 × 31	W16 × 40	W16 × 40	W21 × 44	W18 × 50	W18 × 50	W18 × 50	W21 × 50	W21 × 50	W21 × 50	W21 × 50	W21 × 50	W21 × 50	W21 × 50	W24 × 55	W24 × 55	W24 × 55	Energy

TABLE 6: Results of the analyses of LRDF, energy, and E-WOA methods in 8-story structures.

Average capacity of beams to columns	Minimum capacity of beams to columns	Maximum capacity of beams to columns	Average stress ratio	Minimum stress ratio	Maximum stress ratio	Design methods
0.8669	0.6357	0.9664	0.7243 0.7006	0.5541 0.3723	0.9398 0.9346	Beams Columns LRFD
0.8492	0.3757	1.0	0.7655 0.6882	0.5634 0.3155	0.9722 1.011	Beams Columns Energy

TABLE 7: Results of the analyses of LRDF, energy, and E-WOA methods in 16-story structures.

Average capacity of beams to columns	Minimum capacity of beams to columns	Maximum capacity of beams to columns	Average stress ratio	Minimum stress ratio	Maximum stress ratio	Design methods
0.5278	0.01	0.9039	0.7703 0.6650	0.5321 0.3234	0.9438 0.9793	Beams Columns LRFD
0.310	0.01	0.7412	0.8532 0.5619	0.5126 0.2845	1.018 0.8175	Beams Columns Energy

TABLE 8: Results of the analyses of LRDF, energy, and E-WOA methods in 24-story structures.

Average capacity of beams to columns	Minimum capacity of beams to columns	Maximum capacity of beams to columns	Average stress ratio	Minimum stress ratio	Maximum stress ratio	Design methods
0.2722	0.01	0.6528	0.8064 0.5301	0.4388 0.2242	0.9621 0.9394	Beams Columns LRFD
0.1937	0.01	0.6812	0.8429 0.4333	0.4691 0.2395	1.00 0.6505	Beams Columns Energy

columns in the energy method is, on average, lower than that in the LRFD methods.

4.3. Lateral Displacement Control of the Structure. Lateral displacement control of the structure is performed according to the clause 12.12.1 of the ASCE7-16 code [29]. Accordingly, the relative nonlinear lateral displacement of the story, δ_M , will be calculated by equation (33). In this relation, C_d refers to the magnification coefficient of the structure's lateral displacement owing to the nonlinear behavior, δ_{xe} indicates the relative linear displacement of the story, and I_e is the coefficient of the importance of the building.

$$\delta_M = \frac{C_d \times \delta_{xe}}{I_e}. \quad (33)$$

The value of δ_M , as obtained by considering the effects of $-\Delta$, should not exceed the allowable value of equation (34). In the above relation, h_{sx} is the story height.

$$\Delta_a = 0.02h_{sx}. \quad (34)$$

Figure 11 shows the relative lateral displacement diagrams of 8-, 16-, and 24-story structures using the energy and LRFD methods.

5. Results of the Nonlinear Static Analysis of Frames

In all three examples, following the design of the structures by energy and LRFD methods, for the purpose of comparison, after adjusting the plastic hinges of the frame members and conducting nonlinear static analysis, dead and live loads are applied as the dynamic loads; by

continuing to apply gravitational loads, pushing of structures is done with the lateral static load pattern introduced in the paper. The frames are pushed to a greater displacement than the target displacement and to the point to better study the behavior of the structure and the formation of plastic hinges.

5.1. Example 1: 8-Story Frame. Figure 12 shows the plastic hinges created on 8-story frames designed by the energy and LRFD methods.

Figures 13 and 14 have been applied to better understand the process of forming plastic hinges on the frames. In these figures, on the diagram, the pushing images of plastic hinge formation in different stages are shown.

According to the diagram represented in Figure 13, which is related to the LRFD method, the poor performance of the frame in the nonlinear range can be seen. Also, in the initial stages, the pushing of the side column of the second story has entered its nonlinear state; then, the other columns of this story and the last one have also entered the nonlinear state. However, the optimal position for the frame mechanism is the plastic hinge of the two ends of all beams; this is followed by plastic hinges of the foot of the ground story columns. In this figure, the red line shows that the plastic hinges are not formed properly.

In the graph presented in Figure 14, which is related to the energy design method, the area below the force-displacement curve is quite larger than in the previous case, and in the nonlinear mode, the nonlinear capacity of the members is being used more appropriately. Also, after the formation of plastic hinges of the two ends of the frame beams and the ground story column bases, the columns of the other stories have entered their own nonlinear area.

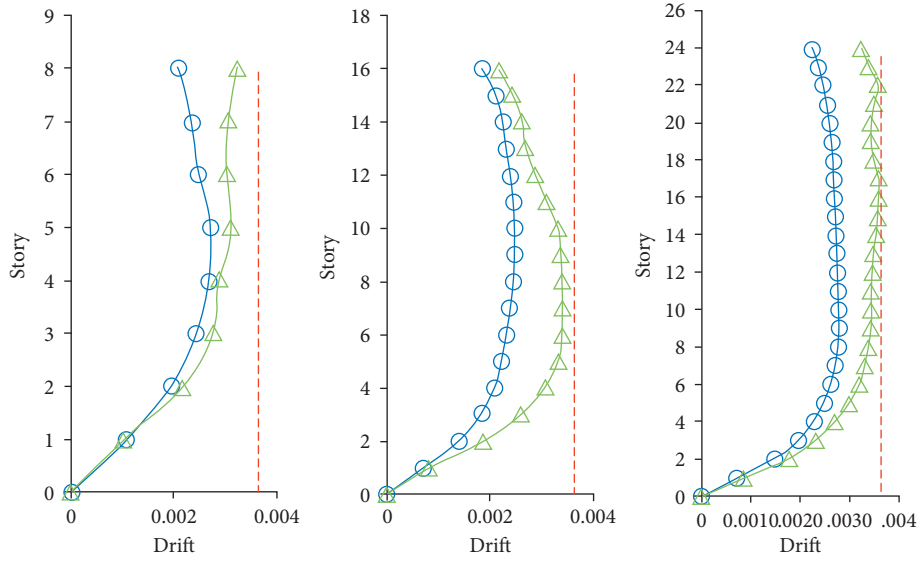


FIGURE 11: Comparing diagrams of the relative lateral displacement of 8-, 16-, and 24-story buildings.

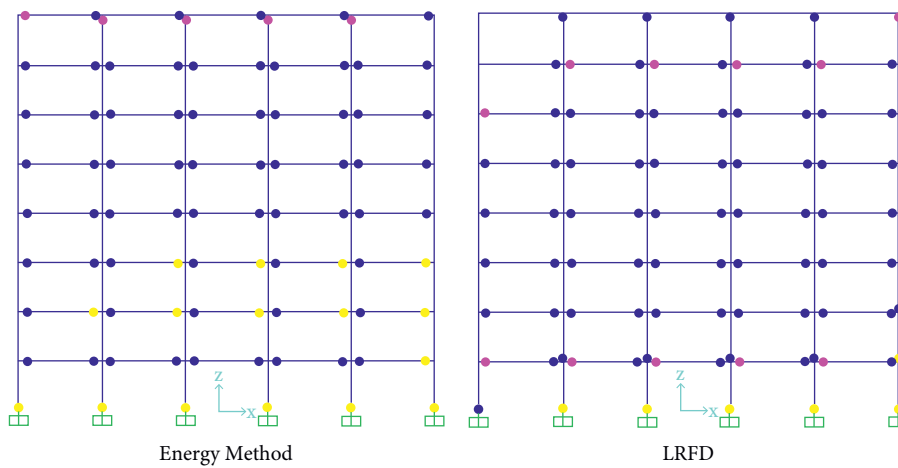


FIGURE 12: Plastic hinge created on an 8-story frame designed by the energy and LRFD methods.

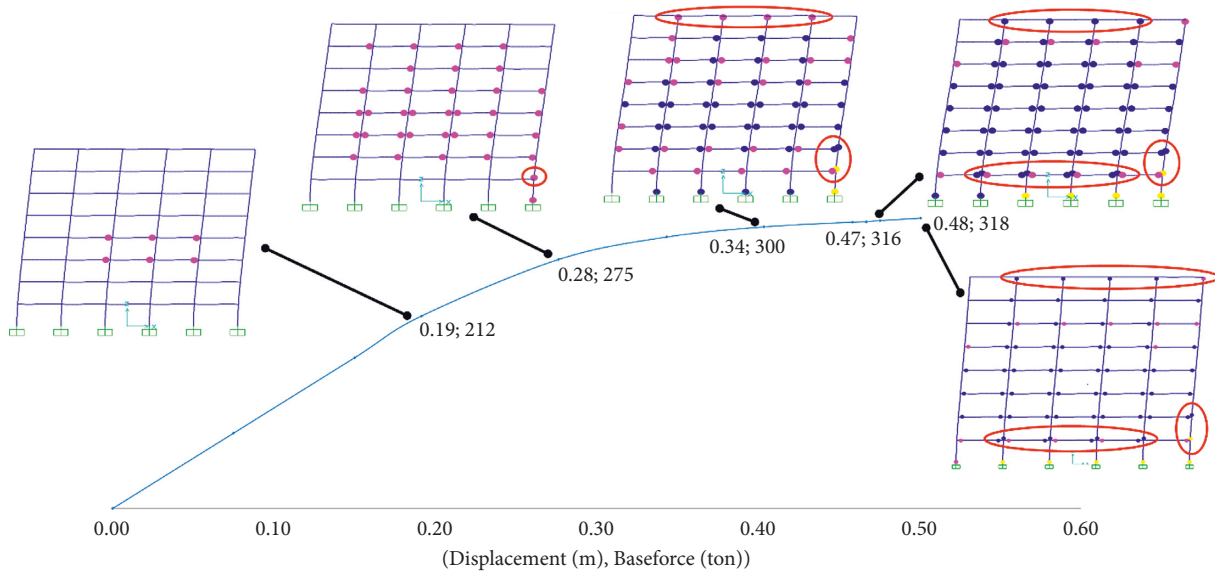


FIGURE 13: Pushover graph of an 8-story frame designed by the LRFD method.

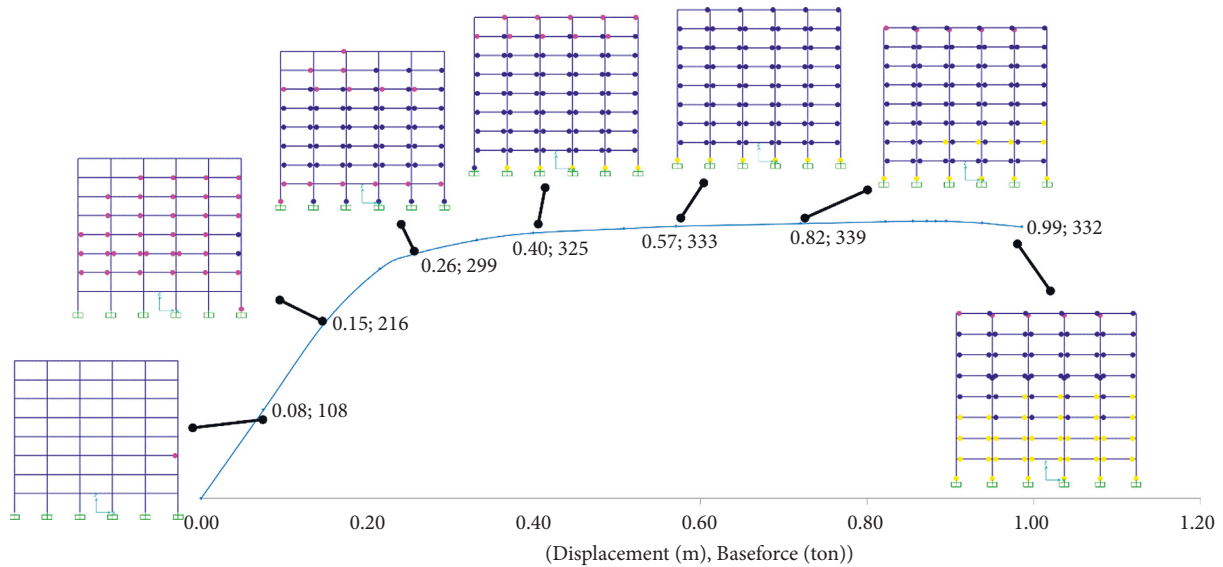


FIGURE 14: Pushover graph of an 8-story frame designed by the energy method.

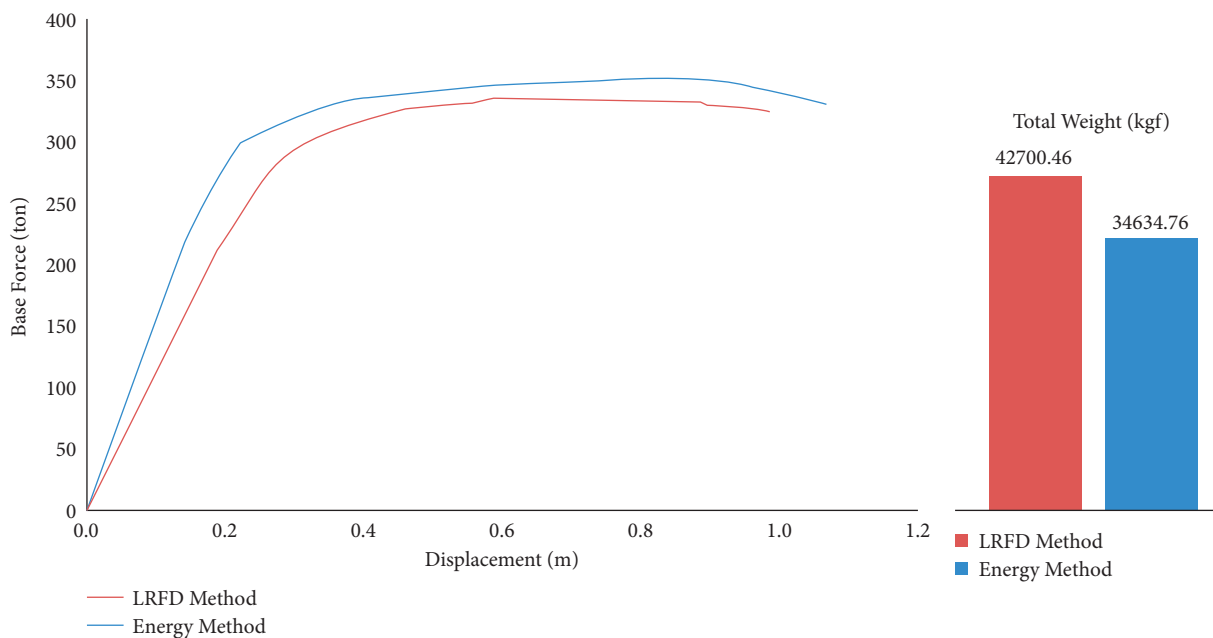


FIGURE 15: Comparing the push diagrams and the weight of the 8-story steel frame designed by the energy and LRFD methods.

As can be seen in Figures 13 and 14, in the target displacement of the 8-story frame, which is 0.35 m, for the frame which is designed by the energy method, the formation of plastic hinges is expanded in higher stories and beams. However, in the frame designed by the LRFD method, with the plastic hinge formation in the upper stories' columns, a local mechanism has been created, reducing the resistance. In Figure 15, which represents the push diagram of LRFD methods, energy along with the structure's weight is compared. The structure's weight by energy method is 34.634 tons, which is lower than that of the LRFD method with a weight of 42.7 tons. In the frame designed by the energy method, the surface below the frame diagram is larger than that of the

LRFD method, thus showing that the energy method has used the nonlinear capacity of the members more appropriately.

5.2. *Second Example: 16-Story Frame.* Figure 16 shows the plastic hinges created in the 16-story frames, designed by the energy and LRFD methods.

Figures 17 and 18 have been used to better understand how plastic hinges are formed in the frames. In these figures, on the push diagram, the images related to plastic hinge formation in different stages are shown.

Figure 17 represents the diagram of a frame designed by the LRFD method. In this diagram, the poor performance of

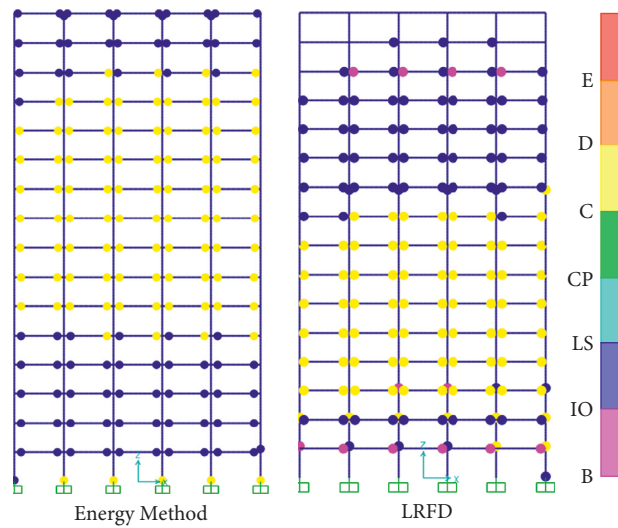


FIGURE 16: Plastic hinges created in the 16-story frames designed by the energy and LRFD methods.

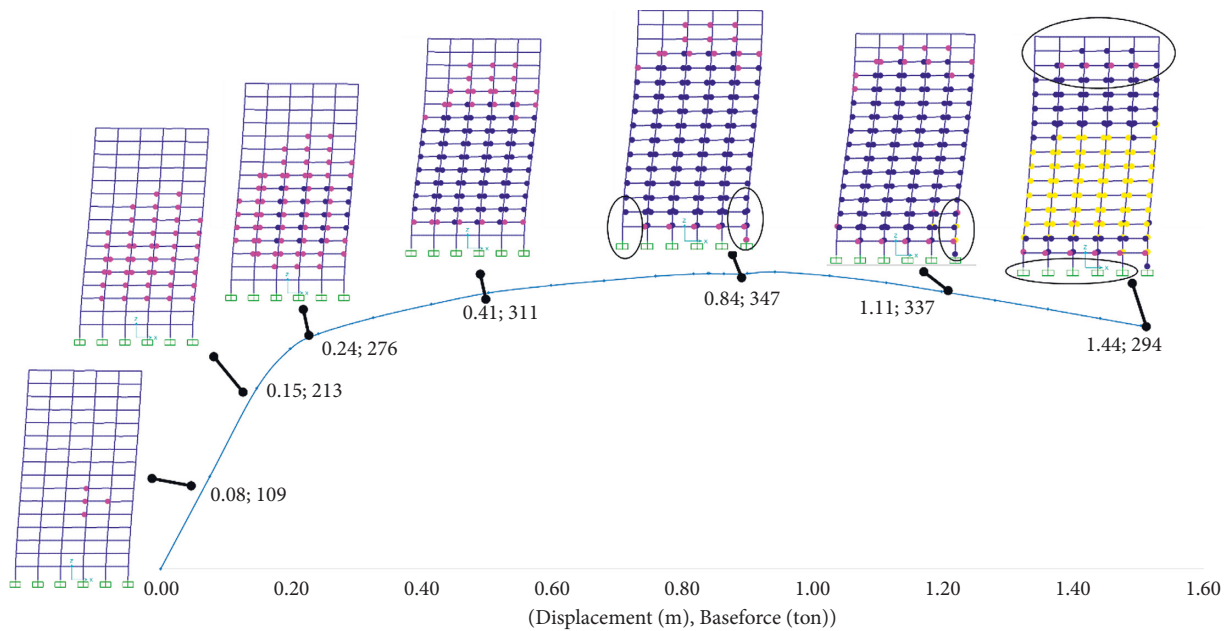


FIGURE 17: Push diagram of the 16-story frame designed by the LRFD method.

the frame in the nonlinear range can be seen. Also, beyond the 40 cm deformation of the roof, plastic hinges have been formed in many columns of the second story. Then, the plastic hinges have been created in the middle stories. In this diagram, it can be seen that some of the beams in the upper story and the base of the ground story columns still maintain their linear state, thus indicating the weakness of the LRFD method in the optimal use of the member’s capacity.

Figure 18 shows the push diagram along with the steps of plastic hinges of the members in the frame designed by the energy method. In this figure, as can be seen, the area below the force-displacement diagram of the frame is quite large, and in the nonlinear mode, the energy design method uses the nonlinear capacity of the members more appropriately. Also, the columns did not enter their nonlinear state until

the plastic hinges were formed in the beams at the two ends of the frame and the ground story columns.

As can be seen in Figures 17 and 18, in the target displacement of the 16-story frame, which is 0.6 m, like the 8-story one, for the frame designed by the energy method, plastic hinge formation is expanded in the upper stories and in the beams. However, in the frame designed by the LRFD method, due to the plastic hinge formation in the columns of the upper stories, a local mechanism has been created, thus reducing the strength. Meanwhile, in the structure, which is designed by the energy method, the plastic hinge formation at the columns’ foot indicates that the capacity of the structure is used more extensively.

Figure 19 shows a comparison of the energy and weight of the 16-story structure designed by two methods. The

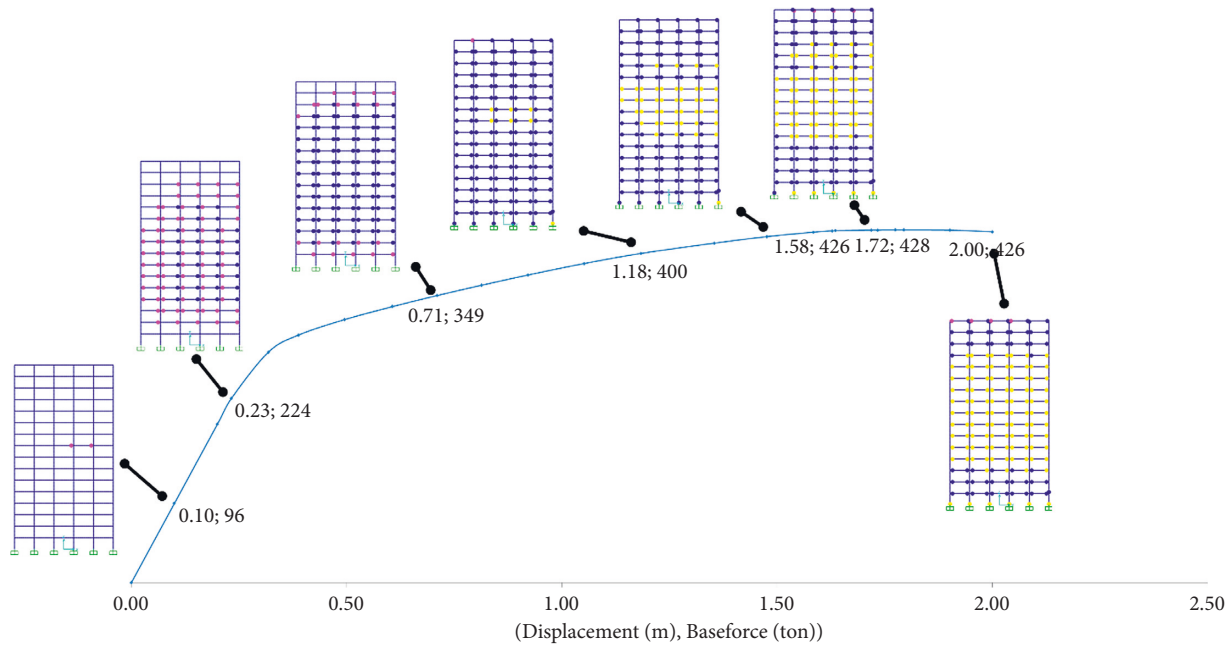


FIGURE 18: Push diagram of the 16-story frame designed by the energy method.

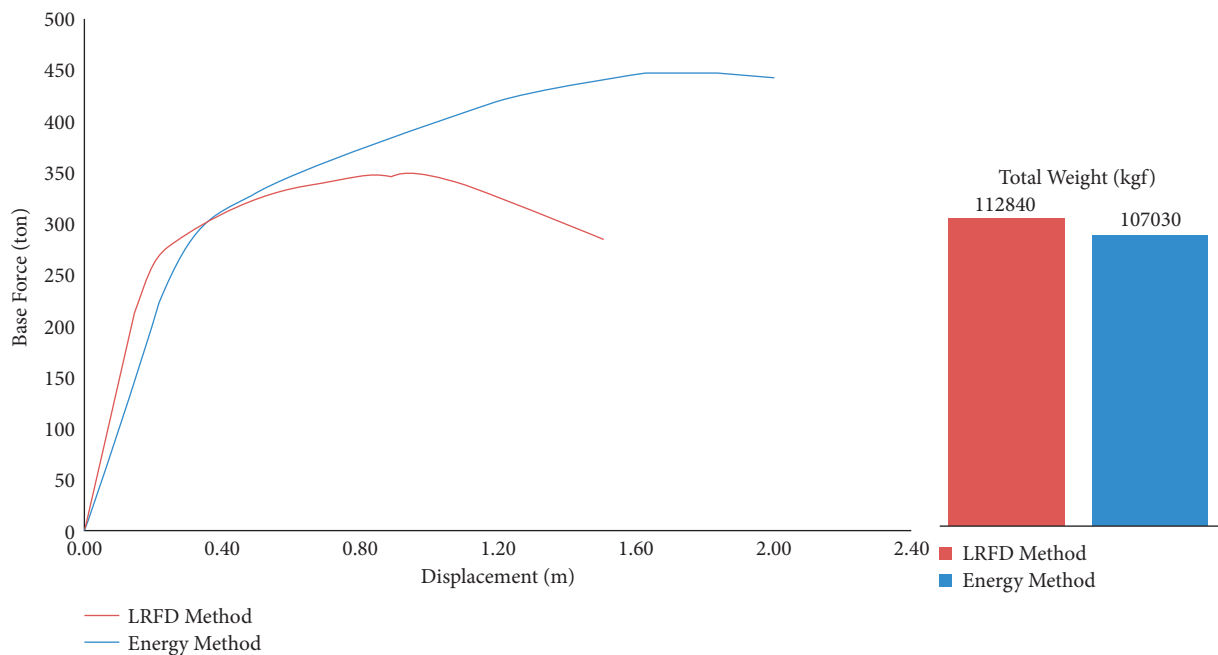


FIGURE 19: Comparing the push diagram and weight of the 16-story steel frame designed by the energy and LRFD methods.

structure’s weight by the energy method is 107.030 tons, which is slightly lower than that of the LRFD method (112.840 tons). Also, in the frame designed by the energy method, the area below the force-displacement diagram is larger than that of the LRFD method, thus showing that the energy method has used the nonlinear capacity of the members more appropriately.

5.3. *Third Example: 24-Story Frame.* Figure 20 shows the plastic hinges created in the 24-story frames designed by the energy and LRFD methods.

Figures 21 and 22 help to better understand how plastic hinges are formed in the frames. In these figures, on the push diagram, the images of plastic hinge formation in different stages are shown.

Figure 21 represents the diagram of a frame designed by the LRFD method. In this diagram, the poor performance of the frame in the nonlinear range can be seen. It is worth noting that, beyond the target displacement of the roof, plastic hinges are formed in almost all columns of the second story. Then plastic hinges are created in the columns of the middle stories. In this diagram, it can be seen that some of

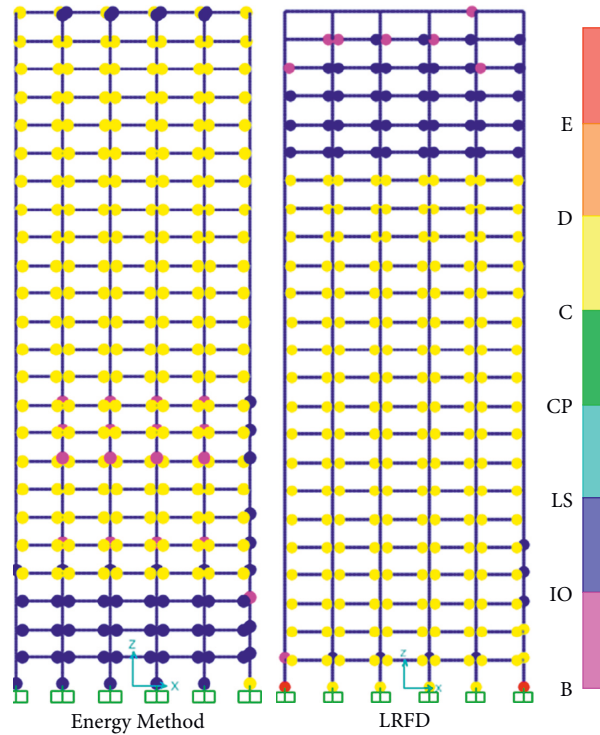


FIGURE 20: Plastic hinges created in the 24-story frames designed by the energy and LRFD methods.

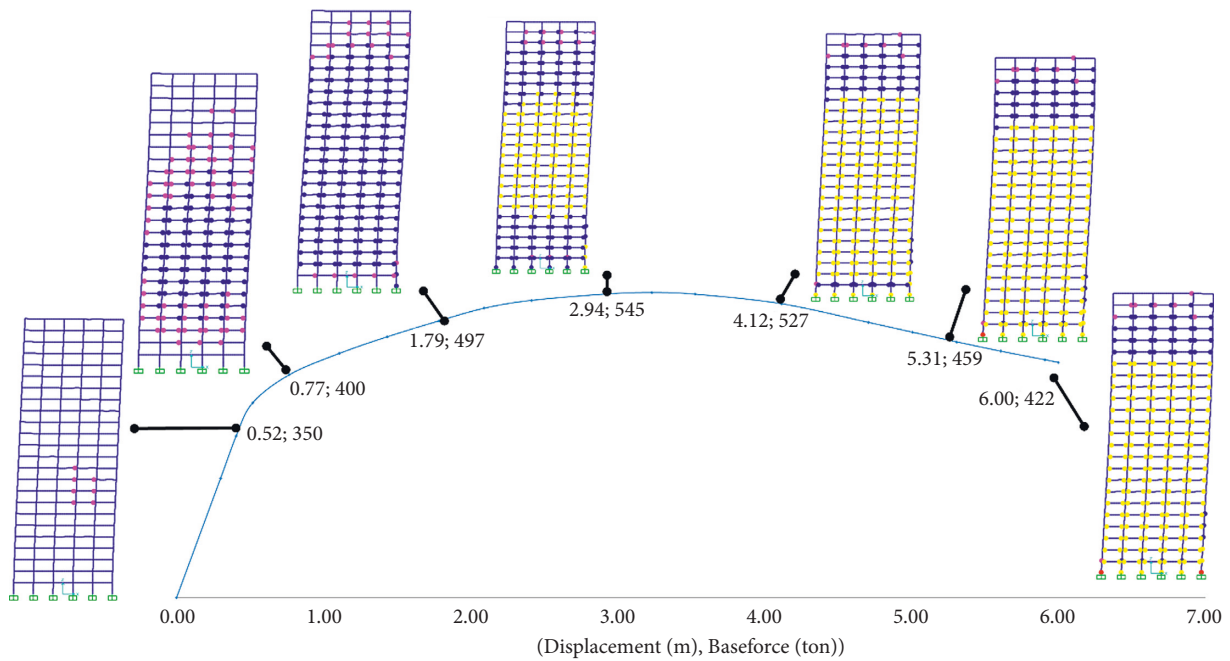


FIGURE 21: Push diagram of a 24-story frame designed by the LRFD method.

the beams in the upper story and the footings of the ground story columns still maintain their linear state, thus indicating the weakness of the LRFD method in the optimal use of the member’s capacity.

Figure 22 shows the push diagram along with the steps of plastic hinges formed in the members of the frame designed by the energy method. In this figure, as can be seen, the area below the push diagram of the frame is larger,

and in the nonlinear mode, the energy design method uses the nonlinear capacity of the members more extensively. It is notable that the columns did not enter their nonlinear area until the plastic hinges were created in the beams at the two ends of the frame and at the base of the ground story columns.

As can be seen in Figures 20 and 21, in the target displacement of the 24-story frame, which is 0.9 m, such as the

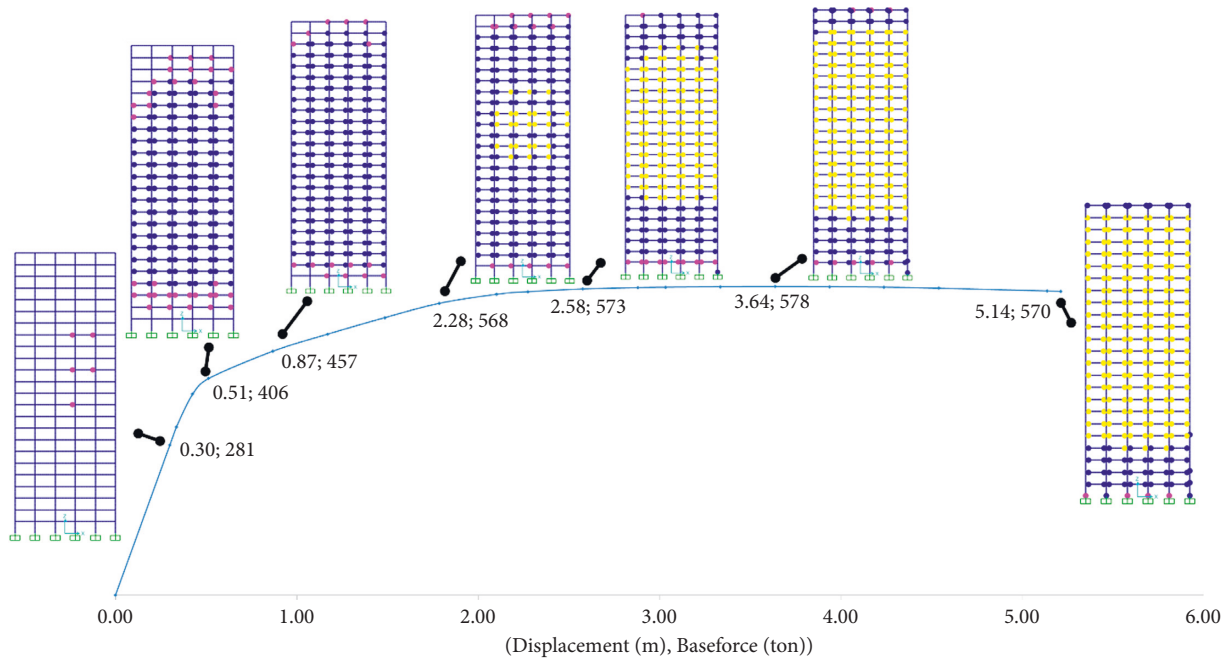


FIGURE 22: Push diagram of the 24-story frame designed by the energy method.

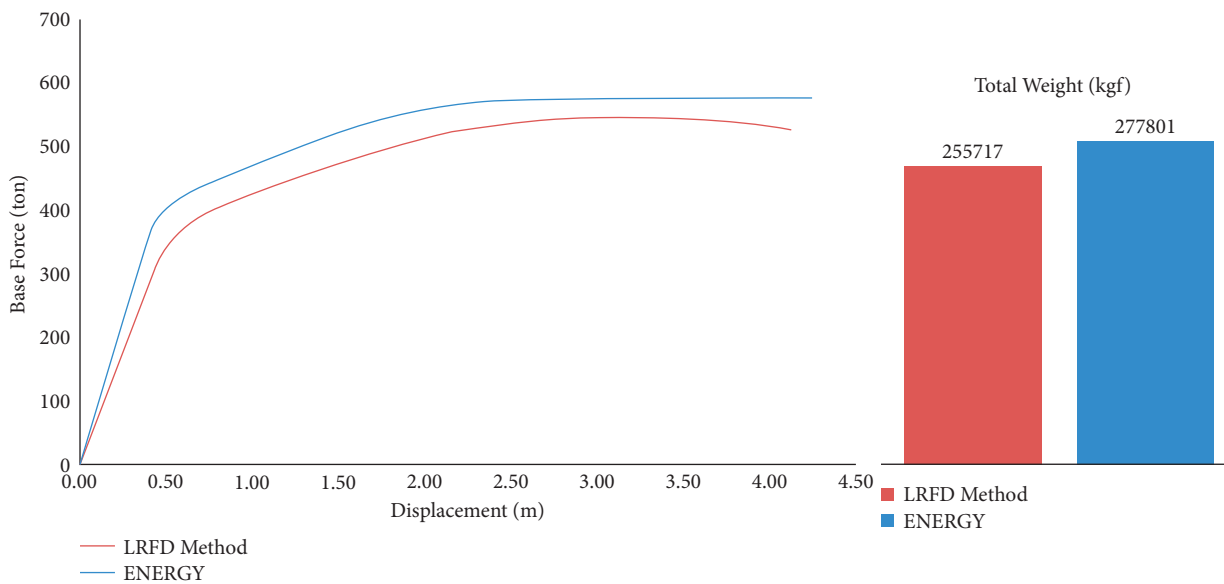


FIGURE 23: Comparing the push diagram and weight of the 24-story steel frames designed by the energy and LRFD methods.

8- and 16-story buildings, for the frame designed by the energy method, the plastic hinge formation was expanded in the upper stories and beams. However, in the frame designed by the LRFD method, due to the plastic hinge formation in the columns of the upper stories, a local mechanism has been created, reducing the strength. It is worth noting that, in the structure designed by the energy method, the plastic hinge formation at the columns foot indicates that the capacity of the structure is used more extensively.

Figure 23 compares the push diagrams of the structure designed by LRFD and the energy methods. Although the weight of the structure by the energy method (277.801 tons)

is slightly higher than that of the LRFD method (255.717 tons), the nonlinear state and the energy absorption level of the former are better, showing that the LRFD method has not well used the capacity of its structural members.

6. Conclusion

In this paper, based on the modified equilibrium energy method, a new formulation is proposed for design of moment frames subjected to seismic loading. The damping effect of hysteresis cycles, the effects of different modes on the seismic input energy, the $P - \Delta$ effects, and the target

displacement have been seen in the formulation. Furthermore, the correction factor, as the ratio of the energy absorbed by the inelastic system to that of the equivalent elastic system, has been considered.

In this paper, 8-, 16-, and 24-story frames with lateral force resisting system of special steel moment frames have been designed by the proposed modified energy methods, as well as the design force method, according to AISC2016 code. Performance level criteria of ASCE41-17 code have been applied in a nonlinear analysis and design based on the desired performance of the frames. The results showed the following:

- (i) The distribution of the plastic hinges in the frames designed by the proposed energy method was more desirable than that in the frames designed by the LRFD method.
- (ii) For the frame, which is designed by the proposed energy method, the plastic hinges are formed and expanded in the upper stories and beams. However, for the frame, which is designed by the LRFD method, the plastic hinges are created in the columns of the upper stories, and a local mechanism is formed.
- (iii) For the structure designed by the energy method, the formation of plastic hinges at the columns' foot indicates that the structure's capacity is used more.
- (iv) A more uniform distribution of drift is seen in the structure, which is designed by the energy method compared to the LRFD method.
- (v) In the 8- and 16-story structures, the weight of the structure, which is designed by the energy method, is less than that obtained by the LRFD method.
- (vi) In the 24-story structure, a lower weight was obtained in the LRFD method as compared to the modified energy method.
- (vii) The study showed that the relationships presented in the codes in regard to the Strong-Column Weak-Beam rule cannot prevent local and undesirable mechanisms in severe earthquakes. Meanwhile, in structures designed by the energy method, undesirable mechanisms did not occur.

In general, using the modifications made on the input-output energy balance relations applied to the structure, the modified energy method can lead to more favorable results in the optimal distribution of plastic hinges and seismic energy dissipation as compared to the LRFD method.

Data Availability

The data used to support the findings of the study can be obtained from the corresponding author upon request.

Conflicts of Interest

The authors declare that there are no conflicts of interest regarding the publication of this paper.

References

- [1] G. W. Housner, "Limit design of structures to resist earthquakes," in *Proceedings of the 1st World Conference on Earthquake Engineering*, pp. 5.1–5.13, Oxford, England, March, 1956.
- [2] H. Akiyama, *Earthquake-Resistant Limit-State Design for Buildings*, University of Tokyo Press, Tokyo, Japan, 1985.
- [3] Fakhri-Niasar and Mohsen, "The energy spectrum of the Iranian earthquakes," Master of Science Thesis, Islamic Azad University, Science and Research Branch, Tehran, 1998.
- [4] H. Maleki and M. Ghafory-Ashtiany, "Study on the energy of earthquakes in reinforced concrete moment frames," *Journal of Seismology and Earthquake Engineering*, vol. 3, no. No. 2, p. 11, 2000.
- [5] A. Ruzi, "Energy concept in earthquake-resistant design," Master of Science Thesis, Istanbul Technical University, Department of Civil Engineering, 2003.
- [6] F. Mollaioli and L. Decanini, "An energy-based methodology for the assessment of seismic demand," *Soil Dynamics and Earthquake Engineering*, vol. 21, no. 2, p. 25, 2001.
- [7] L. Ye, G. Cheng, and Z. Qu, "Study on energy-based seismic design method and the application for steel braced frame structures," in *Proceedings of the Sixth International Conference on Urban Earthquake Engineering*, p. 12, Tokyo Institute of Technology, Tokyo, Japan, August, 2009.
- [8] G. Ghodrati-Amiri, G. Abdollahzadeh-Darzi, and M. Khanzadi, "Earthquake duration and damping effects on input energy," *International Journal of Civil Engineering*, vol. 5, no. 1, p. 16, 2007.
- [9] F. Haddad-Shargh and M. Hosseini, "An optimal distribution of stiffness over the height of shear buildings to minimize the seismic input energy," *Journal of Seismology and Earthquake Engineering (JSEE)*, vol. 13, no. 1, p. 8, 2011.
- [10] G. Havaei and E. Mobedi, "Effect of interaction and rocking motion on the earthquake response of buildings," *Journal of Structural and Construction Engineering (JSCE)*, vol. 1, no. 1, p. 11, 2015 (In Persian).
- [11] R. Bemanian and H. Shakib, "Evaluation of nonlinear behavior of dual steel frame-shear wall system by a group of real earthquakes," *Journal of Structural and Construction Engineering (JSCE)*, vol. 2, no. 4, p. 13, 2016.
- [12] R. Vahdani, M. Gerami, and M. A. Vaseghi Nia, "Structural damping and displacement ductility effects on input energy spectrum of earthquake," *Journal of Structural and Construction Engineering*, vol. 5, no. 2, pp. 5–21, 2018.
- [13] T. Ucar, "Computing input energy response of MDOF systems to actual ground motions based on modal contributions," *Earthq. Struct.*, vol. 18, no. 2, pp. 263–273, 2020.
- [14] T. T. Tran and B. Adhikari, "Energy based seismic design coefficients," in *AIP Conference Proceedings*, vol. 2420, AIP Publishing LLC, Article ID 020036, 2021.
- [15] R. Bagherzadeh, A. Riahi Nouri, M. S. Massoudi, M. Ghazi, and F. Haddad Shargh, "AN effective hybrid method for optimizing steel frames with improved seismic performance," *Iran University of Science & Technology*, vol. 12, no. 3, pp. 365–398, 2022.
- [16] A. Committee, *Seismic Provision for Structural Steel Buildings (ANSI/AISC 341-16)*, American Institute of Steel Construction, Chicago, 2016.
- [17] ASCE, "ASCE/SEI 7-16 Minimum Design Loads for Buildings and Other Structures," *American Society of Civil Engineers*, vol. 2, 2016.

- [18] I. MathWorks, *MATLAB and Statistics Toolbox Release 2012b*, I. MathWorks, Natick (Massachusetts, United States), 2012.
- [19] CSI (Computers & Structures, Inc), *CSI Analysis Reference Manual for SAP2000 Ver*, CSI, Walnut Creek, CA, 2017.
- [20] S. S. Lee, *Performance-based Design of Steel Moment Frames Using Target Drift and Yield Mechanism*, University of Michigan, Ann Arbor, Michigan, 2002.
- [21] S. Leelataviwat, W. Saewon, and S. C. Goel, "Application of energy balance concept in seismic evaluation of structures," *Journal of Structural Engineering*, vol. 135, no. 2, pp. 113–121, 2009.
- [22] C. M. Uang and V. V. Bertero, *Use of energy as a design criterion in earthquake-resistant design*, vol. 88, Earthquake Engineering Research Center, University of California, Berkeley, California, 1988.
- [23] N. M. Newmark and W. J. Hall, *Earthquake Spectra and Design. Engineering Monographs on Earthquake Criteria*, Earthquake Engineering Research Institute, Oakland, CA, 1982.
- [24] J. Bai and J. Ou, "Plastic limit-state design of frame structures based on the strong-column weak-beam failure mechanism," in *Proceedings of the 15th World Conference on Earthquake Engineering*, Lisbon, Portugal, September, 2012.
- [25] G. Manfredi, "Evaluation of seismic energy demand," *Earthquake Engineering & Structural Dynamics*, vol. 30, no. 4, pp. 485–499, 2001.
- [26] S. Leelataviwat, S. C. Goel, and B. Stojadinović, "Toward performance-based seismic design of structures," *Earthquake Spectra*, vol. 15, no. 3, pp. 435–461, 1999.
- [27] H. M. Dwairi, M. J. Kowalsky, and J. M. Nau, "Equivalent damping in support of direct displacement-based design," *Journal of Earthquake Engineering*, vol. 11, no. 4, pp. 512–530, 2007.
- [28] S.-S. Lee, S. C. Goel, and S.-H. Chao, "Performance-based Design of Steel Moment Frames Using Target Drift and Yield Mechanism," Report No. UMCEE 01-17, Department of Civil and Environmental Engineering, University of Michigan, Ann Arbor, Michigan, 2001.
- [29] Asce 41-17, *Seismic Evaluation and Retrofit of Existing Buildings*, American Society of Civil Engineers, Reston, Virginia, 2017.

Research Article

Estimating the Geological Strength Index (GSI) in Regional Seismic-Landslide Zonation Using the Empirical Regression Model

M. E. Mirabedini ¹, E. Haghshenas ², and N. Ganjian³

¹Department of Civil Engineering, Science and Research Branch, Islamic Azad University, Tehran, Iran

²International Institute of Earthquake Engineering and Seismology (IIEES), Tehran, Iran

³Department of Civil Engineering, Science and Research Branch, Islamic Azad University, Tehran, Iran

Correspondence should be addressed to E. Haghshenas; haghshen@iiees.ac.ir

Received 2 May 2022; Revised 10 May 2022; Accepted 18 May 2022; Published 25 June 2022

Academic Editor: S. Mahdi S. Kolbadi

Copyright © 2022 M. E. Mirabedini et al. This is an open access article distributed under the Creative Commons Attribution License, which permits unrestricted use, distribution, and reproduction in any medium, provided the original work is properly cited.

The assessment of the strength parameters of geological formations in regional scale which encounters thousands of slopes is a complicated approach and time consuming and needs huge field work. This issue is an important research topic concerning the regional seismic-landslide susceptibility analysis or hazard zonation. An empirical regression model was presented to estimate the Geological Strength Index (GSI) with an implication on geological quadrangle of Gorgan region at Alborz mountains range (north of Iran). Two main sets of data were applied in this study: (1) geomorphological data including the slope height, aspect, and distance from faults and distance from thrusts and (2) the physical and mechanical properties of rocks including the unit weight, uniaxial compressive strength (σ_{ci}), and the petrographic constant (m_i) of intact rock. The first group was extracted from a 1 : 100,000 digital geologic map and 10 m digital elevation model (DEM) and the second group was obtained from the Hoek–Brown failure criterion recommended tables. Linear regression equations were generated applying data collected from 294 studied stations using SPSS software. The regression equation predicted GSI in terms of (1) the distance from faults, (2) the distance from thrusts, and (3) the uniaxial compressive strength (σ_{ci}). The equation had an R^2 value of 0.739 and thus fit well to the data. The new method in its present state was recommended for the estimation of the GSI values in regional scale conditions for the assessment of landslide susceptibility and hazard mapping or post events landslide occurrence prediction in the case of probable big earthquakes in Alborz area that is required for emergency responses. The results indicated that the estimation error was about ± 30 while the average error was within +5 and –5 and average error percentage was about 3%.

1. Introduction

Since the last decade, using Newmark's displacement method [1–6] accompanied by the Geographic Information System (GIS) has become a useful deterministic approach to prepare the seismic-landslide hazard map. Although many general studies have been conducted on the identification and description of landslides in general, the application of GIS based on Newmark's method is relatively new in Iran, and these types of studies have been just carried out in recent years [7]. Mahdaviifar [8] generated a fully automatic version of a GIS-based system based on a simplified Newmark's displacement method which could provide a seismic-

landslide hazard zonation map immediately after the occurrence of an earthquake, [2, 4]. This study was conducted in Alborz and central areas of Iran. In this method, hazard zonation is performed by calculating safety factor, using slopes steepness indices, material parameters (shear strength), and the characteristics of the expected earthquake. Accordingly, in this method, the shear strength of the geological units is a fundamental issue.

In recent years, the Geological Strength Index (GSI) classification system, proposed by Hoek [9] and Hoek et al. [10], has been considered as the most acceptable empirical method to estimate the rock mass strength and deformation parameters, and it can be said that there are no other suitable

alternatives for it [11, 12]. The GSI is a technique to estimate the rock mass strength in different geological conditions, using some standard charts, site observation, and rock mass description. The rock mass properties can be determined considering the degree of crushing and conditions of discontinuities surfaces, indicated by roughness and alteration. Combining these two parameters provided a principal basis to describe rock mass types with diversified rock structure ranging from very tightly interlocked strong rock fragments to heavily crushed rock masses. Based on the rock mass description, the GSI value could be estimated by the contours to reach a value of 0–100, representing the overall geotechnical quality of rock masses. Since the last decade, the GSI approach has been modified by many researchers [12–17]. Bieniawski [18] and Hoek and Brown [10] suggested the relationship between GSI and rock mass quality index Q and rock mass rating (RMR), respectively. Hoek et al. [19] presented a proposed quantification of the GSI chart based on the rock quality designation (RQD) and the joint condition rating of the RMR system. Data from four different rock masses were used to extend the case history which was proposed by Hoek et al. [19] and provided by Bertuzzi et al., [20] and the good correlation between the GSI qualitatively assessed from the standard GSI chart and the quantified GSI was found. Han et al. [21], Poulsen et al. [22], and Wang et al. [23] also suggested different methods focusing on quantifying the GSI chart to facilitate the use of the system to determine the strength and deformation parameters of the rock mass. Morelli [24] analyzed different GSI calculation methods based on the Monte–Carlo simulations. He found the highest and the lowest GSI values from the equations which applied the conventional RMR_{1989} values and the RMI method, respectively. Iran is located on the Alpidic earthquake belt, in the active collision zone between the Eurasian and Arabian plates. This issue makes Iran a country that suffers from geotechnical seismic hazards associated with frequent destructive earthquakes. Also, according to the rapid growth of population and demands for construction lifelines, the risk assessment studies which should be carried out in order to reduce the probable damage is necessary [25]. A principal cause of earthquake damage is landsliding, and the ability to predict earthquake-triggering landslide displacements is important for many types of seismic hazard analyses and for the design of engineered slopes [26].

Sari [27] found similar results. The digital face mapping, as a practical tool to characterize rock masses, was been investigated by [27–29] which could significantly reduce the time required in the field. Hong et al. [29] proposed a method to determine the GSI quantitatively using photographic images of an in situ jointed rock mass with an image processing technology, fractal theory, and artificial neural network (ANN). Bozorgzadeh et al. [30] and Contreras et al. [31] used Bayesian statistics to quantify the uncertainty of intact rock strength. Hoek and Brown [32] introduced relatively few fundamental changes to demonstrate practical applications of the criterion and the GSI system. Day et al. [33] presented a modified GSI chart and a new Composite Geological Strength Index (CGSI) methodology to combine multiple suites of rock mass structure using a weighted

harmonic average to evaluate complex rock masses. Vásárhelyi and Bögöly [34] presented a new method for calculating the GSI value using the “integral-geometric method.” It provided another GSI value calculation method that broadened the determination range of the GSI in case of poor rock mass. Hussian et al. [35] presented the review of the 19 years of research studies conducted by different researchers on the GSI. Although the GSI tool is applicable and capable of estimating the shear strength parameters of the rock mass, estimating regional scale shear strength parameters with thousands of slopes, it tends to be costly and almost impossible.

For helping the planners in selection of suitable locations to implement development projects, a landslide hazard zonation map has been produced for the Golmakan Watershed as part of Binaloud northern hillsides (northeast of Iran) [36]. In this study, we intended to develop an effective empirical regression equation to estimate GSI in Alborz mountains range in Iran, based on the generalized Hoek–Brown failure criterion and effective parameters which were obtained from geological maps, published charts and tables. In this regard, Gorgan geological quadrangle was selected as the main study area and Roudbar geological quadrangle was chosen for the verification of the model. The two regions are located at highly active seismic zone and are very susceptible to landslides, which can be triggered by any significant earthquake in the north of Iran. This model can be used to prepare initial data for the applications in the primary landslide susceptibility or hazard analysis of the entire Alborz zone at the regional scale.

2. Material and Methods

2.1. Study Area. In quantitative techniques, prediction for landslide susceptibility is based on the actual realistic data and interpretations. Further, the quantitative techniques also overcome the subjectivity of qualitative approaches [37]. From strong ground motion perspective, the Zagros thrust fault zone and Alborz and Central Iran zones are two tectonic provinces of the Iranian territory as shown in Figure 1 [26]. The study area (Gorgan geological quadrangle) with an area of 2400 km^2 is located between 54° and $54^\circ 30'$ longitudes and $36^\circ 30'$ and 37° latitudes (Figure 2) at eastern Alborz tectonic zone. The area is distinguished by two major geomorphological units including the Alborz mountainous terrains in the southern parts and the Gorgan plain in northern regions. These two areas are separated by late Mesozoic Khazar (Caspian) fault. The formation of northern areas dates back to the late Tertiary as well as early Quaternary tectonics activities, causing a rapid subsidence in the north part of Khazar fault filled by a thick sequence of marine and continental deposits. These deposits were covered by aeolian deposits (known as Gorgan Loess soils) with a thickness of 5–70 meters, which were deposited during climate changes due to frozen and melting periods of Ice Age in the late Quaternary. Mountainous areas with plenty of forests, comprising the two Alborz and Gorgan-Rasht structural subzone, are separated by the North Alborz fault. The compressional tectonic regime of the region resulted in

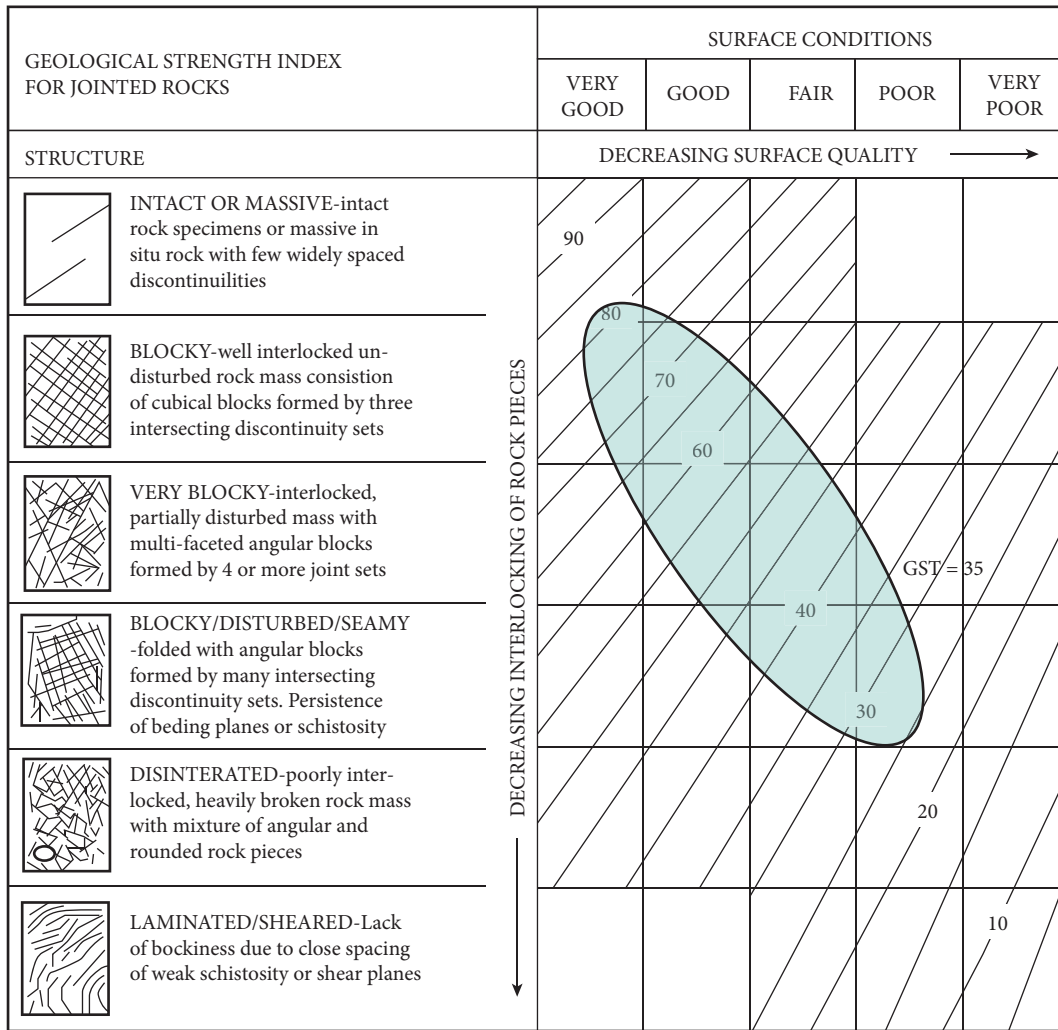


FIGURE 1: The chart shows the GSI values of Gorgan Quadrangle, Hoek et al. [38].

faulting and folding with overall E-W to NE-SW trends. Gorgan (Khazar) and North Alborz faults as well as Jahan-Nama syncline and Chahar-bagh anticline are some of the major structural features around the study area. A wide range of geological strata from the Palaeozoic to Quaternary periods outcrop in the study area. Metamorphic schists known as Gorgan schist with a probable age of late Precambrian is known as the oldest rock in the region [40]. Digital geologic maps of the quadrangle formed the basis of the study to assign material properties throughout the area.

2.2. *GSI Estimating.* As pointed out by Hoek, the GSI classification system is applicable to intact or heavily jointed rock masses. It is important that the Hoek-Brown failure criterion is widely accepted for rock masses which are assumed to be isotropic. In other words, the behavior of the rock mass would not depend on the direction of the applied loads. Therefore, the slopes in which failure surface are imposed by singular discontinuities are highly anisotropic and GSI system is not applicable [41]. When the failure plane passes through several zones, the GSI values require special

judgment and the mean values may not be appropriate. A systematic study was conducted to analyze the nature and behavior of rock masses in the study area. For this purpose, firstly an 8-day field investigation into 320 geological stations was carried out by the leading authors and staff from Gorgan quadrangle. Based on the mapping of the rock exposures, all the data were collected by visual chart assessments at the scale suitable for slopes. The sampling stations were identified based on good lithological exposures and the condition of slope stability. The collected data included rock mass structure, rock type, joint condition, joint roughness, and hydrological condition. The difference image of GIS-derived landslide susceptibility zonation maps prepared for pre- and post-Chamoli earthquake shows the effect of seismic shaking on the occurrence of landslides in the Garhwal Himalaya. An attempt has been made to incorporate seismic shaking parameters in terms of peak ground acceleration with other static landslide causative factors to produce landslide susceptibility zonation map in geographic information system environment [42]. The GSI values were estimated qualitatively based on thorough geological visual field observations.

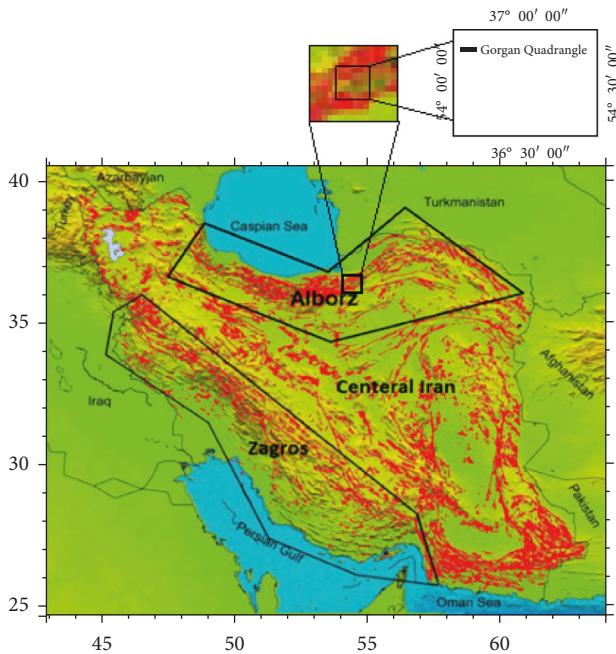


FIGURE 2: Iran could be divided into two regions: Zagros region and Alborz and Central Iran region (the remaining area of Iran) [26, 39].

The rock mass was classified into four classes, i.e., blocky, very blocky, blocky disturbed, and disintegrated. The surface condition generally varies from smooth to poor, slightly weathered to highly weathered with soft clay infillings. Surface roughness data showed a wide range from rough to slickenside. From the hydrogeological point of view, all the visited slopes were dry. Three hundred twenty locations were considered for performing GSI calculations as shown in Figure 2. The GSI evaluation showed the typical diagonal trend from top-left to bottom-right that depicted decreasing rock mass quality. It also showed that GSI values ranged from 25 to 80, i.e., from the crushed rock to almost intact rock (Figure 1). Field photographs were taken at all slopes. The reevaluation of photographs revealed a structurally controlled behavior in some stations. Therefore, the GSI system was inappropriate. For this reason, the corresponding data of 26 stations were ignored and 294 stations were considered for representing the area. Figure 3 shows the GSI measuring for two types of rock structure.

2.3. Data Used. The main data set used in the present study was extracted from Gorgan Geological map (1:100,000), digital elevation model (DEM) of the studied region, and Hoek–Brown criterion table. The medium-sized geological map shows a large amount of geological information, some of which can be used to estimate the GSI. The database used in this study included lithology, distance from faults and thrusts, unit weight (γ), uniaxial compressive strength (σ_{ci}), and the values of constant m_i in intact rock. These data were divided into two groups. The first group consisted of the slope aspect, slope height, distance from faults, and thrust, which were extracted from the geological maps and digital

elevation map (DEM). The second group included the unit weight, uniaxial compressive strength (σ_{ci}), and constant m_i of the intact rock which were selected from published tables and charts as discussed in the following sections.

2.4. The First Group of Data. This group of data contains the slope aspect, slope height, distance from faults, and distance from thrusts. The Gorgan 1:100,000 geological map (Figure 4) and Digital Elevation Model (DEM) of the study area with a resolution of 10 meters were applied for the preparation of the database. The geological map was used as a basis to extract the material properties and geological structure throughout the area. The existing rock types at this area included sandstone, shale, limestone, dolomite, marl, schist, marly limestone, conglomerate, monzodiorite, dolomitic limestone, and silty shale (Figure 4). A Digital Elevation Model (DEM) of the study area was prepared based on the digital elevation contours with intervals of 10 m. All maps were obtained from the Geological Survey and Mineral Exploration of Iran. The slope aspect is one of the basic parameters capable of influencing landslide occurrences [44]. According to the previous studies, northern slopes (N) tend to have more landslide susceptibility than southern (S) ones because of higher soil moisture and thicker soil coverage [45]. Mirsanei and Mahdaviar [12] studied 4143 landslides in Iran. They reported 1433 landslides in Alborz Mountains, the majority of which have occurred on the north and northwest aspect. In general, it seems that GSI values in northern slopes are fewer than other slope aspects due to the moisture effect on rock mass weathering and joints surface conditions.

In this study, the slope aspect was divided into eight classes: North (N), Northwest (NW), West (W), Southwest (SW), South (S), Southeast (SE), East (E), and Northeast (NE). Table 1 shows the weighting factors assigned to the different slope groups, based on the numerical scale proposed by Mirsanei et al. [12]. Outcrops were considered as a valuable source of data but they might be influenced by surface relaxation, weathering, and the alteration of rock mass components. Larger rock masses had lower overall strength compared to smaller rock masses because of scale effect. The larger rock mass involved the greater number of potential failure paths and it showed that rock masses had the ability to find failure paths with least resistance. Figure 5 shows the scale effect on rock mass compressive strength [28]. In this regard, the total-slope-height is defined as the elevation difference between the slope top and the slope toe.

2.5. The Second Group of Data-Extracted Form Charts and Tables. The second group of data comprises of the unit weight, the uniaxial compressive strength (σ_{ci}), and the petrographic constant m_i of the intact rock considered in Hoek–Brown failure criterion. The uniaxial compressive strength σ_{ci} and the material constant m_i are determined by laboratory testing or estimated from published tables. Due to the lack of experimental data, σ_{ci} of the intact rock and m_i were directly selected from Table 2 and Table 3, based on Hoek–Brown's recommendation. Table 2 was the source for

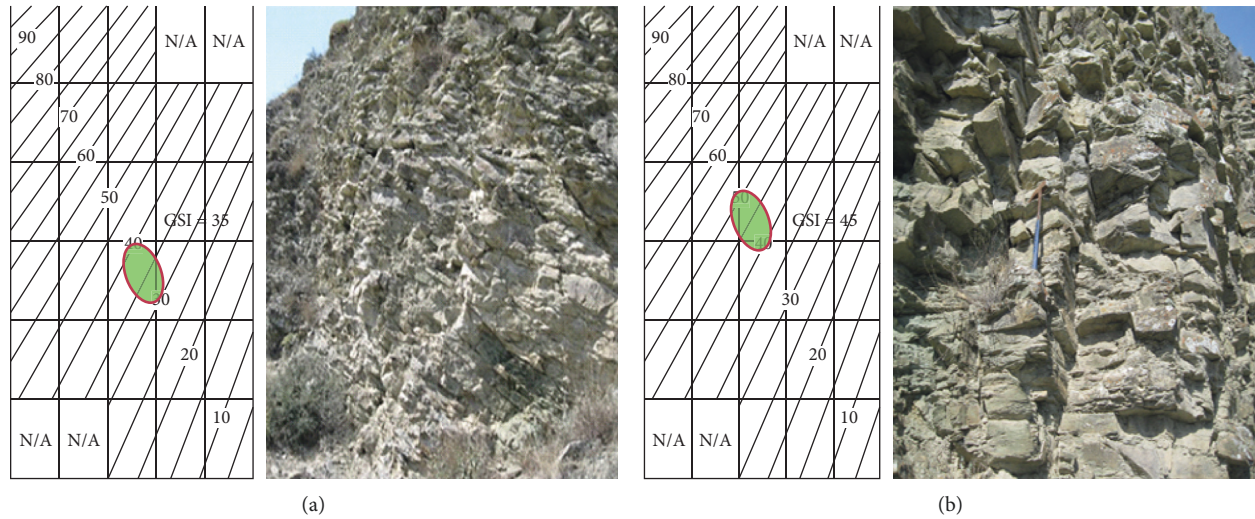


FIGURE 3: GSI measuring at two geological stations: (a) completely disintegrated rock mass and (b) blocky structure, Hoek et al. [38].

selecting σ_{ci} as well as the updated values of m_i available in Hoek et al. [46] (Table 3) or in the RocLab program (2007). The minimum value of σ_{ci} and m_i was assumed in order to prevent the removal of the sensitive slopes. Unit weights were selected from published tables or similar data like Barton and Choubey [47] due to the lack of experimental data.

2.6. The Regression Model for Predicting GIS. Determining the rock mass shear strength parameters including internal friction angle (φ) and cohesion (c) according to Mohr–Coulomb criterion is an important step in performing landslide susceptibility analysis or hazard mapping based on Newmark’s simplified displacement method. The method to determine the strength parameters depends on the size of the study area. Hoek et al. [48] presented equations to find equivalent Mohr–Coulomb parameters predicted by the Hoek–Brown failure criterion. Hence, by estimating the GSI values, the equivalent c and φ could be obtained. Due to the limitation of the common methods such as the laboratory and field testing and failure criteria for the regional scale study, a regression model was applied to develop an empirical formula to predict the GSI. In the first step, a linear regression model was considered to determine the model coefficients. As mentioned earlier, the database contained seven input parameters. In order to investigate the effect of predictors on GSI and also to propose a comprehensive model for determining GSI, the regression (MR) analysis was performed. The aim of this method was to develop a linear regression equation for approximating science and engineering problems. When there is more than one input model, MR can be performed to obtain the best-fit equation. By using a constructed database consisting of 294 geological stations datasets in which the distance to fault (FD), uniaxial strength of intact rock (σ_{ci}), rock constant (m_i), slope height (H), slope aspect, and distance to fold axis (DFA) were considered as model predictors to estimate GSI,

IBM SPSS Statistics 20 program was employed and the MR model was developed. Table 4 shows the summary of the model.

3. Results and Evaluation

The value of R^2 is 0.86 and the adjusted R^2 is 0.73 showing that seven predictors entered in the regression analysis account for 73% of the variations of GSI (Table 4) and this will fit the data at a very high level of statistical significance. Table 5 shows that the F-value is equal to 89.4 significant to a level of 5%, which is much greater than 1. Therefore, this indicates a linear relationship between the variables. The following parameters were found to be significant for GSI: distance to fault, distance to fold axis, and σ_{ci} . The parameters that were found insignificant are m_i , slope height, slope aspect, and unit weight. Table 5 shows the computation for the model. The estimation regression model for the GSI is presented as follows:

$$\begin{aligned} \text{GSI}_{\text{pre}} &= 25.2 + 0.001\text{FD} + 0.368\sigma_{ci} - 0.001\text{DFA}, \\ \text{GSI}_{\text{pre}} &\geq 25, \end{aligned} \quad (1)$$

where FD is the distance to fault, σ_{ci} is the uniaxial strength of intact rock, and the last term is DFA, which is the distance to the fold axis of the model.

3.1. Testing the Assumptions of the Regression Analysis. The linear regression model is based on four assumptions. These postulate the properties that the variables should have in the population. The regression model only provides proper inference if the assumptions are held true (although the model was robust to mild violations of these assumptions). The reliability and validity of the model were considered by checking the model assumptions of the null hypothesis, irrespective of the residuals, linearity, and normality.

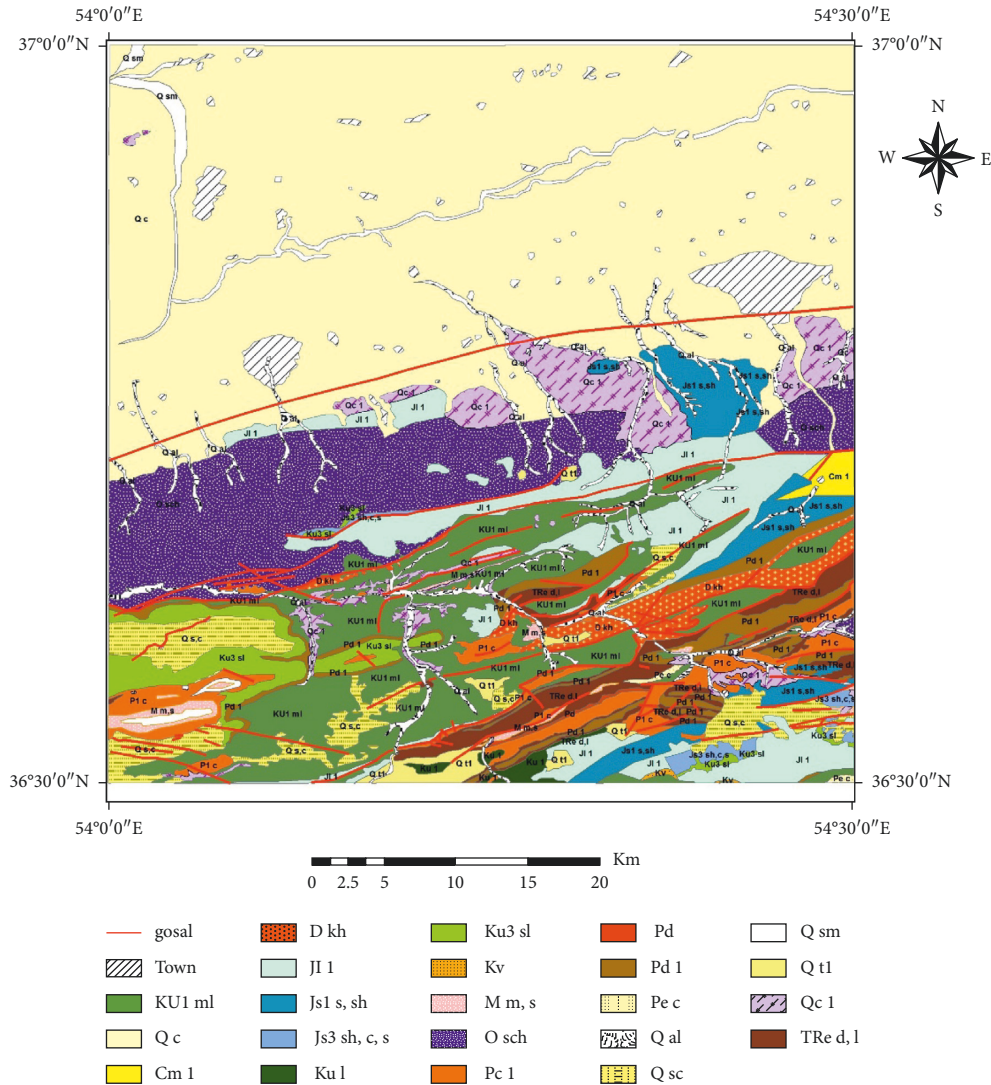


FIGURE 4: The geological map of Gorgan quadrangle (Mirsanei and Mahdaviar [43]).

TABLE 1: The slope aspect categories and weight.

N	Slope aspect	Weight
1	North (N)	4
2	Northwest (NW)	4
3	West (W)	3
4	Northwest (NW)	3
5	South (S)	2
6	Northeast (NE)	2
7	South (S)	1
8	Southeast (SE)	1

3.1.1. *F-Test*. The F-test is used in regression analysis to test the hypothesis that all model parameters are zero versus the alternative that at least one slope coefficient is nonzero. The Hypothesis test determines whether there is a relationship between the response and the predictor. When there is no relationship between the response and any of the predictors, the model will not explain much of the variation in the response. The Mean Square Model and Mean Square Error

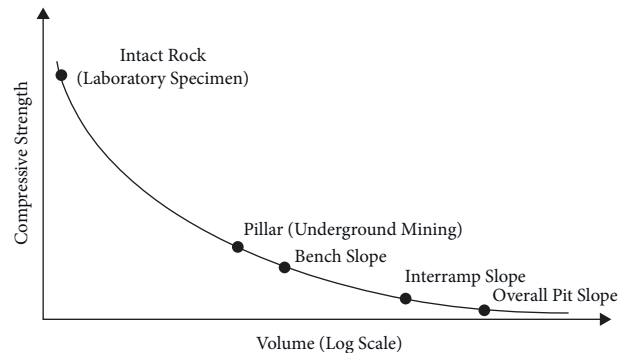


FIGURE 5: The scale effect on rock mass compressive strength [28].

will be approximately the same, and the F Ratio will be close to 1. On the other hand, if the alternative hypothesis is true, at least one coefficient is nonzero. The Mean Square Model will be greater than the Mean Square Error, and the F Ratio will be greater than 1. According to Table 6, the F Ratio was

TABLE 2: The field estimates of the uniaxial compressive strength of intact rock pieces, Hoek et al. [38].

Grade ^a	Term	Uniaxial compressive strength (MPa)	Point load index (MPa)	Field estimate of strength	Examples
R6	Extremely strong	>250	>10	Specimen can only be chipped with a geological hammer	Fresh basalt, chert, diabase, quartzite
R5	Very strong	100–250	4–10	Specimen requires many blows of geological hammer to fracture it	Gabbro, gneiss, granodiorite limestone, marble, rhyolite, tuff
R4	Strong	50–100	2–4	Specimen requires more than one blow of a geological hammer to fracture it	Limestone, marble, phyllite, sandstone, schist, shale
R3	Medium strong	25–50	1-2	Cannot be scarped or peeled with a pocket knife specimen can be fractured with a single blow from a geological hammer	Claystone, coal, concrete, schist shale, siltstone
R2	Weak	5–25	b	Can be peeled with a pocket knife with difficulty, shallow indentation made by firm blow with a point of a geological hammer	Chalk, rocksalt, potash
R1	Very weak	1–5	b	Crumbles under firm blows with a point of a geological hammer can be peeled by a pocket knife	Highly weathered or altered rock
R0	Extremely weak	0.25–1	b	Indented by thumbnail	Stiff fault gouge

TABLE 3: The values of the constant m_i for intact rock, by rock group. Note that values in parentheses are estimates of Hoek et al. [38].

Rock name	m_i	Rock name	m_i	Rock name	m_i	Rock name	m_i
Conglomerate	(22)	Micritic limestone	8	Gneiss	33	Diorite	(28)
Sandstone	19	Gypstone	16	Schists	4–8	Andesite	19
Siltstone		Anhydrite	13	Phyllites	(10)	Gabbro	27
Claystone	4	Marble	9	Slate	9	Dolerite	(19)
Greywacke	(18)	Hornfels	(19)	Granite	33	Basalt	(17)
Chalk	7	Quartzite	24	Rhyolite	(16)	Norite	22
Coal	(8–21)	Migmatite	30	Obsidian	(19)	Agglomerate	(20)
Breccia	20	Amphibolite	25–31	Granodiorite	30	Breccia	(18)
Sparitic limestone	10	Mylonites	6	Dacite	17	Tuff	(15)

TABLE 4: The model summary.

Model	R	R square	Adjusted R square	Std. error of the estimate	Durbin–Watson
1	0.860a	0.739	0.731	7.2244	1.624

a. Predictors: (constant), X1, X2, X3, X4, X5, X6. b. Dependent variable: GSI.

TABLE 5: The coefficients.

Model	Unstandardized coefficients		Standardized coefficients beta	t	Sig.	Collinearity statistics	
	B	Std. error				Tolerance	VIF
Constant	25.2	5.534		4.996	0.000		
Fault D	0.001	0.000	0.072	2.141	0.033	0.801	1.248
Mi	0.061	0.127	0.017	0.481	0.631	0.736	1.359
Height	0.005	0.009	0.018	0.592	0.554	0.945	1.059
Slope aspect	–0.244	0.401	–0.019	–0.607	0.545	0.921	1.086
Fold axis	–0.001	0.000	–0.082	–2.229	0.027	0.687	1.456
γ	–1.161	1.674	–0.022	–0.693	0.489	0.898	1.113
σ_{ci}	0.368	0.018	0.807	20.669	0.000	0.603	1.658

a. Dependent variable: GSI.

TABLE 6: ANOVA.

Model	Sum of squares	Df	Mean square	F	Sig. (b)
Regression	42010.821	9	4667.869	89.437	.000
Residual	14822.512	284	52.192		
Total	56833.333	293			

a. Dependent variable: GSI. b. Predictors: (constant), SIGMA, H, slope aspect, fault D, mi, fold axis.

89.437 and it was concluded that at least one term in our model was significant.

3.1.2. The Durbin-Watson Test. The Durbin-Watson (DW) statistic is a test for autocorrelation in the residuals from a statistical regression analysis. The Durbin-Watson statistic will always have a value between 0 and 4. A value of 2.0 means that there is no autocorrelation detected in the sample. Values from 0 to less than 2 indicate positive autocorrelation and values from 2 to 4 indicate negative autocorrelation. As shown in Table 4, $d = 1.624$ is the critical value in the range of $1.5 < d < 2.5$. Therefore, it could be assumed that there was no first-order linear autocorrelation in the multiple linear regression data. In addition, the errors were independent, and as a result, the utility of the regression model was confirmed.

3.1.3. The Multicollinearity. Multicollinearity is known to be undesirable when one independent variable is a linear function of other independent variables. According to the last column of Table 5, the value of VIF in all independent variables was less than 5 ($VIF < 5$). Accordingly, there was no multicollinearity between independent variables; hence it validated the fitted model.

3.1.4. The Normality. Normality is defined as the normal distribution of residuals in predicted responses with an average of zero. Figure 6 illustrates normality checks in this study. For the standardized residual histogram to appear normal, a fitted normal distribution aid was considered. The average value, presented at the right side of the diagram, was very small (close to zero) and the standard deviation was approximately equal to unity. Figure 7 shows the P-P plot, which plots variable cumulative proportions against the cumulative proportions of any number of test distributions. Probability plots are generally used to determine whether the distribution of a variable matches a given distribution. If the selected variable matches the test distribution, the points would cluster around a straight line. The estimation error is also calculated for the comparison. Figure 8 shows the error values based on

$$e_i = y_i - \hat{y}_i \tag{2}$$

y_i and \hat{y}_i are the measured and predicted values of GSI, respectively. The estimation error is between -15 and 15, while the average error is between -5 and 5.

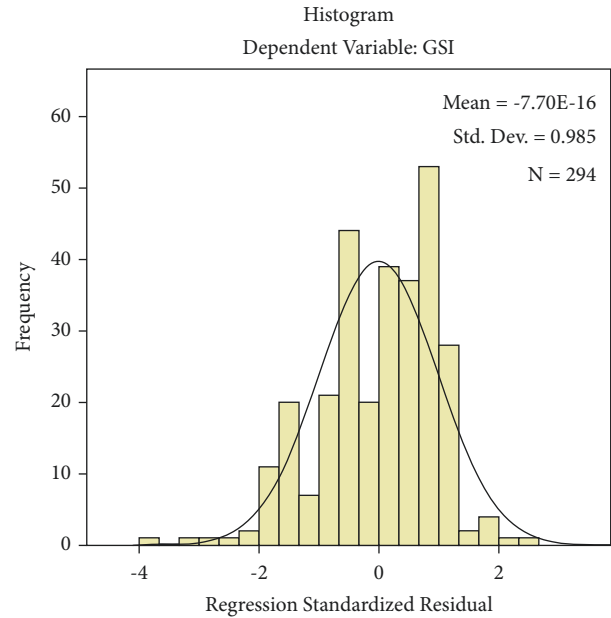


FIGURE 6: Histogram of regression standardized residual.

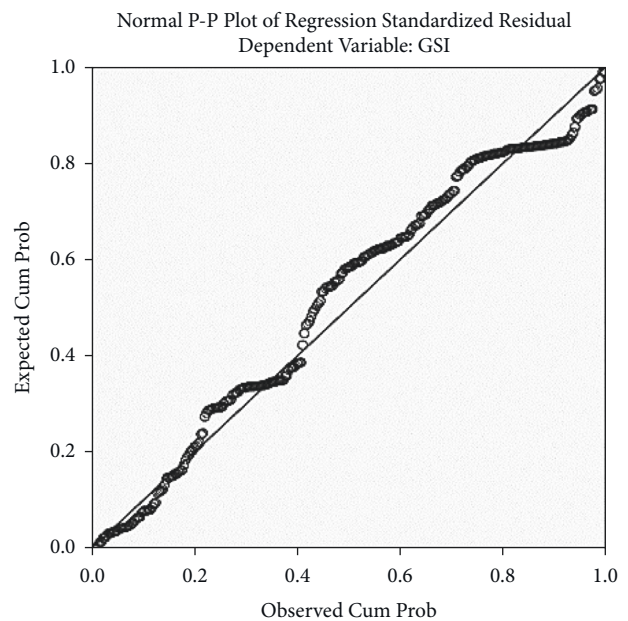


FIGURE 7: The normal P-P plot of regression standardized residual.

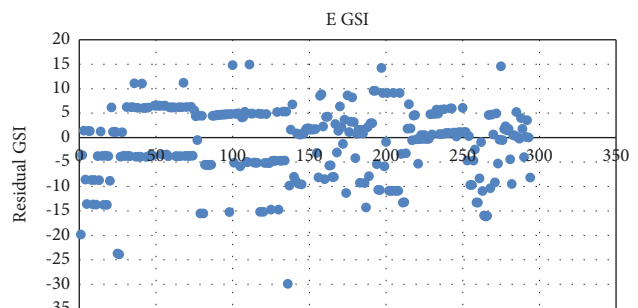


FIGURE 8: Graph showing the comparison between mapped GSI and GSI predicted by (1) in Gorgan quadrangle.



FIGURE 9: Roudbar quadrangle index map [49].

3.2. *The Verification of Formula and Results.* In this section, the applicability of the regression equation in Alborz zone using the Roudbar geological quadrangle data set was verified. This data set was prepared based on (1) and includes σ_{ci} , the distance to fault, and the distance to the fold axis. The testing area (Roudbar geological quadrangle) is 2400 km², located at 49° and 49° 30' longitudes and 36° 15' and 37° latitudes (Figure 9).

It faces Alborz zone and the Caspian Sea with a humid climate which might deeply affect the occurrence of landslides, and it is also mountainous (the height differs from 150 to 2,800 meters above the sea level). All of these properties along with the seismic potential of the region make it a landslide-prone area. The study area tends to comprise a wide range of geological materials, from the metamorphic rocks of Precambrian to Quartz sediments. In Alborz, the

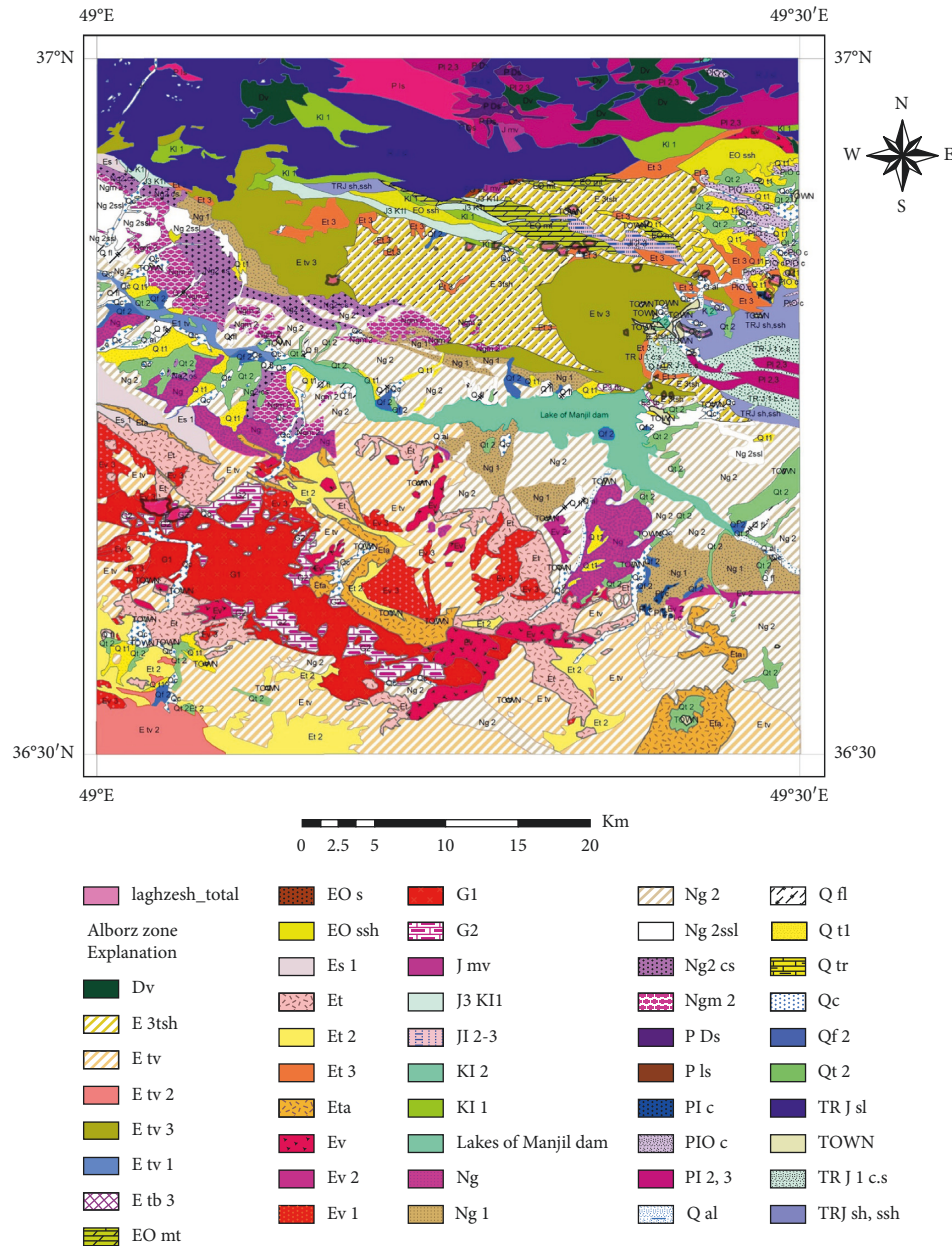


FIGURE 10: The geologic map of Roudbar quadrangle [49].

red sandstone deposits can be seen almost everywhere, from the Infracambrian, with no changes in sedimentation and geological characteristics, to the Palaeozoic. There are no Silurian and Carboniferous, representing two top volume bulges; i.e., Triassic rocks are left uncomfortably overlying Permian deposits, with the other being observed at the base of Shemshak formation (Jurassic) [49]. 1 : 100,000 geological map and Digital Elevation Model (DEM) of the study area with the resolution of 10 meters were applied (Figure 10). These maps were obtained from the Central Geological Survey and mineral exploration of Iran.

The field data were collected from 300 slopes of varied geological and slope stability conditions. The selected slopes presented a variety of rock types having various discontinuities. Surface condition generally showed a wide range of

quality with different infilling cases. Three-hundred locations were considered for performing GSI calculations as shown in Figure 11. Equation (1) was applied for this area and all locations mapped GSI were compared with predicted values. Figure 12 shows that the GSI difference values are between -30 and +30 and the mean error is between -5 and +5. This result shows that (1) can estimate GSI values with an average error percentage of about 3%.

3.3. Discussion. The ability to predict landslide displacements is important for many types of seismic hazard or susceptibility analysis and Newmark’s approach provides a useful means to predict landslide displacement. This method requires knowing the static factor of safety and the landslide

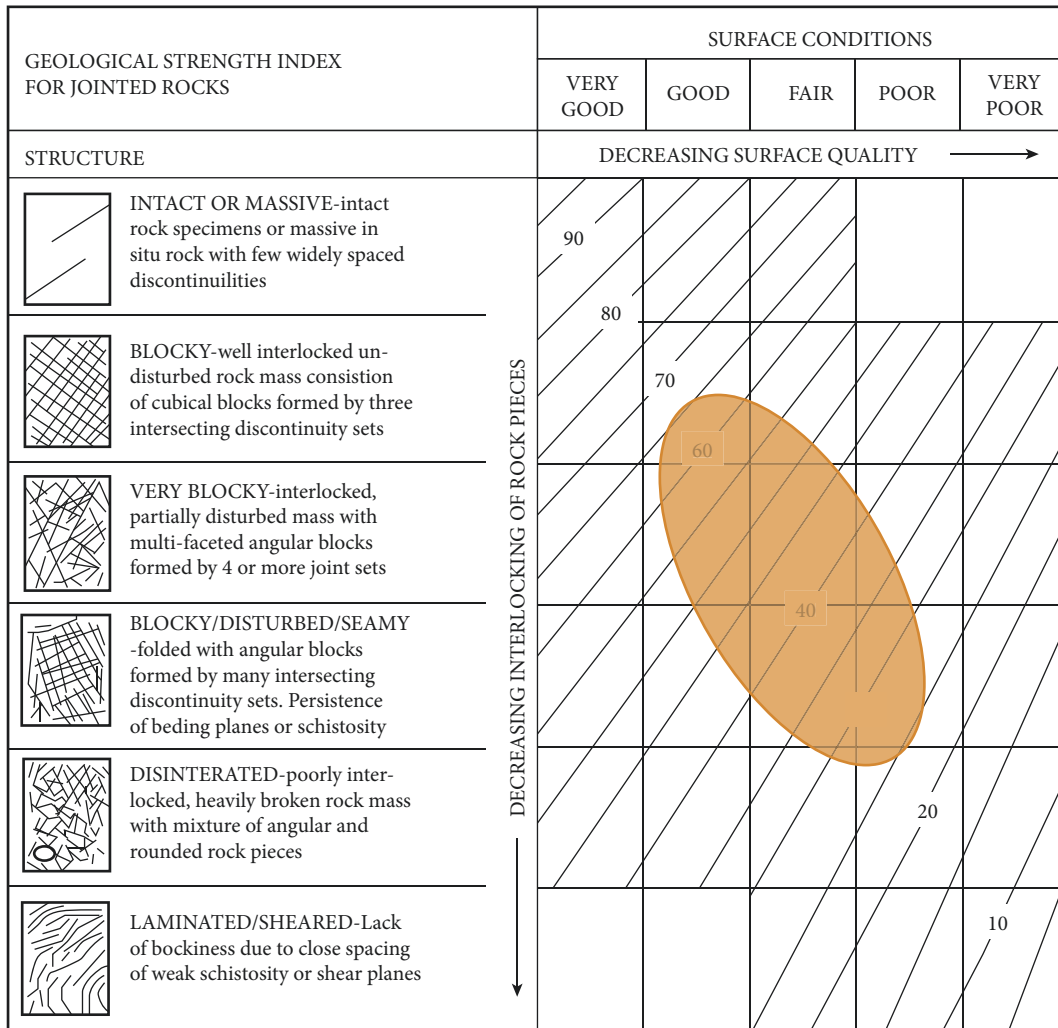


FIGURE 11: Chart showing GSI values of Roudbar quadrangle [49].

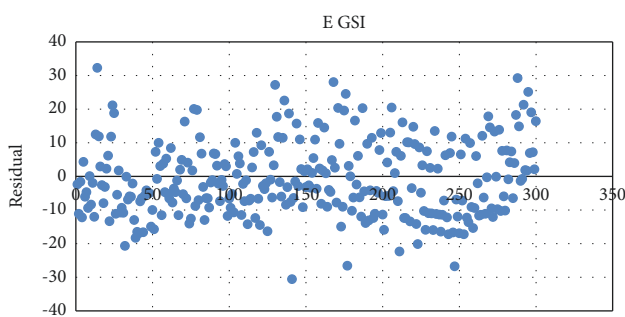


FIGURE 12: The graphic representation of GSI error computed with (1) and filed measurement of Roudbar geological quadrangle.

geometry. Determining the representative shear strength values for geological formations is necessary to calculate the factor of safety. Although the GSI system could be considered as a more appropriate and rapid method in comparison with other methods, this method needs huge field studies. In this study, an empirical regression equation was developed among some geological and geomorphological parameters, extractable from geological maps and DEM of an area and GSI

values of rock masses that can reduce large field works. The parameters used to generate the model were obtained from digital geological map, DEM, and published charts and tables. For the sample area, Gorgan geological quadrangle, the database, which was prepared, contained 7 parameters. The developed model revealed that only 3 of 7 parameters made significant contribution to the model, while 4 of them made insignificant contribution; therefore, they were removed from the model. In order to test the model, another area (Roudbar geological quadrangle) was considered. Figure 11 shows the comparison between the results of GSI obtained from empirical equation and the field work. All the results indicated the GSI values predicted by the empirical equation were generally in good agreement with field data. On the other hand, the dispersion of the predicted GSI does not follow any particular pattern. Therefore, it is not clear which predictor variable has a significant effect on the dispersion of the GSI. There are many simplified assumptions for regional assessment of input data, in spite of the mentioned limitations. It should be noted that this method provides a rapid estimation of shear strength parameters and can be used for emergency responses.

4. Conclusion

Landslides are one of the most damaging geotechnical hazards associated with earthquakes. In addition, the prediction of triggered areas after an eventual earthquake is an important issue for engineers as well as risk managers. The shear strength parameters of geological formation are important elements in such types of analyses. In the present study, a simple method based on the geological map and published tables were used to develop a regression equation between GSI value and easily accessible parameters for a study area. For this study, an area was selected as a pilot area (the Gorgan geological quadrangle in the northeast of Alborz region). The regression relationship was extracted based on observation in 294 natural or excavated slopes, their GSI identification, and the linear correlation determination between these GSI values and some geological and geomorphological parameters. The regression model presented in (1) is well constrained ($R^2 = 74\%$) and predicts GSI in terms of (1) distance from the fault (FD), (2) the uniaxial strength of the intact rock (σ_{ci} , determined from published table for different rock types), and (3) the distance from fold axis (DFA). The approach used is so simple that results can easily be updated. In the next steps, another area (the Rudbar geological quadrangle in the west of Alborz) was selected as the validation area and the evaluation of predictive ability of regression relationship. This validation step showed that the accuracy of this model was in an acceptable range. The average error of this model ranges between ± 5 . To examine the supplication of the model in other regions, Roudbar region at the south of Gilan province with geological and seismic similarity was considered to predict the GSI and compare it with the observed data [23, 50, 51].

Data Availability

The data used to support the findings of the study can be obtained from the corresponding author upon request.

Conflicts of Interest

The authors declare that there are no conflicts of interest regarding the publication of this paper.

References

- [1] R. Wilson, *Predicting Areal Limit of Earthquake-Induced Landsliding, Evaluating Earthquake Hazards in the Los Angeles Region-An Earth-Science Perspective*, pp. 317–345, US Geological Survey Professional Paper 1360, Washington, DC, USA, 1985.
- [2] R. W. Jibson and D. K. Keefer, “Analysis of the seismic origin of landslides: examples from the New Madrid seismic zone,” *The Geological Society of America Bulletin*, vol. 105, no. 4, pp. 521–536, 1993.
- [3] E. L. Harp and R. C. Wilson, “Shaking intensity thresholds for rock falls and slides: evidence from 1987 Whittier Narrows and Superstition Hills earthquake strong-motion records,” *Bulletin of the Seismological Society of America*, vol. 85, no. 6, pp. 1739–1757, 1995.
- [4] R. W. Jibson, E. L. Harp, and J. A. Michael, *A Method for Producing Digital Probabilistic Seismic Landslide Hazard Maps: An Example from the Los Angeles, California, Area*, pp. 98–113, US Department of the Interior, US Geological Survey, Virginia, U.S.A, 1998.
- [5] R. W. Jibson, E. L. Harp, and J. A. Michael, “A method for producing digital probabilistic seismic landslide hazard maps,” *Engineering Geology*, vol. 58, no. 3-4, pp. 271–289, 2000.
- [6] C. W. Liao and C. T. Lee, “Probabilistic hazard analysis of earthquake-induced landslides—an example from kuohsing, taiwan,” in *Proceedings of the International Symposium on Landslide and Debris Flow Hazard Assessment*, pp. 7–1, Taiwan, China, July 2004.
- [7] S. Dehghan, M. A. Aliabadi, and A. M. Rajabi, “The Earthquakes-Induced Landslides Zoning Using Monte Carlo Simulation (A Case Study; Manjil Earthquake-Iran),” *Journal of Materials and Environmental Science*, vol. 9, no. 2, pp. 424–435, 2018.
- [8] M. Mahdaviifar, M. Jafari, and M. Zolfaghari, “GIS-based real time prediction of Arias intensity and earthquake-induced landslide hazards in Alborz and Central Iran,” in *Landslides and Engineered Slopes. From the Past to the Future*, pp. 1427–1432, Taylor and Francis Group, London, 2008.
- [9] E. Hoek, “Strength of rock and rock masse,” *ISRM News Journal*, vol. 2, no. 2, pp. 4–16, 1994.
- [10] E. Hoek and E. T. Brown, “Practical estimates of rock mass strength,” *International Journal of Rock Mechanics and Mining Sciences*, vol. 34, no. 8, pp. 1165–1186, 1997.
- [11] M. Akin, “Slope stability problems and back analysis in heavily jointed rock mass: a case study from Manisa, Turkey,” *Rock Mechanics and Rock Engineering*, vol. 46, no. 2, pp. 359–371, 2013.
- [12] P. Marinos, E. Hoek, and V. Marinos, “Variability of the engineering properties of rock masses quantified by the geological strength index: the case of ophiolites with special emphasis on tunnelling,” *Bulletin of Engineering Geology and the Environment*, vol. 65, no. 2, pp. 129–142, 2006.
- [13] H. Sonmez and R. Ulusay, “Modifications to the geological strength index (GSI) and their applicability to stability of slopes,” *International Journal of Rock Mechanics and Mining Sciences*, vol. 36, no. 6, pp. 743–760, 1999.
- [14] M. Cai, P. K. Kaiser, H. Uno, Y. Tasaka, and M. Minami, “Estimation of rock mass deformation modulus and strength of jointed hard rock masses using the GSI system,” *International Journal of Rock Mechanics and Mining Sciences*, vol. 41, no. 1, pp. 3–19, 2004.
- [15] M. Cai, P. K. Kaiser, Y. Tasaka, and M. Minami, “Determination of residual strength parameters of jointed rock masses using the GSI system,” *International Journal of Rock Mechanics and Mining Sciences*, vol. 44, no. 2, pp. 247–265, 2007.
- [16] H. Sonmez, C. Gokceoglu, and R. Ulusay, “Indirect determination of the modulus of deformation of rock masses based on the GSI system,” *International Journal of Rock Mechanics and Mining Sciences*, vol. 41, no. 5, pp. 849–857, 2004.
- [17] M. A. Brideau, D. Stead, D. Kinakin, and K. Fecova, “The Influence of Tectonic Structures on Rock Mass Quality and Implications for Rock Slope Stability,” vol. 80, no. 3–4, pp. 242–259, Department of Earth Sciences-Simon Fraser University, Doctoral dissertation, Burnaby, BC, Canada, 2005.

- [18] Z. T. Bieniawski and Z. T. Bieniawski, *Engineering Rock Mass Classifications: A Complete Manual for Engineers and Geologists in Mining, Civil, and Petroleum Engineering*, John Wiley & Sons, Hoboken, NJ, USA, 1989.
- [19] E. Hoek, T. G. Carter, and M. S. Diederich, "Quantification of the geological strength index chart," in *Proceedings of the 47th US Rock Mechanics/Geomechanics Symposium*, San Francisco, CA, USA, June 2013.
- [20] R. Bertuzzi, K. Douglas, and G. Mostyn, "Comparison of quantified and chart GSI for four rock masses," *Engineering Geology*, vol. 202, pp. 24–35, 2016.
- [21] X. J. Han, F. M. Zhang, M. L. Dong, and C. X. Cao, "Determination of mechanical parameters of unloading rock mass based on GSI," *Science Technology and Engineering*, vol. 14, no. 30, pp. 237–240, 2014.
- [22] B. A. Poulsen, D. P. Adhikary, M. K. Elmouttie, and A. Wilkins, "Convergence of synthetic rock mass modelling and the Hoek-Brown strength criterion," *International Journal of Rock Mechanics and Mining Sciences*, vol. 80, pp. 171–180, 2015.
- [23] X. G. Wang, B. Hu, J. D. Wang, P. Jia, and W. Jiao, "Quantitative study of Hoek-Brown strength criterion based on GSI," *Chinese Journal of Rock Mechanics and Engineering*, vol. 34, no. 2, pp. 3805–3812, 2015.
- [24] G. L. Morelli, "Variability of the GSI index estimated from different quantitative methods," *Geotechnical & Geological Engineering*, vol. 33, no. 4, pp. 983–995, 2015.
- [25] S. Farahani, B. Behnam, and A. Tahershamsi, "Macrozonation of seismic transient ground displacement and permanent ground deformation of Iran," *Nat. Hazards Earth Syst. Sci. Discuss*, vol. 20, no. 1, pp. 1–20, 2020.
- [26] M. Mahdaviifar, M. K. Jafari, and A. M. Zou, "Real-time Generation of Arias Intensity and Seismic Landslides Hazards Maps Using GIS," *Journal of Seismology and Earthquake Engineering*, vol. 10, no. 2, pp. 81–90, 2008.
- [27] M. Sari, "Incorporating variability and/or uncertainty of rock mass properties into GSI and RMI systems using Monte Carlo method," in *Engineering Geology for Society and Territory - Volume 6*, pp. 843–849, Springer, Cham, 2015.
- [28] L. J. Lorig, "Challenges in current slope stability analysis methods," in *Proceedings of the Slope Stability 2009: International Symposium on Rock Slope Stability in Open Pit Mining and Civil Engineering*, Santiago, Chile, November 2009.
- [29] K. Hong, E. Han, and K. Kang, "Determination of geological strength index of jointed rock mass based on image processing," *Journal of Rock Mechanics and Geotechnical Engineering*, vol. 9, no. 4, pp. 702–708, 2017.
- [30] N. Bozorgzadeh, M. D. Escobar, and J. P. Harrison, "Comprehensive statistical analysis of intact rock strength for reliability-based design," *International Journal of Rock Mechanics and Mining Sciences*, vol. 106, pp. 374–387, 2018.
- [31] L. F. Contreras, E. T. Brown, and M. Ruest, "Bayesian data analysis to quantify the uncertainty of intact rock strength," *Journal of Rock Mechanics and Geotechnical Engineering*, vol. 10, no. 1, pp. 11–31, 2018.
- [32] E. Hoek and E. T. Brown, "The Hoek-Brown failure criterion and GSI - 2018 edition," *Journal of Rock Mechanics and Geotechnical Engineering*, vol. 11, no. 3, pp. 445–463, 2019.
- [33] J. J. Day, M. S. Diederichs, and D. J. Hutchinson, "Composite geological strength index approach with application to hydrothermal vein networks and other intrablock structures in complex rockmasses," *Geotechnical & Geological Engineering*, vol. 37, no. 6, pp. 5285–5314, 2019.
- [34] B. Vászrhelyi and G. Bögöly, "New method for determining the Geological Strength Index (GSI) value of boreholes," in *Proceedings of the Geotechnical Challenges in KARST ISRM Specialised Conference*, Omiš – Split, Croatia 11.-1304, Omiš – Split, Croatia, April 2019.
- [35] S. Hussain, M. Mubeen, A. Ahmad et al., "Using GIS tools to detect the land use/land cover changes during forty years in Lodhran district of Pakistan," *Environmental Science and Pollution Research*, vol. 27, no. 32, pp. 39676–39692, 2020.
- [36] M. R. D. Mansouri and A. Bagherzadeh, "Landslide hazard zonation assessment using GIS analysis at Golmakan Watershed, northeast of Iran," *Frontiers of Earth Science*, vol. 5, no. 1, pp. 70–81, 2011.
- [37] L. Shano, T. K. Raghuvanshi, and M. Meten, "Landslide susceptibility evaluation and hazard zonation techniques - a review," *Geoenvironmental Disasters*, vol. 7, no. 1, p. 18, 2020.
- [38] E. Hoek, P. Marinos, and M. Benissi, "Applicability of the Geological Strength Index (GSI) classification for very weak and sheared rock masses. The case of the Athens schist formation," *Bulletin of Engineering Geology and the Environment*, vol. 57, no. 2, pp. 151–160, 1998.
- [39] A. Ghasemi and C. J. Talbot, "A new tectonic scenario for the Sanandaj-Sirjan Zone (Iran)," *Journal of Asian Earth Sciences*, vol. 26, no. 6, pp. 683–693, 2006.
- [40] A. R. Eskenati, A. Mahboob, A. Alirezaie, R. Askari, and S. M. S. Kolbadi, "Investigating the effect of longitudinal gallery on dynamical response of gravity concrete dams using fem," *Journal of Southwest Jiaotong University*, vol. 56, no. 4, 2021.
- [41] A. J. Li, A. V. Lyamin, and R. S. Merifield, "Seismic rock slope stability charts based on limit analysis methods," *Computers and Geotechnics*, vol. 36, no. 1-2, pp. 135–148, 2009.
- [42] N. Pareek, M. L. Sharma, M. K. Arora, and S. Pal, "Inclusion of earthquake strong ground motion in a geographic information system-based landslide susceptibility zonation in Garhwal Himalayas," *Natural Hazards*, vol. 65, no. 1, pp. 739–765, 2013.
- [43] M. R. Mahdaviifar, "Analytical evaluation and design of landslide risk management system of the earthquake in Iran," Ph. D Thesis, IIEES (International Institute of Earthquake Engineering and Seismology), Tajrish, Iran, 2006.
- [44] S. Zhou, G. Chen, and L. Fang, "Distribution pattern of landslides triggered by the 2014 Ludian earthquake of China: implications for regional threshold topography and the seismogenic fault identification," *ISPRS International Journal of Geo-Information*, vol. 5, no. 4, p. 46, 2016.
- [45] H. X. Lan, C. H. Zhou, L. J. Wang, H. Y. Zhang, and R. H. Li, "Landslide hazard spatial analysis and prediction using GIS in the Xiaojiang watershed, Yunnan, China," *Engineering Geology*, vol. 76, no. 1-2, pp. 109–128, 2004.
- [46] E. Hoek and M. S. Diederichs, "Empirical estimation of rock mass modulus," *International Journal of Rock Mechanics and Mining Sciences*, vol. 43, no. 2, pp. 203–215, 2006.
- [47] N. Barton and V. Choubey, "The shear strength of rock joints in theory and practice," *Rock Mechanics*, vol. 10, no. 1-2, pp. 1–54, 1977.
- [48] E. Hoek, C. Carranza-Torres, and B. Corkum, "Hoek-Brown criterion—2002 edition," in *Proceedings of the 5th North American Rock Mechanics Symp. And 17th Tunneling Association of Canada*, pp. 267–273, Toronto, Canada, July 2002.

- [49] M. Mahdaviyar and P. Memarian, "Assessment of earthquake-induced landslides triggered by roudbar-manjil earthquake in rostamabad(Iran) quadrangle using knowledge-based hazard analysis approach," in *Earthquake-Induced Landslides*, pp. 769–780, Springer, Berlin, Heidelberg, 2013.
- [50] Rocscience, *RocLab*, Rocscience Inc, Toronto, 1.031 edition, 2007.
- [51] V. Marinos, P. Marinos, and E. Hoek, "Geological Strength Index (GSI). A characterization tool for assessing engineering properties for rock masses," *Underground Works under Special Conditions*, Taylor & Francis, Lisbon Portugal, pp. 13–21, 2007.

Research Article

Fire Risk Assessment and Experimental Study of Transformer Insulating Oil

Ji Jun,^{1,2} Chen Xin,^{1,2} Li Lin,³ Zhu Hui ,⁴ Nie Jingkai,^{1,2} and Han Yu^{1,2}

¹State Key Laboratory of Advanced Power Transmission Technology, State Grid Smart Grid Research Institute Co., Ltd., Beijing 102201, China

²State Grid Smart Grid Research Institute Co., Ltd., Future City for Science and Technology, Beijing 102201, Changping District, China

³State Key Laboratory of Alternate Electrical Power System with Renewable Energy Sources (North China Electric Power University), Beijing 102206, Changping District, China

⁴Sichuan Fire Research Institute of MEM, Chengdu 610036, Sichuan, China

Correspondence should be addressed to Zhu Hui; zhuhui@126.com

Received 2 April 2022; Revised 18 May 2022; Accepted 26 May 2022; Published 15 June 2022

Academic Editor: Angelo Marcelo Tusset

Copyright © 2022 Ji Jun et al. This is an open access article distributed under the Creative Commons Attribution License, which permits unrestricted use, distribution, and reproduction in any medium, provided the original work is properly cited.

Most previous works concentrated on burning characteristics of pool fire using common fuels such as heptane, propane, biodiesel, and diesel, whereas burning characteristics for transformer oil are barely involved, although transformer oil is arguable of more practical importance in power system. This study performed a series of pool fire experiments using transformer oil to study the burning characteristics in open and confined spaces. Three fuel thicknesses and five initial temperatures are changed in open space. The essential parameters of mass loss rate, flame height, and fire plume temperature are obtained and analyzed. Moreover, three oil pool diameters are varied in a chamber. The main conclusions are summarized as follows: the variations of mass loss rate, flame height, and fire plume temperature not only obviously increase as the fuel thickness increases from 0.5 cm to 1.0 cm, but also insignificantly increase as the fuel thickness changes from 1.0 cm to 2.0 cm. The mass loss rate is less sensitive to the initial temperature of transformer oil, but the flame height and fire plume temperature significantly rise with the initial temperature. Moreover, the modified models to predict the flame height and fire plume temperature for 25°C initial temperature conditions are proposed, but the fitting coefficients are obviously different from that for common liquid fuels. The flame height in confined space is higher and will rapidly increase to the maximum, then decreases, and tends to be stable, which is obviously different from the oil pool fire burning in open space. In addition, the phenomenon of burning blast and the ignition of the adjacent oil pool will be observed with a high-temperature ignition source and a certain high temperature in a chamber under 30 cm oil pool diameter, which will not be recorded in 15 cm and 20 cm.

1. Introduction

As an important part of the electric power transmission system, the normal operation of transformers is an increasingly prerequisite for daily life and industrial production. The transformer oil, as an electrical insulation and heat transfer fluid, is widely used in oil-immersed transformers [1]. However, the accidental leakages of transformer oil into surrounding space can form a hazardous pool fire once an ignition source is available [2], which may result in

serious economic losses and human casualties. On November 11, 2019, the transformer fire occurred in Jinan, Shandong Province, China, causing one death, two injuries, and significant economic losses. On December 13, 2021, Taiwan's Wanlong Transformer No. 5 distribution substation failed and then the transformer oil caught fire, causing the insulation to fail and forcing the power supply system to shut down. The fire safety issues of transformer oil have attracted increasing attention because it is characterized by flammability and highly calorific. Therefore, it is very

necessary to investigate the burning characteristics of pool fire for transformer oil in order to evaluate the fire risks.

In recent years, the burning characteristics of pool fires, such as burning rate [3–7], flame height [4, 6, 8–12], fire plume temperature [9, 13–15], and pulsation frequency [16, 17], have been widely investigated as an important issue. Previous investigations mainly focused on the combustion behaviors of pool fire using common fuels such as heptane, propane, biodiesel, and diesel. However, there are only a limited number of studies addressing the burning characteristics of transformer oil pool fire although transformer oil is arguable of more practical importance in power systems. Heskestad and Dobson [18] performed the pool fires of transformer oil over a rock bed in a 1.2 m diameter pan to study the effects of oil drainage on heat release rate. The burning tests conducted by Zhu et al. [19] studied the suppression of transformer oil pool fire by water mist. Zhang et al. [20] carried out a series of experiments to study the burning characteristics of different types of transformer oils using a cone calorimeter and found that the mass loss rate, heat release rate, and smoke production rate of 10# and 25# transformer oils were basically similar, whereas the corresponding values are smaller than that for 45# transformer oils. Zhao et al. [21] experimentally studied the burning behaviors of thin-layer transformer oil on a water layer considering the effects of initial fuel thickness and demonstrated the insignificant effects of initial fuel thickness on the steady burning rate. Moreover, it is worth noting that oil pool fires occurred in confined space are extremely different from open space. The burning characteristics are influenced by the heat feedback, the radiation of the space, and the ventilation condition. Compared with open space, confined space oil pool fires have a greater fire risk and may cause flashover. There have been some studies on burning characteristics of confined space oil pool fire [23, 24], but at present, there is still a lack of reports on transformer oil in confined space. As a basic and important issue in the research of transformer oil, Chen et al. [24] studied the influence of the amount of transformer oil and the volume of iron core on the formation and development of fire in a confined space. Based on the previous work mentioned above, researchers have attempted to reveal the burning behaviors of transformer oil pool fires, but the comprehensive information on combustion characteristics of transformer oil, such as flame shape, mass loss rate, flame height, and fire plume temperature, was barely involved, in particular, in confined space. In particular, in the process of transformer fire development, the phenomenon that the transformer upper oil pillow, the transformer lower oil collection pit, and flowing fire together constituted a multiscale transformer fire [25] will be emphatically studied by setting multiple fire sources in the chamber in this experiment.

In order to ensure the safety of the substation, the fire requirements for the transformers are specified. The “Code for fire protection design of buildings GB 50016-2014 (2018)” divides the total oil of transformers into three classes and makes requests for the fire separation distance under each of the three classes. Meanwhile, the “Code for design of 20 kV

and below substation GB50053-2013” defines the fire protection of the transformer. According to “Operation specification for power transformer DL/T572-2010,” the working temperature of the top-layer transformer oil in oil-immersed transformers can be as high as 70°C–95°C. Li et al. [26] experimentally reported that an increase in initial fuel temperature could enhance the fuel evaporation rate and consequently lead to an increase in flame spread using spilling aviation kerosene. Ji et al. [27] also found that the initial temperature could affect the flame spread characteristics of diesel and gasoline-diesel blends. However, the studies mentioned above related to transformer oil pool fires were carried out at fixed initial temperature without considering different initial temperatures. Hence, it is very important to understand the effects of initial temperature on the burning characteristics of pool fire for transformer oil. In addition, the essential parameters of fuel thickness are directly related to the burning behaviors of pool fires [21, 28]. Zhao et al. [21] studied the effects of fuel thickness on the combustion characteristics of pool fire for transformer oil, but only focused on the burning process, and did not quantitatively analyze the flame height and flame temperature. Therefore, it is necessary to carry out further studies on the burning characteristics of transformer oil pool fire taking the effects of initial temperature and fuel thickness into account.

In this study, a series of comparative laboratory-scale experiments are conducted to investigate the effects of fuel thickness and initial temperature on the burning behaviors of pool fire using transformer oil in open space and the difference between transformer oil between open and confined spaces. The essential parameters of mass loss rate, flame height, and fire plume temperature are obtained and compared. The results are not only helpful in a better understanding of the burning characteristics of transformer oil pool fires but also provide some basic data for the prevention and control of transformer oil fires.

2. Materials and Methods

As concluded above, the burning characteristics of transformer oil are different in open space and confined space. Therefore, two experimental apparatus were designed in the experiments reported, which were illustrated in Figures 1(a) and 1(b), respectively. The chamber used in confined space experiments is 1.2 m (length) × 1.2 m (width) × 1.2 m (height). The front side of the chamber is fireproof glass, and the other side is a stainless steel plate with a fireproof board. A circular pool with a diameter of 20.0 cm and 10.0 cm side wall is used as a burning project in open space, while the diameters of the pools used in confined space are 15 cm, 20 cm, and 30 cm. The diameters of the oil pool applied in this study have been widely used in previous studies [21, 29, 30]. Kunlun transformer oil labeled by KI25X is selected as the test oil, which is widely used as insulation in electrical equipment, such as transformers. The detailed thermophysical parameters of transformer oil are shown in Table 1.

The data acquisition systems used in open space are mainly composed of electronic balance, high-definition

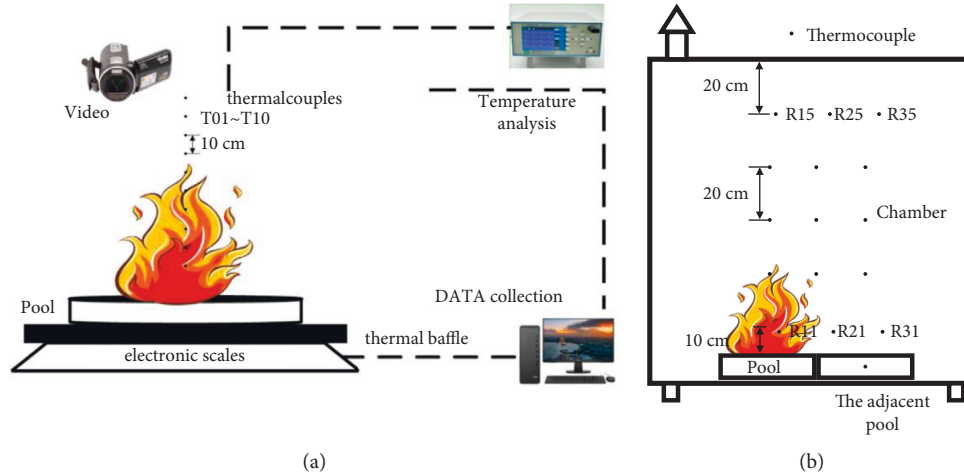


FIGURE 1: Schematic diagrams of the experimental setup. (a) For open space. (b) For confined space.

TABLE 1: Thermophysical parameters of Kunlun transformer oil KI25X.

Pour point	Density, 20°C	Flashpoint (°C)	Viscosity, 40°C
-45°C	885 kg/m	143	9.9 mm ² /s

(HD) camera, heat flux meter, and thermocouple tree. However, considering the high temperature will cause damage to equipment, only thermocouples and high-definition (HD) camera are used for data acquisition in confined space experiments. The electronic balance with an accuracy of 0.01 g is placed under the burning project to record the mass loss rate at an interval of 1.0 s during the combustion process. A Sony 4K HD camera with a resolution of 1920 × 1080 and a frame rate of 25 frames per second is set at the side to monitor the flame geometry. A flame image processing software is applied to process the video-captured images frame by frame to obtain the flame height. The thermocouple tree of open space consisting of 10 K thermocouples with the first and the last thermocouples at 0.2 m and 1.1 m from the burning pool at 0.1 m interval is arranged to monitor the flame temperature. Three thermocouple trees are arranged above the two pools along the central axis of each pool and the centerline of two pools in the chamber. Each thermocouple tree consists of 5 K thermocouples with the first and the last thermocouples at 0.1 m and 0.9 m from the pool at 0.2 m interval. All the thermocouples used in this work have a temperature range and data collection interval of 0~1 100°C and 1.0 s, respectively. The use of K-type thermocouples to measure the temperature above the pool of a transformer oil fire has been successfully adopted in previous studies [21].

In order to investigate the effects of fuel thickness and initial temperature on pool fire of transformer oil, the variables of three fuel thickness and five initial temperatures are considered in open space in this study. The initial fuel thicknesses of 0.5 cm~3.0 cm for heptane pool fires and 1.0 cm for transformer oil fires were applied in previous work [20, 31]. Therefore, a total of three popular fuel thicknesses (h) used in oil pool fire of 0.5 cm, 1.0 cm, and

2.0 cm are designed, which can be achieved by controlling the volume of the test transformer oil. As is well known, the maximum working temperature of transformer oil in the oil-immersed transformer can be as high as 70°C~95°C. Five initial temperatures (T_i) of 25°C, 45°C, 75°C, 85°C, and 95°C are considered in this study, and the transformer oil is heated to the desired initial temperature by a heating device before each experiment. To investigate the combustion characteristics of transformer oil in a confined space and whether the adjacent transformer oil pool can be ignited, two oil pools of the same size are placed next to each other in the chamber. All the experiments are carried out in a test hall with the environmental conditions of 26°C ± 4°C ambient temperature and 70 ± 5% relative humidity. Generally, each burning test with the same condition is repeated at least three times to reduce the experimental uncertainty.

3. Results

3.1. Burning Characteristics in Open Space

3.1.1. *Burning Behavior.* Figure 2 represents the typical flame images in the steady stage under different fuel thickness and initial temperature conditions, respectively. According to the video analysis, the pool fire of transformer oil rapidly reaches a steady stage after a short initial period. Hence, the typical flame images in the steady stage under different fuel thickness and initial temperature conditions are selected to compare and analyze in this study. Obviously, the flame of the pool fire is basically perpendicular to the fuel surface and the flame geometry is generally conical in still-air conditions. It can be seen from Figure 2(a) that the flame height apparently increases when the fuel thickness increases from 0.5 cm to 1.0 cm, while the flame height does not significantly change as the fuel thickness increases from 1.0 cm to 2.0 cm. The previous work by Suo-Anttila et al. [32] and Vali et al. [33] reported that when the pool fire of liquid fuel burned, about 3.0 mm isothermal layer would be formed below the fuel surface, which would absorb the majority of the heat generated by combustion. When the fuel thickness

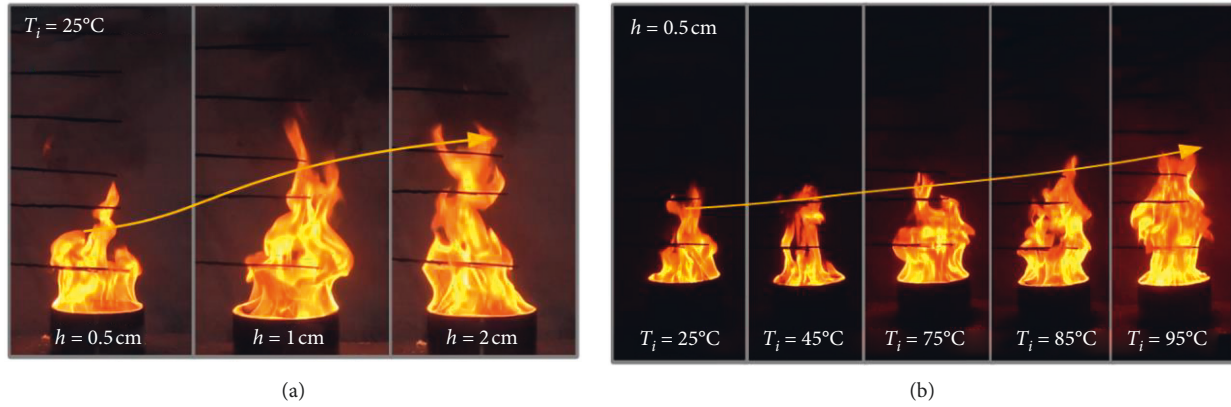


FIGURE 2: Typical flame images in steady stage under different experimental conditions. (a) Different fuel thickness conditions. (b) Different initial temperature conditions.

increases beyond a critical value, the fuel can be regarded as infinitely deep; consequently, the insignificant influence of fuel thickness on the combustion process of pool fire was observed. In this study, as the fuel thickness increases beyond 1.0 cm, the flame height and geometry cannot be significantly affected by the fuel thickness, which coincides well with the previous work.

Moreover, it is noted from Figure 2(b) that the flame height obviously increases with the increase in the initial temperature of transformer oil fuel. This may be caused by the fact that the enhancement of initial temperature will promote the combustion reaction activity of transformer oil, and subsequently, the combustion efficiency of transformer oil would be strengthened, which results in an increase in flame height.

3.1.2. Mass Loss Rate. Figure 3 plots the variations of mass loss rate as a function of time for various fuel thickness and initial temperature conditions, respectively. Generally, the mass loss rate of the pool fire drops slowly in the initial time, and then shows a steady and rapid decrease until the pool fire begins to decay and extinguish. It can be found from Figure 3(a) that the deeper the fuel depth and the larger the volume of transformer oil, the longer the burning duration time. In order to the study effects of fuel thickness and initial temperature on mass loss rate, the average value of mass loss rate in the steady stage is taken as a characteristic value to compare and analyze, as summarized in Table 2.

It is worth noting that the mass loss rate in the steady stage increases when the fuel thickness increases from 0.5 cm to 1.0 cm, whereas the values of mass loss rate in the steady stage do not significantly change as the fuel thickness is beyond 1.0 cm. This is mainly due to that when the fuel thickness is less than 1.0 cm, the pool fire can be recognized as a small-thickness pool fire and consequently the heat loss by side wall conduction should be considered, while with the fuel thickness increases beyond 1.0 cm, the oil pool gradually turns to a deep pool, and then, the heat loss by side wall conduction can be gradually neglected [34]. In addition, the variation of mass loss rate with fuel thickness is similar to the

results in a previous work by Chen et al. [34]. Moreover, the mass loss rate in the steady stage is less sensitive to the initial temperature of transformer oil. This observation is similar to results in previous work by Chen et al., which demonstrated that the burning rate in the stabilization stage did not significantly vary with initial fuel temperature for n-heptane [35]. To the best of our knowledge, the heat release rate of fire during the combustion process can be determined by mass loss rate, combustion heat, and combustion efficiency, which can be expressed by the following formula:

$$Q = \varphi \dot{m} \Delta H, \quad (1)$$

where Q denotes the heat release rate, φ is the combustion efficiency, \dot{m} is the mass loss rate, and ΔH is combustion heat. Therefore, as the fuel thickness increases from 0.5 cm to 1.0 cm, the mass loss rate rises and then the heat release rate increases, while when the fuel thickness increases from 1.0 cm to 2.0 cm, the mass loss rate and consequently heat release rate do not vary significantly. In addition, although the mass loss rate is found to be independent of the initial temperature of transformer oil, the combustion efficiency φ and the heat release rate may change with the initial fuel temperature.

3.1.3. Flame Height. Figure 4 shows the variations of flame height versus time for various fuel thickness and initial temperature conditions, which are obtained from the video analyzed frame by frame. It can be noted that after the transformer oil is ignited, the flame height rapidly rises for a period of time and then pool fires reach a relatively steady stage, and the flame frequently fluctuates but remains changing around a stable value. Appreciably, the deeper the fuel thickness, the larger the flame height, but the effects of fuel thickness on the flame height significantly reduce when the fuel thickness is greater than 1.0 cm. Moreover, as the initial temperature of the transformer oil rises, the flame height shows a significant increase. As mentioned above, the initial temperature had a small effect on mass loss rate, but the flame height increases as the initial temperature increases. This can be attributed to the fact that the increase in

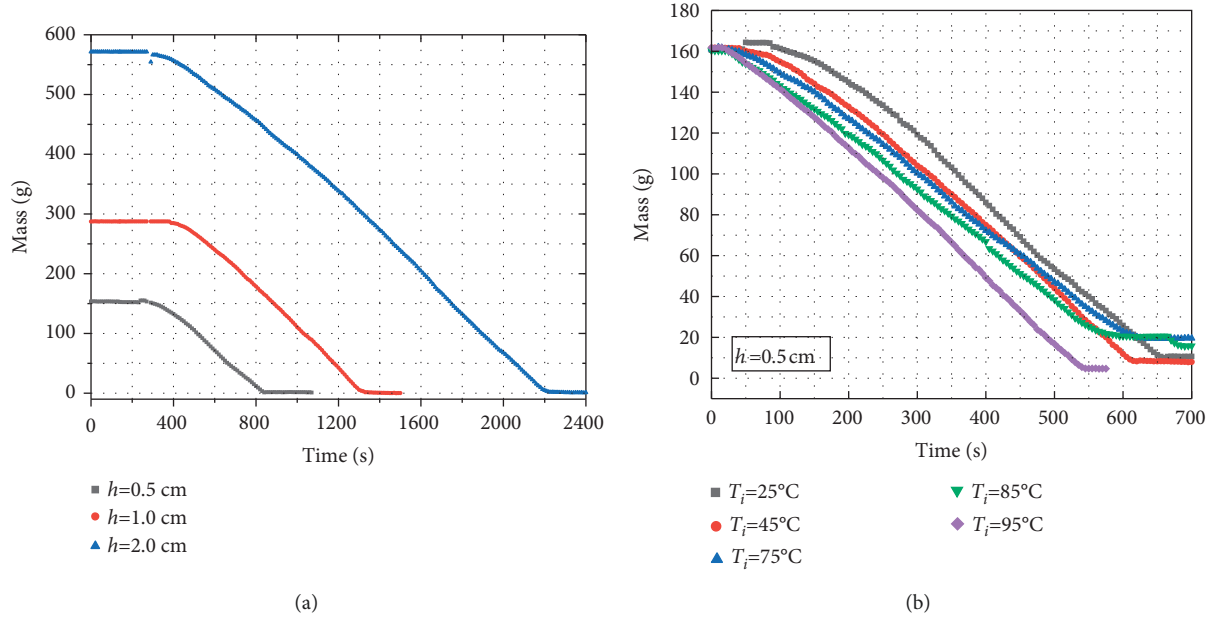


FIGURE 3: Variations of mass loss rate as a function of time under different experimental conditions, (a) different fuel thicknesses, and (b) different initial temperatures.

TABLE 2: Average values of mass loss rate for different experimental conditions.

Fuel thickness (cm)	Initial temperature ($^\circ\text{C}$)	Mass loss rate (g/s)
0.5	25	0.291
1.0	25	0.314
2.0	25	0.315
0.5	45	0.280
0.5	75	0.285
0.5	85	0.283
0.5	95	0.295

initial temperature may enhance the reaction activation energy and combustion efficiency, which results in the rise in the flame height. At present, some investigations have been performed to propose a prediction model to describe the flame height of pool fire. For circular pool fire, a modified model for predicting the flame height was established by Heskestad [36], which is shown as follows:

$$\frac{Z_f}{D} = 3.7\dot{Q}^{*2/5} - 1.02, \quad (2)$$

where Z_f is the flame height of the pool fire, D is the diameter of the circular pool, and \dot{Q}^* is the dimensionless heat release rate, which can be calculated by the following equation [4]:

$$\dot{Q}^* = \frac{\dot{Q}}{\rho_\infty c_p T_\infty g^{1/2} D^{5/2}} = \frac{\varphi \dot{m} \Delta H}{\rho_\infty c_p T_\infty g^{1/2} D^{5/2}}, \quad (3)$$

where ρ_∞ , c_p , and T_∞ are the density, specific heat, and temperature of the ambient air, respectively, and g is the gravity acceleration. Subsequently, equation (2) can be further simplified as follows:

$$Z_f \propto (\varphi \dot{m})^{2/5}. \quad (4)$$

Based on equation (4), the flame height of the pool fire as a function of $\dot{m}^{2/5}$ is plotted in Figure 5, in which the red dotted line presents the linear fitting between the flame height and $\dot{m}^{2/5}$ for 25°C initial temperature conditions. The value of Adj. R-Square is more than 0.94, and the residual sum of squares is only 0.85, which demonstrates that the flame height linearly increases with the increase in $\dot{m}^{2/5}$ for 25°C initial temperature conditions. However, as the initial temperature increases, the flame height is significantly larger than the predictions of 25°C initial temperature conditions. This indicates that the increase in initial temperature will promote the combustion efficiency of the transformer oil, which is consistent with the analysis mentioned above.

3.1.4. Fire Plume Temperature. Figure 6 shows the fire plume temperature at different heights as a function of time for various fuel thicknesses and initial temperature conditions. It can be seen that the temperature at different heights rapidly increases, then remains basically stable for a period of time, and eventually begins to decay. Obviously, as the height rises from the fuel surface, the fire plume temperature drops. Moreover, it can be noted that the temperature of the fire plume is different as the fuel thickness and initial temperature varying. Hence, the average temperature of fire plume at different heights in a steady stage for different experimental conditions is plotted in Figure 7.

It can be noted that the fire plume temperature at a fixed height shows an increase with fuel thickness and initial temperature. Heskestad [8] carried out a series of pool fire

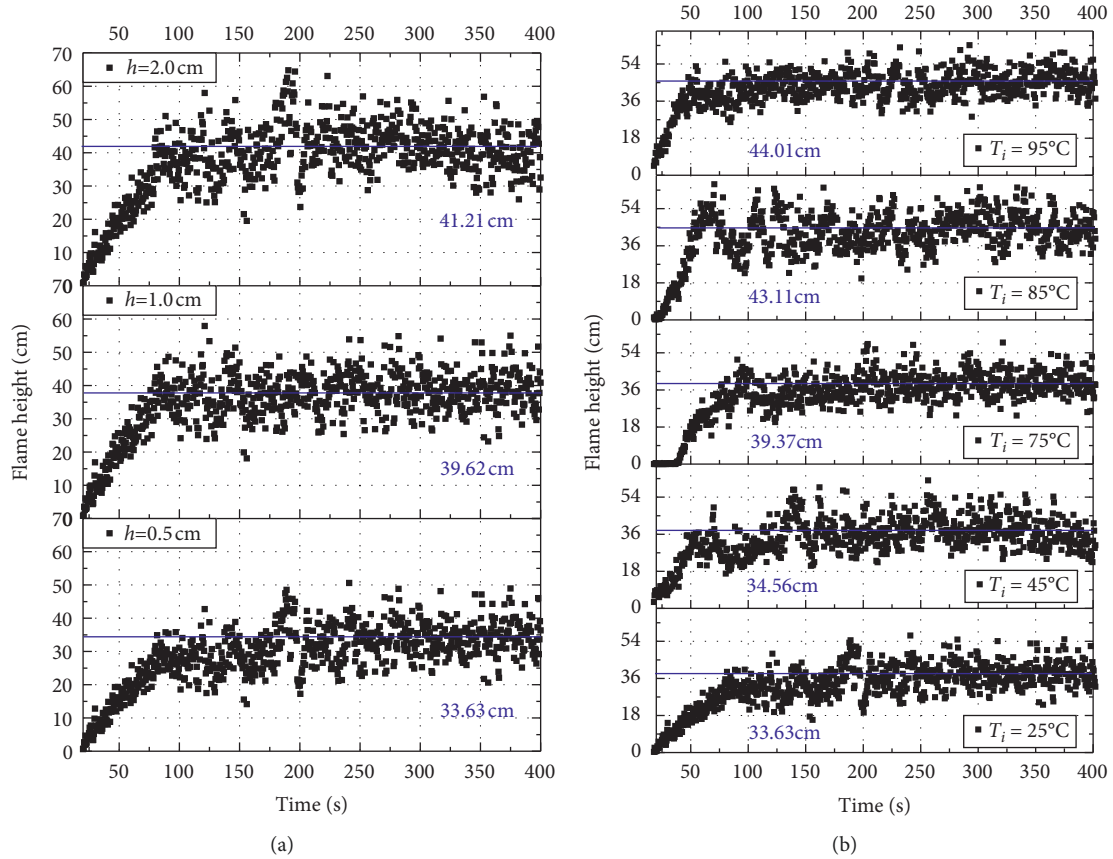


FIGURE 4: Variations of flame height as a function of time under different experimental conditions, (a) different fuel thicknesses, and (b) different initial temperatures.

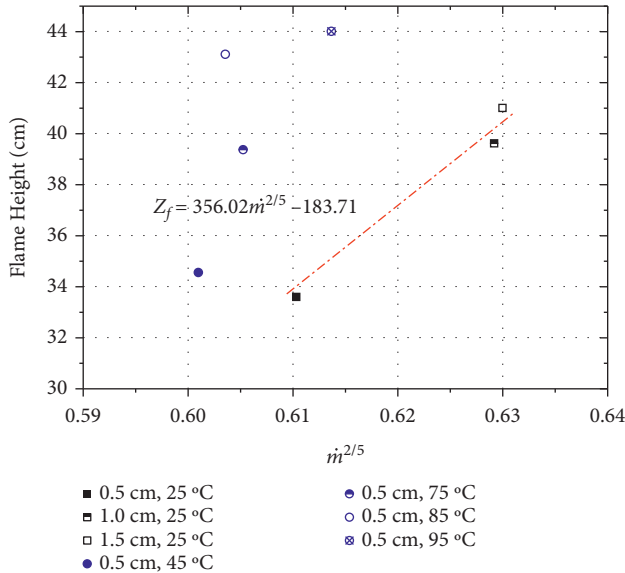


FIGURE 5: Flame height as a function of $\dot{m}^{2/5}$ for different experimental conditions.

experiments and established a modified equation to describe the axial fire plume temperature rise, which can be calculated by the following:

$$\Delta T_0 = 9.1 \left(\frac{T_\infty}{g c_p^2 \rho_\infty^2} \right)^{1/3} \dot{Q}_c^{(2/3)} (Z - Z_0)^{-(5/3)}, \quad (5)$$

where ΔT_0 is the axial fire plume temperature rise, \dot{Q}_c is the convective heat release, which can be determined by approximately $0.7\dot{Q}$ [13], Z is the height from the fuel surface, and Z_0 is the height of virtual origin, which can be expressed by the following formula (8):

$$Z_0 = 0.083\dot{Q}^{2/5} - 1.02 D. \quad (6)$$

According to equation (5), the axial temperature profile of the fire plume can be simplified as follows:

$$\left(\frac{\Delta T_0/T_\infty}{\dot{Q}^{2/3}} \right) \propto \left(\frac{Z - Z_0}{D} \right)^{-5/3}. \quad (7)$$

Then, equation (7) above can be converted to [14] the following:

$$\left(\frac{\dot{Q}^{2/3}}{\Delta T_0/T_\infty} \right) \propto \frac{Z}{D}. \quad (8)$$

Figure 8 represents the dimensionless temperature profile of the fire plume as a function of normalized vertical height Z/D . Notably, the values of $(\dot{Q}^{2/3}/(\Delta T_0/T_\infty))$

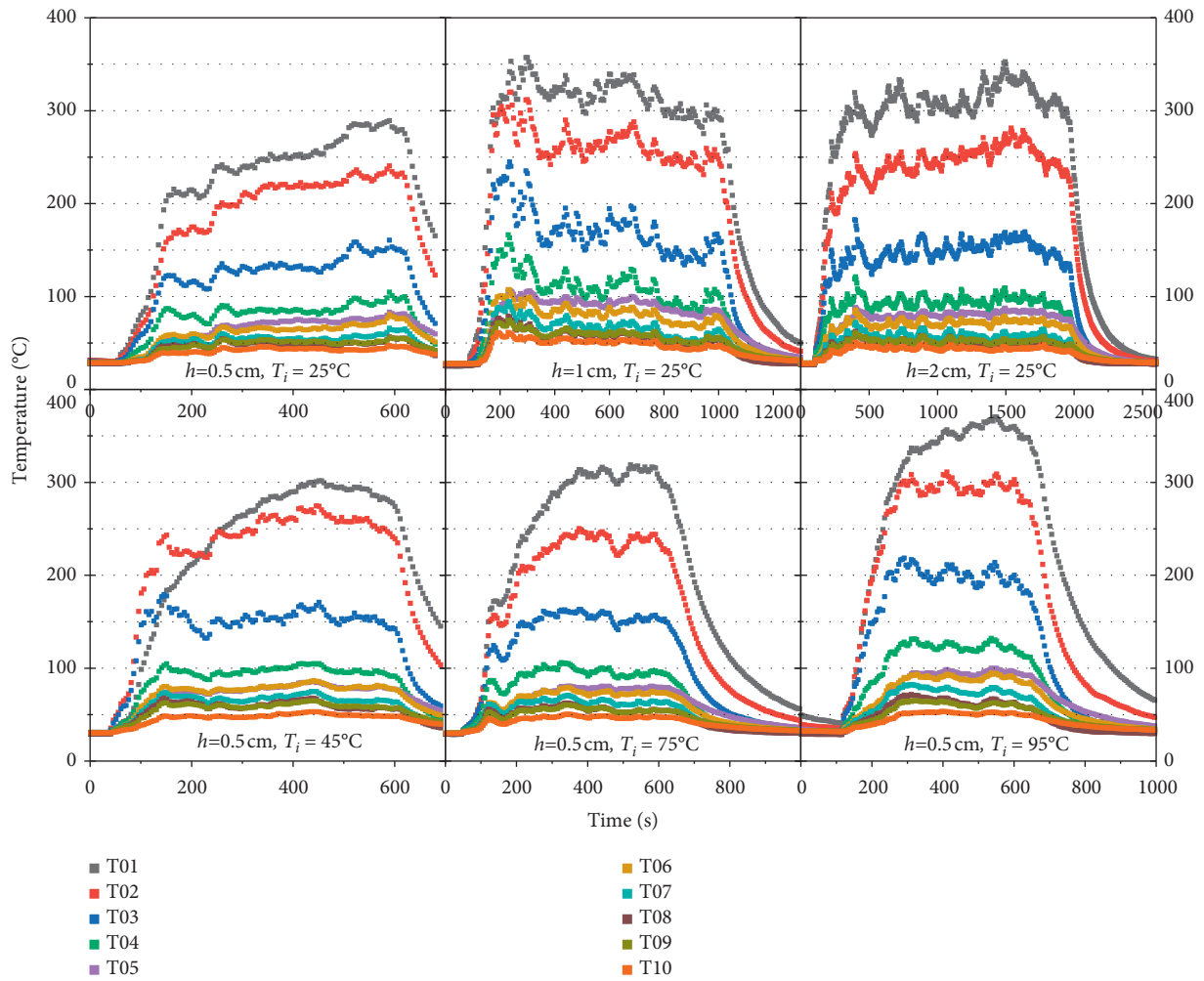


FIGURE 6: Fire plume temperature as a function of time under different experimental conditions.

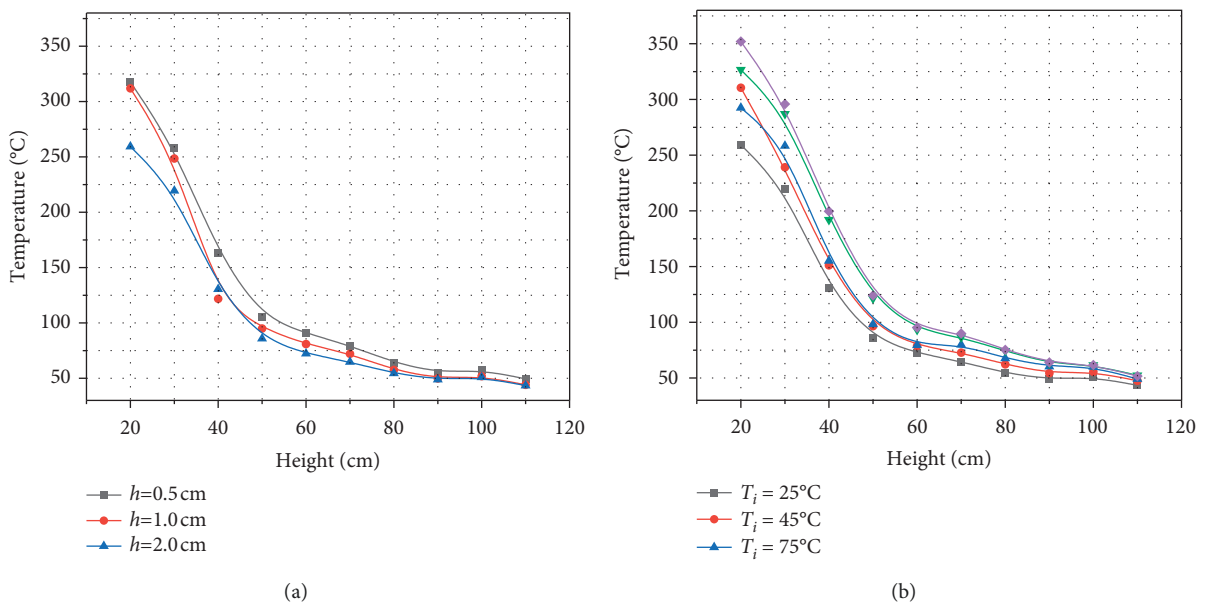


FIGURE 7: Fire plume temperature as a function of height for different experimental conditions, (a) different fuel thicknesses, and (b) different initial temperatures.

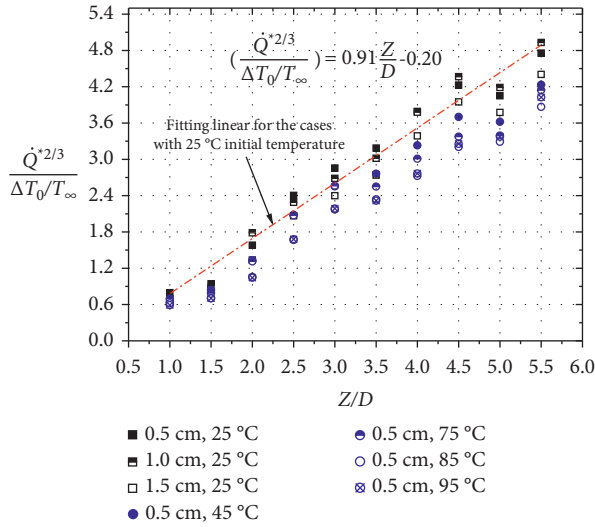


FIGURE 8: Dimensionless temperature profile of the fire plume as a function of normalized vertical height Z/D .

linearly increase with the increase in normalized height Z/D . Equation (8) is applied to describe the axial temperature profile of the fire plume for the cases with 25°C initial temperature, as shown by the red dot solid line in Figure 8, which can be expressed as follows:

$$\left(\frac{\dot{Q}^{*2/3}}{\Delta T_0/T_\infty} \right) = 0.91 \frac{Z}{D} - 0.20. \quad (9)$$

The value of Adj. R-Square is well above 0.98, and the residual sum of squares is less than 1.23, which demonstrates that the experimental results match the predicated data reasonably well. The fitting coefficient of 0.91 is obviously different from the corresponding result of 0.44 for biodiesel pool fire reported by Fan et al. [10]. Tang et al. [15] and Hayasaka [37] also pointed out that the combustion characteristics of a pool fire are essentially related to the properties of the fuel. In addition, since the combustion efficiency φ is not considered in the data processing of \dot{Q}^* , the experimental data of $(\dot{Q}^{*2/3}/(\Delta T_0/T_\infty))$ for cases with larger initial temperatures are lower than the predicted value, which also shows that the initial temperature of transformer oil has a significant effect on combustion efficiency φ .

3.2. Burning Characteristics in Confined Space

3.2.1. Burning Behavior. Flame shapes of oil pools with diameters of 15 cm and 20 cm burning in the chamber at typical times are displayed in Figure 9. As can be seen, after being ignited, the flame height rapidly increases to the maximum, and then decreases and becomes stable. The stabilization phase will last for a long time until extinction. In addition, when the diameter of the oil pool is 15 cm or 20 cm, another adjacent oil pool is not ignited. However, when the diameter of the oil pool is 30 cm, the adjacent oil

pool is ignited and the burning blast phenomenon occurs, which will be discussed later. Compared with open space, the fire flame in confined space is darker and the particles generated by combustion will adhere to the glass that will affect the observation.

3.2.2. Flame Height. The camera could not shoot through the fireproof glass when the combustion and burning blast characteristics of the oil pool with a diameter of 30 cm are tested in the chamber. Therefore, only the flame height of oil pools with diameters of 15 cm and 20 cm in the chamber is analyzed, as shown in Figure 10.

The fire growth in the chamber is similar to the development of compartment fire, which can be regarded as the initial stage, rapid growth stage, stable stage, and decay stage. In the beginning, the flame height rapidly increases over time in a trend similar to t^2 fires. Subsequently, as more and more combustible pyrolysis gas is accumulated in the chamber, the flame height will rapidly increase to the maximum. Accordingly, a large amount of accumulated combustible pyrolysis gas is rapidly consumed, oxygen content in the chamber decreases, and the flame height gradually begins to decline. The flame height then stabilizes due to the opening of smoke exhaust and air-supply holes in the side wall of the chamber. The average flame height is 33.63 cm in an open space of 20 cm oil pool, which is a little lower than the flame height in the confined space. The results suggest that due to the restriction of oxygen supply, the flame needs to be extended longer in the vertical to entrainment air, making the flame of confined space higher than in open space.

3.2.3. Fire Plume Temperature. The temperature of each measuring point in the chamber under different conditions is plotted in Figure 11. For $D = 15$ cm and 20 cm, the temperature variation above the burning pool (R11~R15) can be divided into three stages: rapid temperature growth stage, temperature stability stage, and temperature attenuation stage, while the temperature stability stage is replaced by the temperature steady growth stage when focusing on the temperature of the centerline of two pools (R21~R25) and temperature above the unburning pool (R31~R35). As a result, the temperature in the chamber is discussed by taking the average of the temperature in the temperature stability stage or temperature steady growth stage as shown in Figure 12. The temperatures in the chamber found an obvious increase with the oil pool diameter, and R1 is much higher than R2 and R3. It can be noted that the temperature of R1 decays with increasing height, which is consistent with the variation trend of flame temperature in open space. According to the analysis in section 3.1, the dimensionless temperature profile of the fire plume is proportional to the normalized vertical height, as shown in Figure 13. The relationship between the dimensionless temperature profile of the fire plume and normalized vertical height can be expressed by the following:

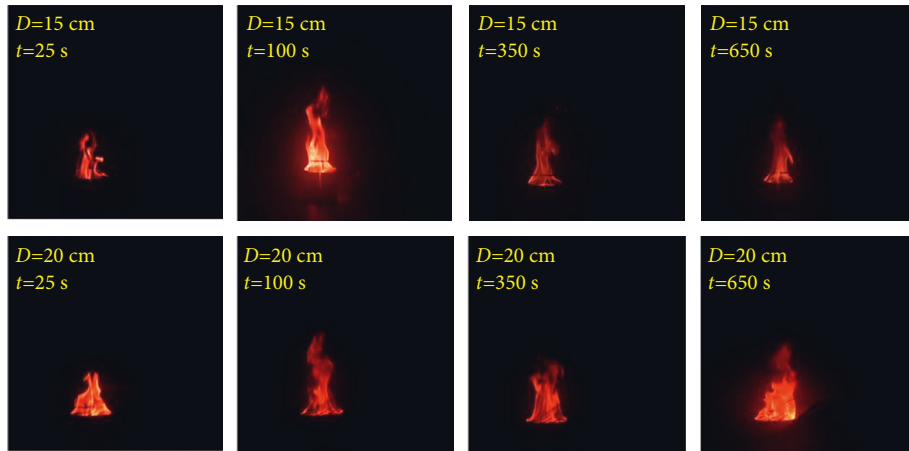


FIGURE 9: Sequence diagram of flame shape at a typical time in the chamber.

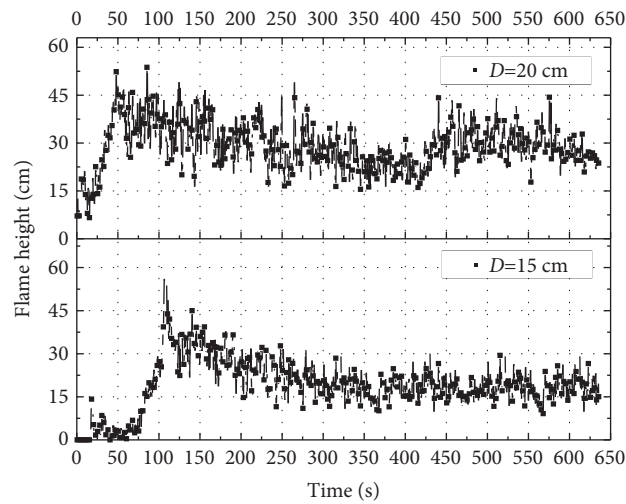


FIGURE 10: Flame height in the chamber varies with time.

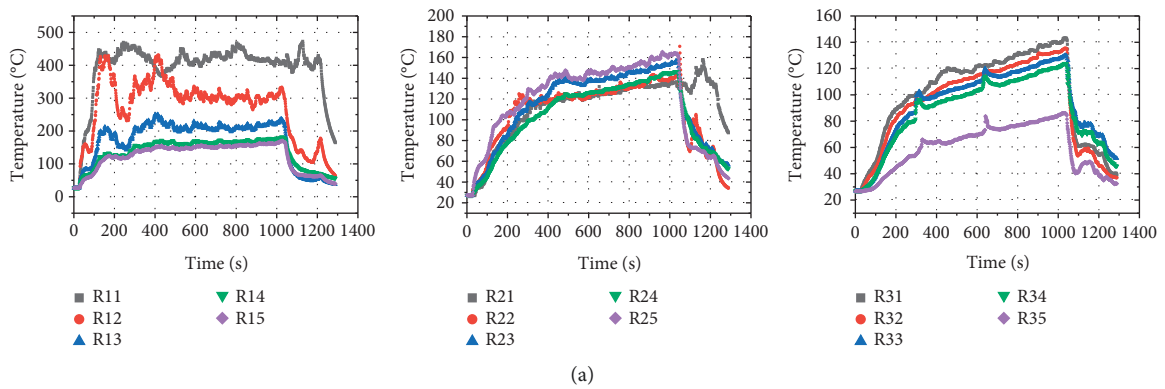


FIGURE 11: Continued.

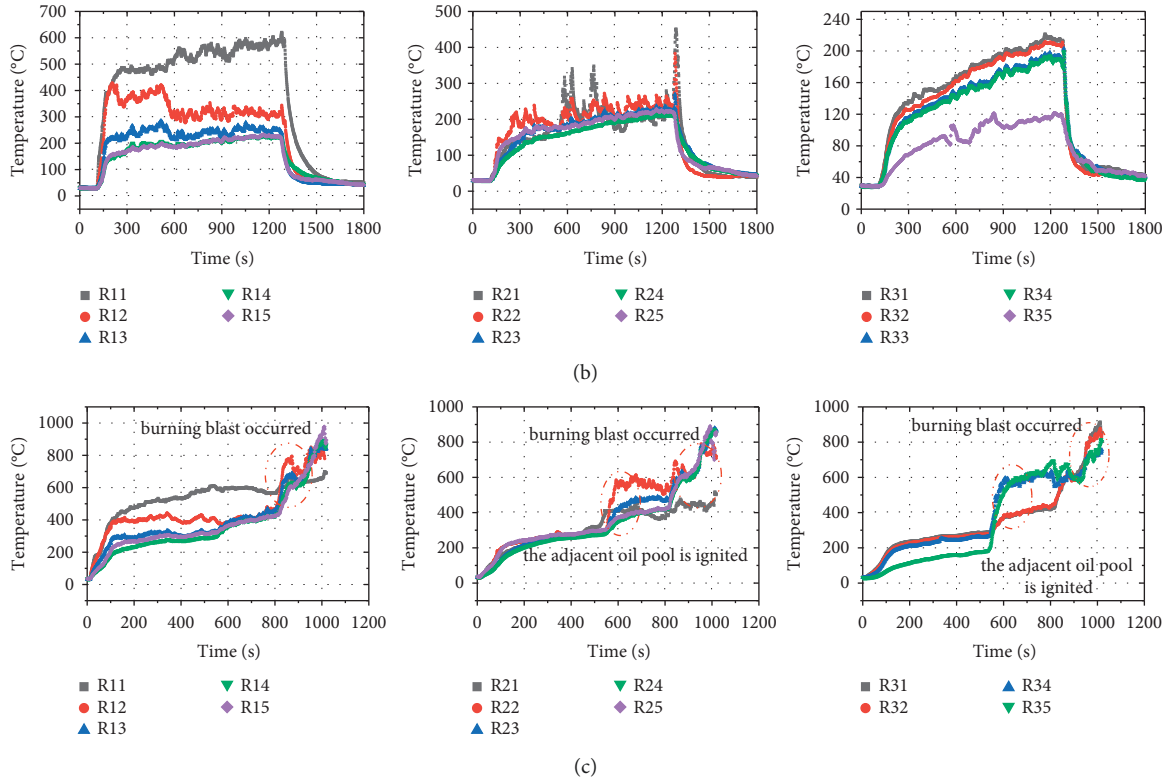


FIGURE 11: Temperature of each measuring point in the chamber of different conditions. (a) $D = 15$ cm. (b) $D = 20$ cm. (c) $D = 30$ cm.

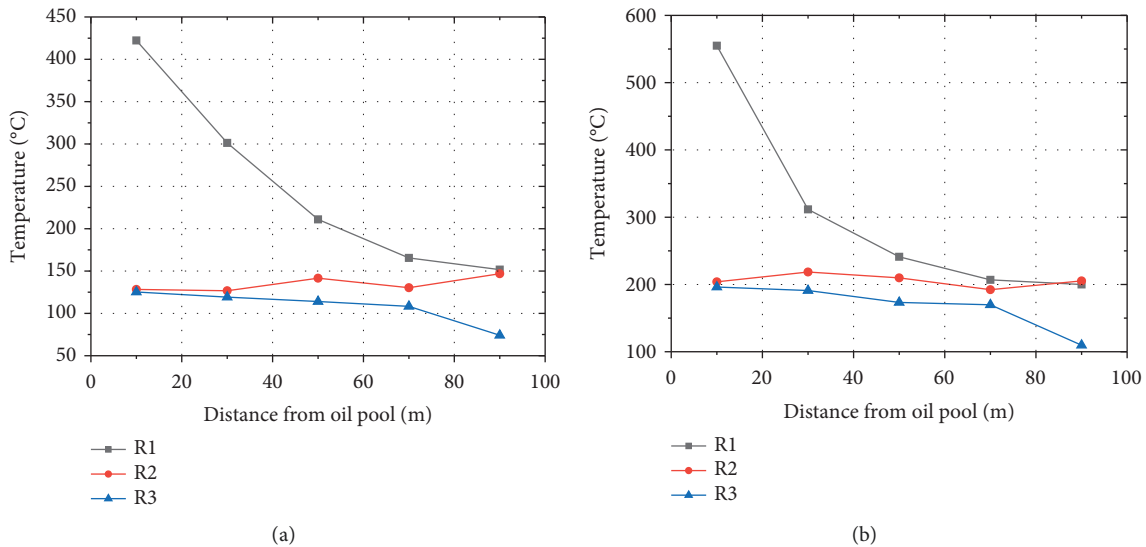


FIGURE 12: Average temperatures in different diameters vary with distance. (a) $D = 15$ cm. (b) $D = 20$ cm.

$$\left(\frac{\dot{Q}^{*2/3}}{\Delta T_0/T_\infty} \right) = 0.25 \frac{Z}{D} + 0.31. \quad (10)$$

The value of Adj. R-Square is well above 0.95, and the residual sum of squares is only 1.94, which demonstrates that the experimental results coincide well with the predicted data. The fitting coefficient differs from the corresponding

result of in open space, which may be due to the difference in experimental configuration.

The phenomenon of burning blast and the ignition of the adjacent oil pool are observed when the combustion experiment of oil pool fire with a diameter of 30 cm is carried out in the chamber, which will be analyzed by considering the temperature in the chamber displayed in Figure 11(c). At the beginning of 550 s, the temperature

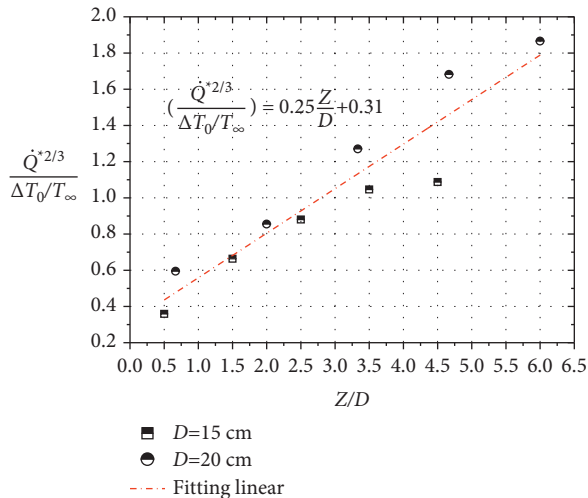


FIGURE 13: Dimensionless temperature profile of the fire plume as a function of normalized vertical height Z/D .

variation trend is similar to that of oil pool fire with diameters of 15 cm and 20 cm, which rapidly increases to a certain value and maintains for a long time. But at this time, the temperature of the chamber is about 270°C , which is much higher than the oil pool fire with diameters of 15 cm and 20 cm. When it comes to 580 s, the adjacent oil pool is ignited by a high-temperature ignition source, the temperature of R2 and R3 thermocouple trees rapidly increases and exceeds 400°C , and the temperature of the upper part of the chamber even reaches 600°C . Between 600 s and 800 s, the two oil pools burn at the same time, and the temperature in the chamber reaches a relatively stable stage again. Finally, at 800 s, due to the continuous high temperature, the chamber door deforms, which leads to a certain gap between the door and the chamber. Immediately, fresh air is filled into the chamber, and the burning blast happens. It can be inferred from the experiment that when the temperature in the chamber reaches 270°C , the adjacent oil pool can be ignited only under the condition of the high-temperature ignition source. Moreover, the temperature of the chamber exceeds 400°C , and the temperature of the upper part of the chamber reaches 600°C . Only when fresh air is added, the phenomenon of a burning blast can occur.

4. Conclusions

In this study, a series of comparative experiments were carried out using transformer oil to investigate the effects of fuel thickness and initial temperature on the burning characteristics of pool fires in open space and the difference between transformer oil between open and confined spaces. The variables of three fuel thickness and five initial temperatures are considered in open space, and the characteristics of mass loss rate, flame height, and fire plume temperature are quantitatively analyzed and compared. The variations of mass loss rate, flame height, and fire plume temperature apparently increase as the fuel thickness increases from 0.5 cm to 1.0 cm, whereas the insignificant

influence of fuel thickness on the corresponding burning characteristics as the fuel thickness increases from 1.0 cm to 2.0 cm. The mass loss rate is less sensitive to the initial temperature of transformer oil, but the flame height and fire plume temperature significantly rise with the initial temperature. Moreover, the modified models to predict the flame height and fire plume temperature for 25°C initial temperature conditions are proposed. For cases that burning in the chamber, the flame height is higher and will rapidly increase to the maximum, then decreases, and tends to be stable, which is obviously different from the oil pool fire burning in an open space. In addition, when the diameter of the oil pool is 30 cm and the temperature in the chamber reaches 270°C , the adjacent oil pool can be ignited by a high-temperature ignition source. At the time the temperature of the upper part of the chamber comes to 600°C , fresh air added to the chamber will cause a burning blast.

Based on the results of this study, the quality of transformer oil and the size of pool fire formed by flowing transformer oil have a significant influence on the scale of fires. In addition, despite its high flash point, the transformer oil has the potential to be ignited by a nearby large enough fire source. Therefore, in the process of use, transportation, and storage of transformer oil, the total amount of transformer oil should be fully considered and it should be kept away from other dangerous combustibles. A further study is in progress to investigate the effects of spacing and size on the ignition and combustion characteristics of multiple oil pools in a confined space. Moreover, the characteristics of large-scale fires for transformer oil will be also studied.

Data Availability

The data used to support the findings of the study can be obtained from the corresponding author upon request.

Conflicts of Interest

The authors declare that there are no conflicts of interest regarding the publication of this paper.

Acknowledgments

This research was funded by the State GRID Company Science and Technology Projects (5455DW210005).

References

- [1] T. O. Rouse, "Mineral insulating oil in transformers," *IEEE Electrical Insulation Magazine*, vol. 14, no. 3, pp. 6–16, 1998.
- [2] D. Kamikawa, W. G. Weng, K. Kagiya, Y. Fukuda, R. Mase, and Y. Hasemi, "Experimental study of merged flames from multifire sources in propane and wood crib burners," *Combustion and Flame*, vol. 142, no. 1-2, pp. 17–23, 2005.
- [3] S. Schälike, H. Chun, K. B. Mishra, K.-D. Wehrstedt, and A. Schönbacher, "Mass burning rates of di-tert-butyl peroxide pool fires-experimental study and modeling," *Combustion Science and Technology*, vol. 185, no. 3, pp. 408–419, 2013.
- [4] K. B. Mishra and K.-D. Wehrstedt, "Diffusive burning of blended peroxy-fuels: some experimental results," *Fuel Processing Technology*, vol. 140, pp. 324–330, 2015.

- [5] C. Wang, J. Guo, Y. Ding, J. Wen, and S. Lu, "Burning rate of merged pool fire on the hollow square tray," *Journal of Hazardous Materials*, vol. 290, pp. 78–86, 2015.
- [6] H. Wan, Z. Gao, J. Ji, Y. Zhang, K. Li, and L. Wang, "Effects of pool size and spacing on burning rate and flame height of two square heptane pool fires," *Journal of Hazardous Materials*, vol. 369, pp. 116–124, 2019.
- [7] C. Kuang, L. Hu, X. Zhang, Y. Lin, and L. W. Kostiuk, "An experimental study on the burning rates of n-heptane pool fires with various lip heights in cross flow," *Combustion and Flame*, vol. 201, pp. 93–103, 2019.
- [8] G. Heskestad, "Virtual origins of fire plumes," *Fire Safety Journal*, vol. 5, no. 2, pp. 109–114, 1983.
- [9] H. Sun, C. Wang, H. Liu, M. Li, A. Zhang, and M. Xu, "Burning behavior and parameter analysis of biodiesel pool fires," *Combustion Science and Technology*, vol. 190, no. 2, pp. 1–17, 2017.
- [10] C. G. Fan, J. Ji, Y. Z. Li, H. Ingason, and J. H. Sun, "Experimental study of sidewall effect on flame characteristics of heptane pool fires with different aspect ratios and orientations in a channel," *Proceedings of the Combustion Institute*, vol. 36, no. 2, pp. 3121–3129, 2017.
- [11] C. Tao, Y. Liu, F. Tang, and Q. Wang, "An experimental investigation of the flame height and air entrainment of ring pool fire," *Fuel*, vol. 216, pp. 734–737, 2018.
- [12] P. He, P. Wang, K. Wang et al., "The evolution of flame height and air flow for double rectangular pool fires," *Fuel*, vol. 237, pp. 486–493, 2019.
- [13] B. Karlsson, *Quintiere JG Enclosure Fire Dynamics*, CRC Press, Boca Raton, USA, 2000.
- [14] L. Hu, Q. Wang, F. Tang, M. Delichatsios, and X. Zhang, "Axial temperature profile in vertical buoyant turbulent jet fire in a reduced pressure atmosphere," *Fuel*, vol. 106, pp. 779–786, 2013.
- [15] F. Tang, L. Hu, Z. Qiu, and Q. Wang, "A global model of plume axial temperature profile transition from axisymmetric to line-source pool fires in normal and reduced pressures," *Fuel*, vol. 130, pp. 211–214, 2014.
- [16] T. L. Henriksen, T. A. Ring, E. G. Eddings, and G. J. Nathan, "Puffing frequency and soot extinction correlation in JP-8 and heptane pool fires," *Combustion Science and Technology*, vol. 180, no. 4, pp. 699–712, 2008.
- [17] F. Tang, L. Hu, Q. Wang, and Z. Ding, "Flame pulsation frequency of conduction-controlled rectangular hydrocarbon pool fires of different aspect ratios in a sub-atmospheric pressure," *International Journal of Heat and Mass Transfer*, vol. 76, pp. 447–451, 2014.
- [18] G. Heskestad and P. H. Dobson, "Pool fires of transformer oil sinking into a rock bed," *Fire Safety Journal*, vol. 28, no. 1, pp. 33–46, 1997.
- [19] P. Zhu, X. Wang, Z. Wang, H. Cong, and X. Ni, "Experimental study on transformer oil pool fire suppression by water mist," *Fire Science and Technology*, pp. 895–901, 2015.
- [20] B. Zhang, J. Zhang, Y. Huang, Q. Wang, Z. Yu, and M. Fan, "Burning process and fire characteristics of transformer oil," *Journal of Thermal Analysis and Calorimetry*, vol. 139, no. 3, pp. 1839–1848, 2019.
- [21] J. Zhao, J. Zhang, C. Chen, H. Huang, and R. Yang, "Experimental investigation on the burning behaviors of thin-layer transformer oil on a water layer," *Process Safety and Environmental Protection*, vol. 139, pp. 89–97, 2020.
- [22] R. Feng, R. Huo, and Y. U. Hai-Chun, "Experimental study on the character of oil-pool-fire burning in enclosed space," *Fire Science and Technology*, vol. 3, pp. 289–291, 2005.
- [23] H. Pretrel, P. Querre, and M. Forestier, "Experimental study of burning rate behaviour in confined and ventilated fire compartments," *Fire Safety Science*, vol. 8, pp. 1217–1228, 2005.
- [24] Q. Chen, W. Xu, and G. Chen, "Study on influence factors of formation and development of jet fire in confined space," *China Safety Science Journal*, vol. 30, no. 7, pp. 35–40, 2020.
- [25] C. R. Dai, G. Chen, B. Zhu, L. Xu, P. Chen, and R. B. Sun, "Full scale experimental research on combustion characteristics of outside transformer fire," *Fire Science and Technology*, vol. 39, no. 3, pp. 318–321, 2020.
- [26] M. Li, S. Lu, J. Guo, R. Chen, and K.-L. Tsui, "Initial fuel temperature effects on flame spread over aviation kerosene in low- and high-altitude environments," *Fire Technology*, vol. 51, no. 3, pp. 707–721, 2014.
- [27] J. Ji, S. Lin, C. Zhao, K. Li, and Z. Gao, "Experimental study on initial temperature influence on flame spread characteristics of diesel and gasoline-diesel blends," *Fuel*, vol. 178, pp. 283–289, 2016.
- [28] Y. Li, H. Huang, Z. Wang, J. Zhang, C. Jiang, and R. Dobashi, "An experimental and modeling study of continuous liquid fuel spill fires on water," *Journal of Loss Prevention in the Process Industries*, vol. 33, pp. 250–257, 2015.
- [29] C. Wu, T. Zhou, B. Chen, Y. Liu, and P. Liang, "Experimental study on burning characteristics of the large-scale transformer oil pool fire with different extinguishing methods," *Fire Technology*, vol. 57, no. 1, pp. 461–481, 2021.
- [30] M. H. Fan, W. Li, X. F. Du, J. Qi, S. P. Wang, and H. C. Wu, "Experimental study of combustion characteristics of a typical transformer oil," *East China Electric Power*, vol. 41, no. 9, pp. 1865–1870, 2013.
- [31] X. Chen, S. Lu, and Z. Ding, "Initial fuel depth effect on the burning characteristics of thin-layer pool fire in a confined enclosure," *Journal of Thermal Analysis and Calorimetry*, vol. 139, no. 2, pp. 1409–1418, 2020.
- [32] J. M. Suo-Anttila, T. K. Blanchat, A. J. Ricks, and A. L. Brown, "Characterization of thermal radiation spectra in 2m pool fires," *Proceedings of the Combustion Institute*, vol. 32, no. 2, pp. 2567–2574, 2009.
- [33] A. Vali, D. S. Nobes, and L. W. Kostiuk, "Transport phenomena within the liquid phase of a laboratory-scale circular methanol pool fire," *Combustion and Flame*, vol. 161, no. 4, pp. 1076–1084, 2014.
- [34] C. Chen, J. Q. Deng, Z. F. Ju, Z. G. Wang, P. Chen, and J. L. Zhao, "Experimental study on combustion laws of transformer oil pool fire," *J. Saf. Sci. Technol*, vol. 16, no. 8, pp. 63–68, 2020.
- [35] B. Chen, S. X. Lu, C. H. Li, Q. S. Kang, and V. Lecoustre, "Initial fuel temperature effects on burning rate of pool fire," *Journal of Hazardous Materials*, vol. 188, no. 1-3, pp. 369–374, 2011.
- [36] G. Heskestad, "Engineering relations for fire plumes," *Fire Safety Journal*, vol. 7, no. 1, pp. 25–32, 1984.
- [37] H. Hayasaka, "Unsteady burning rates of small pool fires," *Fire Safety Science*, vol. 5, pp. 499–510, 2011.

Research Article

Stress Performance Evaluation of Shield Machine Cutter Head during Cutting Piles under Masonry Structures

Fei Peng,^{1,2} Shiju Ma ,¹ Mingyu Li,¹ and Kui Fu³

¹School of Civil Engineering, Zhengzhou University, Zhengzhou, China

²Henan Provincial Communications Planning & Design Institute Co., Ltd., Zhengzhou, China

³China Railway 18th Bureau Group First Engineering Co., Ltd., Hebei, China

Correspondence should be addressed to Shiju Ma; mashiju2010@126.com

Received 7 March 2022; Revised 26 March 2022; Accepted 29 March 2022; Published 29 April 2022

Academic Editor: S. Mahdi S. Kolbadi

Copyright © 2022 Fei Peng et al. This is an open access article distributed under the Creative Commons Attribution License, which permits unrestricted use, distribution, and reproduction in any medium, provided the original work is properly cited.

In the construction of the metro, the development and operation of large-scale underground space in the city cause the construction of metro tunnels near the original underground structures, and the complex environment for passing structures at close range has increased significantly. Comparing the actual load data of the actual project with the data obtained with the proposed new method, it is proved that the predicted load range corresponds essentially to the measured average curve of the project, which is commonly used with the experimental load formula. Subsequently, the load calculation method is used to guide the construction of the composite base of the protective cutting pile of one of the Zhengzhou metro lines under the existing masonry structure. Based on the existing building damage grade evaluation standards, the professional house inspection agency checked the intersection of the tunnel and the building space and realized that the main structure of the house during the tunnel construction process would be still safe; thereby, Zhenghe Community Building 1# can be used normally after partial repairs.

1. Introduction

The pile-soil composite foundation is considered as a composite soil and provides an efficient approach to shield loading when the composite foundation of the shield shear pile group penetrates the existing masonry structure. Compared with the past, recent projects are large-scale and more adjacent to underground systems, even touching underground piles. It can cause severe environmental problems of rock and soil such as tilting, cracking, and even collapse of the building. This not only affects the routine use of buildings and causes significant economic losses but also poses a serious threat to the lives and property of nearby residents. When there are buildings at the top of the tunnel, subsidence and soil deformation are different from buildings without buildings. Hence, internal and external researchers have conducted extensive research on the impact of underground tunnel construction on adjacent structures. Finno et al. in connection with theoretical/analytical explorations of the problem [1] created a new building model under reasonable and simple conditions. They used this

model to study surface displacement due to shield drilling. Han et al. [2] revised the pack formula [3] and proposed a method for predicting the building sitting curve by considering the structural rigidity of the building—the stiffness correction method, but this method is only suitable for building seats with a Gaussian distribution curve. Match Ouyang et al. [4] considered the effect of building stiffness but did not consider the stiffness of the foundation. Using the principle of equivalent stiffness, the building was equivalent to a layer of soil with similar properties to the subsoil using the Verruijt and Booker solution. The calculation formula is derived for the settlement of buildings on the surface resulting from the construction of the shield. The performance of the shield device is mainly reflected by its operating parameters such as forward speed, thrust, torque, and rotation speed of the cutter head [5].

According to the measured analysis method, Shen [6] analyzed the subsidence and slope characteristics of the buildings resulting from the construction of the shield based on an engineering example of the shield section passing through a subset of buildings on Line 1 of the Chengdu

Metro. Sun and Guan [7] monitored the installation of the floor and ceiling of the building resulting from the construction of a two-lane bumper, along with the case of Hangzhou Metro Line 1 from the underpass of 13 residential complexes. It was found that the next meeting of the masonry structure, which is considered to be the ratio of the accumulated meeting, is obviously more than the natural surface meeting. Xu et al. [8] analyzed the measured data of the shield tunneling stage and studied the characteristics and rules of building deformation due to the shield tunneling. Based on typical engineering examples of six subway tunnels that pass under buildings in the Beijing city, as mentioned by Sun et al. [9], they show that the bending point of the significant impact zone of the base depression is about 0.3 to 0.6 H from the tunnel axis, and the depression law almost follows Peck's correction formula.

Given the development of a finite element method for such a problem, Milliziano et al. [10] used a 2D numerical method to analyze the impact of tunnel construction on a particular masonry structure and obtain the building subsidence curve. Peng et al. [11] used a three-dimensional numerical analysis method to calculate the building structure subsidence resulting from the construction of a two-line parallel shield tunnel. Giardina et al. [12] studied the interactions between sand-tunnel-ground structures through 3D numerical simulation and concluded that the impact of tunnel drilling on buildings is not just relative stiffness between soils and soil it depends, but it also depends on the weight of the building. Ding et al. [13] simulated the effect of shield drilling on the building stress distribution through the finite element method and proposed reinforcement measures to improve the rigidity and integrity of the building based on the finite element simulation results. Most of the above research focuses on ground subsidence resulting from the construction of shield tunnels and uneven subsidence of buildings. Quantitative analysis and research have been done on the selection of construction parameters when the shield penetrates into the masonry structure.

Here, based on the underlying structure of the composite base structure of the Zhengzhou Metro Line 5 bumper pile-cutting group, theoretical calculations are used to obtain the recommended values of construction parameters such as total thrust, total torque, and injection pressure length. Making a shield candle: along with the actual on-site measurements, the settling rules and the deformation of the masonry structure are analyzed during the construction process of shield pile-cutting piles. Finally, the theoretical results obtained with the observed data for the shield construction parameters are successfully confirmed. Successful completion of a project can certainly be a reliable source for similar works in the future.

2. Materials and Methods

2.1. Engineering Background. Currently, research on protective structures in such layers mainly focused on construction technology innovation, excavation surface stability and configuration, and cutter and cutting headwear. [14] For the shield section of Zhengzhou Metro Line 5 with staggered

assembly construction, the geometrical data are as follows: the length of the left tunnel is 1214.457 m, the maximum longitudinal slope of the line is 26.78%, the minimum slope is 2%, and the minimum radius of curvature of the shield tunnel is 400 m, and the buried depth of the interval tunnel is in the range of 15.7 to 28.5 m. The inner and outer diameters of the segment, thickness, and width in order are 5.5, 6.2, 0.35, and 1.5 m. The concrete strength is categorized into the group C50, and the impermeability grade is P12.

The mileage of the left line of the interval section is DK13 + 662.558~DK13 + 711.322 (685~715 ring, length is about 48.764 m) obliquely crosses the 7-story masonry structure in the northwest-southeast direction, and the height is 18.8 m. The foundation adopts reinforced concrete strips, the foundation concrete is C30, there is no basement, and it was constructed in 2007. The foundation is cement deep mixing pile composite foundation $\varnothing 500@950$, the pile length is 11.5 m, and the pile end extends into the bearing layer not less than 750 mm. The shield machine will cut off the cement-soil mixing pile of the original building by 2.6~3.7 m. The number of left-line shields that invaded the mixing piles was about 175, accounting for about 16% of the total piles of the masonry structure composite foundation. The thickness of the top cover of the shield tunnel's lining structure crossing the masonry structure section is 12.1~13.5 m. The geographical location of the project is shown in Figure 1.

2.2. Geological Conditions. The principle of operation of this method is to cut the soil from the front cutter and transfer it out of the cave by transport vehicles, while the next part is done by jacks [15]. The site of the shield section belongs to the alluvial plain of the Yellow River. The layer at a depth of 30 meters of the site is mainly the Holocene Quaternary layer (Q4), and the initial layer is 0~20 meters of sand silt, clay silt, and silt clay with silt and fine sand. This layer varies from medium-dense to fine-grained sand. The tunnel structure is mainly located in the fine sand layer and the silty clay layer. The depth of cover above the tunnel is 12.1 to 13.5 meters, and the water depth above the tunnel varies in the range of 4.4 to 6.4 meters. Figure 2 shows the shield tunneling in different layers, and Table 1 shows the soil parameters.

3. Suggested Values for Construction Parameters of Shield Cut Piles

During the tunneling process, the propulsive torque provided by the multiple inverter motor is transmitted from the planetary reducer and the pinions to the gears that are permanently attached to the cutting head [16]. Under normal conditions of construction, the impedance of drilling piles to cut the shield to the ground and the composite foundation should be reduced. The main construction parameters to be determined are total thrust, total torque, injection pressure, advance speed, and cutting head speed [16].

3.1. Prediction of the Total Thrust and Total Twist. Regardless of the load transfer effect of the pile, the composite gravity method is adopted, and the displacement

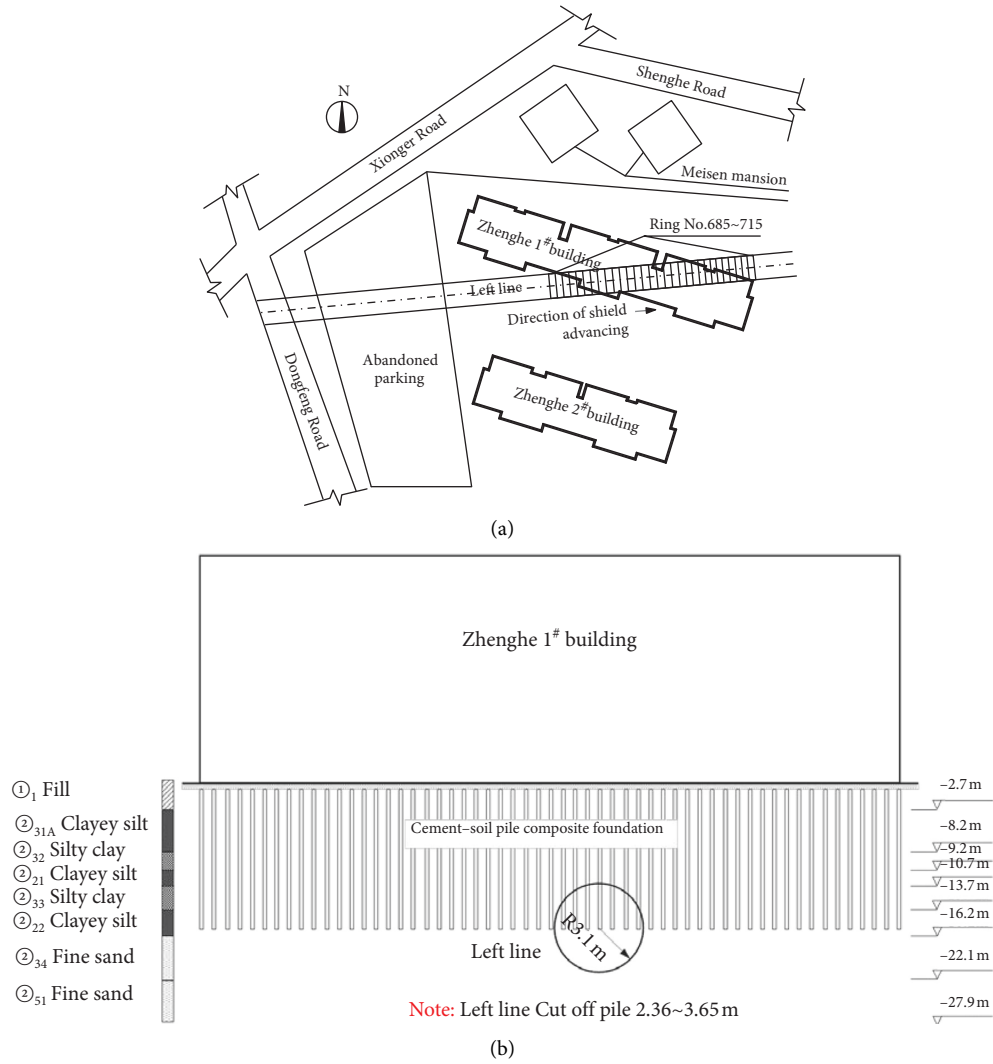


FIGURE 1: Relative position of the Zhenghe 1#: (a) schematic plane location of the tunnel and Zhenghe 1# building; (b) schematic elevation of the tunnel and Zhenghe 1# building.

effect of the pile on the soil is considered. The composite foundation reinforcement area is regarded as a composite soil body, and the gravity of the composite soil body is determined by the following equations:

$$m = \frac{\pi d^2}{4l^2} (\text{Plane and squar layout of piles}), \quad (1)$$

where m is the replacement rate of composite foundations (a dimensionless factor), d denotes the pile diameter in meter, and l is the pile spacing of unit meter. Further,

$$\gamma' = m\gamma_p + (1 - m)\gamma_s, \quad (2)$$

where γ' /(kN/m³) is the weight of the composite soil; γ_p /(kN/m³) is the weight of the pile material; and γ_s /(kN/m³) is the weight of the natural foundation soil. The calculations performed and the results obtained are shown in Table 2 [17].

Krause [18] evaluated the construction load data of 397 Japanese and 12 German shields and proposed the following

empirical calculation formulas for total thrust force and total shield torque:

$$\begin{aligned} F &= \beta D^2, \\ T &= \alpha D^3, \end{aligned} \quad (3)$$

where F /kN is the total thrust of the shield, T /(kN·m) is the total torque, D /m is the shield's diameter, α and β are empirical coefficients whose values chiefly rely on the formation conditions, shield type, and shield structure. At present, the commonly used value ranges of the earth pressure balance shield in examining engineering problems are $\alpha = 8\sim 23$ and $\beta = 500\sim 1200$ [19]. It is noteworthy that the above experimental formula is strongly influenced by the diameter of the bumper machine. When the diameter of the bumper machine is small, the total thrust force and the total torque obtained will be very small, which is reflected in the insufficient thrust and cutting ability during the protective tunneling. Conversely, in the case of a larger diameter bumper machine, the bumper tunneling and drilling ability

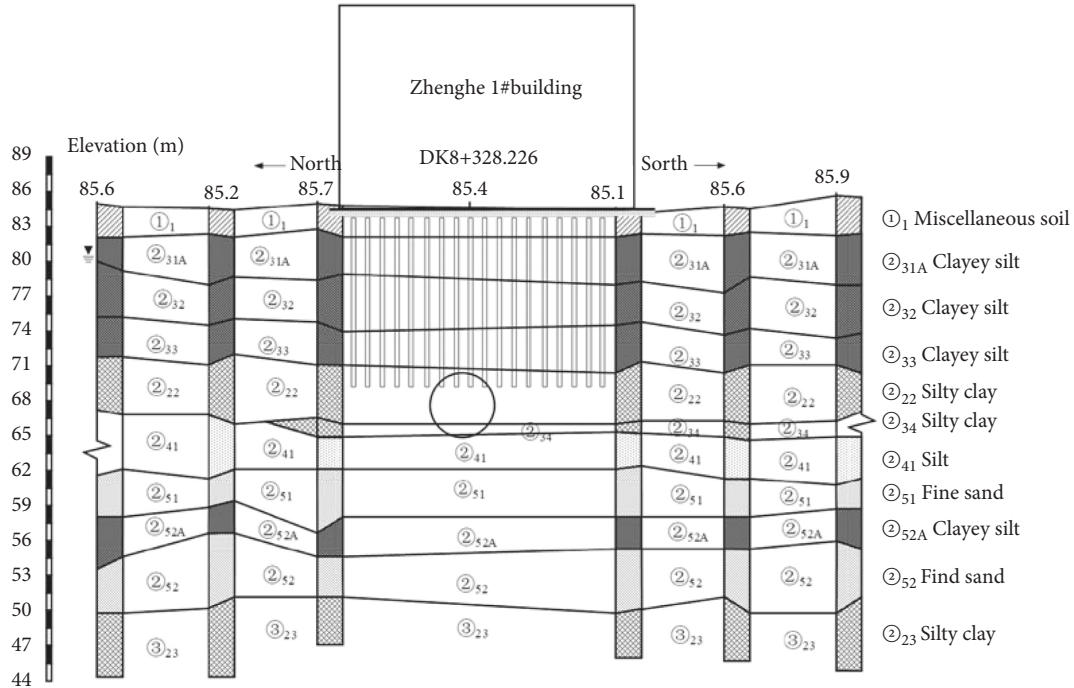


FIGURE 2: Shield crossing geological section.

TABLE 1: Parameters of soils.

Numbering	Layer	C (kPa)	φ ($^{\circ}$)	μ	γ (kN/m 3)	Thickness (m)
① ₁	Fill soil	20	20	0.333	18	2.7
② _{31A}	Clay silt	20	22.1	0.296	18.9	2.6
② ₃₂	Clay silt	19.9	21.2	0.301	19.4	2.9
② ₂₁	Silty clay	29.5	16.4	0.355	19.6	1.0
② ₃₃	Clay silt	19	20.4	0.324	19.9	1.5
② ₂₂	Silty clay	31.2	15.6	0.375	19.4	3.0
② ₃₄	Clay silt	19.3	20.7	0.333	20.2	2.5

TABLE 2: Heaviness of the composite soil.

Soil layer number	Name	The natural weight of soil (kN/m 3)	Composite soil weight (kN/m 3)
① ₁	Fill soil	18.0	18.4340
② _{31A}	Clay silt	18.9	19.1387
② ₃₂	Clay silt	19.4	19.5302
② ₂₁	Silty clay	19.6	19.6868
② ₃₃	Clay silt	19.9	19.9217
② ₂₂	Silty clay	19.4	19.5302
② ₃₄	Clay silt	20.2	20.1566

cannot be fully utilized. Based on the experimental formula, the total thrust and total torque intervals of the shield are relatively wide, and determining the best construction parameters while cutting the piles is somewhat difficult and more accurate calculations are required [5].

As shown in Figure 3, when the shield machine excavates the composite foundation pile group underground, the power system of the shield machine provides the total thrust F and the full torque T to overcome the resistance and the resistance torque during the excavation. In Figure 3, the main factors affecting the total thrust of the shield are explained in the following: F_1 is the

frictional resistance between the shield shell and the soil, F_2 is the frontal resistance of the excavation surface, and F_3 is the penetration resistance of the cutter head. The main factors affecting the total torque of the shield are as follows: T_1 is the friction torque generated by the front of the cutter head and the composite soil, T_2 is the friction torque generated by the side of the cutter head and the composite soil, and T_3 is the torque between the stirring rod and the muck in the sealed chamber, resulting in stirring torque [15]. The remaining impacts are fairly small and will not be considered in this analysis. According to the mechanical balance relationship:

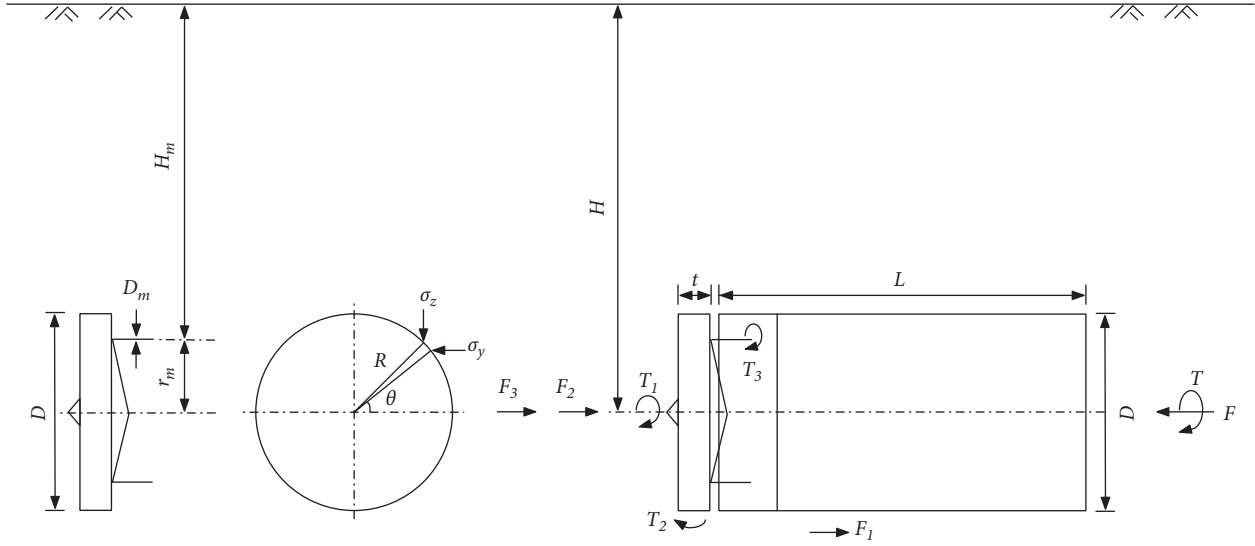


FIGURE 3: Force analysis of the shield tunneling.

$$F = F_1 + F_2 + F_3, \quad (4)$$

$$T = T_1 + T_2 + T_3. \quad (5)$$

The normal stress σ_N acting on the shield shell is as follows:

$$\sigma_N = \sigma_y \sin \theta + \sigma_z \cos \theta. \quad (6)$$

$$\sigma_z = \sum \gamma_i' h_i + P_0, \quad (7)$$

$$\sigma_x = \sigma_y = K_0 (\sum \gamma_i' h_i + P_0), \quad (8)$$

where γ_i' and h_i in order are the gravity and thickness of i th layer of the composite soil, and p_0/kPa is the building's additional load. The latter factor is estimated according to the "Code for Loads of Building Structures" (GB50009-2012) [20]: $P_0 = 7$ (number of floors) $\times 18$ kPa (load on each floor of residential buildings) + 20 kPa (load on basement) + 10 kPa (foundation load) = 156 kPa, and K_0 is the static lateral pressure coefficient of the soil, which can be evaluated by the semi-empirical formula $K_0 = 1 - \sin \phi$. Through multiplying equation (6) by the friction coefficient μ_1 and integrating the resulting expression over the contact area, the friction resistance F_1 between the shield shell and the composite soil is obtained as follows:

$$\begin{aligned} F_1 &= 2 \int_0^L \int_0^\pi (\sigma_y \sin \theta + \sigma_z \cos \theta) \mu_1 r d\theta dl \\ &= 4K_0 \mu_1 r (\sum \gamma_i' h_i + P_0) L. \end{aligned} \quad (9)$$

In (9), we assume $\mu_1 = 0.3$ [21], L/m is the length of the shield shell, and r/m is the radius of the shield machine. The frontal resistance F_2 of the excavation surface is calculated according to the static earth pressure. The frontal strength is equal to the sum of the ground pressure due to the gravity of the composite body and the additional load on the building:

$$\begin{aligned} F_2 &= \int_0^{2\pi} \int_0^{\frac{D}{2}} K_0 \gamma' (H - r \sin \theta) r dr d\theta \\ &+ K_0 P_0 = \frac{\pi D^2}{4} K_0 \gamma' H + K_0 P_0, \end{aligned} \quad (10)$$

where H/m indicates the vertical distance between the ground and the axis of the cutter head of the bumper device. Cutter head penetration resistance, F_3 , is calculated as follows:

$$F_3 = D\pi L' [\tan \varphi (\sum \gamma_i' h_i + P_0) + c], \quad (11)$$

where L' is the length of the notched ring, and its value is estimated to be the ratio of the shield's tunneling speed to the cutter head's rotating speed. The frictional torque T_1 between the front of the cutter head and the composite soil is as follows:

$$T_1 = \int_0^{2\pi} \int_0^{\frac{D}{2}} \frac{D}{2} (1 - \eta^2) K_0 \mu_2 \gamma' (H - r \sin \theta) r^2 dr d\theta (1 - \eta)^2 \frac{\pi D^3}{12} K_0 \mu_2 \gamma' H, \quad (12)$$

where μ_2 the coefficient of friction between the cutting head and the soil. Normal tension on the cutter consists of two parts: the vertical stress σ_2 and the lateral stress σ_y . Then, the friction torque (i.e., T_2) between the side of the cutter head and the composite soil can be calculated as follows:

$$\begin{aligned} T_2 &= \int_0^{2\pi} r^2 \mu_2 \gamma' t (H - r \sin \theta) \sin^2 \theta d\theta \\ &+ \int_0^{2\pi} r^2 \mu_2 \gamma' t K_a (H - r \sin \theta) \cos^2 \theta d\theta \\ &= \pi r^2 (1 + K_a) \mu_2 \gamma' H t, \end{aligned} \quad (13)$$

where t denotes the width of the cutter head's outer edge, and K_a is the active earth pressure coefficient. The stirring

torque (i.e., T_3) generated between the stirring rod and the residue in the sealed chamber is given as follows [21]:

$$T_3 = \sum_n \gamma' H_m D_m l_m r_m \mu_3, \quad (14)$$

where H_m/m is the vertical distance between the ground and the stirring rod, D_m and l_m are the diameter and length of the stirring rod, respectively, r_m is the distance between the stirring rod and the central axis of the shield cutter head, μ_3 is the coefficient of friction, and n is the number of stirring rods. In summary, equations (5), (9)–(11) give the theoretical calculation formula for the total thrust during the penetration of the shield cut pile group composite foundation as follows:

$$F = 2K_0\mu_1 r \left(\sum \gamma' h_i + P_0 \right) L + \frac{\pi D^2}{4} K_0 \gamma' H + K_0 P_0 + D\pi L' \left[\tan\phi \left(\sum \gamma' h_i + P_0 \right) + c \right]. \quad (15)$$

Based on equations (5), (12), (13), and (14), the theoretical formula for the total torque would be derived as follows:

$$T = (1 - \eta) \frac{\pi D^3}{12} K_0 \mu_2 \gamma' H + \pi r^2 (1 + K_a) \mu_2 \gamma' H t + \sum_n \gamma' H_m D_m l_m r_m \mu_3. \quad (16)$$

3.2. Propulsion and Cutter Head Speed. During the entire construction of the shield cut pile group composite foundation traversing the existing masonry structure, the shield advancement speed is maintained at a uniform speed, controlled within the range of 10 to 20 mm/min. Progress rates can be appropriately accelerated or reduced according to ground speed and building monitoring conditions. The speed setting range of the cutter head during pile cutting is 1.07 to 1.12 r/min.

4. Comparative Analysis of Shield Cutting Pile Cutter Head Force Calculation

The total thrust (F) and the total torque (T) of the shield are calculated using the suggested load calculation method for shield cutting pile excavation, and then, these values are compared with the actual measured values of the project. The selected pile-cutting engineering section of Zhengzhou Metro Line 5 has a total of 31 tunnels. Figures 4 and 5 show the total thrust and total torque curves predicted by the proposed calculation method and those measured by the project. Besides, the empirical formula estimates are given as load range. The comparison shows that the load range obtained based on the calculation method proposed in this study is basically the same as the measured average curve of the project. Compared with the current commonly used load empirical formula to estimate the range, the prediction accuracy has been greatly improved. In addition, as shown in Figure 6, this study calculated the proportion of each load

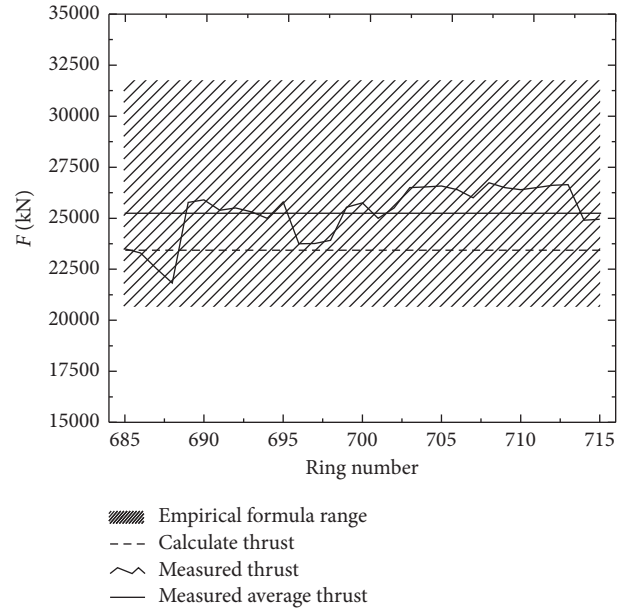


FIGURE 4: Comparison of total thrust during shield cutting piles.

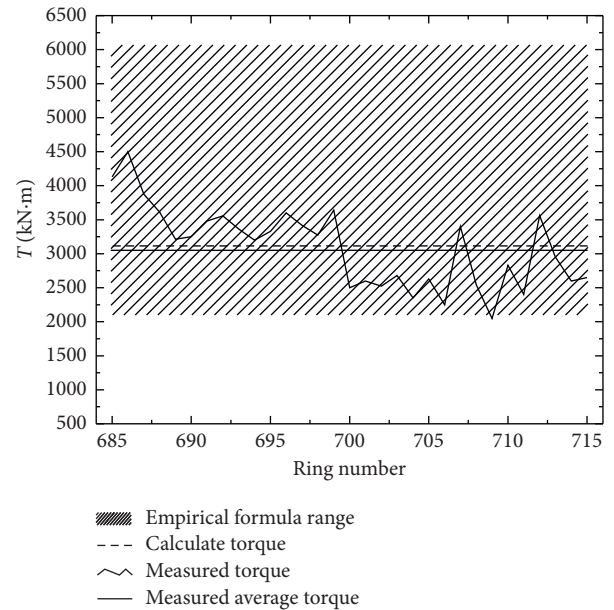


FIGURE 5: Comparison of total torque during shield cutting piles.

component in the total load in the project. The penetration resistance of the cutter head is 40.3% of the total drift. For the front of the cutter head and the composite soil, the friction torque makes up 81.2% of the total torque, which is the load ratio with the highest ratio.

In summary, the calculation method of cutter head load when shield cutting piles is proposed in this study can be used as a supplement to the empirical formula, providing more comprehensive and effective theoretical guidance for the current shield cutting pile construction and design. Of course, there is still a certain difference between the load calculation and the actual load. The work of this study aims to establish an effective method for determining the load

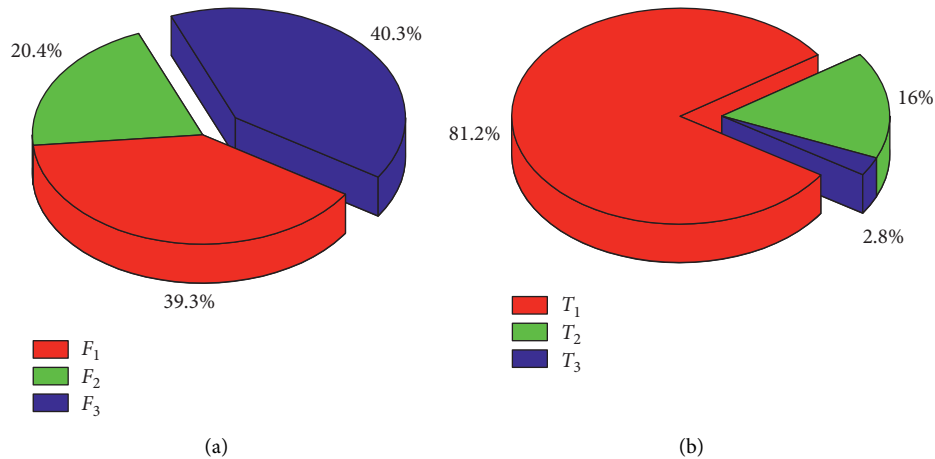


FIGURE 6: Percentage of various forces in the shield cutter head load.

range of shield cutting pile excavation that is convenient for engineering applications. Therefore, the pile-soil composite foundation is equivalently simplified in the calculation model, and only several main load action forms and the most critical influencing factors, in the follow-up research work, will improve and refine the calculation model in this study, to further provide prediction accuracy.

5. Building Deformation Monitoring during Shield Cutting Pile Tunneling

5.1. Monitoring Data Analysis. Under the requirements of “Urban Rail Transit Engineering Monitoring Technical Specifications” [22] and “Urban Rail Transit Engineering Measurement Specifications” [23], combined with the geological conditions of the project and the characteristics of the building, the building settlement monitoring points along the outer wall of the building are separated about 10 to 15 m. Concerning the outer wall, there should be a monitoring point control layout at the corners. The measuring points are arranged clockwise at the corners of the building, marked F1~F19 (i.e., 19 measuring points in total). The layout of the deformation monitoring points of Zhenghe 1# building is shown in Figure 7.

Prior to passing through the composite base of the cut tunnels in the bumper tunnel, # 1 building was closely monitored for deformation to fully understand the condition and safety level of # 1 building. As shown in Figure 8(a), the monitoring results show that the maximum differential subsidence between the south and north facades of the Zhenghe 1# building and the maximum distortion are 0.55 mm/m and 3.05×10^{-3} rad/m, respectively. Currently, in the actual measurement and analysis of the impact of shield tunnel intersection construction on existing buildings, the greatest concern of buildings is whether the cumulative assembly exceeds the control standard after the assembly has been established. The more in-depth research is only about the settlement along a particular facade of the building. However, during the shield tunnel’s excavation process, there is a considerable time difference in the cutter head reaching the two facades of the building. This issue will cause

these facades’ settlement to be inconsistent, producing permanent distortion of the building. This study mainly analyzes the distortion and deformation characteristics of the masonry structure caused by the underpass of the shield pile group pile composite foundation. Figures 8(b)–8(d), respectively, present the change in the settlement surface at each critical moment during the bottom plane of Zhenghe 1# building under the left-line tunnel cut pile composite foundation. Based on the sequence of tunnel construction, we select three critical moments for analysis. Figure 8(b) shows the case when the left-line shield cutter cuts into the composite foundation and starts to cut piles (indicated by time B). Figure 8(c) corresponds to when the shield’s tail on the left line breaks out of the composite foundation, and the pile cutting is completed (indicated by time C). Finally, Figure 8(d) is related to the case of stabilized settlement of the building (don’t use time D to indicate).

It can be observed from Figures 8 and 9 that during the whole process of the left-line cut pile composite foundation of the shield tunnel, most of the measurement points on the bottom plane of the building showed settlement. The north facade’s maximum settlement was approximately the same as that of the south front, and its value is twice the maximum settlement at the intersection of the tunnel and the building space. Nevertheless, the settlement of the measurement points on the same plane is quite different, indicating the occurrence of distortion in the bottom plane, and the magnitude of the distortion is constantly changing with the shield construction process. After stabilizing the settlement, the bottom plane of the building was permanently twisted and deformed. According to Table 3 and Figures 8 and 9, the locations where the largest differential settlement and the largest distortion of the building occur are close to the central axis of the left tunnel. Among understudy critical times, the largest differential settlement for the north-south façade would be 8.42 mm/m, detectable at time C, and the maximum distortion occurs at time B, whose value is 3.376×10^{-2} rad/m. When the settlement is finally stabilized at time D, the maximum values of settlement, differential settlement, and distortion of the building’s measuring point would be -10.98 mm, 8.37 mm/m, and 3.12×10^{-2} rad/m, respectively.

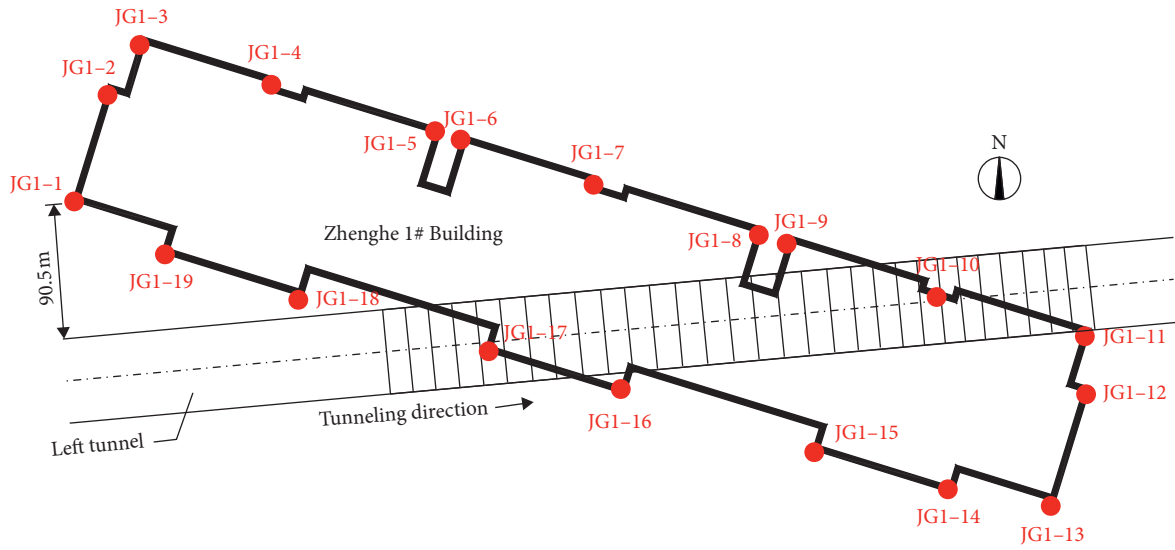


FIGURE 7: Layout drawing of the monitoring points in Zhenghe 1# building.

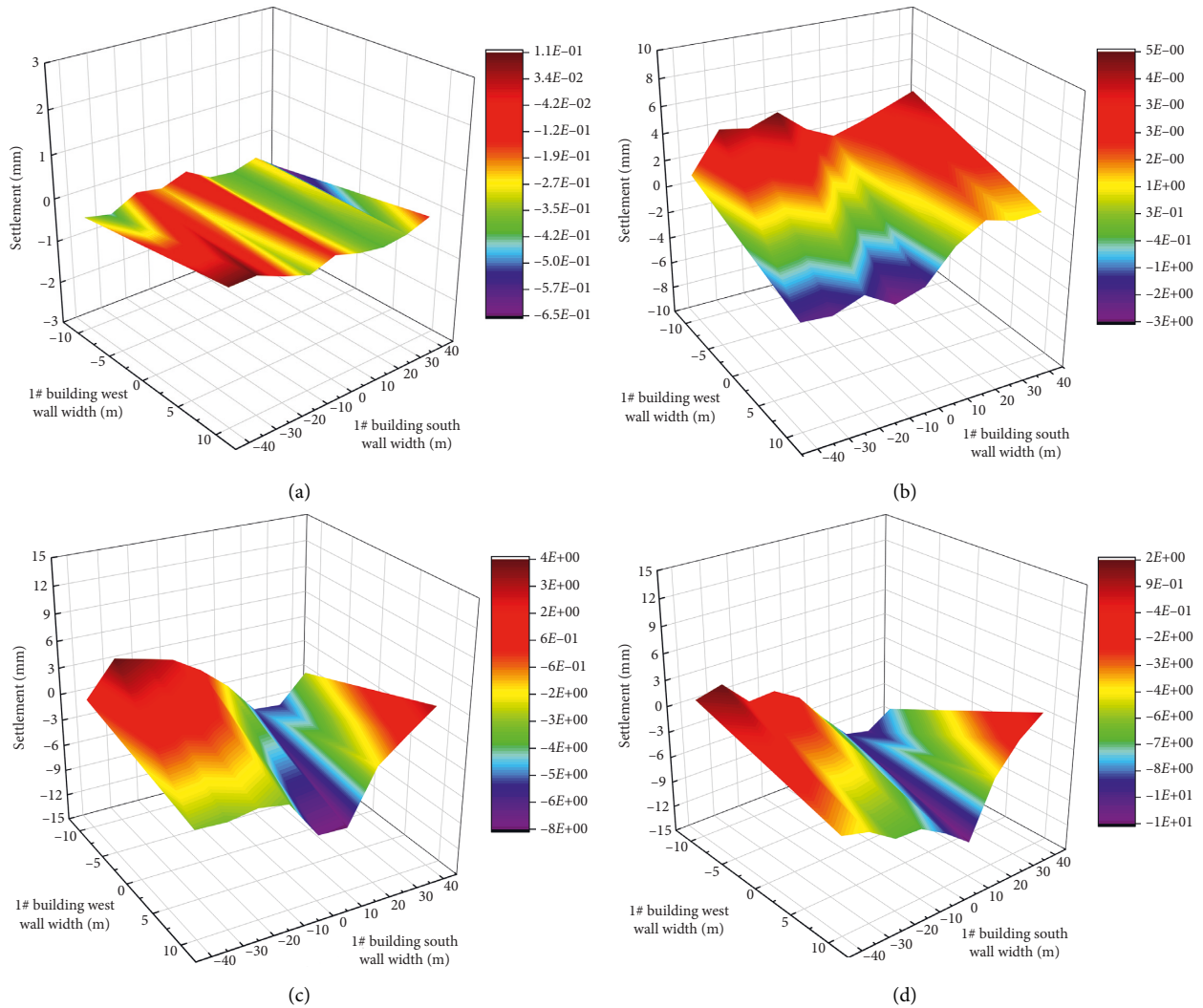


FIGURE 8: Deformation of buildings at various critical moments of shield cutting pile group construction. (a) Deformation of buildings when shield tunnels are not under construction. (b) The left-line shield cutter head starts to cut the pile group composite foundation. (c) Left-line shield tail separated from pile group composite foundation. (d) The shield tail of the left line is away from the pile group composite foundation for 15 days.

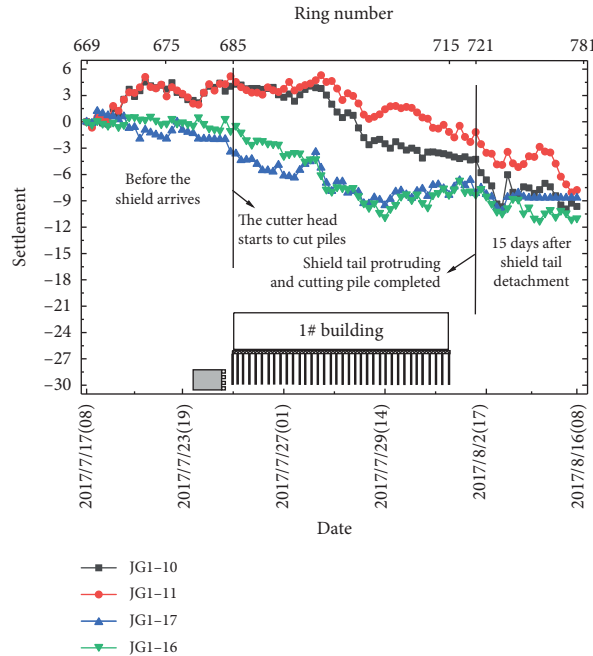


FIGURE 9: Settlement time history of the crucial measuring points in the whole process of the cut pile construction.

TABLE 3: Maximum differential settlement and maximum distortion of the building at each critical moment in the construction of shield cut group piles.

Monitoring items	Time A	Time B	Time C	Time D
Maximum differential settlement (mm/m)	7.43	8.18	8.42	8.37
Maximum distortion (rad/m)	1.65×10^{-2}	3.376×10^{-2}	3.368×10^{-2}	3.12×10^{-2}

TABLE 4: Building damage grade evaluation standard.

Risk level	Maximum slope	Differential settlement* (mm/m)	Building distortion* (rad/m)	Risk description
1	$< 1/500$	< 2	$< 4 \times 10^{-3}$	Ignorable: shallow damage is unlikely
2	$1/500 \sim 1/200$	$2 \sim 5$	$4 \times 10^{-3} \sim 1 \times 10^{-2}$	Minor: may be damaged in shallow parts, but has no effect on the structure
3	$1/200 \sim 1/50$	$5 \sim 20$	$10^{-2} \sim 4 \times 10^{-2}$	Moderate: shallow damage, possible structural damage, possible related rigid pipe damage
4	$> 1/50$	> 20	$> 4 \times 10^{-2}$	Serious: building structure damage, rigid pipeline damage, possible other pipeline damage

Note.* newly added evaluation annotations by Yang and Zhang [24].

5.2. Zhenghe 1# Safety Evaluation Based on Existing Deformation. According to the judgment criteria of Yang and Zhang [24] based on the scrutiny of Rankin [25], the proposed damage grade correction evaluation standard considering both differential settlement and distortion of the building has been provided in Table 4. The damage degree of Zhenghe 1# building before the shield tunnel is negligible, and the risk level would be equal to 1. According to Table 3, the maximum differential settlement of the north and south facades of Zhenghe 1# building at each moment is less than 10 mm/m, and the maximum distortion value of the building is less than 4×10^{-2} rad/m. On the other hand, the maximum values of distortion and differential settlement of the building are also less than 5% of their maximum allowable values.

According to the building damage grade evaluation mark given in Table 4, after the shield cutting pile group composite foundation is penetrated, the damage degree of Zhenghe 1# building is medium, and the risk grade would be 3. Since the largest differential settlement and the largest distortion are located at the diagonal intersection of the tunnel and the building, the corresponding location of Zhenghe 1# building should be tested to see whether necessary reinforcement and repair measures are required. After examination by a professional house inspection agency, it was found that the main structure of the house is still safe during the tunnel construction process. Further, the 1# building of Zhenghe Community meets the normal standards of the building usage and can be utilized normally after partial repair.

6. Conclusions

From the engineering point of view, a comprehensive analysis of the cutter head force during cutting the piles by the shield machine is carried out. To this end, the pile-soil composite foundation is equivalently simplified into a composite soil body, and the calculation formula for the cutter head load when the shield machine cuts the composite foundation pile group is given. Based on the above method, the comparison of the total load of the cut pile group under the masonry structure of Zhengzhou Metro Line 5 with the actual measured value is performed and it is observed that the suggested method can effectively predict both total thrust and torque during the excavation of the shield pile group. The load calculation method in this study is used to guide the construction of the shield-bored cut pile composite foundation of Zhengzhou Metro Line 5 through the existing masonry structure. By monitoring the deformation of Zhenghe 1# building, the final maximum differential settlement of the north and south facades of the building and the maximum distortion are 8.42 mm and 3.376×10^{-2} rad/m. Analysis of monitoring data shows that the differential assembly and the distortion of the masonry structure are in the safe range.

Data Availability

The data used to support the findings of this study are available from the corresponding author upon request.

Conflicts of Interest

The authors declare that they have no conflicts of interest.

Acknowledgments

The remarkable assistance from China Railway 18th Engineering Bureau Group First Engineering Co. Ltd. is highly appreciated. The research described in this study was financially supported by the National Science Foundation of China (51508520).

References

- [1] R. J. Finno, F. T. Voss, E. Rossow, and J. T. Blackburn, "Evaluating damage potential in buildings affected by excavations," *Journal of Geotechnical and Geoenvironmental Engineering*, vol. 131, no. 10, pp. 1199–1210, 2005.
- [2] X. Han, J. R. Standing, and N. Li, "Stiffness correction method for prediction of building deformation caused by tunnel construction," *Journal of Geotechnical Engineering*, vol. 31, no. 4, pp. 539–545, 2009, in Chinese.
- [3] R. B. Peck, "Deep excavations and tunneling in soft ground," in *Proceedings of the 7th Int. Conf. Soil Mech. & Found. Eng., Mexico, State of the Art*, pp. 225–290, Mexico, USA, 1969.
- [4] W. B. Ouyang, Q. W. Ding, and D. W. Xie, "Calculation method of settlement caused by shield construction considering building stiffness," *Chinese Journal of Underground Space and Engineering*, vol. 9, no. 1, pp. 155–166, 2013, in Chinese.
- [5] C. Wan and Z. Jin, "Adaptability of the cutter-head of the earth pressure balance (epb) shield machine in water-rich sandy and cobble strata: a case study," *Advances in Civil Engineering*, vol. 2020, Article ID 8847982, 12 pages, 2020.
- [6] J. Y. Shen, "Analysis of the impact of shield tunneling of Chengdu metro line 1 on building safety," *Modern Tunnel Technology*, vol. 45, no. 2, pp. 63–68, 2008, in Chinese.
- [7] Y. K. Sun and F. L. Guan, "Impact of shield tunneling on settlement of masonry structures," *China Railway Science*, vol. 33, no. 4, pp. 38–44, 2012, (in Chinese).
- [8] Z. M. Xu, Q. H. Han, and G. Zheng, "Measurement and analysis of the influence of metro tunnels passing through historical building," *Chinese Journal of Geotechnical Engineering*, vol. 35, no. 2, pp. 354–364, 2013, in Chinese.
- [9] X. Y. Sun, C. Y. Heng, and Z. Zhou, "Field measurement of the induced settlement of the foundation of Beijing subway tunnels through masonry structures," *Journal of Civil Engineering*, vol. 1, no. S2, pp. 304–308, 2015, in Chinese.
- [10] S. Miliziano, F. M. Soccodato, and A. Burghignoli, "Evaluation of damage in masonry buildings due to tunneling in clayey soils," in *Proceedings of the 3th Int. Conf. Geotechnical engineering technology for soft soil base*, pp. 49–54, Lyon, France, 2002.
- [11] C. Peng, Y. L. Ji, and H. B. Luo, "Numerical simulation of influence of double-line shield construction on adjacent buildings," vol. 27, no. S2, pp. 3868–3874, 2008, in Chinese.
- [12] G. Giardina, M. J. Dejong, and R. J. Mair, "Interaction between surface structures and tunnelling in sand: centrifuge and computational modelling," *Tunnelling and Underground Space Technology*, vol. 50, pp. 465–478, 2015.
- [13] L. Ding, X. Wu, L. Zhang, and M. J. Skibniewski, "How to protect historical buildings against tunnel-induced damage: a case study in China," *Journal of Cultural Heritage*, vol. 16, no. 6, pp. 904–911, 2015.
- [14] F. Ye, N. Qin, X. Gao, X.-yong Quan, X.-zhuo Qin, and B. Dai, "Shield equipment optimization and construction control technology in water-rich and sandy cobble stratum: a case study of the First Yellow river metro tunnel undercrossing," *Advances in Civil Engineering*, 8358013, vol. 2019, 12 pages, 2019.
- [15] Y. Zhu, J. Wang, B. Zhang, X. Zhang, and J. Zhu, "Research studies on the thrust of special-shaped full-sectional cutter-heads of quasirectangular shield," *Advances in Civil Engineering*, vol. 2021, Article ID 8830512, 12 pages, 2021.
- [16] W. Sun, H. Ma, X. Song, L. Wang, and X. Ding, "Modeling and dynamic analysis of cutterhead driving system in tunnel boring machine," *Shock and Vibration*, vol. 2017, Article ID 7156816, 12 pages, 2017.
- [17] X. Zou, H. Zheng, and Y. Mi, "Performance evaluation of hard rock TBMs considering operational and rock conditions," *Shock and Vibration*, vol. 2018, Article ID 8798232, 17 pages, 2018.
- [18] B. Maidl, M. Herrenknecht, and L. Anheuser, *Mechanized Shield tunneling*, Ernst & Sohn, Berlin, Germany, 1996.
- [19] W. Zhu, *Standard Specification for Tunnels (Shield Tunnel) and Explanation*, China Construction Industry Press, Beijing, China, 2001.
- [20] Ministry of housing and urban-rural development of the people's Republic of China, *Building Structure Load Code (GB50009-2012)*, Building Industry Press, Beijing, China, 2012.
- [21] Q. Lv and D. M. Fu, "Simulation test research on torque of earth pressure balance shield tunnel boring machine cutter-

- head,” *Chinese Journal of Rock Mechanics and Engineering*, vol. 25, no. S1, pp. 3137–3143, 2006, in Chinese.
- [22] Ministry of housing and urban-rural development of the people’s Republic of China, *Technical Specifications for Urban Rail Transit Engineering Monitoring*“ (GB50911-2013), Building Industry Press, Beijing, China, 2013.
- [23] Ministry of housing and urban-rural development of the people’s Republic of China, *Urban Rail Transit Engineering Survey Specification*“(GB50308-2008), Building Industry Press, Beijing, China, 2008.
- [24] Y. Y. Yang and Z. X. Zhang, *Shield Tunnel Construction Disaster Mechanism and Engineering practice*, China Building Industry Press, Beijing, China, 2014.
- [25] W. J. Rankin, “Ground movements resulting from urban tunnelling: predictions and effects,” *Geological Society, London, Engineering Geology Special Publications*, vol. 5, no. 1, pp. 79–92, 1988.

Research Article

Prediction of Long-Term Prestress Loss and Crack Resistance Analysis of Corroded Prestressed Concrete Box-Girder Bridges

Yiming Yang ^{1,2}, Huang Tang ¹, Yu Mao ¹ and Xinzhong Wang ¹

¹School of Civil Engineering, Hunan City University, Yiyang, Hunan 413000, China

²Key Laboratory of Safety Control of Bridge Engineering, Ministry of Education, Changsha, Hunan 410114, China

Correspondence should be addressed to Huang Tang; 1303780926@qq.com and Xinzhong Wang; 417056269@qq.com

Received 8 February 2022; Revised 17 March 2022; Accepted 24 March 2022; Published 9 April 2022

Academic Editor: Angelo Marcelo Tuset

Copyright © 2022 Yiming Yang et al. This is an open access article distributed under the Creative Commons Attribution License, which permits unrestricted use, distribution, and reproduction in any medium, provided the original work is properly cited.

Reasonable assessment of long-term prestress loss and crack resistance is essential to ensure the service performance of prestressed concrete (PC) bridges. In this paper, a novel prediction model of long-term prestress loss considering the coupling effect of shrinkage and creep of concrete, prestressing steel relaxation, and presence of nonprestressing steel as well as the corrosion of prestressing and nonprestressing steel is proposed. Then, the probability analysis approach of long-term prestress loss considering the uncertainties of calculation parameters and models is introduced. Moreover, the assessment approach of crack resistance of local and overall structure is also developed, taking into account the effect of corrosion and time-dependent long-term prestress loss. The previously proposed approaches are applied to a three-span PC box-girder bridge. It is found that the prediction results of long-term prestress loss have high uncertainty, and the upper bound of long-term prestress loss at the confidence level of 95% is approximately 50% higher than the result obtained by deterministic analysis. The effect of corrosion on the long-term prestress loss is basically negligible, and the crack resistance of bottom slab and web is more sensitive to the coupled effect of corrosion and long-term prestress loss than that of top slab. Additionally, setting vertical prestressing tendons is conducive to improving the crack resistance level of web and whole section.

1. Introduction

Reasonable prediction of long-term prestress loss is the basis for durability assessment of prestressed concrete (PC) structures in service [1–3]. For structures whose long-term performance changes will significantly affect the overall performance, such as long-span PC box-girder bridges, long-term prestress loss is not only closely related to unexpected cracking and excessive deflection [4, 5] but also critical to the formulation of maintenance strategies. In addition, concrete cracking caused by prestress loss or environmental attack is one of the typical defects of PC box-girder bridge [6]. Concrete cracking not only significantly reduces the section stiffness and increases the bridge deflection but also accelerates the corrosion of prestressing and nonprestressing steels. These result in a reduction of service performance and durability of structure. Therefore, particular attention should be given to reasonable assessment of

long-term prestress loss and time-dependent crack resistance of box-girder bridges.

Prediction of long-term prestress loss in current codes is mainly formed by the following three methods: (1) the time-step analysis methods were adopted by the ACI-209 code [7] and PCI Bridge Design Manual [8]; (2) the subitem superposition methods were used in the CEP-FIB 90 code [9], AASHTO LRFD specification [10], and JTG3362-2018 specification [11]; (3) the overall estimation methods were recommended by the AASHTO specification [12] and NCHRP 496 report [13]. Although these methods are widely used, most of them have more or fewer defects. For example, the effect of nonprestressing steel on long-term prestress loss is neglected in the CEP-FIP 90 code. The coupled effect of concrete shrinkage and creep is not considered in the JTG3362-2018 specification. Therefore, some scholars have actively explored other methods to overcome the shortcomings of the aforementioned methods. Considering the

effects of concrete shrinkage and creep, Cao et al. [14] improved the prestress loss prediction model caused by prestressing steel relaxation in Chinese code JTG D62-2004 [15]. Additionally, different prediction models of long-term prestress loss are proposed based on the internal force equilibrium and strain compatibility conditions [16, 17] or the finite element method [18, 19]. However, existing methods do not analyse the coupled effect of corrosion, concrete shrinkage and creep, prestressing steel relaxation, and presence of nonprestressing steel and also ignore the uncertainty of time-dependent prestress loss.

Since the reliability-based assessment method of long-term service performance of PC structures can effectively deal with the time-dependent and uncertainty of influencing parameters, it has gradually become a research hotspot in this field. Pillai et al. [20] developed a time-dependent predict method of service reliability (mainly related to crack resistance) of posttensioned (PT) segmental concrete bridges under different corrosion environments and load models. Stewart and Mullard [21] developed a probability calculation model of severe cracking of concrete surface under different durability design specifications, and the corresponding research results provide better guidance for the design of concrete structures. Based on the definition of the limit state that the main tensile stress of concrete in the web reaches the specified allowable stress value, Chen [22] established a probability assessment model of web cracking of box-girder and carried out the sensitivity analysis of web crack resistance. However, these studies ignore the coupled effect of concrete shrinkage and creep, time-dependent prestress loss and corrosion, and the variation regularity of local and overall crack resistance of structure, which are also not involved. A few scholars use the probabilistic finite element analysis method to make up for the shortcomings of the above research. For example, Guo et al. [23, 24] developed a reliability assessment of PC box-girder bridges under the combined action of creep, shrinkage, and corrosion based on an advanced probabilistic finite element method. Based on the finite element grillage model, Tu et al. [25] proposed a computational probabilistic framework for time-dependent reliability analysis of widened concrete highway bridges considering shrinkage and creep of concrete. Tong et al. [26] estimated the coupled effects of concrete shrinkage, creep, and cracking on the long-term behavior of postconnected prestressed steel-concrete composite girders by using the three-dimensional finite element model. Although the probabilistic finite element method can consider the complex spatial stresses, the coupling effect of various factors, and uncertain parameters, its computational cost is very high, and the rationality verification of the finite element model is also difficult. Therefore, it is urgent to develop a theoretical assessment method of crack resistance of PC structure under the multivariable coupling effects.

The objective of this study is to propose a novel prediction model of long-term prestress loss under the coupled effect of multiple factors and then to assess the reliability

degradation of cracking resistance of box-girder bridges considering the effect of prestress loss on concrete stress. First, the well-established step-by-step approach is adopted to estimate long-term prestress loss in combination with the coupled effect of shrinkage and creep of concrete, prestressing steel relaxation, and presence of nonprestressing steel as well as corrosion of prestressing and nonprestressing steel. Then, the uncertainty analysis approach of long-term prestress loss is introduced. After that, the assessment approach of crack resistance of local and overall structure considering the effect of corrosion and long-term prestress loss is also proposed. Finally, the long-term prestress loss, effective prestressing force, and crack resistance of a three-span PC box-girder bridge are analysed.

2. Prediction Model of Long-Term Prestress Loss

2.1. Derivation of Prediction Model. To predict long-term prestress loss more reasonably, the well-established step-by-step method (denoted as SSM) with higher accuracy provided in [27, 28] is adopted to perform superposition calculation of long-term prestress loss, taking into account the coupled effect of shrinkage and creep of concrete, prestressing steel relaxation, and the presence of nonprestressing steel. In addition, the effect of corrosion on the cross-sectional area of prestressing and nonprestressing steel is also integrated into the calculation process.

In the calculation process, the assumptions of plane cross-section, linear behavior, and uncracked state of concrete, perfect bond performance between concrete and prestressing as well as nonprestressing steels are used. The age of concrete at loading, t_0 , to the calculation time of prestress loss, t , is divided into w time intervals, and each time interval has the same length of $(t - t_0)/w$. The parameters, such as stress and cross-sectional area of prestressing and nonprestressing steel, are assumed to be constant in a small-time interval. For any time interval $[t_{i-1}, t_i]$, when the external load remains constant, the cross section of members must satisfy the equilibrium equation of internal force increment, compatibility equation of strain increment, and the corresponding constitutive equation of each material.

2.1.1. Equilibrium Equation of Internal Force Increment. The relationship between the concrete compressive force increment $\Delta F_c(t_{i-1}, t_i)$, the internal force variation of nonprestressing steels $\Delta F_s(t_{i-1}, t_i)$, and the tensile force loss of prestressing tendons $\Delta F_p(t_{i-1}, t_i)$ in time interval $[t_{i-1}, t_i]$ can be expressed as

$$\Delta F_c(t_{i-1}, t_i) + \Delta F_p(t_{i-1}, t_i) + \Delta F_s(t_{i-1}, t_i) = 0. \quad (1)$$

Then, the stress changes of concrete at the centroid of prestressing tendons and nonprestressing steels in time interval $[t_{i-1}, t_i]$ can be further derived, which are

$$\Delta\sigma_{c,p}(t_{i-1}, t_i) = -\frac{1}{A_c(t_i)} \left[\Delta\sigma_p(t_{i-1}, t_i) A_p(t_i) \left(1 + \frac{e_p^2(t_i) A_c(t_i)}{I_c(t_i)} \right) + \Delta\sigma_s(t_{i-1}, t_i) A_s(t_i) \left(1 + \frac{e_p(t_i) e_s(t_i) A_c(t_i)}{I_c(t_i)} \right) \right], \quad (2)$$

$$\Delta\sigma_{c,s}(t_{i-1}, t_i) = -\frac{1}{A_c(t_i)} \left[\Delta\sigma_s(t_{i-1}, t_i) A_s(t_i) \left(1 + \frac{e_s^2(t_i) A_c(t_i)}{I_c(t_i)} \right) + \Delta\sigma_p(t_{i-1}, t_i) A_p(t_i) \left(1 + \frac{e_p(t_i) e_s(t_i) A_c(t_i)}{I_c(t_i)} \right) \right], \quad (3)$$

where $A_c(t_i)$ and $I_c(t_i)$ are the area and inertia moment of net cross section of concrete at time t_i , respectively. $A_p(t_i)$ and $A_s(t_i)$ are the cross-sectional areas of prestressing tendons and nonprestressing steels at time t_i , respectively. $\Delta\sigma_p(t_{i-1}, t_i)$ and $\Delta\sigma_s(t_{i-1}, t_i)$ are the stress changes of prestressing tendons and nonprestressing steels in time interval $[t_{i-1}, t_i]$, respectively. $e_p(t_i)$ and $e_s(t_i)$ are the eccentricity from the centroid of prestressing tendons and nonprestressing steels to the centroid of concrete cross section at time t_i , respectively.

2.1.2. Compatibility Equation of Strain Increment. Figure 1 shows the strain increment of a typical cross section of the bonded PC box-girder member. According to the strain increment compatibility between the prestressing tendons, nonprestressing steels, and concrete at the same height of box-girder section, the strain increment equation in time interval $[t_{i-1}, t_i]$ is expressed as

$$\Delta\varepsilon_p(t_{i-1}, t_i) = \Delta\varepsilon_{c,p}(t_{i-1}, t_i), \quad (4)$$

$$\Delta\varepsilon_s(t_{i-1}, t_i) = \Delta\varepsilon_{c,s}(t_{i-1}, t_i), \quad (5)$$

where $\Delta\varepsilon_{p(s)}(t_{i-1}, t_i)$ and $\Delta\varepsilon_{c,p(s)}(t_{i-1}, t_i)$ are the strain increment of prestressing tendons (nonprestressing steels) and the concrete at its centroid, respectively.

For an uncracked PC box-girder, the total strain of concrete at time t can be calculated by the age-adjusted effective modulus method. The algebraic expression can be written as [28]

$$\varepsilon_c(t) = \frac{\sigma_c(t_0)}{E_c(t_0)} [1 + \varphi(t, t_0)] + \sum_{t_j=t_0}^t \frac{\Delta\sigma_c(t_j)}{E_c(t_j, t_0)} [1 + \varphi(t, t_j)] + \varepsilon_{sh}(t, t_0). \quad (6)$$

Then, the strain increment of concrete at the centroid of prestressing tendons or nonprestressing steels can be derived based on (6), and they are expressed as

$$\begin{aligned} \Delta\varepsilon_{c,p(s)}(t_{i-1}, t_i) &= \Delta\varepsilon_{cf-p(s)}(t_{i-1}, t_i) + \frac{\Delta\sigma_{c,p(s)}(t_{i-1}, t_i)}{E_c(t_i)} = \frac{\sigma_{c,p(s)}(t_0)}{E_c(t_0)} [\varphi(t_i, t_0) - \varphi(t_{i-1}, t_0)] \\ &+ \sum_{j=1}^{i-1} \frac{\Delta\sigma_{c,p(s)}(t_{j-1}, t_j)}{E_c(t_j)} [\varphi(t_i, t_j) - \varphi(t_{i-1}, t_j)] \\ &+ \varepsilon_{sh}(t_i, t_0) - \varepsilon_{sh}(t_{i-1}, t_0) + \frac{\Delta\sigma_{c,p(s)}(t_{i-1}, t_i)}{E_c(t_i)}. \end{aligned} \quad (7)$$

When $i=1$, the above formula can be simplified as

$$\begin{aligned} \Delta\varepsilon_{c,p(s)}(t_0, t_1) &= \Delta\varepsilon_{cf-p(s)}(t_0, t_1) + \frac{\Delta\sigma_{c,p(s)}(t_0, t_1)}{E_c(t_1)} \\ &= \frac{\sigma_{c,p(s)}(t_0)}{E_c(t_0)} \varphi(t_1, t_0) + \varepsilon_{sh}(t_1, t_0) \\ &+ \frac{\Delta\sigma_{c,p(s)}(t_0, t_1)}{E_c(t_1)}, \end{aligned} \quad (8)$$

where $\sigma_{c,p(s)}(t_0)$ is the initial stress of concrete at the centroid of prestressing tendons (or nonprestressing steels) generated by the effective prestressing force and external load at time t_0 . $E_c(t_0)$ is the elasticity modulus of concrete at time t_0 . $\varphi(t_i, t_0)$ and $\varepsilon_{sh}(t_i, t_0)$ are the creep coefficient and shrinkage strain of concrete at time t_i , respectively. $\Delta\varepsilon_{cf-p(s)}(t_{i-1}, t_i)$ is the free strain increment of concrete at

the centroid of prestressing tendons (nonprestressing steels) without considering the constraint effect of prestressing and nonprestressing steels. $E_c(t_i)$ is the elasticity modulus of concrete, and it is expressed as [29]

$$E_c(t_i) = \frac{E_c(t_0)}{1 + \chi(t_i, t_0) \varphi(t_i, t_0)}, \quad (9)$$

where $\chi(t_i, t_0)$ is the concrete aging coefficient, and it can be calculated by (10) [9].

$$\chi(t_i, t_0) = \frac{1}{1 - 0.91e^{-0.686\varphi(t_i, t_0)}} - \frac{1}{\varphi(t_i, t_0)}. \quad (10)$$

2.1.3. Constitutive Equations of Materials. Since the strain of concrete at the upper and lower edge of uncracked box-girder section is relatively small under the effect of prestressing force and external load, the prestressing and

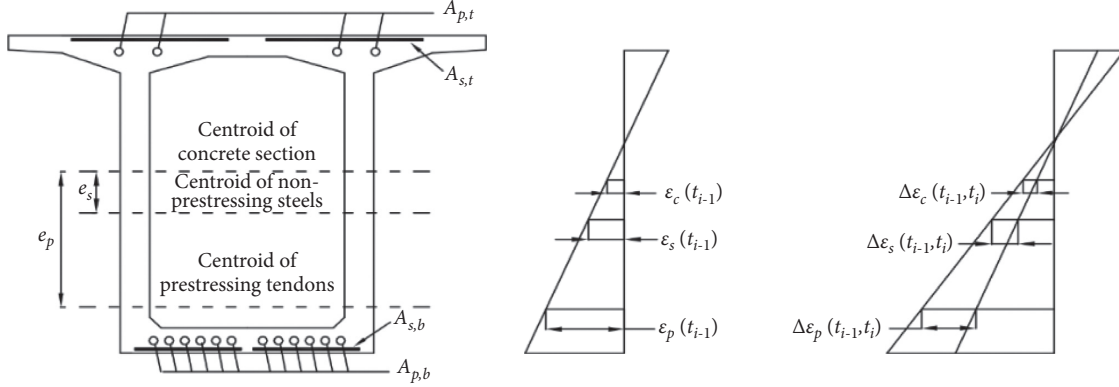


FIGURE 1: Strain increment of a typical box-girder section.

nonprestressing steel as well as concrete can be considered in elastic deformation stage. That is, their corresponding constitutive equations can adopt the linear elastic model for simplicity. It is worth noting that the prestressing steel relaxation does not cause the corresponding strain increment of prestressing tendons, and the stress relaxation effect should be reasonably reduced by the relaxation coefficient because of the length change of prestressing tendons. Thus, considering the effect of stress relaxation and reasonable reduction, the stress-strain relationship of the prestressing steel can be expressed as

$$\Delta\epsilon_p(t_{i-1}, t_i) = \frac{[\Delta\sigma_p(t_{i-1}, t_i) - \chi_r \Delta\sigma_{pr}(t_{i-1}, t_i)]}{E_p}, \quad (11)$$

where E_p is the elastic modulus of prestressing tendons, χ_r is the reduced relaxation coefficient, and its value can be taken as 0.75 [17, 30]. $\Delta\sigma_{pr}(t_{i-1}, t_i)$ is the inherent relaxation loss in time interval $[t_{i-1}, t_i]$ and can be calculated as [10]

$$\Delta\sigma_{pr}(t_{i-1}, t_i) = \frac{\log[24(t_i - t_{i-1})]}{45} \left[\frac{\sigma_p(t_{i-1})}{f_{py}} - 0.55 \right] \sigma_p(t_{i-1}), \quad (12)$$

where $\sigma_p(t_{i-1})$ is the stress value of prestressing tendons at time t_{i-1} and f_{py} is the yield stress of prestressed tendons.

By substituting (4) and (11) into (2) and the linear stress-strain relationship of nonprestressing steel and (5) into (3), the strain changes of prestressing tendons, nonprestressing steels, and concrete at their centroids can be deduced as follows:

$$\begin{aligned} \Delta\epsilon_p(t_{i-1}, t_i) &= \Delta\epsilon_{cp}(t_{i-1}, t_i) \\ &= \frac{\Delta\epsilon_{cf-p}(t_{i-1}, t_i)(M + m_s) - m_{ps}\Delta\epsilon_{cf-s}(t_{i-1}, t_i) - M/E_p N \Delta\sigma_{pr}(t_{i-1}, t_i) [m_p + 1/M(m_p m_s - m_{ps}^2)]}{M + M/N m_p + m_s + 1/N(m_p m_s - m_{ps}^2)}, \end{aligned} \quad (13)$$

$$\begin{aligned} \Delta\epsilon_s(t_{i-1}, t_i) &= \Delta\epsilon_{cs}(t_{i-1}, t_i) \\ &= \frac{\Delta\epsilon_{cf-s}(t_{i-1}, t_i)(N + m_p) - m_{ps}\Delta\epsilon_{cf-p}(t_{i-1}, t_i) - m_{ps}/E_p \Delta\sigma_{pr}(t_{i-1}, t_i)}{N + m_p + N/M m_s + 1/M(m_p m_s - m_{ps}^2)}, \end{aligned} \quad (14)$$

where $M = A_c(t_i)E_c(t_i)/[A_s(t_i)E_s]$ and $N = A_c(t_i)E_c(t_i)/[A_p(t_i)E_p]$. E_s is the elastic modulus of nonprestressing steel, $m_{p(s)} = 1 + e_p^2(t_i)A_c(t_i)/I_n(t_i)$, and $m_{ps} = 1 + e_p(t_i)e_s(t_i)A_c(t_i)/I_n(t_i)$.

For the cross section of actual PC box-girder, the longitudinal nonprestressing steels are often constructed according to the design code. As a result, their centroid is often very close to the centroid of the concrete section [17].

Therefore, the value of e_s can be taken as 0, and the corresponding values of m_s and m_{ps} are 1. Then, (13) and (14) can be rewritten as

$$\begin{aligned}\Delta\varepsilon_p(t_{i-1}, t_i) &= \Delta\varepsilon_{cp}(t_{i-1}, t_i) \\ &= \frac{\Delta\varepsilon_{cf-p}(t_{i-1}, t_i)(M+1) - \Delta\varepsilon_{cf-s}(t_{i-1}, t_i) - (M+1)m_p - 1/E_p N \Delta\sigma_{pr}(t_{i-1}, t_i)}{M+1 + (M+1)m_p - 1/N}, \\ \Delta\varepsilon_s(t_{i-1}, t_i) &= \Delta\varepsilon_{cs}(t_{i-1}, t_i) \\ &= \frac{\Delta\varepsilon_{cf-s}(t_{i-1}, t_i)(N+m_p) - \Delta\varepsilon_{cf-p}(t_{i-1}, t_i) - 1/E_p \Delta\sigma_{pr}(t_{i-1}, t_i)}{N+m_p + N + (m_p - 1)/M}.\end{aligned}\quad (15)$$

For the web section of the actual PC box-girder, the centroids of vertical prestressing tendons, stirrups, and concrete are basically the same [28]. As a result, the absolute value of strain increment at their centroids is equal. Therefore, (13) and (14) can be integrated and simplified as

$$\begin{aligned}\Delta\varepsilon_p(t_{i-1}, t_i) &= \Delta\varepsilon_s(t_{i-1}, t_i) \\ &= \Delta\varepsilon_c(t_{i-1}, t_i) \\ &= \frac{\Delta\varepsilon_{cf}(t_{i-1}, t_i)N - 1/E_p \Delta\sigma_{pr}(t_{i-1}, t_i)}{N+1 + N/M}.\end{aligned}\quad (16)$$

Finally, the prestress variation in time interval $[t_{i-1}, t_i]$ can be further obtained according to the constitutive equation, and then the corresponding prestress loss in this period and the effective prestress value at time t_i are obtained. The above calculation results are all used as the initial value in the next time interval for stepwise calculation. The prestress variation of the prestressing tendons in time interval $[t_{i-1}, t_i]$ and the effective prestress at time t_i can be calculated as

$$\begin{aligned}\Delta\sigma_p(t_{i-1}, t_i) &= E_p \Delta\varepsilon_p(t_{i-1}, t_i) + \Delta\sigma_{pr}(t_{i-1}, t_i), \\ \sigma_p(t_i) &= \sigma_{p0} - \sum_{k=1}^i \Delta\sigma_p(t_{k-1}, t_k),\end{aligned}\quad (17)$$

where σ_{p0} is the initial prestress of prestressing tendons.

2.2. Time-Dependent Corrosion Model. Corrosion is the main cause of the deterioration of concrete structure [31–33], and one of its direct effects is the cross-sectional area loss of prestressing and nonprestressing steels [24]. Here, the most used pitting model proposed in [34] is adopted to calculate the cross-sectional area of nonprestressing steel after corrosion. The cross-sectional area loss model of prestressing steel strands proposed in [35] is also adopted because of its simplicity and rationality. Therefore, the net cross-sectional area of a 7-wire prestressing steel strand at time t can be expressed as [36]

$$\begin{aligned}A_p(t) &= \sum_{q=1}^6 A_{ow,q} [t, p_{ow,q}^M(t, i_{corr}, t_c, l)] \\ &\quad + A_{iw} [t, p_{iw}^M(t, i_{corr}, t_c, l)],\end{aligned}\quad (18)$$

where $A_{ow,q}(t, p_{ow,q}^M)$ and $A_{iw}(t, p_{iw}^M)$ are, respectively, the cross-sectional areas of the q th outer wire and inner wire of prestressing steel strand at time t , which are assumed to be calculated using the pit model proposed in [34]. $p_{ow,q}^M(t, i_{corr}, t_c, l)$ and $p_{iw}^M(t, i_{corr}, t_c, l)$ are the maximum pit depths of the q th outer wire and inner wire, respectively. They can be simulated as the extreme-value distribution (type I) when the corrosion current density i_{corr} , corrosion initiation time t_c (years), and wire length l (mm) are given. t_c is related to corrosion environment and concrete cover. The corresponding probability model of maximum pit depth is shown in [25].

2.3. Model Verification. After deducting all the instantaneous prestress loss produced in tension stage, the value of effective prestress at any time can be obtained by bringing the initial effective prestress into the prediction model of long-term prestress loss. To verify the validity of the prediction model, the long-term prestress loss considering and not considering the effect of corrosion is predicted in turn, and the prediction results are compared with the experimental results.

The measured data of time-dependent prestress loss of seven bonded PC members under the noncorrosion condition and laboratory environment in [17] are selected here to verify the validity of the proposed method. Due to the length limitation of the paper, the relevant test parameters are not listed here and can be found in [17]. Their long-term prestress loss is calculated by the proposed prediction model, and the time-dependent results are compared with that of JTG3362-2018, CEB-FIP 90, and AASHTO LRFD specifications, as shown in Table 1.

Due to the lack of measured value of prestress loss under the effect of corrosion, an indirect method is used to verify the validity of the prediction model of long-term prestress loss. That is to say, it is verified by comparing the effective

TABLE 1: Comparison of experimental and theoretical values of long-term prestress loss.

Beam	Initial prestressing force of each tendon (kN)	Quantity and layout form of prestressing tendon	Measured value (MPa)	Theoretical value (MPa)	JTG3362-2018 (MPa)	CEB-FIP 90 (MPa)	AASHTO LRFD (MPa)
PC1	100.1	1 (curve)	48.0	45.0	52.8	66.5	67.4
PC3	102.3	1 (curve)	45.7	45.4	52.8	66.5	67.4
PC4	135.9	1 (curve)	70.6	66.3	65.6	78.6	80.1
PC5	108.7	1 (straight)	55.2	53.8	59.6	69.5	69.4
PC6	101.4	2 (straight)	53.3	56.2	56.5	62.4	68.8
PC7	102.6	1 (straight)	46.8	48.1	50.4	65.6	64.1
PC8	106.0	1 (straight)	49.0	51.2	55.1	66.0	67.6

prestress calculated by the measured cracking load with the theoretical calculation results [5, 35]. Considering that the higher corrosion rate tends to produce serious corrosion-induced concrete cracking in the electrochemical accelerated corrosion test of PC members, four corroded PC beams (PCB8 and CB5 to CB7) with relatively low cross-section corrosion rate in [37] are selected to predict the effective prestressing force. These beams have a rectangular cross section of 150×220 mm while the span is 2000 mm. The lower relaxation steel strand with a diameter of 15.24 mm was used as prestressed tendons, the control stress of tensioning was 1395 MPa, and the concrete was prestressed at the age of 28 days. The actual measured values of yield and ultimate strength of lower relaxation steel strand are 1830 MPa and 1910 MPa, respectively. Two deformed bars with a diameter of 8 mm and yield strength of 235 MPa were arranged at the bottom of each beam, while the corresponding values at the top were 12 mm and 335 MPa. These beams were corroded after being immersed in 5% NaCl solution for 3 days, and the average corrosion current density was $180 \mu\text{A}/\text{cm}^2$. The nonprestressed reinforcement was not corroded due to the use of epoxy resin. The average value of concrete compressive strength of beams PCB8, CB5, CB6, and CB7 is 34.28 MPa, 32.35 MPa, 32.35 MPa, and 34.28 MPa, respectively. The average unit weight of concrete is $2400 \text{ kg}/\text{m}^3$. The average temperature and humidity of the area where the laboratory is located are, respectively, 17.2°C and 78% according to the data given by the China Meteorological Administration (CMA).

In addition, two posttensioned PC members (PCB-2 and PCB-8) with a rectangular cross section of 150×250 mm and a span of 2000 mm in [38] are also considered. The concrete grade and the corrosion duration of beam PCB-2 are 51.3 MPa and 30 days and 44.6 MPa and 60 days of beam PCB-8. The average corrosion current density was $200 \mu\text{A}/\text{cm}^2$, and these beams were corroded after immersing the PC beams for 3 days. The yield strength and initial elasticity modulus of the lower relaxation steel strand with a diameter of 15.24 mm were 1661 MPa and 2.02×10^5 MPa. The ordinary steel reinforcement consisted of four bars with a diameter of 12 mm and yield stress of 400 MPa. The tensile stress was calculated as 1312.1 MPa according to the given prestress level. The average temperature and humidity during the experiment were, respectively, 11.8°C and 72% based on the data provided by CMA. The comparison of experimental and theoretical values of effective prestressing force is shown in Table 2.

As indicated in Table 1, the calculation results of the prediction model proposed in this paper and the JTG3362-2018 specification are closer to the experimental values than the CEB-FIP 90 model and AASHTO LRFD refined method. However, compared with the proposed prediction method, the prediction method in JTG3362-2018 specification ignores the interaction between shrinkage, creep of concrete, and prestressing steel relaxation. Moreover, the calculated values of effective prestressing force are in good agreement with the experimental values in Table 2, which indirectly verifies the validity of the proposed prediction model. In conclusion, the proposed model considering the coupled effect of multifactor is applicable to the prediction of long-term prestress loss.

3. Uncertainty Analysis of Long-Term Prestress Loss

As indicated in the previous section, the proposed prediction model of long-term prestress loss involves a large number of calculation parameters, including the material, structural dimensions, environmental parameters, load effects, and corrosion-related parameters [39]. Since the values of these parameters are usually obtained by the statistical analysis of limited data, their uncertainties should be considered in the prediction of long-term prestress loss.

Additionally, the uncertainty of relevant calculation models in the prediction process of long-term prestress loss should also be considered. The shrinkage and creep models of concrete in the existing codes are mostly empirical or semiempirical and semitheoretical models based on experimental data, and there are inevitable errors in their calculation results compared with the actual effect of shrinkage and creep of concrete. Therefore, the uncertainty coefficients of concrete shrinkage and creep model are incorporated within the prediction process. According to the statistical analysis results in [40], the uncertainty coefficients of creep and shrinkage models in CEB-FIP 90 code are subject to the standard normal distribution, in which the mean values of both are 1, and the coefficient of variation is 0.339 and 0.451, respectively. Moreover, the maximum pit depth of prestressing steel strand also has great uncertainty under the effect of corrosion. The maximum pit depth at different times can be simulated as a random variable subject to the extreme-value type I distribution, and the probability model proposed in [36] is also incorporated within the prediction process.

TABLE 2: Comparison of experimental and theoretical values of effective prestressing force.

Beam	Tension stress (MPa)	Corrosion rate (%)	M_c (kN·m)	T_{exp} (kN)	T_{cal} (kN)	T_{cal}/T_{exp}	Source
PCB8	1395	1.28 (m_c)	18	194	184.3	0.95	[37]
CB5	1395	12.06 (m_c)	16.5	177.2	166.4	0.94	
CB6	1395	19.47 (m_c)	15	160.3	158.3	0.99	
CB7	1395	26.96 (m_c)	13.5	143.5	149.3	1.04	
PCB-2	1312.1	3.22 (m_s)	20.7	130.1	131.9	1.01	[38]
PCB-8	1312.1	7.53 (m_s)	17.5	103.9	99.6	0.96	

Note. m_c = maximum cross-sectional area loss rate, m_s = mass loss rate, M_c = cracking moment, T_{exp} = experimental value of effective prestressing force calculated based on the cracking moment, and T_{cal} = theoretical value of effective prestressing force.

4. Reliability Analysis of Crack Resistance of Box-Girder Bridge

According to the provisions of JTG3362-2018 [11], the normal tensile stress of concrete at the edge of normal section and inclined section of PC box-girder members under the effect of long-term load should satisfy $\sigma_{lt} \leq \sigma_{pc}$ and $\sigma_{tp} \leq 0.4f_{tk}$, respectively. Moreover, the maximum compressive stress of concrete at the compression zone of the normal section also needs to satisfy $\sigma_{kc} + \sigma_{pt} \leq 0.5f_{ck}$, in which σ_{lt} is the normal tensile stress of concrete at the bottom edge of the section under the effect of long-term

load, and σ_{pc} is the precompression stress of concrete at the bottom edge of the section under the effect of effective prestressing force. σ_{tp} , σ_{kc} , and σ_{pt} are principal tensile stress, normal compressive stress, and tensile stress of concrete under the combined effect of long-term load and effective prestressing force, respectively. f_{tk} and f_{ck} are standard values of axial tensile and compressive strength of concrete, respectively.

Based on the previous provisions relating to concrete cracking and reliability theory, the limit state functions of concrete cracking at the bottom slab, top slab, and web of PC box-girder can be expressed in turn as

$$\begin{aligned}
 g_b(t_i) &= \frac{F_{tp}(t_i)}{A_c(t_i)} + \frac{F_{tp}(t_i)e_p(t_i)y_b(t_i)}{I_c(t_i)} - \frac{[M_{dle}(t_i) + M_{lle}(t_i)]y_b(t_i)}{I_c(t_i)}, \\
 g_t(t_i) &= 0.5f_{ck} - \left[\frac{F_{tp}(t_i)}{A_c(t_i)} - \frac{F_{tp}(t_i)e_p(t_i)y_t(t_i)}{I_c(t_i)} + \frac{M_{dle}(t_i) + M_{lle}(t_i)}{I_c(t_i)}y_t(t_i) \right], \\
 g_w(t_i) &= 0.4f_{tk} - \sigma_{tp}(t_i),
 \end{aligned} \tag{19}$$

where $g_b(t_i)$, $g_t(t_i)$, and $g_w(t_i)$ are the value of crack resistance limit state functions of the bottom slab, top slab, and web at time t_i , respectively. $F_{tp}(t_i)$ is the total effective prestressing force of this section, and $y_b(t_i)$ is the distance from the bottom edge to the centroid of the concrete section. $M_{dle}(t_i)$ and $M_{lle}(t_i)$ are the bending moment values of the section under dead and live load effect, respectively. $\sigma_{tp}(t_i)$ is the principal tensile stress of concrete in web, and it can be calculated by the simplified two-dimensional stress model provided by JTG3362-2018 specification [11]. It is worth noting that the time-dependent effect of model parameters is further considered here.

After obtaining the limit state function of concrete cracking, the cracking probability and reliability index of crack resistance of local area or whole section can be calculated by different classical reliability calculation methods, including the sampling simulation method, JC method, and response surface method (RSM). It is worth noting that as long as the value of any limit state function related to concrete cracking is less than 0, the whole section is considered to be cracked in this calculation. The reliability index of crack resistance of local area or whole section at time t_i is, respectively, given in (20) and (21)

$$\beta_{l,z}(t_i) = \Phi^{-1} [1 - P_{f,z}(t_i)] = \Phi^{-1} \{1 - P[g_z(t_i) < 0]\}, \quad z = b, t, w, \tag{20}$$

$$\beta_{os}(t_i) = \Phi^{-1} \{ [1 - P_{f,b}(t_i)] [1 - P_{f,t}(t_i)] [1 - P_{f,w}(t_i)] \}, \tag{21}$$

where $\beta_{l,z}(t_i)$ and $P_{f,z}(t_i)$ are the reliability index of crack resistance and cracking probability of local area, respectively. The subscript z denotes that b , t , and w , respectively,

correspond to the above two indexes of bottom slab, top slab, and web. $\Phi^{-1}(\cdot)$ is the inverse of the cumulative distribution function of standard normal distribution, $P(\cdot)$ is the

probability function, and $\beta_{os}(t_i)$ is the reliability index of crack resistance of the whole section.

5. Application Example

5.1. Bridge Description. The proposed prediction model of long-term prestress loss and crack resistance analysis approach is applied to a three-span PC box-girder bridge located in a marine environment. The span layout of the superstructure of the main bridge is 80 m + 150 m + 80 m. The superstructure is made of C55 concrete, of which the 28-day standard cubic compressive strength is 50 MPa and the initial elasticity modulus $E_c(t_0)$ is 3.55×10^4 MPa. Considering that the bottom slab of the midspan section is easy to crack and the crack also has a great impact on the deflection of the bridge, the midspan section is selected as the research object. Two hot-rolled ribbed steel bars of the JL32 type are arranged as the vertical prestressing steel in webs on both sides of the midspan section. The corresponding tension control stress is 706.5 MPa, and the average value of the initial elastic modulus E_p is 2×10^5 MPa. Twenty-four (excluding one pair of the spare prestressing tendon) and two longitudinal prestressing tendons (PTs) are equipped in the bottom and top slab, respectively. The corresponding tension control stress, nominal tensile strength, and cross-sectional area of longitudinal prestressing steel strands are 1395 MPa, 1860 MPa, and 140 mm^2 , respectively. The HRB400 grade hot-rolled ribbed steel bar and the HPB300 grade hot-rolled plain steel bar are, respectively, used for longitudinal nonprestressing steel with a diameter greater than 12 mm and less than 12 mm, and the corresponding average values of initial elastic modulus are 2.0×10^5 MPa and 2.1×10^5 MPa, respectively. The initial cross-sectional area $A_0 = 9.09 \times 10^6 \text{ mm}^2$, initial section inertia moment $I_0 = 1.3485 \times 10^{13} \text{ mm}^4$, and the external perimeter of section is 30020 mm. The initial total cross-sectional area of longitudinal PTs at the bottom and top slab is $A_{bpo} = 5.04 \times 10^4 \text{ mm}^2$ and $A_{tpo} = 4.2 \times 10^3 \text{ mm}^2$, respectively. The initial total cross-sectional area of longitudinal nonprestressing steels $A_{s0} = 3.7486 \times 10^4 \text{ mm}^2$. The initial distance from the centroid of all longitudinal PTs to the centroid of the concrete section and bottom edge is $e_{p0} = 1593.6 \text{ mm}$ and $y_{bpo} = 368.5 \text{ mm}$, respectively. In addition, the bending moment values generated by the dead and live load are obtained by Midas Civil finite element analysis, which are $7.65 \times 10^4 \text{ kN}\cdot\text{m}$ and $4.02 \times 10^4 \text{ kN}\cdot\text{m}$, respectively. The overall layout of the case bridge, cross-section dimensions, and arrangement of longitudinal PTs of the midspan section is shown in Figure 2, and the random parameters related to the calculation are shown in Table 3.

In the calculation process, all external load effects are assumed to be imposed according to the design value after all PTs are tensioned, and the effect of system conversion is also no longer considered. Table 4 shows the mean value of effective prestress of longitudinal and vertical PTs in the midspan section after deducting all instantaneous losses. It is noteworthy that, in the analysis of crack resistance of the web, only three typical positions of the upper and lower haunch and the centroid of the initial concrete section are

selected as the calculation points of principal tensile stress for simplifying. In addition, the corresponding failure probability of concrete cracking in the midspan section is very small due to the high compressive stress reserve at the beginning of service, so the JC method is selected here to calculate the reliability index of crack resistance. The creep coefficient and shrinkage strain of concrete are calculated by the CEB-FIP 90 model.

5.2. Results and Discussion

5.2.1. Long-Term Prestress Loss. The time-dependent probability density curve of long-term prestress loss of typical tendons CT1 and CB1 is presented in Figure 3. As indicated, the long-term prestress loss at different times can be modelled by a normal distribution when considering the effect of corrosion. With the increase of service time, the corresponding time-dependent probability density curve tends from steep to gentle, and the range of long-term prestress loss is also gradually expanded. This shows that the dispersion of long-term prestress loss gradually increases with the service time.

Figure 4 shows the variation of long-term prestress loss of CT1 and CB1 and the average loss of all longitudinal PTs. The corresponding loss interval at the confidence level of 95% is also presented. As indicated in Figures 4(a) and 4(b), when the service time of case bridge is 10, 30, and 100 years, the mean value of long-term prestress loss of CT1 is 127.3 MPa, 144.4 MPa, and 157.3 MPa, respectively. They account for 9.13%, 10.35%, and 11.28% of the initial tensile stress. The corresponding values of CB1 are, respectively, 78.7 MPa, 89.1 MPa, and 98.4 MPa, accounting for 5.64%, 6.62%, and 7.29% of the initial tensile stress. This indicates that the long-term prestress loss of PTs has the characteristics of rapid growth first and then slow growth, and more than 90% of long-term prestress loss will be completed within 30 years of service.

The coefficient of variation (COV) of long-term prestress loss decreases first, then remains unchanged, and finally stabilizes above 0.24 after 20 years of service (Figure 4(d)). This also shows that the uncertainty of parameters and calculation models will lead to the significant variability of long-term prestress loss. After 10, 30, and 100 years of service, the upper bound of long-term prestress loss of CT1 at the confidence level of 95% is 51.04%, 51.12%, and 50.64% higher than the results obtained by the deterministic analysis, respectively. The corresponding results of CB1 are 50.25%, 49.38%, and 49.60%, respectively. This indicates that the final effective prestressing force of CT1 and CB1 will be 7.60% and 4.2% lower than that of the deterministic analysis when the degradation and uncertainty of the cross-sectional area of prestressed tendons are not considered. Moreover, with the increase of long-term prestress loss, number of uncertain parameters, or uncertainty strength of each parameter, the upper bound of long-term prestress loss is all significantly higher than the result obtained by deterministic analysis. Therefore, it is recommended to estimate the long-term prestress loss at a reasonable confidence level and select

TABLE 3: Statistical characteristics of parameters related to long-term prestress loss prediction.

Classification of parameters	Description of parameters	Distribution	(Mean, COV)	Source
Material and dimension parameters	Initial elastic modulus of concrete, E_{c0} (MPa)	Normal	$(3.55 \times 10^4, 0.04)$	[41]
	Concrete cover	Normal	$(1.0178^*, 0.0496)$	
	Initial elastic modulus of prestressing steel strand, E_p (MPa)	Normal	$(1.95 \times 10^5, 0.04)$	
	Initial elastic modulus of HRB400 grade nonprestressing steel (MPa)	Normal	$(2 \times 10^5, 0.04)$	
	Initial elastic modulus of HPB300 grade nonprestressing steel (MPa)	Normal	$(2.1 \times 10^5, 0.04)$	
	Strength of HRB400 grade nonprestressing steel (MPa)	Normal	$(434, 0.0791)$	
Environmental parameters	Strength of HPB300 grade nonprestressing steel (MPa)	Normal	$(324.6, 0.1211)$	D
	Initial compressive strength of concrete, f_{c0} (MPa)	Normal	$(55.2, 0.137)$	
	Annual relative humidity, RH (%)	Normal	$(76.9, 0.061)$	
	Annual average temperature, T ($^{\circ}$ C)	Normal	$(21.7, 0.251)$	
Model parameters	Uncertainty coefficient of concrete creep model, Ψ_c	Normal	$(1, 0.339)$	CMA
	Uncertainty coefficient of concrete shrinkage model, Ψ_s	Normal	$(1, 0.541)$	
Load effect parameters	Dead load effect (bending moment), M_{dle} (kN·m)	Normal	$(1.0148^*, 0.0431)$	[41]
	Live load effect (bending moment), M_{lle} (kN·m)	Extreme I	$(0.7995^*, 0.0862)$	
	Shear force, V_s (kN)	Normal	$(1.0148^*, 0.0431)$	
Corrosion-related parameters	Initial tension control stress, σ_{con} (MPa)	Normal	$(1^*, 0.04)$	[42]
	Surface chloride concentration, C_s (kg/m^3)	Normal	$(3.5, 0.5)$	[24]
	Threshold chloride concentration, C_{cr} (kg/m^3)	Normal	$(0.9, 0.2)$	
	Chloride diffusion coefficient, D_0 (cm^2/year)	Log normal	$(0.631, 0.2)$	
	Corrosion current density, i_{corr} ($\mu\text{A}/\text{cm}^2$)	Normal	$(1, 0.2)$	
		Penetration ratio, R	Normal	$(6.0, 0.18)$

Note. *The ratio of actual value to nominal value, D = design data, and CMA = china meteorological administration.

TABLE 4: Mean value of effective prestress after deducting all instantaneous losses.

Prestressing tendons	CB1	CB2	CB3	CB4	CB4'	CB5	CB5'	CB6	CB7	CB8	CB9	CB10	CT1	N138
Initial tension control stress (MPa)	1395	1395	1395	1395	1395	1395	1395	1395	1395	1395	1395	1395	1395	706.5
Effective prestress (MPa)	1204.9	1243.3	1261.4	1271.4	1271.4	1269.9	1269.9	1264.2	1254.1	1244.9	1235.9	1227.3	1261.8	626.5

Note. CB = PTs in bottom slab, CT = PTs in top slab, and N = vertical PTs.

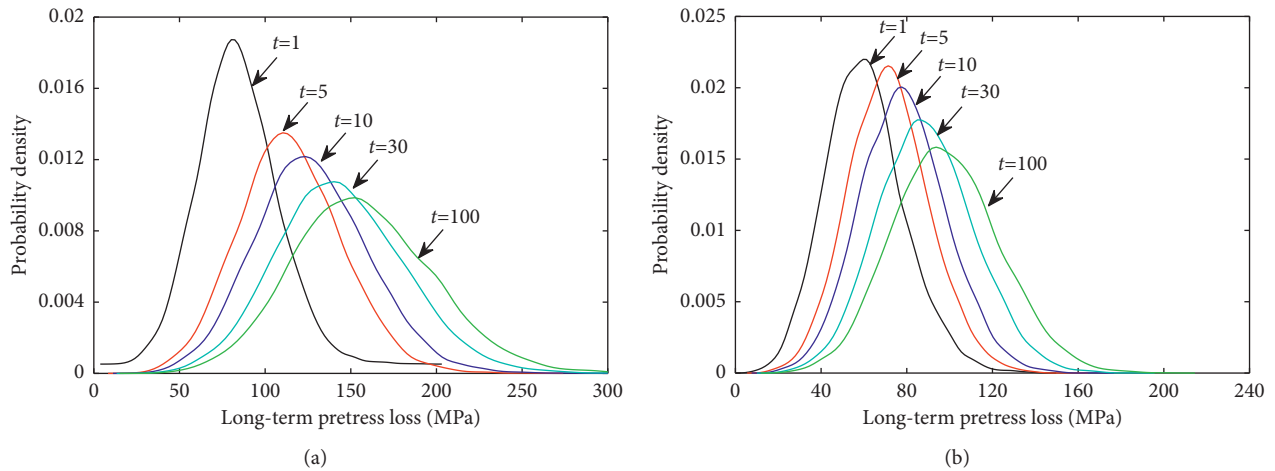


FIGURE 3: Probability density of long-term prestress loss of CT1 and CB1 at different time. (a) CT1. (b) CB1.

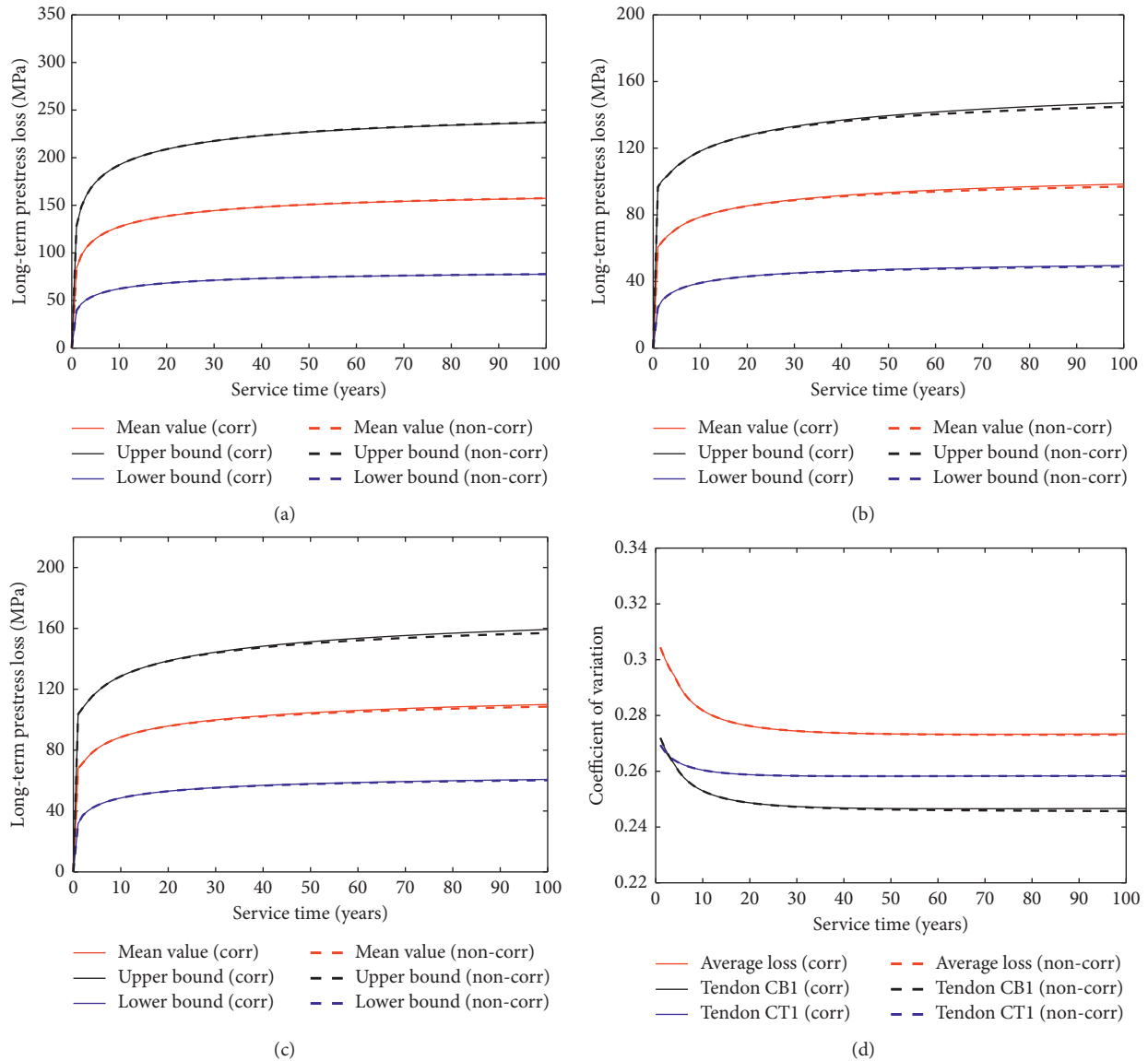


FIGURE 4: Time-dependent curve related to long-term prestress loss. (a) CT1. (b) CB1. (c) Average loss of all longitudinal PTs. (d) Coefficient of variation.

5.2.3. Effective Prestressing Force. The long-term prestress loss and the reduction of the cross-section area of the tendon will reduce the effective prestressing force, which will cause the change of concrete stress and structural crack resistance. Thus, the variation of effective prestressing force also needs to be analysed. As indicated in Figure 5, the effective prestressing force of CT1 is only slightly reduced in service, and the mean value of effective prestressing force at 100 years of service is only decreased by about 12.7% compared with the initial value. While the effective prestressing force of CB1 and whole section is greatly reduced when considering the effect of corrosion, the corresponding mean values are only 29.2% and 33.8% of the initial mean value, respectively. This is mainly because the corrosion of CT1 does not occur during the service period due to the protection of the larger concrete cover and the deck pavement larger than 17 cm, but the cross-section area loss of CB1 and all longitudinal PTs

gradually increases with the development of corrosion process. Therefore, it can be considered that the reduction of the cross-sectional area of prestressed tendons caused by corrosion is the main reason for the decrease in effective prestressing force.

Additionally, Figures 5(b) and 5(c) also show that the variation of effective prestressing force of CB1 and all longitudinal PTs in this section can be divided into three phases. In the first phase (the first year of service), the significant increase of long-term prestress loss is the main reason for the rapid reduction of effective prestressing force of CB1 and the whole section. In the second phase (about 1 to 9 years of service), the time-dependent prestress loss caused by concrete shrinkage and creep is the main reason for the decrease of effective prestressing force, and the pace of decline is obviously slower than before. This is because the PTs have not been corroded and the prestress loss caused by

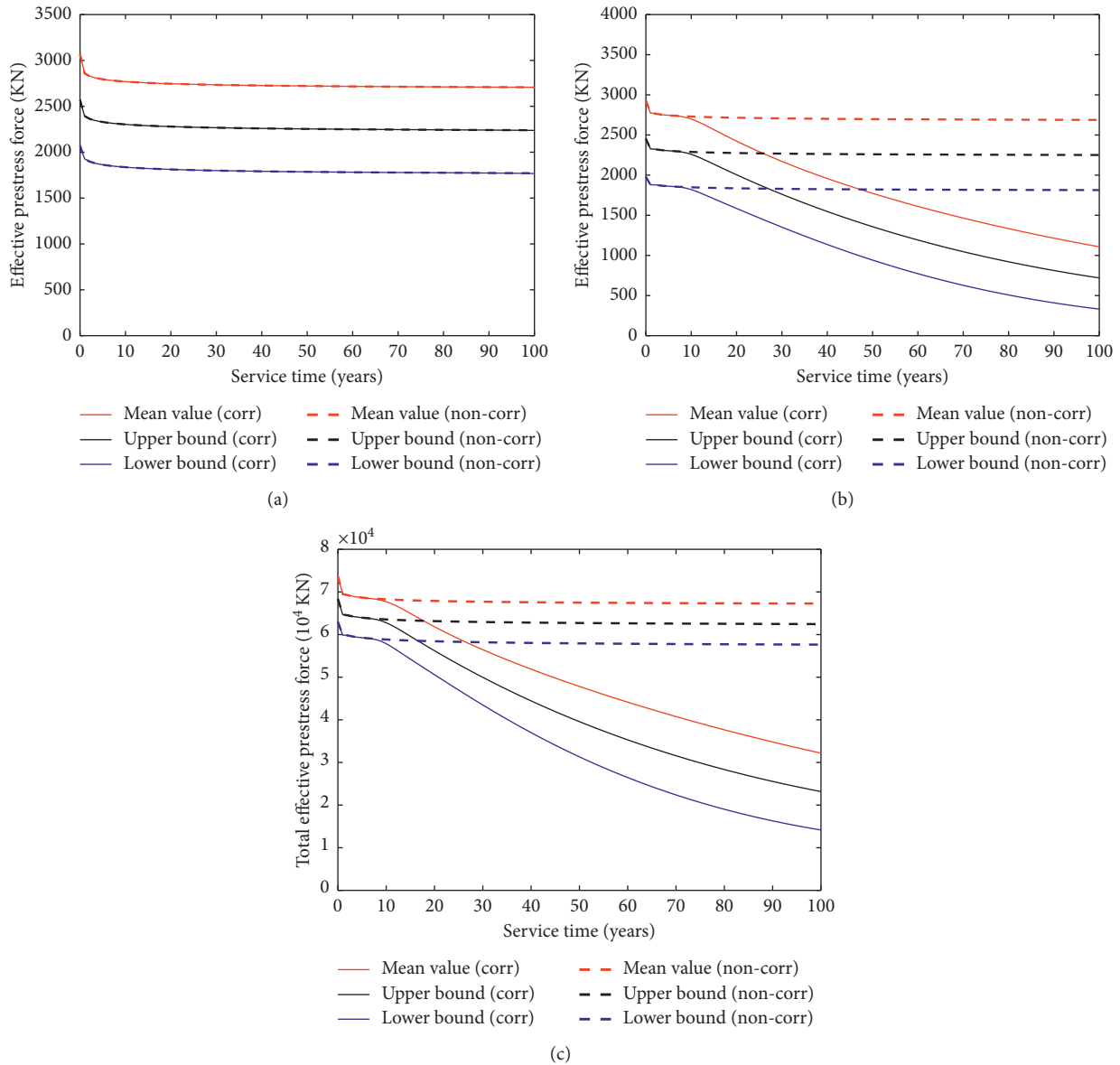


FIGURE 5: Time-dependent curve of effective prestress force. (a) CT1. (b) CB1. (c) The whole section.

prestressing steel relaxation is very minor in this phase. In the third phase (after about 9 years of service, i.e., PTs have been corroded), the cross-sectional area loss of all longitudinal PTs becomes the primary reason for the decrease of effective prestressing force, and its degradation rate increases first and then slows down as the corrosion turn worse.

5.2.4. Crack Resistance. The reliability index of crack resistance of the midspan section is shown in Figure 6. As indicated, the reliability indexes of crack resistance of all local areas gradually decrease with the increasing service time. After about 9 years of service, the decreasing rate of reliability index considering the effect of corrosion is much higher than that without considering. When the corrosion effect is not considered, only the long-term prestress loss leads to the decrease of effective prestressing force. At this

time, the concrete at the bottom slab edge and three calculated fibers at the web still maintain highly precompressive stress, and the increase of compressive stress of concrete at the top slab is relatively low. Accordingly, the bottom slab, top slab, and web of the section all maintain good performance of crack resistance during the whole service period, and the whole structure will not crack. When the corrosion effect is considered, the reliability indexes of crack resistance of the bottom slab and web reduce to the target reliability of 1.5 (failure probability is about 0.067) in the 27th and 38th years, respectively. At this time, the concrete in the above areas should be repaired. For the top slab, the change of effective prestressing force has little effect on the compressive stress growth of concrete at the edge of the top slab, and the discreteness of the compressive stress of concrete at the top slab is also small in this case. As a result, the reliability index of crack resistance of top slab after 100 years of

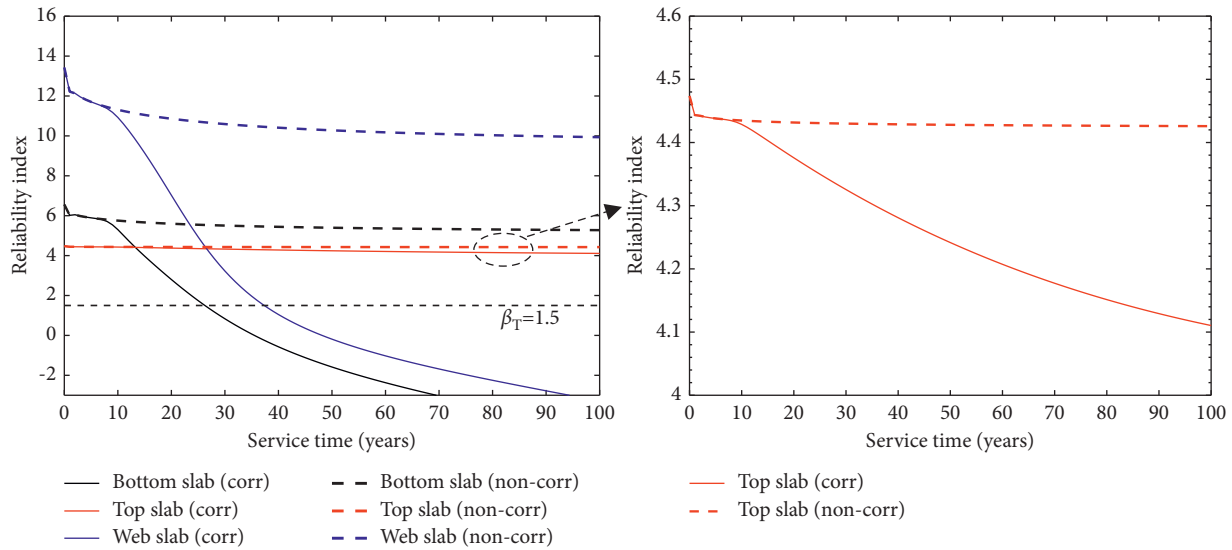


FIGURE 6: Time-dependent reliability index of crack resistance of local area of box-girder section.

service is only 8.11% lower than the initial value, and its value is 4.11 (Figure 6). As such, the crack resistance of concrete at bottom slab and web is more sensitive to the coupled effect of corrosion and long-term prestress loss than that of top slab.

For the concrete at the edge of the bottom slab, its initial compressive stress is greatly improved by the application of prestressing force, and the mean and lower bound of the confidence interval are up to 7.41 MPa and 5.19 MPa, respectively. In addition, the standard deviation of the initial compressive stress is also relatively small. As such, the bottom slab has good crack resistance performance at first, and its initial reliability index of crack resistance is 6.55. After that, the variation of crack resistance of the bottom slab can also be divided into three phases similar to the change of effective prestressing force. In the first stage, the rapid decrease of effective prestressing force (Figure 5(c)) leads to a significant reduction of compressive stress of concrete at the bottom slab. The corresponding reliability index of crack resistance also decreases rapidly, with a decrease of 7.86% in the first year. In the second phase, since the degradation rate of concrete compressive stress caused by the total effective prestressing force of the section is minor, the reliability index of crack resistance decreases slowly. The final reliability index is only 10.36% lower than the initial value. In the following service period (i.e., the third phase), the significant reduction of total effective prestressing force causes the rapid decrease of concrete compressive stress. This eventually leads to tensile stress or cracking of concrete at the edge of the bottom slab after the precompression stress is completely eliminated. The variations of crack resistance of the top slab and web during the service period are very similar to that of the bottom slab (Figure 6); thus, they are not described in detail here.

5.2.5. *Effect of Vertical PTs on Crack Resistance.* The variation of crack resistance of web and whole section with and without vertical PTs is shown in Figures 7 and 8. As

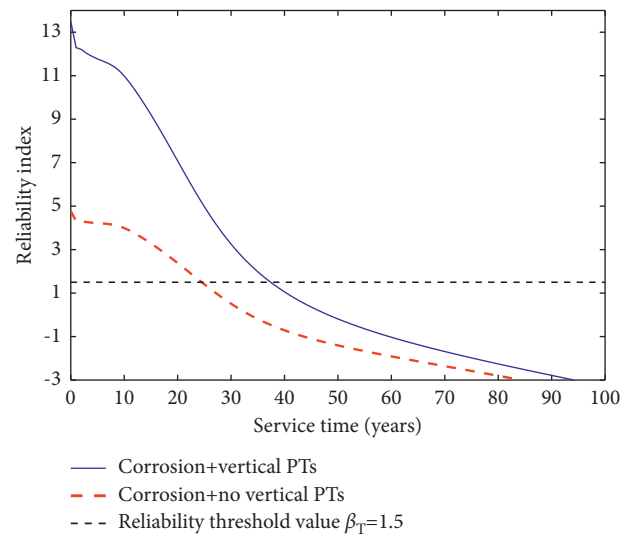


FIGURE 7: Effect of vertical PTs on crack resistance of web.

indicated in Figure 8, the initial reliability index of web is only 4.83 without setting vertical PTs due to the lack of vertical compressive stress reserve of web concrete, which is much lower than that of setting vertical PTs. In this case, the concrete fibers at three calculation points are all subjected to principal tensile stress, in which the maximum value of principal tensile stress is 0.41 MPa. With the increase of prestress loss and corrosion degree, the reliability index of web decreases to the threshold value in about 25 years, which is 13 years (accounting for 34.2%) ahead of the corresponding value when setting vertical PTs. For sections near support or at 1/4 span, the web crack resistance is worse, and the cracking time of web is also greatly advanced due to the greater shear force and shear stress of these sections. Therefore, the vertical PTs should be reasonably arranged, and the prestress loss should be minimized to ensure that web concrete has sufficient compressive stress reserve.

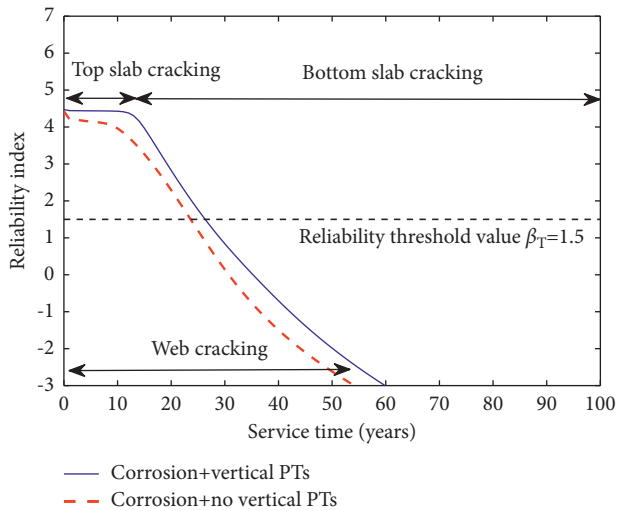


FIGURE 8: Effect of vertical PTs on crack resistance of the whole section.

As indicated in Figure 8, the time when the reliability index of the whole section decreases to the threshold value is about 14.8% earlier than that of setting vertical PTs. In addition, according to the comprehensive analysis of Figures 6 to 8, the section is more prone to web cracking before 54 years of service without setting vertical PTs. At this time, the reliability index of the whole section has already fallen below the reliability threshold value. This indicates that the overall crack resistance performance of the section under this condition is mainly determined by the crack resistance performance of web. When the web is provided with vertical PTs, the cracking position is more likely to be at the top slab in the first 13 years of service, and it will change to the bottom slab during subsequent service. Accordingly, based on the previous evaluation results of local crack resistance, the targeted protection or repair measures for concrete in different regions and times can be formulated by the bridge management department to improve the durability and safety of the bridge in service.

6. Conclusions and Recommendations

This paper uses the well-established step-by-step approach to estimate long-term prestress loss in combination with the expressions estimating the cross-sectional area loss of nonprestressing and prestressing steels caused by corrosion. In addition, an assessment approach of crack resistance reliability of box-girder is developed considering the coupled effect of corrosion and time-dependent long-term prestress loss. The proposed approach is applied to a three-span PC box-girder bridge. The following conclusions are drawn:

- (1) Considering the coupled effect of shrinkage and creep of concrete, prestressing steel relaxation, presence of nonprestressing steel, and corrosion, a prediction model of long-term prestress loss is established by using the well-established step-by-step method, and its validity is also verified by the existing test data.

- (2) The prediction results of long-term prestress loss have high uncertainty, and the upper bound of long-term prestress loss at the confidence level of 95% is approximately 50% higher than the result obtained by deterministic analysis. It is recommended to select the upper bound of confidence interval as the most unfavorable value of long-term prestress loss from the perspective of preventing early cracking.
- (3) The effect of corrosion on the long-term prestress loss is basically negligible, but it is closely related to the effective prestressing force and crack resistance of the section. In addition, the crack resistance of bottom slab and web is more sensitive to the coupled effect of corrosion and long-term prestress loss than that of top slab.
- (4) Setting vertical PTs can greatly improve the crack resistance of web and whole section. In this case study, the time when the reliability index of crack resistance of web without setting vertical PTs decreases to the reliability threshold value is at least 36.8% earlier than that of setting vertical PTs.

The limitation of this study is that the effect of corrosion on bond between strand and concrete is not considered. In future research, the effect of bond degradation due to strand corrosion on prestress loss needs to be further considered. Moreover, a series of monitoring tests of long-term prestress loss of corroded PC structure need to be carried out so as to obtain more measured data to improve the applicability of the proposed prediction method.

Data Availability

The data used to support the findings of this study are available from the corresponding author upon request.

Conflicts of Interest

The authors declare no conflicts of interest.

Acknowledgments

This study was supported by the National Natural Science Foundation of China (Grant no. 52108135), the Hunan Provincial Natural Science Foundation of China (Grants nos. 2022JJ40024, 2021JJ50153, and S2022JSSLH0137), and the Research Foundation of Education Bureau of Hunan Province (Grants nos. 21B0723, 18A401, 21C0671, and 21B0721).

References

- [1] L. A. Caro, J. R. Martí-Vargas, and P. Serna, "Prestress losses evaluation in prestressed concrete prismatic specimens," *Engineering Structures*, vol. 48, pp. 704–715, 2013.
- [2] I. H. Yang, "Uncertainty and updating of long-term prediction of prestress forces in PSC box girder bridges," *Computers & Structures*, vol. 83, no. 25–26, pp. 2137–2149, 2005.
- [3] S. Biswal and A. Ramaswamy, "Uncertainty based model averaging for prediction of long-time prestress losses in

- concrete structures,” *Construction and Building Materials*, vol. 153, pp. 469–480, 2017.
- [4] S. A. Youakim, A. Ghali, S. E. Hida, and V. M. Karbhari, “Prediction of long-term prestress losses,” *PCI Journal*, vol. 52, no. 2, pp. 116–130, 2007.
 - [5] L. Dai, H. Bian, L. Wang, M. Potier-Ferry, and J. Zhang, “Prestress loss diagnostics in pretensioned concrete structures with corrosive cracking,” *Journal of Structural Engineering*, vol. 146, no. 3, Article ID 04020013, 2020.
 - [6] M. Yuan, D. Yan, H. Zhong, and Y. Liu, “Experimental investigation of high-cycle fatigue behavior for prestressed concrete box-girders,” *Construction and Building Materials*, vol. 157, pp. 424–437, 2017.
 - [7] ACI 209R-92, *Prediction of Creep, Shrinkage and Temperature Effects in concrete Structures*, vol. 209, pp. 1–10, ACI Committee, Farmington Hills, MI, USA, 1992.
 - [8] PCI, *Bridge Design Manual*, Precast/Prestressed concrete institute, Chicago, Chicago, IL, USA, 3rd edition, 2011.
 - [9] CEB-FIP 90, *CEB-FIP Model Code 1990: Design Code*, Thomas Telford, London, UK, 1993.
 - [10] AASHTO, *LRFD Bridge Design Specifications*, American Association of State Highway and Transportation Officials, Washington, DC, USA, 3th edition, 2012.
 - [11] MOT (Ministry of Transport of the People’s Republic of China), *Specifications for Design of Highway Reinforced concrete and Prestressed concrete Bridges and Culverts (JTG 3362-2018)*, MOT, Beijing, China, 2018.
 - [12] AASHTO, *Standard Specifications for Highway Bridges*, American Association of State Highway and Transportation Officials, Washington, DC, USA, 17th edition, 2002.
 - [13] M. K. Tadros, N. Al-Omaishi, S. J. Seguirant, and J. G. Gallt, “Prestress losses in pretensioned high-strength concrete bridge girders,” Transportation Research Board, Washington, DC, USA, 2003.
 - [14] G.-h. Cao, J.-x. Hu, and K. Zhang, “Coupling model for calculating prestress loss caused by relaxation loss, shrinkage, and creep of concrete,” *Journal of Central South University*, vol. 23, no. 2, pp. 470–478, 2016.
 - [15] Mot (Ministry of Transport of the People’s Republic of China), *Specifications for Design of Highway Reinforced concrete and Prestressed concrete Bridges and Culverts (JTG D62-2004)*, MOT, Beijing, China, 2004.
 - [16] Y. L. Gao, “Calculation of long-term stress losses in prestressed concrete members,” Doctoral Dissertation, Central South University, China, Changsha, 2014.
 - [17] T. Guo, Z. Chen, S. Lu, and R. Yao, “Monitoring and analysis of long-term prestress losses in post-tensioned concrete beams,” *Measurement*, vol. 122, pp. 573–581, 2018.
 - [18] T. Lou, S. M. R. Lopes, and A. V. Lopes, “Nonlinear and time-dependent analysis of continuous unbonded prestressed concrete beams,” *Computers & Structures*, vol. 119, pp. 166–176, 2013.
 - [19] P. M. Páez and B. Sensale, “Improved prediction of long-term prestress loss in unbonded prestressed concrete members,” *Engineering Structures*, vol. 174, pp. 111–125, 2018.
 - [20] R. G. Pillai, M. D. Hueste, P. Gardoni, D. Trejo, and K. F. Reinschmidt, “Time-variant service reliability of post-tensioned, segmental, concrete bridges exposed to corrosive environments,” *Engineering Structures*, vol. 32, no. 9, pp. 2596–2605, 2010.
 - [21] M. G. Stewart and J. A. Mullard, “Spatial time-dependent reliability analysis of corrosion damage and the timing of first repair for RC structures,” *Engineering Structures*, vol. 29, no. 7, pp. 1457–1464, 2007.
 - [22] Q. Chen, “Analysis on probability of web cracking risk of box girder bridge based on traditional prestress tensioning technology,” *Journal of Highway and Transportation Research and Development*, vol. 31, no. 8, pp. 91–95, 2014.
 - [23] T. Guo, R. Sause, D. M. Frangopol, and A. Li, “Time-dependent reliability of PSC box-girder bridge considering creep, shrinkage, and corrosion,” *Journal of Bridge Engineering*, vol. 16, no. 1, pp. 29–43, 2011.
 - [24] T. Guo, Z. Chen, T. Liu, and D. Han, “Time-dependent reliability of strengthened PSC box-girder bridge using phased and incremental static analyses,” *Engineering Structures*, vol. 117, pp. 358–371, 2016.
 - [25] B. Tu, Z. Fang, Y. Dong, and D. M. Frangopol, “Time-variant reliability analysis of widened deteriorating prestressed concrete bridges considering shrinkage and creep,” *Engineering Structures*, vol. 153, pp. 1–16, 2017.
 - [26] T. Tong, Q. Yu, and Q. Su, “Coupled effects of concrete shrinkage, creep, and cracking on the performance of post-connected prestressed steel-concrete composite girders,” *Journal of Bridge Engineering*, vol. 23, no. 3, Article ID 04017145, 2018.
 - [27] L. Zhou and Y. C. Chen, *Shrinkage and Creep*, China Railway Press, Beijing, China, 1994.
 - [28] X. Shao, R. Pan, H. Zhao, and Z. Shao, “Prestress loss of a new vertical prestressing anchorage system on concrete box-girder webs,” *Journal of Bridge Engineering*, vol. 19, no. 2, pp. 210–219, 2014.
 - [29] Z. P. Bazant, “Prediction of concrete creep effects using age-adjusted effective,” *ACI Journal*, vol. 69, pp. 212–217, 1972.
 - [30] D. E. Branson, *Deformation of Concrete Structures*, Mc Graw Hill Book Company, New York, NY, USA, 1997.
 - [31] Y. Yang, J. Peng, C. S. Cai, and J. Zhang, “Improved interval evidence theory-based fuzzy AHP approach for comprehensive condition assessment of long-span PSC continuous box-girder bridges,” *Journal of Bridge Engineering*, vol. 24, no. 12, Article ID 04019113, 2019.
 - [32] J. Peng, S. Hu, J. Zhang, C. S. Cai, and L.-y. Li, “Influence of cracks on chloride diffusivity in concrete: A five-phase mesoscale model approach,” *Construction and Building Materials*, vol. 197, pp. 587–596, 2019.
 - [33] J. Peng, Y. Yang, H. Bian, J. Zhang, and L. Wang, “Optimisation of maintenance strategy of deteriorating bridges considering sustainability criteria,” *Structure and Infrastructure Engineering*, vol. 18, no. 3, pp. 395–411, 2022.
 - [34] D. V. Val and R. E. Melchers, “Reliability of deteriorating RC slab bridges,” *Journal of Structural Engineering*, vol. 123, no. 12, pp. 1638–1644, 1997.
 - [35] G. P. Osborn, P. J. Barr, D. A. Petty, M. W. Halling, and T. R. Brackus, “Residual prestress forces and shear capacity of salvaged prestressed concrete bridge girders,” *Journal of Bridge Engineering*, vol. 17, no. 2, pp. 302–309, 2012.
 - [36] Y. Yang, J. Peng, X. Liu, S. C. S. Cai, and J. Zhang, “Probability analysis of web cracking of corroded prestressed concrete box-girder bridges considering aleatory and epistemic uncertainties,” *Engineering Structures*, vol. 228, Article ID 111486, 2021.
 - [37] X. H. Zhang, L. Wang, and J. R. Zhang, “Calculating method of residual prestressing force for corroded PC members,” *Building Structure*, vol. 45, no. 15, pp. 97–101, 2015.
 - [38] K. C. Xu, Y. M. Cao, Z. C. Chen, M. C. Chen, B. Fu, and D. M. Zhu, “Study on the flexural behavior of prestressed concrete beams corroded by simulated acid rain,” *Chinese Journal of Computational Mechanics*, vol. 36, no. 1, pp. 124–131, 2019.

- [39] M. S. Darmawan and M. G. Stewart, "Spatial time-dependent reliability analysis of corroding pretensioned prestressed concrete bridge girders," *Structural Safety*, vol. 29, no. 1, pp. 16–31, 2007.
- [40] Z. P. Bazant and S. Baweja, "Justification and refinements of model B3 for concrete creep and shrinkage 1. Statistics and sensitivity," *Materials and Structures*, vol. 8, no. 7, pp. 415–430, 1995.
- [41] Mohurd (Ministry of Housing and Urban-Rural Development), *Unified Standard for Reliability Design of Highway Engineering Structures (B/T 50283-1999)*, Ministry of Housing and Urban-Rural Development, Beijing, China, 1999.
- [42] A. S. Al-Harthy and D. M. Frangopol, "Reliability-based design of prestressed concrete beams," *Journal of Structural Engineering*, vol. 120, no. 11, pp. 3156–3177, 1994.